ADVANCED GASIFICATION APPLICATIONS OF DIRECT CARBON DIOXIDE UTILISATION IN INTEGRATED BIOMASS ENERGY CYCLES

MICHAEL JOSEPH GREENCORN, BENG, MSC, P.ENG.

SUBMITTED IN FULFILMENT OF THE REQUIREMENTS FOR THE DEGREE OF

Doctor of Philosophy

JAMES WATT SCHOOL OF ENGINEERING

COLLEGE OF SCIENCE AND ENGINEERING

UNIVERSITY *of* GLASGOW

APRIL 2023

Abstract

International agreements seek to limit climate warming to no more than 2°C. For this goal to be achieved, drastic reductions in CO_2 emissions from fossil fuels must be realised in very short timelines. In fact, most climate modelling predictions indicate CO_2 will need to be removed from the atmosphere if the worst effects of climate change are to be avoided. Renewable biomass energy and biomass energy with carbon capture and storage (BECCS) will feature prominently in this substantial decarbonisation regime. Despite this technical forecast, BECCS technologies are unproven at scale. Innovative carbon dioxide utilisation (CDU) strategies are posited as a method for improvement of biomass energy system performance.

Partially recycling CO_2-rich exhaust gases from a syngas fuelled internal combustion engine to a biomass gasifier has the capability to realise a new method for direct carbon dioxide utilisation (CDU) within a bioenergy system. Simulation of an integrated, air-blown biomass gasification power cycle was used to study thermodynamic aspects of this emerging CDU technology. Analysis of the thermodynamic system model at varying gasifier air ratios and exhaust recycling ratios revealed the potential for modest system improvements under limited recycling ratios. Compared to a representative base thermodynamic case with overall system efficiency of 28.14%, employing exhaust gas recycling (EGR) enhanced gasification improved system efficiency to 29.24% and reduced the specific emissions by 46.2 g-CO_2/kWh. Although emissions from biomass power cycles can ultimately be considered CO_2-neutral over time, this reduction in specific emissions from the cycle can minimise the "carbon debt" effect incurred during the initial deployment of biomass power sources.

Further investigation of the EGR-enhanced gasification system revealed the important coupling between gasification equilibrium temperature and exhaust gas temperature through the syngas lower heating value (LHV). Major limitations to the thermodynamic conditions of EGR-enhanced gasification as a CDU strategy result from the increased dilution of the syngas fuel by N_2 and CO_2 at high recycling ratios, restricting equilibrium temperatures and reducing gasification efficiency. N_2 dilution in the system reduces the efficiency by up to 2.5% depending on the gasifier air ratio, causing a corresponding increase in specific CO_2 emissions. Thermodynamic modelling indicates pre-combustion N_2 removal from an EGR-gasification system could decrease specific CO_2 emissions by 9.73%, emitting 118.5 g/kWh less CO_2 than the basic system.

A similar method for improving the efficiency of oxyfuel gasification biomass energy with carbon capture and storage (BECCS) cycles using carbon dioxide recycled from exhaust gases is described and modelled. Thermodynamic simulations show this process can increase the indicated efficiency of a representative cycle by 10.3% in part by reducing the oxygen requirements for the gasification reaction. Exhaust recycling is also shown to have a practical limit beyond which the syngas fuel becomes highly diluted. This diluted syngas results in low combustion and exhaust temperatures which, in turn, negatively influence the gasification process during exhaust recycling. For the system presented here, CO_2-enhanced gasification is thermodynamically limited to equivalence ratios above $\lambda = 0.13$ and equilibrium temperatures above 576°C. This thermodynamically limited case produced an indicated system efficiency of 26.9% based on supplied biomass lower heating value (LHV). Further simulations using both ideal cycles and detailed numerical models highlight the influence of several operational settings on the thermodynamic conditions of the gasification process. Principally, the coupling between exhaust temperatures, allothermal heat, and syngas quality are shown to govern the performance of the gasification reactions.

Although these simulated equilibrium calculations revealed the fundamental thermodynamic benefit of EGR-gasification cycles, variability in typical gasification processes often produces syngas compositions that differ from chemical equilibrium. An examination of the evolution of syngas from a biomass sample during gasification was needed to assess how these differences occur. Particularly, experimental confirmation that the key CO_2 to CO conversion process is achievable under mild temperature conditions was required to verify the feasibility of the novel process described in this work. Results of these experimental investigations have shown the CDU conversion of CO_2 into CO under process conditions similar to earlier thermodynamic modelling. Compared to pyrolysis of soda lignin as a representative biomass sample, CO_2 gasification produced roughly 69% more CO while consuming 1.1 mmol CO_2/g-biomass. Although this conversion process performs poorly under the experimental conditions, it does illustrate the viability of the proposed technology. Significant improvement in CO_2 conversion and CO production is noted as reaction temperature increases, particularly above 700°C. Additional features of lignin pyrolysis are also illustrated that suggest incomplete conversion of pyrolysis products contribute to a product syngas with higher CH_4 content than expected under equilibrium conditions.

Table of Contents

List of Tables

List of Figures

Acknowledgements

Support for this work was generously provided by the University of Glasgow through the Lord Kelvin/Adam Smith PhD Scholarship. With an emphasis on multi-disciplinary research, this programme was helpful in fostering a highly collaborative environment to integrate aspects of mechanical engineering, chemistry, and energy economics into the research project.

I also acknowledge the helpful support and guidance of my supervisor, Prof. Manosh Paul. Indeed, all co-supervisors have provided valuable advice and lent their own particular expertise to my work. Specifically, Profs. David Jackson and Justin Hargreaves have given substantial assistance in my understanding of chemistry principles and experimental work and Dr. Souvik Datta has offered many insights to recognise the significance of this work in the context of energy economics. University technical staff members Mr. Gangi Reddy Ubbara and Dr. Giovanni Enrico Rossi also provided elemental analysis while Mr. John Liddell made specialised glassware in support of my experimental work.

I am also indebted to many colleagues in the schools of engineering and chemistry for contributing to a friendly and collegial working environment. Particular thanks to my fellow research students in the Systems, Power, and Energy research division who offered many helpful discussions on applications of engineering principles to gasification processes. Thanks as well to Dr. Nicola Irvine who contributed significant practical guidance on using mass spectrometry, even amid a pandemic, and Dr. Mustafa Aslan who helped with XRD analysis. A very special acknowledgement to my lab mates, Caitlin, Lucy, and Katy, and all graduate students and research assistants in the Surface Catalysis group whose kindness will never be forgotten. Truly, the braw banter and pure good chat over many cups of tea have been just as helpful as any technical or scientific guidance I've ever received.

Finally, I am grateful to all my family for their encouragement and prayers during my period of study. I am especially thankful for the constant support of my dear wife, Catherine, as we made Glasgow our temporary home for these past years. I am very much looking forward to our next adventures together, wherever that will lead.

Author's Declaration

I certify that the thesis presented here for examination for a PhD degree of the University of Glasgow is solely my own work other than where I have clearly indicated that it is the work of others and that the thesis has not been edited by a third party beyond what is permitted by the University's PGR Code of Practice.

I declare that the thesis does not include work forming part of a thesis presented successfully for another degree.

I declare that this thesis has been produced in accordance with the University of Glasgow's Code of Good Practice in Research.

I acknowledge that if any issues are raised regarding good research practice based on review of the thesis, the examination may be postponed pending the outcome of any investigation of the issues.

Michael Greencorn
April 2023

Nomenclature

a	Species elemental factor (-)
B	Cylinder bore (m)
c_n	Correlation constants (-)
C_p	Constant pressure heat capacity (kJ/mol-K)
C_v	Constant volume heat capacity (kJ/mol-K)
G	Gibbs free energy (kJ/mol)
h	Specific enthalpy (kJ/mol)
ΔH_c	Enthalpy of combustion (kJ)
Δh_{comb}	Specific enthalpy of combustion (kJ/kmol)
h_t	Heat transfer coefficient (W/m^2-K)
$I_{m/z}$	Ion current (A)
k	Thermal conductivity (W/m-K)
K_p	Reaction equilibrium constant (-)
m	Mass quantity (kg)
m/z	Mass to charge ratio (-)
M	Molar mass (g/mol)
Ma	Mach number (-)
n	Molar quantity (kmol)
Nu	Nusselt number (-)
p_n	Partial Pressure (kPa)
P	Pressure (kPa)
Q	Heat energy (kJ)
Q_L	Cylinder heat loss (kJ)
R	Gas constant (kJ/mol-K)
r_c	Compression ratio (-)
Re	Reynolds number
s	Specific entropy (kJ/mol-K)
S	Cylinder stroke (m)
T	Temperature (K or ℃)
$\bar{U}_p$	Mean piston speed (m/s)
V	Volume (m^3)
V_c	Clearance volume (m^3)
W	Indicated work (kJ)
x_i	Mole fraction
X_b	Burned mass fraction (-)

Greek characters

γ	Adiabatic index (-)
ϵ	Crank/rod length ratio (-)

η	Indicated thermal efficiency (%)
θ	Engine crank angle (deg.)
λ	Gasification air or O_2 ratio (-)
μ	Dynamic viscosity (Pa-s)
ρ	Density (kg/m^3)
ϕ	Dimensionless molecular interaction parameter (-)

Abbreviations

A/F	Air to fuel mass ratio
AFOLU	Afforestation and other land use
ATDC	After top dead centre
BECCS	Bioenergy with CCS
BDC	Bottom dead centre
bmep	Brake mean effective pressure
CAD50	Engine crank position at 50% fuel combustion
CCS	Carbon capture and storage
CDR	Carbon dioxide removal
CDU	Carbon dioxide utilisation
CGE	Cold gas efficiency
DACCS	Direct air CCS
DCM	Dichloromethane
DRM	Methane dry reforming reaction
E/FGR	Exhaust (or Flue) gas recycling
EGT	Exhaust gas temperature
fmep	Friction mean effective pressure
ICE	Internal combustion engine
IGC	Integrated gasification cycle
IGCC	Integrated gasification combined cycle
imep	Indicated mean effective pressure
IMP	Illustrative mitigation pathway
IOGC	Integrated oxyfuel gasification cycle
IPCC	Intergovernmental panel on climate change
LHV	Lower heating value
NDIR	Non-dispersive Infrared (spectrometry)
ODH	Oxidative dehydrogenation reaction
QMS	Quadrupole Mass Spectrometry
RCP	Representative Concentration Pathway

RPM	Revolutions per minute
SRM	Methane steam reforming reaction
SSP	Shared Socio-economic Pathway
TDC	Top dead centre
WGS	Water-gas shift reaction

Subscripts/Superscripts

bio	Biomass feed parameter
eng	Engine related parameter
i	Syngas products
j	Element index
k	Gasifier inputs (feedstock and agents)
sys	Overall system parameter
^{0}	SATP reference value
$\cdot$	Time rate of change (s^{-1})

Chapter 1 Introduction

1.1 Background: Understanding and Managing Climate Change

To begin, it must be clearly understood that we are currently in a regime of climate change with a rate of surface temperature increase unprecedented in recent geological history. Consequences of the planetary changes brought on by higher temperatures are creating environmental conditions that put our wellbeing at risk. Extensive work by climatologists and atmospheric scientists has recognised the ultimate source of the observed climate change is a human-induced imbalance to greenhouse effect of the lower atmosphere. Chiefly, anthropogenic gas emissions have shifted the Earth's carbon cycle, thus causing an excess of CO_2 in the atmosphere.

Biomass energy systems are designed to interact with the carbon cycle while generating useful work. Traditionally, the intention of using such a system is produce power with a long-term, net-neutral effect on atmospheric CO_2 concentrations. New applications of biomass energy aim to create conditions for the net-removal of atmospheric CO_2 while effective methods of CO_2 utilisation aim to improve these power cycles. This introductory section, therefore, summarises the current understanding of climate change, the greenhouse effect, and the carbon cycle so that justifications for using biomass-based energy systems to achieve the necessary low-carbon economy can be adequately understood.

1.1.1 Observations of climate warming

Trends in the Earth's temperature record (Figure 1-1) show an accelerating rise in surface temperatures since the beginning of the modern industrial era with average temperatures over the 2011-2020 decade reaching 1.09℃ above the 1850-1900 average. On geological timescales the current decade's global mean surface temperature (GMST) is likely higher than at any other in the past 125,000 years. Furthermore, the rate of temperature increase through the turn of the 21st century is unprecedented in the historical record as the warming rates observed since 1970 are higher than at any point over the past 2000 years [1].

This clear warming trend causes further changes in the highly connected earth climate system. Increased atmospheric temperatures increase the evaporation and precipitation rates by 1-3% per ℃ of warming [2], leading to both an increase in evaporative demand that may have caused more frequent or intense droughts and more atmospheric water

content that have led to more frequent and intense periods of rainfall and increased the proportion of Category 3-5 tropical storms over the past 40 years [3]. Furthermore, the increased surface temperatures have reduced glacier ice mass and average seasonal snow cover for the northern hemisphere [4]. Similarly, ice cover in the Arctic Ocean has diminished at the seasonal minimum by 40% and by 10% at the seasonal maximum compared to the decade 1979-1988 while ice sheets in Greenland and Antarctica have lost 4890 and 2670 Gt of ice, respectively, since 1992 [4]. Regional climate zones and biospheres have also shifted to higher latitudes in the northern hemisphere based on observed trends in seasonal atmospheric CO_2 concentrations [1].

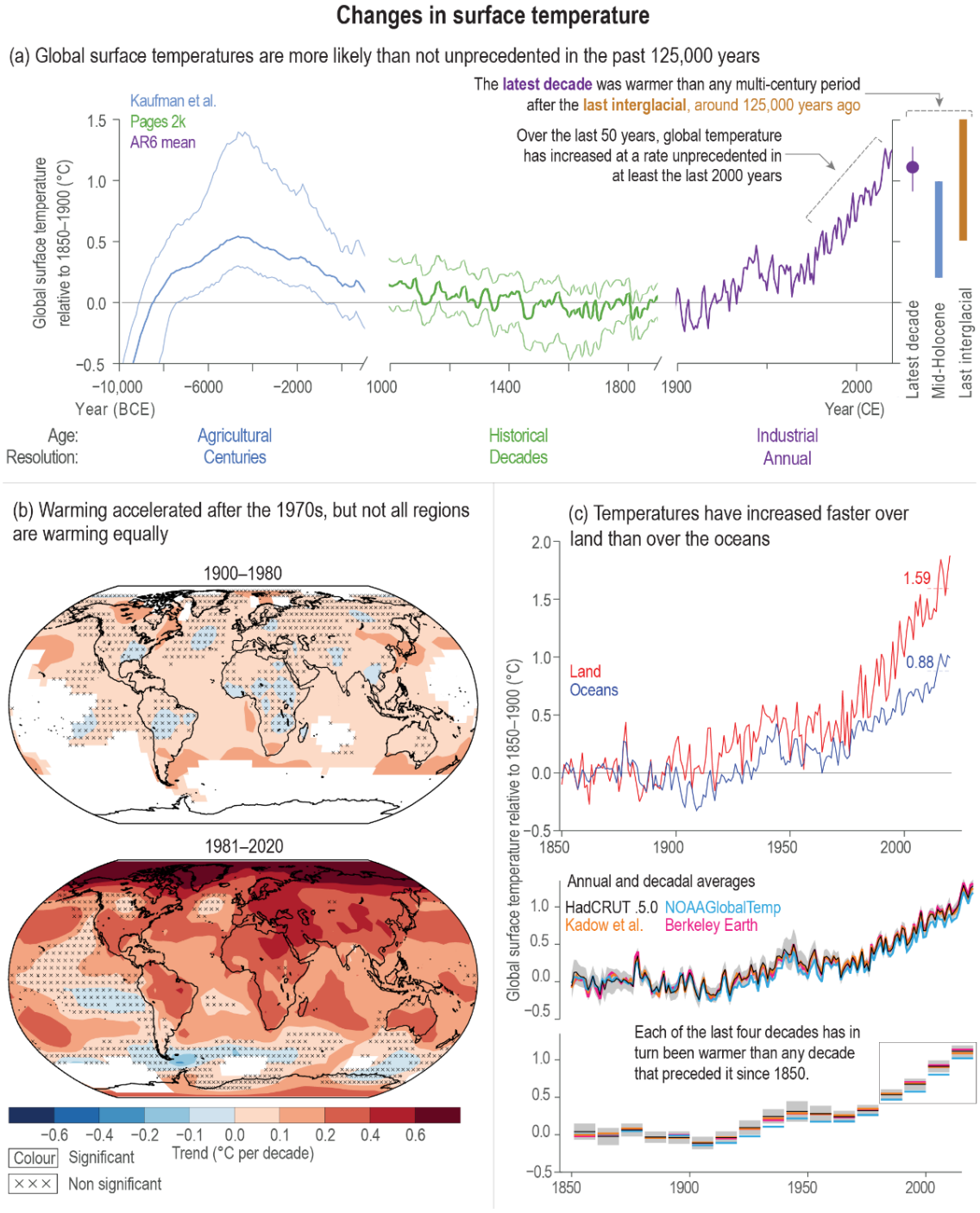

Figure 1-1: Observed Global Mean Surface Temperature Anomalies a) over recent geological timescales, b) decadal rates of change resolved over geographical area, and c) average GMST anomalies over 1850-2020 [1, p. Figure 2.11].

Consequences of these physical changes in the planet's climate pose high levels of risk to the environmental, biological, agricultural, economic, and social systems we rely on for our prosperity. Extreme heat and weather events attributable to climate change have damaged ecosystems, agricultural and fishery systems, and urban areas at an increasing rate that have impacted the livelihoods, health, and security of many populations, particularly in regions with considerable development constraints. Reduced water access and nutrition security, ill health and premature death, and loss of livelihood are expected to continue affecting the most vulnerable populations. These risks associated with continued warming will multiply in magnitude based on the increase in temperature on both the near- and long-term time scales. While some mitigation may be possible, severe residual risks remain even at warming levels as low as 1.5℃ above 1850-1900 average temperatures and are likely to scale non-linearly with further temperature increases [5].

1.1.2 Mechanisms of greenhouse effect

The source of this warming phenomenon has been definitively traced to increasing concentrations of certain gases in the atmosphere through the well-known mechanism of the greenhouse effect, briefly summarised here to highlight the significance of atmospheric CO_2 in this phenomenon. The spectrum of incident solar radiation is predominantly in the shortwave range of ~0.1-10 μm (Figure 1-2A). Atmospheric gases are largely transparent over this wavelength range, thus allowing most visible, near-ultraviolet, and near-infrared solar radiation to reach the Earth's surface unimpeded. An influx of thermal energy carried by this solar radiation is absorbed by planetary surfaces, increasing their temperature.

Again, following Planck's law, these warmed surfaces emit upwards thermal radiation according to their emission temperatures. Since planetary surfaces are well cooler than the Sun, there is a corresponding shift in their radiation spectra towards longer wavelengths [6]. Several atmospheric gases, namely greenhouse gases (GHGs) like CO_2, H_2O, CH_4, and N_2O, have absorption spectra with significant peaks over the thermal infrared range beyond wavelengths of 2 μm (Figure 1-2B). Absorption of radiation in these spectral bands contributes to an additional influx of energy to the lower atmospheric gases causing radiative atmospheric warming. Gases at the bottom of the atmosphere emit thermal radiation according to the Stephan-Boltzman law that causes a further flux of downward longwave radiation back towards the surface of the Earth [6]. The ultimate effect of this downward radiation from the warm atmospheric gases is an increase in the Earth's surface temperature.

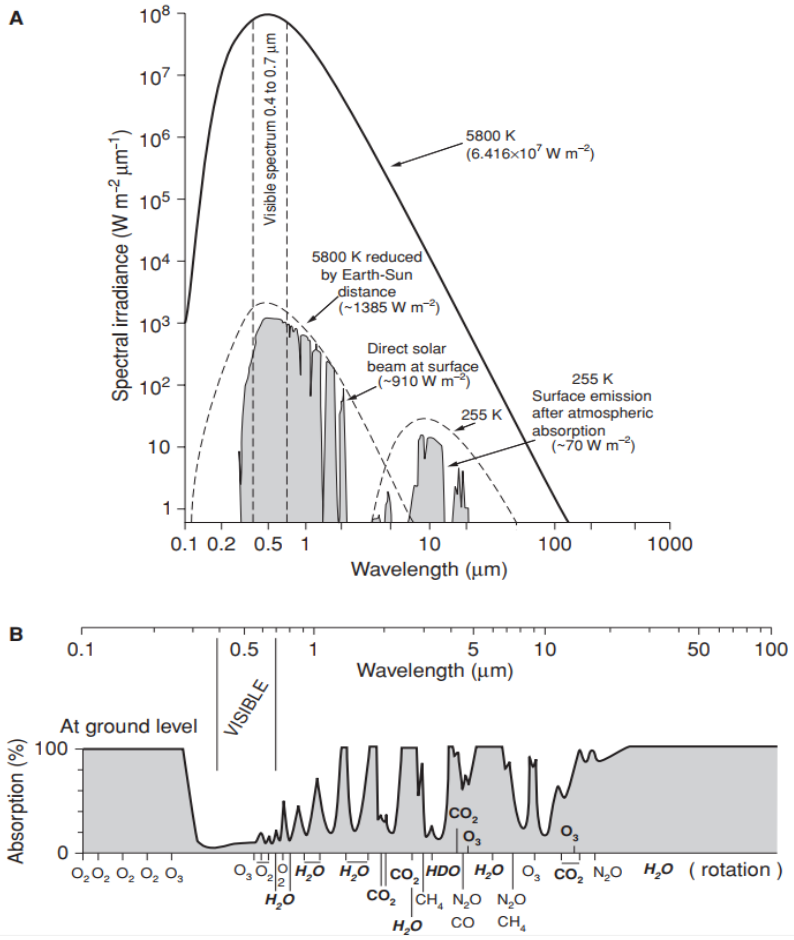

Figure 1-2: Electromagnetic radiation absorption of atmospheric gases A) comparing spectral intensities of short wave solar and long wave surface thermal radiation profiles and B) showing weighted absorption peaks of a typical air mixture [7]. Reproduced with permission from Springer Nature.

Calculated changes over time in the net-downward back radiation from the atmosphere to the Earth's surface are termed radiative forcing [8]. Changes to gas concentrations in the atmosphere that absorb long-wavelength radiation contribute to this radiative forcing. Figure 1-3 illustrates the calculated changes in the climate's energy balance from a range of contributing sources. Anthropogenic CO_2 emissions alone have caused an increase in effective radiative forcing (ERF) of 2.16 W/m^2 over the period 1750-2019 as calculated from the measured changes in atmospheric concentration of CO_2 [9]. Due to ongoing anthropogenic CO_2 emissions, radiative forcing due to atmospheric CO_2 is increasing by ~0.3 W/m^2 per decade [10]. Other GHGs make a significant contribution to the changes in radiative forcing with methane making the largest contribution. Natural cycles that affect the Earth's orbit around the Sun and the intensity of the Sun's radiation will also affect the radiative forcing by changing the incident radiation supplied to the system, however the measured changes in solar output are insignificant compared to anthropogenic influences.

These increases to ERF represent additional inputs of energy into the climate system at the Earth's surface. Responses of the climate to this intensified energy flux are complex and

consist of both positive and negative feedback loops as well as potential tipping points. For instance, over 90% of the excess back radiation has been stored in the oceans, helping to moderate the temperature response to the radiative forcings to date. Modelling the temperature response to a series of feedback systems based on the known radiative forcings allows a prediction of the equilibrium climate sensitivity. Evaluation of these models predicts a doubling of atmospheric CO_2 concentration is likely to result in a long-term temperature increase of 3°C [9].

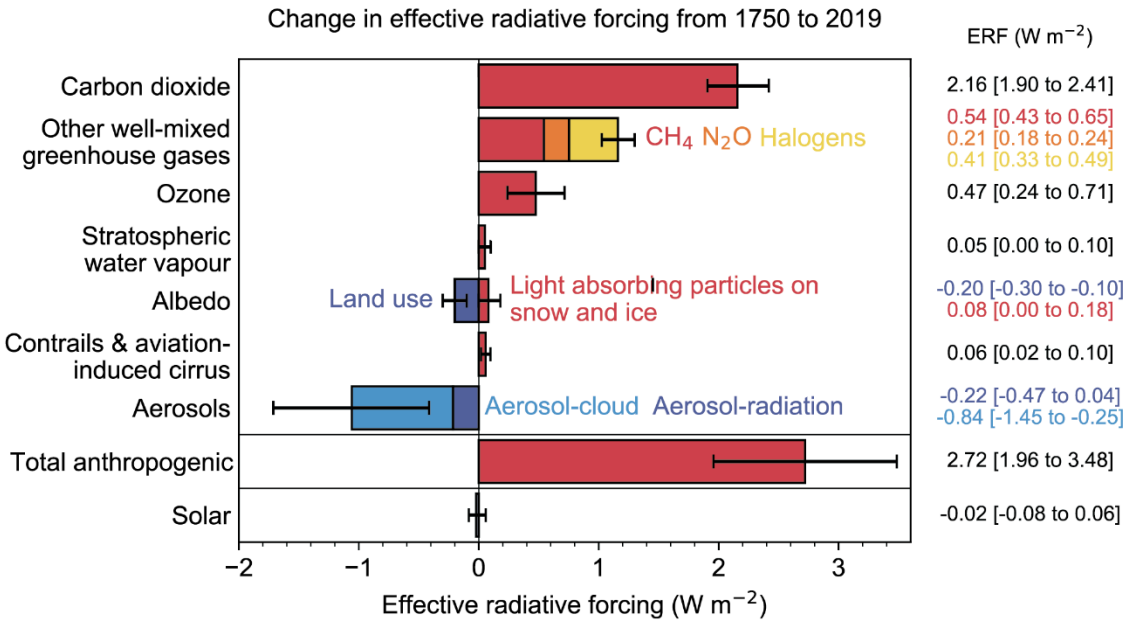

Figure 1-3: Changes in climate radiative forcing from 1750-2019 by contributing sources [9, p. Figure 7.6]. Shared under license CC BY 4.0.

Tracking the historical trends in radiative forcings and climate feedbacks allows for analysis of the recent warming trends. Based on these historical model calculations, the observed temperature record is dominated by anthropogenic radiative forcing, predominantly through the measured net increases in CO_2 concentration in the atmosphere, as seen in Figure 1-4. Further examination reveals the temperature signal since the mid-20th century cannot be recreated by natural radiative forcings alone, demonstrating the ultimate cause of current climate change is human-driven enlargement of CO_2 greenhouse radiative forcing [11].

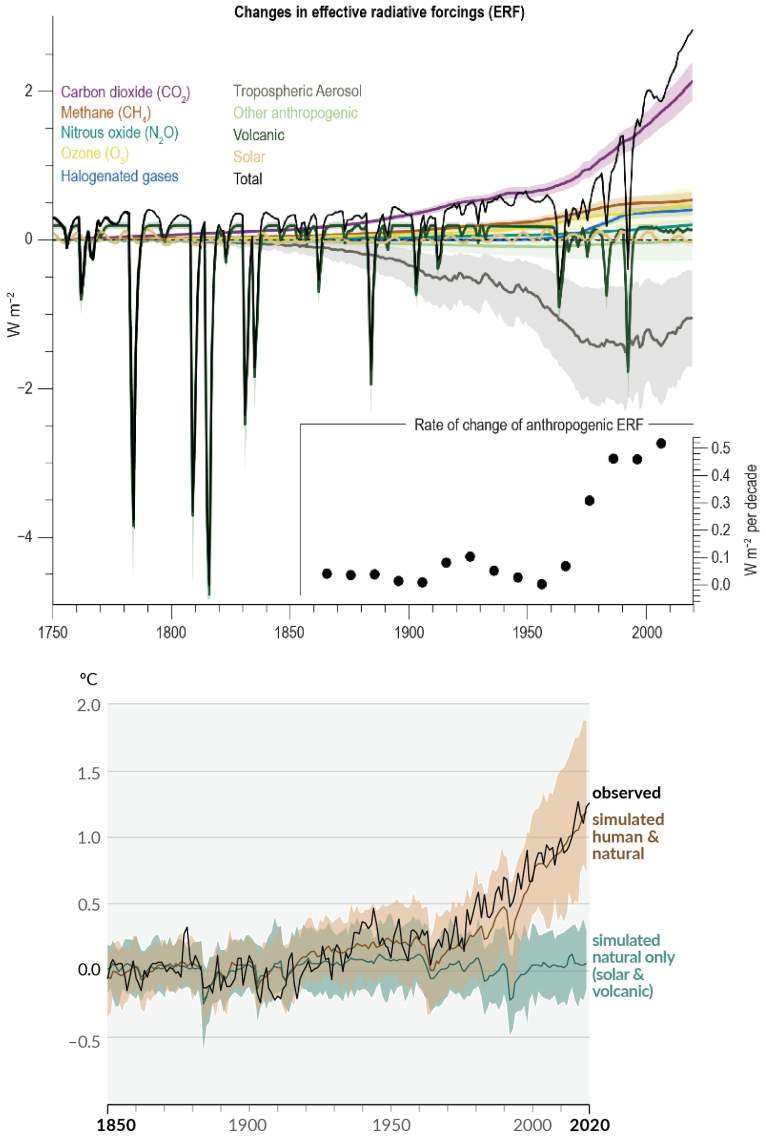

Figure 1-4: Historical radiative forcings (top [1, p. Figure 2.10]) and resulting model calculated temperature signals compared to historical temperature observations (bottom) [11, p. Figure FAQ3.1]

1.1.3 The global carbon cycle and carbon budget

Although the recent climate warming is clearly a result of changes in atmospheric CO_2, an understanding of how the earth system exchanges carbon through the carbon cycle illustrates complexities that influence the CO_2 concentration in the atmosphere. A schematic of the overall carbon stocks and carbon fluxes between these reservoirs is presented in Figure 1-5.

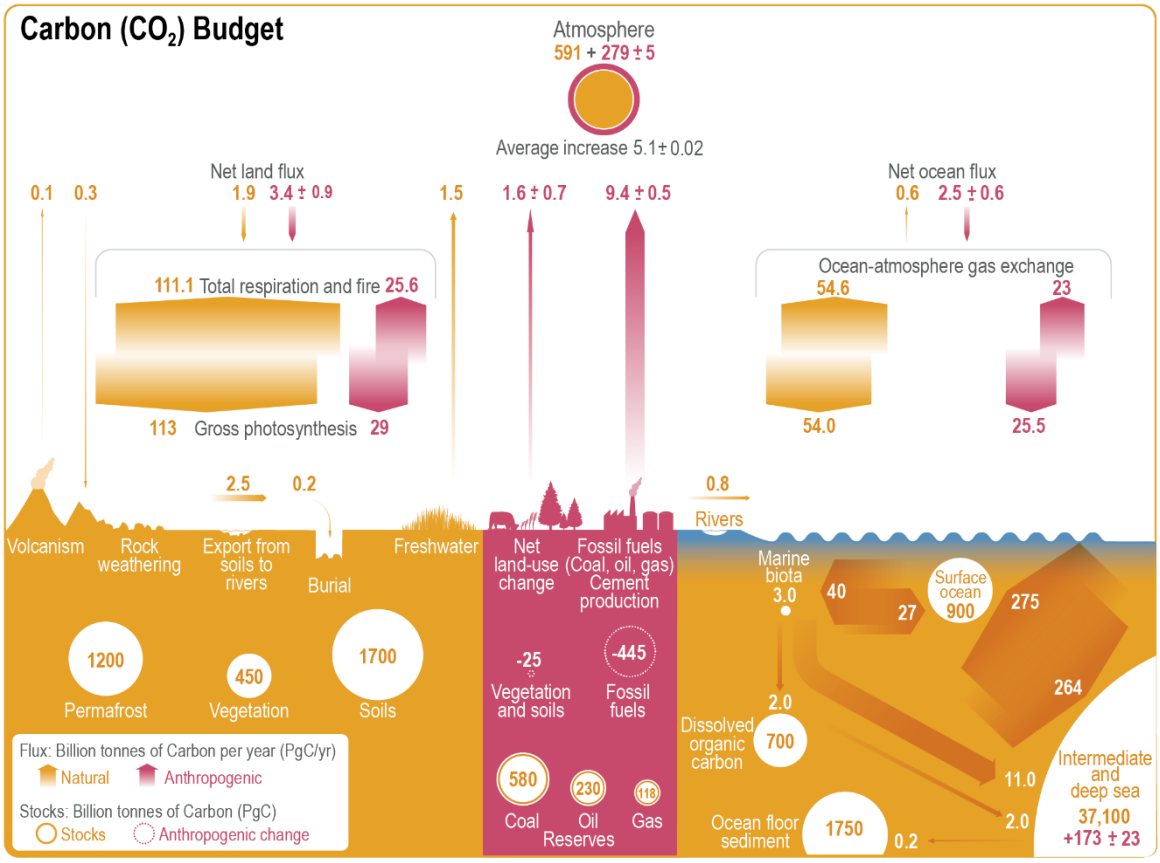

Figure 1-5: Earth system natural and anthropogenic annual carbon fluxes and carbon stocks (2010-2019 averages) [12, p. Figure 5.12]

The ultimate influence on climate warming has been the addition of 279 Pg of carbon to the atmosphere since 1750 in the form of CO_2. Recorded fluxes reveal the largest source of this carbon has been from lithosphere carbon stocks liberated through the combustion of fossil fuels. Current rates of CO_2 emissions to the atmosphere from fossil fuels and cement are 9.4 Pg per year while the replenishment rate of carbon into the lithosphere is merely 0.7 Pg per year through rock weathering, soil burial, and ocean sedimentation. While natural carbon sinks like photosynthesis and ocean gas exchanges do remove large amounts of CO2 from the atmosphere, they are roughly balanced through other natural processes like cellular respiration, fires, and decomposition of organic matter which return the carbon to the atmosphere. Therefore, these fluxes do not balance the anthropogenic fluxes to the atmosphere from fossil fuel use, deforestation and land use, and other industrial processes. As a result, atmospheric carbon stocks are increasing at a rate of 5.1 Pg of carbon per year [12].

Combining the known changes in the carbon cycle and similar processes for other GHGs with climate forcing and feedback models provides a measure of how much additional carbon added to the atmosphere is likely to affect long term climate warming. This

transient climate response to cumulative emissions of carbon dioxide (TCRE) is often described as a carbon budget since it ties total amounts of carbon emitted to a set temperature increase. Table 1-1 provides ranges of calculated carbon budgets resulting in likely warming of 1.3-2.4°C over 1850-1900 temperatures by the end of the 21st century. Remaining carbon budgets to limit warming to 1.5°C are likely 500 $GtCO_2$ while budgets for 2.0°C of warming are 1350 $GtCO_2$ since the beginning of 2020 [12].

Table 1-1: Carbon budget ranges for limited 21st century warming [12]

Additional Warming since 2010-2019	Total Warming since 1850-1900	Remaining Carbon Budget from January 2020				
		Percentile of modelled TCREs · PgC ($GtCO_2$)				
°C	°C	17th	33rd	50th	67th	83rd
0.23	1.3	100 (400)	60 (250)	40 (150)	30 (100)	10 (50)
0.33	1.4	180 (650)	120 (450)	90 (350)	70 (250)	50 (200)
0.43	1.5	250 (900)	180 (650)	140 (500)	110 (400)	80 (300)
0.53	1.6	330 (1200)	230 (850)	180 (650)	150 (550)	110 (400)
0.63	1.7	400 (1450)	290 (1050)	230 (850)	190 (700)	150 (550)
0.73	1.8	470 (1750)	350 (1250)	280 (1000)	230 (850)	180 (650)
0.83	1.9	550 (2000)	400 (1450)	320 (1200)	270 (1000)	210 (800)
0.93	2.0	620 (2300)	460 (1700)	370 (1350)	310 (1150)	250 (900)
1.03	2.1	700 (2550)	510 (1900)	420 (1500)	350 (1250)	280 (1050)
1.13	2.2	770 (2850)	570 (2100)	460 (1700)	390 (1400)	310 (1150)
1.23	2.3	850 (3100)	630 (2300)	510 (1850)	430 (1550)	350 (1250)
1.33	2.4	920 (3350)	680 (2500)	550 (2050)	470 (1700)	380 (1400)

1.1.4 Projections of future emissions and climate

The increasingly detailed understanding of many interacting radiative forcings, environmental, climate, and biogeochemical systems combined with expected socio-economic needs and potential technological developments has provided the means to model possible scenarios of how we might influence the future climate. Use of such interconnected models generate a range of potential pathways for analysis to examine how near and long term political, economic, and technical decisions are likely to influence

climate responses in the near- and long-term [13]. These analyses are called Shared Socio-economic Pathways (SSPs), Representative Concentration Pathways (RCPs), and Illustrative Mitigation Pathways (IMPs) in literature (e.g. Figure 1-6).

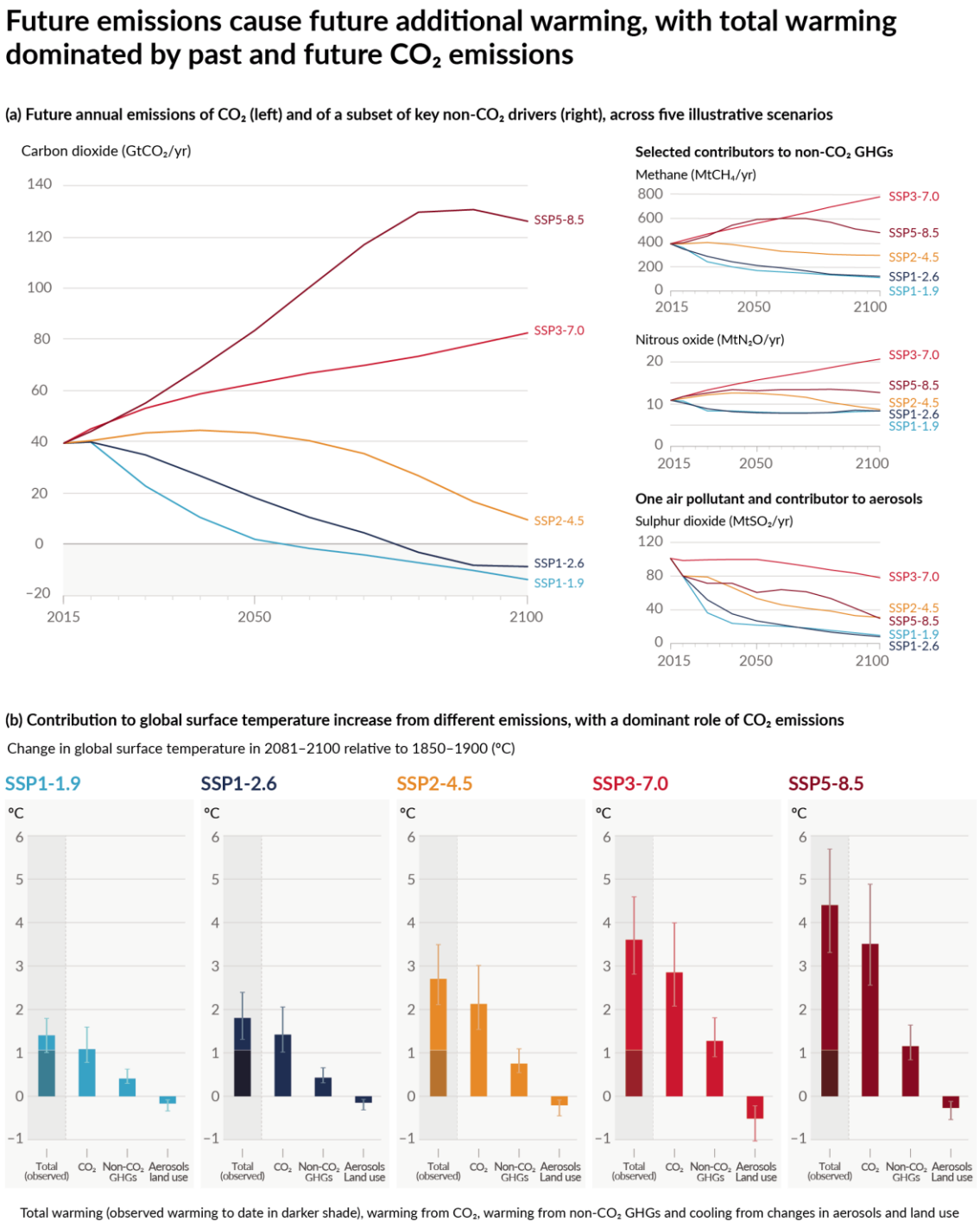

Figure 1-6: Selected SSPs modelling future scenarios of a) anticipated atmospheric emissions and b) corresponding GMST temperature increase [14, p. SPM.4]

A series of SSPs representing an aggregation of many different models and scenarios analysed during the 6th Coupled Model Intercomparison Project (CMIP6) present anticipated climate responses based on emissions profiles (Figure 1-6). High and very high emissions scenarios (SSP5, SSP3) where rates of CO_2 production continue to increase over

the 21st century are very likely to result in long-term warming beyond 3°C. Maintaining relatively constant CO_2 emissions in the near term before a gradual decrease, in line with the intermediate emissions scenarios (SSP2), is likely to limit long-term warming under 3°C. The low emissions scenarios (SSP1s) that keep warming below 2°C require immediate, drastic reductions in GHG production and likely necessitate net-negative emissions later in the 21st century [13].

CO_2 profiles of the low-emissions SSPs indicate achieving net-negative carbon emissions will likely be essential by the second half of the century to minimise climate warming. This requirement arises from the slim carbon budgets remaining and the expected emissions required for future economic development. In practical terms, this means deployment of carbon dioxide reduction technologies (CDRs) that actively remove CO_2 from the atmosphere will be necessary at large scale within the next decades.

1.1.5 Technical solutions using biomass

It is clear that drastic reductions in net CO_2 emissions to the atmosphere are needed in the very short term if the worst effects of climate change are to be avoided. Indeed, this is a remarkable challenge given our current dependency on fossil fuel use for economic output. Yet more demanding is the likelihood that atmospheric CO_2 will need to be actively removed by the second half of the century. While accelerated deployment of traditional renewables (i.e. wind, solar, etc.) will be most useful in replacing fossil fuel energy, particularly in the near term [15], these technologies cannot directly provide a negative pathway for CO_2.

A principal virtue of most renewable energy sources (RESs) is that they strive to be independent from the carbon cycle, save for some incidental lifecycle emissions during construction, maintenance, and decommissioning. This feature thereby decouples energy produced by these types of RES from greenhouse gas emissions. That is to say, the useful work produced in this manner is low carbon since the modes of function of these systems do not principally consume or produce any carbonaceous materials like CO_2. This inherent isolation from the carbon cycle also means that these technologies cannot actively remove CO_2 from the atmosphere without some intermediate process.

In contrast, biomass energy systems are highly integrated with the Earth's carbon cycle. As shown in Figure 1-7, atmospheric carbon is fixed into a biomass feedstock naturally through photosynthesis and harvested as a fuel source. Although this process is indeed a

carbon sink, some methods of generating a feedstock can create unintended secondary GHG emissions from land use changes or agricultural practices that liberate soil-based carbon stocks to the atmosphere. Therefore, feedstock growing, harvesting, and processing techniques must be conscientiously planned to minimise these effects. When used as a fuel in a biomass energy system, the carbon in the biomass is converted back into CO_2 through oxidation and released to the atmosphere, however this carbon had originated from the atmosphere in the recent past so there is no net contribution to atmospheric CO_2 concentrations over a time interval. This particular aspect of biomass energy systems means there may be some time scales where the careless deployment of biomass energy sources causes a "carbon debt" that increases atmospheric CO_2 levels [16, 17]. In order for this cycle to remain carbon-neutral, the biomass source must therefore be managed sustainably such that feedstock regeneration continually balances these CO_2 emissions. Ultimately, this process fills the same niche as other RESs as it creates useful work that has a net-neutral contribution to atmospheric CO_2 despite the integral role of carbon-based compounds in the fundamental process operations.

Although the interactions between biomass energy systems and the carbon cycle create the sensitivities described above, they also create the conditions for a method to reduce atmospheric CO_2 levels. Because careful use of biomass as a fuel source can provide a carbon-neutral energy source, this creates a potential negative CO_2 pathway when used in a bioenergy with carbon capture and storage (BECCS) system. This system becomes net-negative if the power cycle CO_2 emissions are captured in a carbon capture and storage scheme (CCS) and thus never reach the atmosphere (Figure 1-7).

This type of biomass application is particularly attractive since it achieves two desirable outcomes. First, the generation of renewable power which can lower CO_2 emissions by offsetting fossil fuel-based power and also the further reduction of atmospheric CO_2 concentration through the pathway described above. Additionally, whether in a traditional power configuration or in a BECCS cycle, biomass fuel provides a dispatchable source of energy which will complement the increasing deployment of intermittent energy sources by maintaining power grid stability. [18]

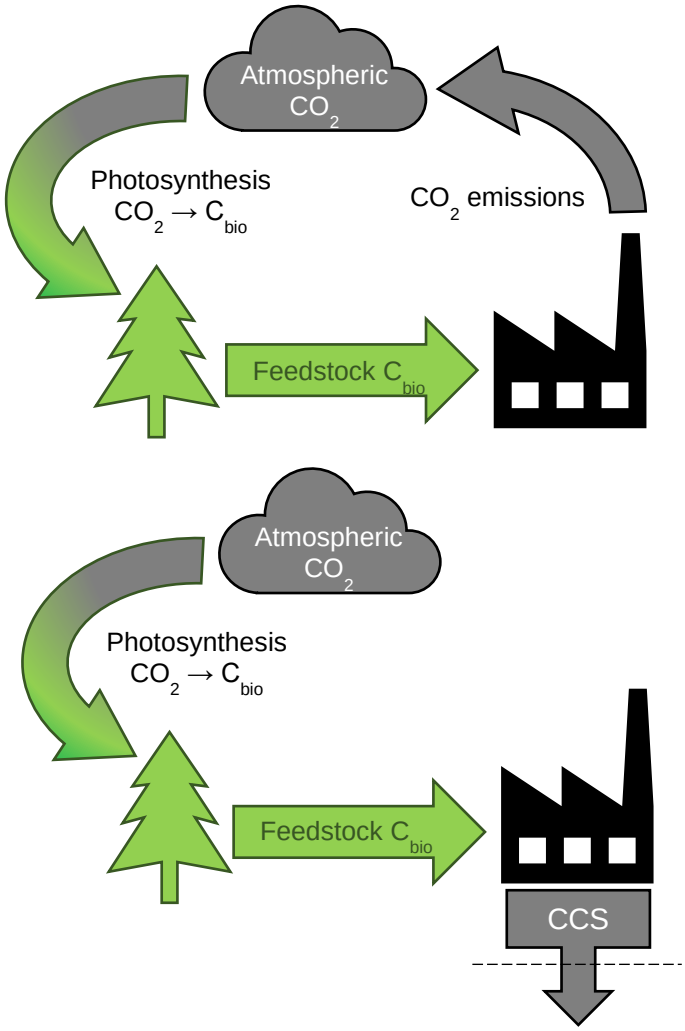

Figure 1-7: Carbon fluxes in biomass energy systems (top) and BECCS systems (bottom)

In conjunction with increasing deployment of intermittent renewable energy sources (iRES), significant growth in bioenergy is anticipated as part of the shift away from fossil fuels. The International Energy Agency (IEA) Net Zero Emissions by 2050 modelling pathway indicates global annual growth rates in electricity from biomass should be at least 7%, or 15 GW of new capacity installed each year, over the next decade to reach annual generation of 1400 TWh by 2030 [18]. Furthermore, BECCS deployment under this modelling scenario should reach approximately 250 $MtCO_2$ removal per year to successfully reach net-zero by 2050. Current projects under development are only likely to reach 40 $MtCO_2$ by 2030, indicating significant acceleration and expansion of BECCS deployment will be required [19].

Analysis of IPCC representative concentration pathways (RCPs) that limit predicted climate warming to 1.5°C with small temperature overshoots (Figure 1-8) require drastic and immediate reductions in anthropogenic CO_2 emissions. These RCPs show 40-60% reduction in emissions from 2010 levels by 2030 with further reductions to net-zero CO_2

emissions by 2050. While there are many areas of variation between RCPs, those that reach 1.5°C of warming with only small overshoots project energy from renewable sources (including biomass) supplying 70-85% of the world's electrical demand by 2050. Primary energy supply from biomass may increase by up to 418% over 2010 levels to achieve this objective. Similar projections demand reductions in industrial CO_2 emissions by 2050 of 75-90% from 2010 levels. These reductions must be realised through technological changes that include electrification and use of biomass feedstocks; energy and process efficiencies are insufficient to limit emissions to the required levels. All 1.5°C pathways require deployment of CO_2 removal (CDR) technologies to remove 100-1000 $GtCO_2$ from the atmosphere over the 21st century, the bulk of which is predicted to come from bioenergy with carbon capture and storage (BECCS). Any delays in either decarbonisation or deployment of CDR technologies will shift the intensity of required atmospheric CO_2 removal toward the latter half of the century, requiring an even greater scale of CDR deployment. [20]

Virtually all 1.5°C pathways require near-term annual emissions to fall below 35 $GtCO_2eq$ by 2030, most indicate emissions should track between 25-30 $GtCO_2eq$ per year by that time. Current Paris Agreement targets, limiting CO_2 emissions to 52-58 $GtCO_2eq$ per year by 2030, are likely insufficient to avoid warming greater than 1.5°C with limited or no overshoot [15]. In cases of warming overshoot, reversing temperature trends will require significant upscaling and increased rate and volume of deployment for CDR technologies, including BECCS. Unless drastic (>50% of projected emissions) reductions to global CO_2 emissions are realised in the short to near term, BECCS technologies will likely be required for intensive atmospheric CO_2 removal beyond 2050. [20]

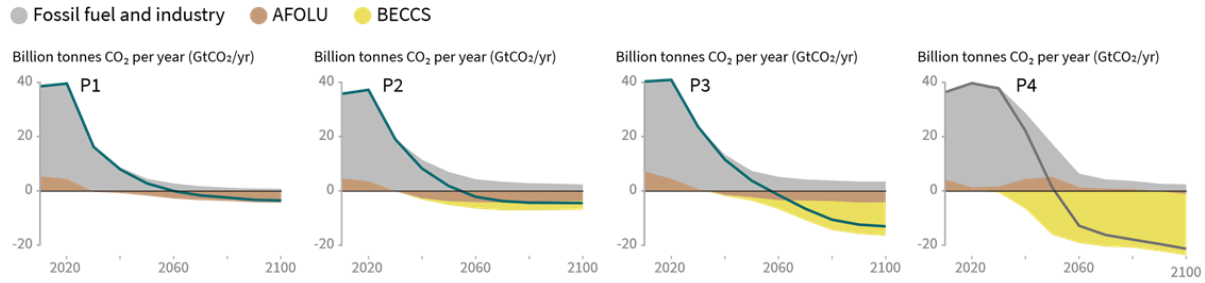

P1: A scenario in which social, business, and technological innovations result in lower energy demand up to 2050 while living standards rise, especially in the global South. A down-sized energy system enables rapid decarbonisation of energy supply. Afforestation is the only CDR option considered; neither fossil fuels with CCS nor BECCS are used.

P2: A scenario with a broad focus on sustainability including energy intensity, human development, economic convergence and international cooperation, as well as shifts towards sustainable and healthy consumption patterns, low-carbon technology innovation, and well-managed land systems with limited societal acceptability for BECCS.

P3: A middle-of-the-road scenario in which societal as well as technological development follows historical patterns. Emissions reductions are mainly achieved by changing the way in which energy and products are produced, and to a lesser degree by reductions in demand.

P4: A resource and energy-intensive scenario in which economic growth and globalization lead to widespread adoption of greenhouse-gas intensive lifestyles, including high demand for transportation fuels and livestock products. Emissions reductions are mainly achieved through technological means, making strong use of CDR through the deployment of BECCS.

Global indicators	P1	P2	P3	P4	**Interquartile range**
Pathway classification	No or low overshoot	No or low overshoot	No or low overshoot	High overshoot	No or low overshoot
CO_2 emission change in 2030 (% rel to 2010)	-58	-47	-41	4	(-59,-40)
└ in 2050 (% rel to 2010)	-93	-95	-91	-97	(-104,-91)
Kyoto-GHG emissions in 2030 (% rel to 2010)*	-50	-49	-35	-2	(-55,-38)
└ in 2050 (% rel to 2010)	-82	-89	-78	-80	(-93,-81)
*Final energy demand** in 2030 (% rel to 2010)*	-15	-5	17	39	(-12, 7)
└ in 2050 (% rel to 2010)	-32	2	21	44	(-11, 22)
Renewable share in electricity in 2030 (%)	60	58	48	25	(47, 65)
└ in 2050 (%)	77	81	63	70	(69, 87)
Primary energy from coal in 2030 (% rel to 2010)	-78	-61	-75	-59	(-78, -59)
└ in 2050 (% rel to 2010)	-97	-77	-73	-97	(-95, -74)
from oil in 2030 (% rel to 2010)	-37	-13	-3	86	(-34,3)
└ in 2050 (% rel to 2010)	-87	-50	-81	-32	(-78,-31)
from gas in 2030 (% rel to 2010)	-25	-20	33	37	(-26,21)
└ in 2050 (% rel to 2010)	-74	-53	21	-48	(-56,6)
from nuclear in 2030 (% rel to 2010)	59	83	98	106	(44,102)
└ in 2050 (% rel to 2010)	150	98	501	468	(91,190)
from biomass in 2030 (% rel to 2010)	-11	0	36	-1	(29,80)
└ in 2050 (% rel to 2010)	-16	49	121	418	(123,261)
from non-biomass renewables in 2030 (% rel to 2010)	430	470	315	110	(243,438)
└ in 2050 (% rel to 2010)	832	1327	878	1137	(575,1300)
Cumulative CCS until 2100 ($GtCO_2$)	0	348	687	1218	(550, 1017)
└ of which BECCS ($GtCO_2$)	0	151	414	1191	(364, 662)
Land area of bioenergy crops in 2050 (million hectare)	22	93	283	724	(151, 320)
Agricultural CH_4 emissions in 2030 (% rel to 2010)	-24	-48	1	14	(-30,-11)
in 2050 (% rel to 2010)	-33	-69	-23	2	(-46,-23)
Agricultural N_2O emissions in 2030 (% rel to 2010)	5	-26	15	3	(-21,4)
in 2050 (% rel to 2010)	6	-26	0	39	(-26,1)

Figure 1-8: Four example RCPs to keep 21st century warming below 1.5°C. [20, p. Figure SPM.3b]

1.1.6 Carbon Dioxide Utilisation

Although CO_2 is commonly a waste product, particularly from energy production, there are several uses for CO_2 in industrial and commercial processes. Carbon dioxide utilisation (CDU) schemes aim to maximise the benefit derived from a source of CO_2 before the gas is released to the atmosphere or sent for long term sequestration. Often, such CDU strategies aim to create new materials derived from the chemical conversion of CO_2. Products could include bulk chemicals or building materials while some processes can even convert CO_2 into a useful fuel for further energy generation or storage. Even in situations where the CO_2 stream remains unconverted, further benefit can still be realised.

Some examples of these latter, direct CDU strategies include enhanced oil recovery, heat transfer and storage, combustion dilution, and acting as a cycle working fluid [21].

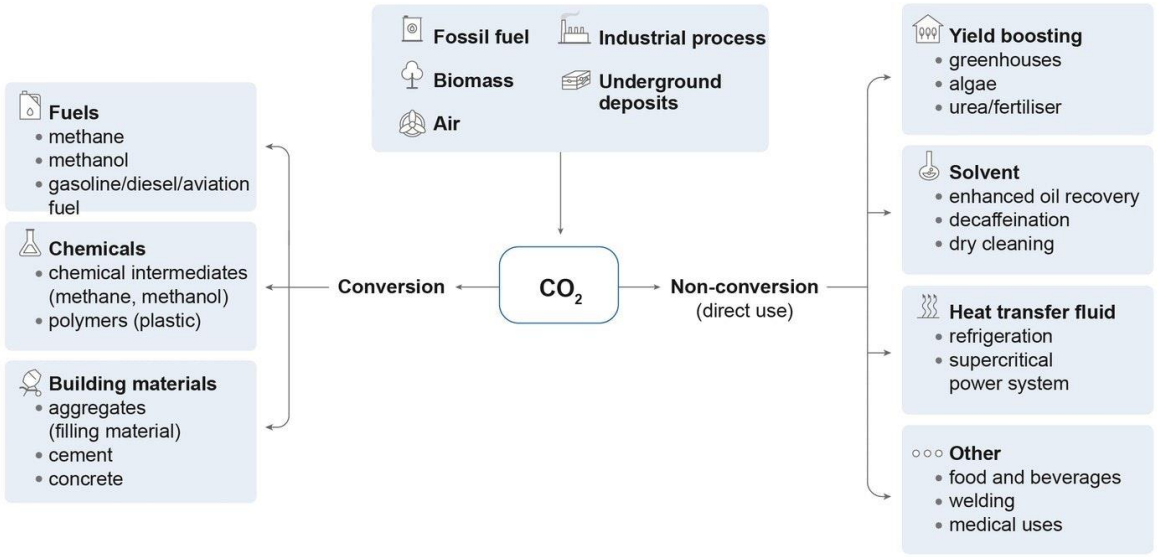

Figure 1-9: Pathways for CO_2 utilisation [21] Shared under license CC BY 4.0.

In the context of biomass energy systems, CDU techniques may become viable given the prevalence of CO_2 in the power generation cycles previously described. Pathways that chemically convert waste CO_2 into a fuel source would be helpful in providing extra primary energy inputs to the system. Meanwhile, non-conversion applications of CDU could influence the power cycle modifying the thermophysical properties of the working fluid or acting as a combustion diluent to better control cycle temperatures and heat release rate. Using cycle CO_2 flows as a heat transfer medium also presents a CDU method particularly beneficial to gasification-based systems that operate at high temperatures with large thermal demands to convert biomass feedstocks into gaseous fuels. Effective control of heat distribution could therefore be helpful in maximising cycle efficiency.

1.1.7 Government responses to climate change

Dealing with climate change and its underlying causes remains one of the most pressing challenges of our age. International commitment to solving this problem was formalised with the adoption of the Paris Agreement at the 21st United Nations Conference of Parties to the Intergovernmental Panel on Climate Change (UN IPCC COP21) in 2015. This created a legally binding treaty between 196 countries to set and monitor progress on individual policies governing GHG emissions with the goal of:

"Holding the increase in the global average temperature to well below 2°C above pre-industrial levels and pursuing efforts to limit the temperature increase to 1.5°C above pre-industrial levels, recognizing that this would significantly reduce the risks and impacts of climate change;" [22]

In conjunction with other EU nations, the UK passed legislation [23] to enforce emissions targets believed to align with the Paris agreement goals. The UK now has legal requirements to lower net greenhouse gas emissions by 2050 to levels at least 100% lower than the 1990 baseline (s 1(1)). An interim requirement further stipulates that annual net carbon budgets for the period covering the year 2020 must be more than 34% below the 1990 baseline (s 5(1)(a)). Law further requires the setting of UK carbon budgets in compliance with EU and other international obligations (s 8(2)). [23]. The 1990 reference baseline for greenhouse gas emissions is 794.2 $MtCO_2eq$. [24]

Five-year, UK net carbon emission budgets are set as the following:

- 2008-2012: 3.018 $GtCO_2eq$ or 24% reduction from 1990 [25]
- 2013-2017: 2.782 $GtCO_2eq$ or 30% reduction from 1990 [25]
- 2018-2022: 2.544 $GtCO_2eq$ or 36% reduction from 1990 [25]
- 2023-2027: 1.950 $GtCO_2eq$ or 51% reduction from 1990 [26]
- 2028-2032: 1.725 $GtCO_2eq$ or 57% reduction from 1990 [27]
- 2033-2037: 0.965 $GtCO_2eq$ or 76% reduction from 1990 [28]

To continue meeting these emissions requirements, the UK government published a ten-point plan that will modernise the national energy system to lower overall carbon intensity. Furthermore, the government has announced its intention to reach net-zero CO_2 emissions by 2050, recognising the need to develop carbon dioxide removal (CDR) and greenhouse gas removal (GGR) technologies to accelerate decarbonisation and to offset emissions from industries that cannot fully cut CO_2 emissions, reaching 80 $MtCO_2$ removed per year by 2050 [29]. Included in this scheme is a commitment for four industrial CCS centres that will capture 10 $MtCO_2$ by 2030 and allow for the required expansion through 2050 [30]. Additionally, government analysis shows it will not be likely for the UK to achieve a net-zero emissions conditions without using BECCS technology. Although BECCS is understood to have a technology readiness level of 7 (prototype demonstration), key areas of research and innovation are principally focused on avenues to maximise process efficiency and flexibility through gasification [31].

1.1.8 Summary

The climate is warming at an unprecedented rate due primarily to human-driven imbalances in the planet's carbon cycle which continue to shift CO_2 into the atmosphere. Corresponding changes in the environment are impacting human health and livelihoods. In order to prevent the worst damage, climate warming must be minimised. International agreements seek to limit future temperature rises to 2°C by drastically reducing CO_2 emissions. Maximising the near-term deployment of renewable energy, including biomass energy, to replace fossil fuel-based energy will be critical to meeting the specified target. Simply reducing emissions is unlikely to achieve these goals, active removal of atmospheric CO_2 using BECCS will be required. UK government policy seeks to reach net-zero by 2050, however innovation to increase the efficiency of BECCS technologies through gasification is required to successfully realise this goal. CDU techniques may be employed to this end in both renewable biomass energy and BECCS cycles given the prevalence of CO_2 within those systems. Detailed analysis of such technologies is required to understand the principal applications of CDU within this context.

1.2 Thesis Objectives and Contributions to Knowledge

The work presented here offers the only detailed assessment of exhaust recycling CDU techniques applied to gasification-based biomass power and BECCS cycles. Novel insights on how the use of exhaust CO_2 as a gasifying agent affects the thermodynamics of a biomass gasification process demonstrate a complex system that is sensitive to reagent concentrations and temperatures while also highlighting the consequences of using CO_2 as a cycle diluent. Furthermore, this investigation reveals for the first time the significant role that recycled CO_2 contributes to exhaust heat recycling within the system. Although the prevailing trends observed are likely applicable in general to CDU use in all biomass gasification systems, some minor novelty is also achieved by focusing this study on systems using internal combustion engines (ICEs) as the power conversion cycle. Despite the prevalence and maturity of ICE technology, this particular system configuration has never been investigated for CDU applications in this context.

This also synthesises with UK government policy which has indicated the current direction for innovation in BECCS technology is to develop techniques for enhancing the efficiency of the process through gasification applications [31]. Furthermore, the potential for synergistic integration of CDU strategies into biomass energy systems is assessed. For these reasons, the present work achieves the following novel aims:

- Evaluates system-level impacts of using a direct method for local CO_2 utilisation within biomass energy cycles.
- Evaluates the potential for direct CO_2 utilisation cycles to improve the efficiency of BECCS systems.
- Understands how CO_2 utilisation within these cycles affects the conversion of biomass feedstocks.
- Assesses both the conversion and non-conversion CO_2 utilisation processes and their effects on the overall cycle performance.
- Determines how underlying gasification processes, particularly under a CO_2 gasifying agent, affect the composition of syngas produced from a sample of biomass.

1.3 List of Publications and Research Communication

Sections of this thesis have previously been communicated in the following publications.

1.3.1 Journal Articles

Greencorn, MJ, Jackson, SD, Hargreaves, JSJ, Datta, S, and Paul, MC, (2023) *Enhancement of Gasification in Oxyfuel BECCS Cycles Employing a Direct Recycling CO_2 Utilisation Process*, Energy Conversion and Management, 277, DOI: 10.1016/j.enconman.2022.116601.

Greencorn, MJ, Jackson, SD, Hargreaves, JSJ, Datta, S, and Paul, MC, (2022) *Thermodynamic Limitations to Direct CO_2 Utilisation within a Small-scale Integrated Biomass Power Cycle*, Energy Conversion and Management, 269, DOI: 10.1016/j.enconman.2022.116144.

Greencorn, MJ, Jackson, SD, Hargreaves, JSJ, Datta, S, and Paul, MC, (2019) *A Novel BECCS Power Cycle Using CO_2 Exhaust Gas Recycling to Enhance Biomass Gasification*, Energy Proceedings, 3, DOI: 10.46855/energy-proceedings-1956.

1.3.2 Conference Presentations

Greencorn, MJ, Jackson, SD, Hargreaves, JSJ, Datta, S, and Paul, MC, (2022) *Exhaust Recycling as a CO_2 Utilisation Strategy in Integrated Biomass Gasification Power Cycles*,

Low-Carbon Combustion: Joint Meeting of the British and French Sections of the Combustion Institute, Cambridge, UK

Greencorn, MJ, Jackson, SD, Hargreaves, JSJ, Datta, S, and Paul, MC, (2021) *CFD Modelling of Biomass Pyrolysis in a Fixed Bed Reactor Using an Eulerian-Eulerian Multiphase Approach*, 7th International Symposium on Gasification and its Applications, Nancy, France (virtually)

Greencorn, MJ, Jackson, SD, Hargreaves, JSJ, Datta, S, and Paul, MC, (2020) *Modelling the performance of a syngas fuelled engine: Effect of excess air and CO_2 as combustion diluents*, Low-Carbon Combustion: Joint Meeting of the British and French Sections of the Combustion Institute, Lille, France (virtually)

1.3.3 Research Posters

Greencorn, MJ, Jackson, SD, Hargreaves, JSJ, Datta, S, and Paul, MC, (November 2019) *Thermodynamics of Enhancing Biomass Gasification using Recycled CO_2*, Lord Kelvin/Adam Smith PhD Research Symposium, Glasgow, Scotland

Greencorn, MJ, Jackson, SD, Hargreaves, JSJ, Datta, S, and Paul, MC, (September 2019) *Power Cycles with Negative CO_2 Emissions: Enhancing Gasification with Recirculated Exhaust Gases*, Systems, Power, and Energy Research Day, Glasgow, Scotland

Paul, MC, and **Greencorn, MJ**, (January 2019) *Low-carbon Energy from Biomass and Waste through Advanced Gasification*, Industrial Biotechnology Innovation Conference 2019, Glasgow, Scotland

1.3.4 Other Presentations

(Invited Talk) **Greencorn, MJ**, and Paul, MC (November 2020) *Sustainability of Bioresources and Methods of Power Generation from Biomass*, Glasgow University Environmental Sustainability Team, Glasgow, Scotland

1.4 Thesis Structure

- Chapter 2: A comprehensive review of biomass gasification power cycles is presented to detail methods for modelling both the thermochemical processes involved in feedstock conversion and aspects of power generation from syngas.

Furthermore, literature investigating CCU applications featuring the use of CO_2 as a gasifying agent is also discussed. This provides the framework necessary to understand the impact and methodology of studying exhaust recycling CDU applications in biomass gasification power cycles.

- Chapter 3: The theoretical basis, derivation, and validation of numerical models to evaluate the performance of integrated gasification power cycles is presented. This includes methods for analysing gasification processes and performance and detailed calculations for syngas-fuelled engines. Validations against experimental data and published numerical models are analysed.
- Chapter 4: Simulations of air fired, integrated biomass gasification power cycles with CO_2 utilisation are evaluated. Details of direct CO_2 recycling are highlighted to show the influence on gasification performance. Simulations are extended to examine aspects of engine-gasifier coupling within the system and the role of gas phase diluents on cycle performance. Here, the principal interactions of recycled exhaust are determined under conditions typical of traditional biomass power systems and evaluated in isolation from any CCS applications.
- Chapter 5: Further simulations of oxyfuel BECCS power cycles investigate the effect of CO_2 recycling on gasification processes and overall cycle performance. Evaluation of model parameters also reveals the sensitivity of the cycle to thermal and operational configurations. The BECCS system studied here uses an oxyfuel CCS strategy to minimise the potential for N_2 dilution, a condition found in the previous chapter to severely limit the thermodynamic benefits of exhaust recycling.
- Chapter 6: Experimental gasification of lignin biomass samples is used to assess the conversion potential of biomass under a CO_2 gasifying agent. Results are compared against pyrolysis and air gasification. Experimental results reveal the effect of underlying chemical processes on the results of gasification. Given the thermodynamic perspective offered in the computational simulations of the previous chapters, this illustration of syngas evolution from a sample of biomass lignin provides insight into how a real syngas may come to differ from the thermodynamic conditions of chemical equilibrium.
- Chapter 7: An overview of the results is summarized and discussed to provide novel insights on the potential applications of CDU in biomass gasification power cycles and BECCS systems. Directions for future investigations are also suggested.

Chapter 2 Literature Review

2.1 Introduction

To best assess potential avenues to improve the efficiency of BECCS technologies, an understanding of critical fundamental processes is necessary. Particular advantages of using gasification in concert with CDU methods present attractive opportunities to realise the required innovation in BECCS systems. An in-depth understanding of gasification is the basis for a novel application of direct CDU in biomass energy cycles.

A review of methods to interpret and model gasification processes highlights the techniques most applicable to assess gasification performance in an integrated cycle. Additionally, understanding aspects of BECCS and CDU technologies allows for a more complete evaluation of prospective innovations. Finally, details of CO_2 based chemistry and thermodynamics are reviewed to build a technical basis for future improvements to gasification applications.

2.2 Gasification processes and representative numerical models

Gasification is a complex process that converts a solid feedstock to a mixture of simple gases, primarily H_2 and CO. Several methods can be used to calculate the outputs of gasification reactions, each with advantages and limitations. Generally, these methods fall within three main approaches based on the fundamental principles from which the equations are derived. Such overarching categorical groups are empirical models, equilibrium or thermodynamic models, and kinetic models.

2.2.1 Empirical models

The most direct way to model a gasification process is to use data from known gasifier outputs. Using the same syngas composition from previous experiments or plant data is a convenient method to directly simulate a syngas composition. Such a static method inherently creates a modelled syngas that is invariant in time or process conditions but is simple to implement by sourcing a typical syngas composition from available data and scaling the output quantities based on the feedstock inputs. This approach is primarily useful for assessing downstream applications of the syngas [32, 20] but does not directly provide meaningful variation in syngas parameters, offering little analysis of the

gasification process. Empirical models nevertheless are effective at simplifying the thermochemical conversion process.

The reference empirical data can also be correlated to process parameters so the model can calculate variable outputs. For example, Gomez-Barea et al [33] have helpfully correlated results of their pyrolysis experiments to give expressions for product yields as polynomials of reaction temperature. Pyrolysis models for similar feedstocks can use these expressions to determine the distribution of char, tar, and gas products based on calculated temperatures. Model outputs for these cases are therefore variable with a relative distribution of products that varies based on reaction temperature.

This approach can be extended to include elemental balances which increase the flexibility of the model to better accommodate variable feedstocks while maintaining mass conservation. Models like those developed by Thunman et al [34] and Neves et al [35] establish systems of simultaneous equations to solve for pyrolysis products based on elemental mass balances and temperature dependent empirical product ratios. Additional correlations of syngas heating value, char composition, and tar composition complete the set of equations for the model. When solved, the system of model equations calculates the distribution of pyrolysis products including individual gaseous species. Applying this conservation constraint within the correlated empirical model ensures that the quantities of all calculated gasification products satisfy the mass balance of each element supplied with the feedstock and gasifying agents, increasing the reliability of the results for novel feedstock and gasifying agent use.

Complexity of empirical models can be scaled up using modern machine learning and artificial neural networks (ANNs). These models, while significantly more sophisticated than traditional empirical models, ultimately source training data from published experimental or operational results and thus fit within this modelling regime. By using a large base of sample data points, advanced statistical methods are applied to determine the effect each parameter considered influences the target variables. The ANN model generates a series of equations in a hidden layer to map a set of input parameters to a set of likely output variables. For a recent example of a gasification ANN, Ascher et al [36] present a model that correlates inputs like feedstock ultimate and proximate analyses, gasifying agents, reactor type, and gasifier temperature to output syngas composition and yield, char residue, and tar generation with root mean square error of 13.07%.

While traditional machine learning models keep the exact calculations of the ANN in hidden layers, more recent advances in these techniques aim to generate interpretable results from the model. These explainable models include supplemental information to add additional detail supporting the calculated simulation outputs. In general, this information should include a meaningful justification of the results, a measure of the accuracy of the results, and an indication whether the simulation parameters are within the operating limits of the empirical model [37]. Naturally, such supplemental information can add a degree of confidence in the model outputs by indicating the relative influence and sensitivity of several key inputs, however this does not change the foundations of the modelling approach. While informative and offering clarity on the functionality of the ANN, the basis of the explainable models ultimately remains a statistical correlation of empirical data to a set of provided inputs. No machine learning or ANN models directly consider the fundamental physical or chemical processes that govern the gasification process.

Empirical models are useful in reliably modelling gasification processes that are similar to previously recorded experiments. Because these models base their outputs only on a selection of chosen reference data, they are biased towards the design and operational conditions prevalent in that background information. Thus, empirical models have limited applications beyond the conditions of the base case. Different gasifying agents, reactor configurations (e.g. Figure 2-1), temperatures, flow rates, and even gasifier dimensions will add uncertainty to the modelled syngas outputs. This approach is very useful in assessing existing gasification technologies and how their products can be effectively used in downstream systems or integrated into other processes. However, these models lack an explicit phenomenological foundation and therefore are limited in their ability to be used as a design tool for novel gasification technologies that do not have an extensive record of proven experimental data. Such an application could be particularly beneficial in assessing how current gasification technology could be deployed in BECCS and bioenergy systems in the near term, however they are not appropriate in developing the innovation needed to accelerate the BECCS deployment that will certainly be required in the second half of the century.

2.2.2 Kinetic Models

Kinetic models approach gasification by detailing each underlying chemical and physical process that make up the overall gasification system. The basis for these methods is a set of reactions (e.g.Table 2-1) which stoichiometrically convert distinct reactants into known

quantities of products at a speed relative to the overall reaction rate, r_i. Relationships between the creation rates of products and consumption rates of reactants for a given chemical reaction are dependent on the stoichiometric ratios of the reaction considered. Generally, the reaction rate governs the rate of change in concentration of a particular chemical species over time.

Rate expressions (equation (2.1)) calculate how quickly a given chemical reaction, *i*, converts product species into reactant species. In typical gasification calculations, this rate is proportional to the product of partial pressures of vapour-phase species, p_i, each weighted by an empirically determined reaction order exponent, v_i. These reaction rates also depend on the reaction rate constant, k_i. This parameter is, in turn, temperature dependant and follows an empirically derived Arrhenius equation (equation (2.2)). Reaction activation energies, E_a, are experimentally determined by calculating the rate of change of the reaction rate at different temperatures while correlation constants A_i and b_i are used to fit the kinetic rate expression to the observed output data. For some kinetic expressions, the species partial pressure, p_i, is replaced with species molar concentration, C_i. Other kinetic models use a modified rate law that uses the difference between reactant gas pressures and their equilibrium pressures [38].

$$r_i = k_i \prod_j p_j^{v_j} \tag{2.1}$$

$$k_i = A_i T^{b_i} \exp\left(-\frac{E_a}{RT}\right) \tag{2.2}$$

Process calculations determine the overall chemical conversions based on these calculated rates of reactions and residence times of reacting species. This time is determined given the flow velocities and geometry within the reactor. Chemical changes predicted by this model therefore depend on the hydrodynamic conditions within the gasifier to determine local residence times of reacting mixtures. Often, the hydrodynamic conditions are simplified to fixed volume continuously stirred tank reactor (CSTR) or one-dimensional plug flow reactor (PFR) models [39]. Therefore, use of kinetic models is highly dependent on the particular design and operating conditions of a given gasifier.

Generally, individual steps of drying, pyrolysis, reduction (sometimes also called gasification), and oxidation are considered constituent steps to gasification (e.g. [40, 41]). Each step is also comprised of several individual chemical reactions (e.g.Table 2-1) that can be simulated using the methods described above. The kinetic rates of reactions

happening within each step or zone are generally described using equation (2.1) with the rate constants calculated by an Arrhenius rate law (equation (2.2)). Different gasifier types (e.g. Figure 2-1) arrange the four gasification sub-processes in different ways. Gas flows through the fixed beds in updraft and downdraft gasifiers follow different sequences of zones. Feedstock and bed material in entrained flow and fluidised bed gasifiers circulate with the gas flow, but the same four principal processes happen over time as the solid particles and gas move around the reaction zone.

Table 2-1: Key reactions in oxidation and reduction processes [42]

Reduction Reactions		
Boudouard reaction:	$C_{(s)} + CO_2 \rightarrow 2CO$	Δh = +172 kJ/mol
Hydrogasification:	$C_{(s)} + 2H_2 \rightarrow CH_4$	Δh = -78.4 kJ/mol
Primary water-gas reaction:	$C_{(s)} + H_2O \rightarrow H_2 + CO$	Δh = +131 kJ/mol
Water-gas shift:	$CO + H_2O \leftrightarrow H_2 + CO_2$	Δh = -41.2 kJ/mol
Sabatier reaction:	$4H_2 + CO_2 \leftrightarrow CH_4 + 2H_2O$	Δh = -165 kJ/mol
Steam reforming:	$CH_4 + H_2O \leftrightarrow 3H_2 + CO$	Δh = +206 kJ/mol
Methane dry reforming:	$CH_4 + CO_2 \leftrightarrow 2H_2 + 2CO$	Δh = +247 kJ/mol
Oxidation Reactions		
Char partial oxidation:	$2C_{(s)} + O_2 \rightarrow 2CO$	Δh = -111 kJ/mol
Char oxidation:	$C_{(s)} + O_2 \rightarrow CO_2$	Δh = -394 kJ/mol
Methane partial oxidation:	$2CH_4 + O_2 \leftrightarrow 4H_2 + 2CO$	Δh = -36 kJ/mol
Methane oxidation:	$CH4 + 2O_2 \rightarrow CO_2 + 2H_2O$	Δh = -803 kJ/mol
Carbon monoxide oxidation:	$2CO + O_2 \rightarrow 2CO_2$	Δh = -284 kJ/mol
Hydrogen oxidation:	$2H_2 + O_2 \rightarrow 2H_2O$	Δh = -242 kJ/mol

*Graphite allotrope, $C_{(s)}$, is assumed for solid carbon heat of formation

In detailed kinetic schemes, each chemical reaction is modelled individually to determine the progress of that reaction. Results from each reaction are then combined to determine the total system outputs of species concentration, temperature, flowrates, etc. For example, oxidation and char reduction processes use a supplied gasifying agent that reacts with the volatiles and char from the pyrolysis step. When air or oxygen is used as the gasifying agent, exothermic oxidation reactions are used to raise the temperature in the gasifier and supply the energy needed to drive the endothermic reduction reactions. The reduction reactions use the gasifying agent to further convert the char to syngas products of CO or

CH_4. Typical reactions for these steps are given in Table 2-1. When each of these reactions is individually calculated using assumed kinetic rate data, the overall method is called a detailed kinetic model.

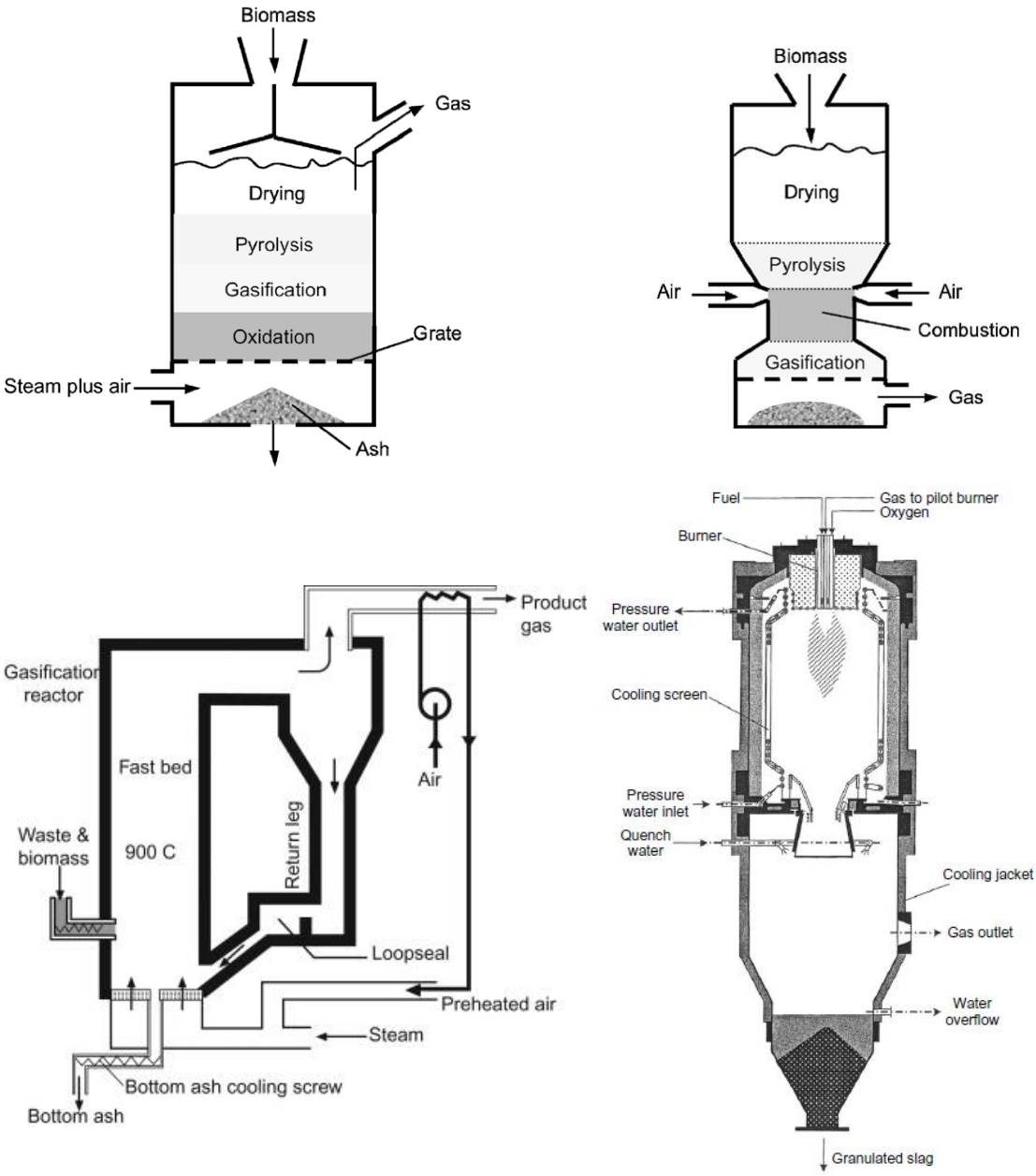

Figure 2-1: Different gasifier configurations (clockwise from top left): Updraft fixed bed, Downdraft fixed bed, Circulating fluidised bed, Entrained flow [42]. Reprinted with permission from Elsevier.

The detailed kinetics of the pyrolysis process are more complex. This devolatilisation separates the solid carbon char and inorganic ash from the volatile vapours contained in the biomass. Some of these vapours can be condensed to form liquid bio-oils or tars but extended residence time under the conditions of pyrolysis initiates secondary cracking reactions that further reduce the condensable vapours into simple gasses. Ranzi et al [43] elaborate a complex detailed kinetic model of pyrolysis with over 30 distinct chemical

species. This procedure details a multistep process that includes the devolatilisation of biomass sub-components cellulose, hemicellulose, and lignin as well as detailed intermediate reactions for tar cracking. Using this detailed model, predictions of gas composition are also possible. It also predicts condensable tar species formed in the pyrolysis process.

Detailed kinetic models of such a complex system are cumbersome and computationally intensive to solve. To simplify the methodology, a lumped kinetic strategy can be implemented. In this style of kinetic approach, a series of pseudo-processes are considered rather than individual specific chemical reactions. Effectively, the underlying detailed kinetic chemical reactions are lumped together into these pseudo-processes which are then evaluated to solve the new reduced order model. Each new pseudo-process will have its own empirically derived kinetic rate which will be solved the same way as for detailed kinetic models, there will simply be fewer kinetic process to calculate in a given step.

Considering the pyrolysis process described earlier, a lumped kinetic model can simplify the scheme from over 30 individual species to relatively few pseudo-components. In this way, Koufpanos et al [44] modelled pyrolysis as three separate pseudo-processes, reducing the number of distinct species from over 30 to only 5 (B, G_1, C_1, G_2, and C_2) as shown in Figure 2-2:

(1) Conversion of biomass feedstocks into initial volatiles and gasses: $B \rightarrow G_1$
(2) Conversion of biomass feedstocks into intermediate char: $B \rightarrow C_1$
(3) Interaction of initial volatiles and gasses with intermediate char to form additional volatiles, gasses and chars: $C_1+G_1 \rightarrow C_2+G_2$

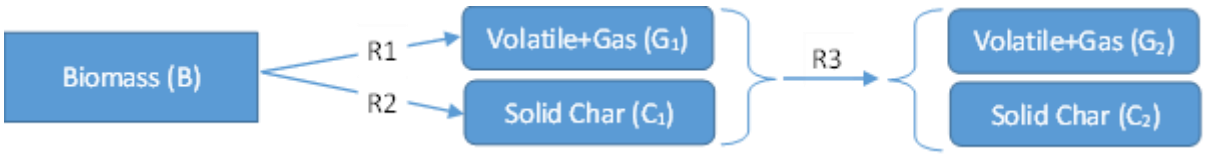

Figure 2-2: Multi-step pyrolysis process using a lumped kinetic model

Kinetic parameters for these pseudo-processes (R1, R2, and R3) are solved by Koufopanos et al. [44] based on best fit matching of experimental results from thermogravimetric analysis of wood residues. Here, the decomposition of the biomass fuel (R1 and R2) was best fit as an order 1. Srivasta et al [45] further determined the best fit of the multistep kinetics with both intermediate char and initial volatiles decaying as an order 1.5 processes

(R3). While pyrolysis reactions will continue as long as reactants exist at a sufficiently high temperature, the rate of pyrolysis decreases dramatically when the mass of raw biomass falls below 3% of its initial amount [46]. Despite the likelihood of small amounts of biomass remaining throughout the entire process, only volatile gasses and chars are considered as the outputs of pyrolysis in this simplified model. Such a lumped approach, while simpler to implement, does not directly calculate the distribution of specific chemical products within each pseudo-component and therefore relies on some supplemental empirical correlations to determine the exact yields of each product species.

Kinetic models can also incorporate other empirically assessed parameters to adjust the calculation routine and produce results calibrated to known operating conditions. Typically this takes the form of a char reduction factor (CRF) that multiplies the kinetic rate function based on some calibration experiment (e.g. [47]). Bianco et al [48] use machine learning techniques in an application equivalent to using CRFs in a detailed kinetic model of a down draft gasifier. Applications of tuned frequency factors in this work modify the kinetic equations of pyrolysis and char reductions to improve the matching of model outputs to known experiments. As with all kinetic and empirical models, this introduces some uncertainty into the results if inputs of a given simulation case are outside the range of empirical cases used to source the correlated data. In this case, the study was constrained to investigating the performance of a particular design of downdraft gasifier and yielded better validation results than an uncalibrated 1-D kinetic model for the same gasifier. The resulting model was then used to determine the ideal gasifier design to minimize tar and CO_2 production for gasification of a particular feedstock. Compared to the initial gasifier design, this model predicted a downdraft gasifier with marginally larger dimensions operating at a slightly higher air equivalence ratio could reduce tar production to < 0.5 wt.% and CO_2 production to < 2 wt.% in the product syngas.

Although the foundation of this method relies extensively on an empirical framework, it differs from the explicitly empirical gasification models described previously because a series of fundamental processes are distinctly simulated rather than using a correlation to directly calculate the model outputs. Furthermore, the kinetic outputs are time-dependant and deterministically linked to the reactor geometry and process parameters like flowrates and temperatures. Nevertheless, building a model on such an empirical framework will always create conditions of uncertainty when used to simulate novel conditions that extend beyond the limits of the empirical cases used to determine the fundamental relationships of the numerical simulation.

These same kinetic principles can be applied to more spatially complex models using higher order domains and incorporating viscous and momentum forces on the fluid flow. Such computational fluid dynamic (CFD) models offer particularly detailed insights on specific aspects and design details of gasifiers. Ultimately, the syngas production in a CFD model is still determined by the kinetic rates of the chemical reactions incorporated into the model and thus is conceptually a kinetic model. For example, the model used by Kumar and Paul [49] applies a series of CFD routines to a geometry of a downdraft gasifier. Standard methods are used to calculate velocity fields, pressure fields, and temperature fields from the Reynolds-averaged Navier-Stokes equations (RANS) coupled with the well-known k-ϵ turbulence sub-model. Additional terms to model the conversion of chemical species in the flow are calculated using the same kinetic rate expressions as for other kinetic models (i.e. equations (2.1) and (2.2)). The nature of this model provides high detail in assessing the hydrodynamic conditions within the gasifier reaction zones and allows for visualisation of output results across the whole reaction space, but the conversion performance is still ultimately determined from the same kinetic basis.

Changing fuel feeding rates or gasifiying agent supply rates will affect not only the concentrations and ratios of chemical species but also the hydrodynamic velocities and residence times for each reaction zone. Results will vary considerably between gasifiers of different configurations, different gasification agents and flow rates (steam, air, CO_2), and even different dimensions within the gasifier. Salem and Paul [50] show how sensitive a kinetic model is to minor changes in gasifier dimensions. Their downdraft air gasifier model uses an empirical, temperature-based pyrolysis zone but then implements kinetic models in the oxidation and reduction zones. This work clearly demonstrates how highly sensitive kinetic models are to gasifier design principles (Figure 2-3). Specifically, they showed how syngas species concentrations vary with changes to the length of a gasifier's reduction zone. CO and H_2 production were particularly affected, with a near sixfold increase in CO and a tenfold increase in H_2 production by changing this dimension by 20 cm. In order for complete feed stock conversion, gasifier reduction zone design lengths varied by 18% based on feedstock moisture, 31% based on equivalence ratio, 92% based on temperature, and up to 19% based on feedstock alone. Beyond just the reduction zone dimension, this work also shows optimum sizing for other gasifier dimensions also change if different biomass fuels are selected as a feedstock. This plainly shows that kinetic models are primarily useful for design and analysis of specific gasifiers and cannot be generalised to address wider process-level aspects of gasification integrated cycles.

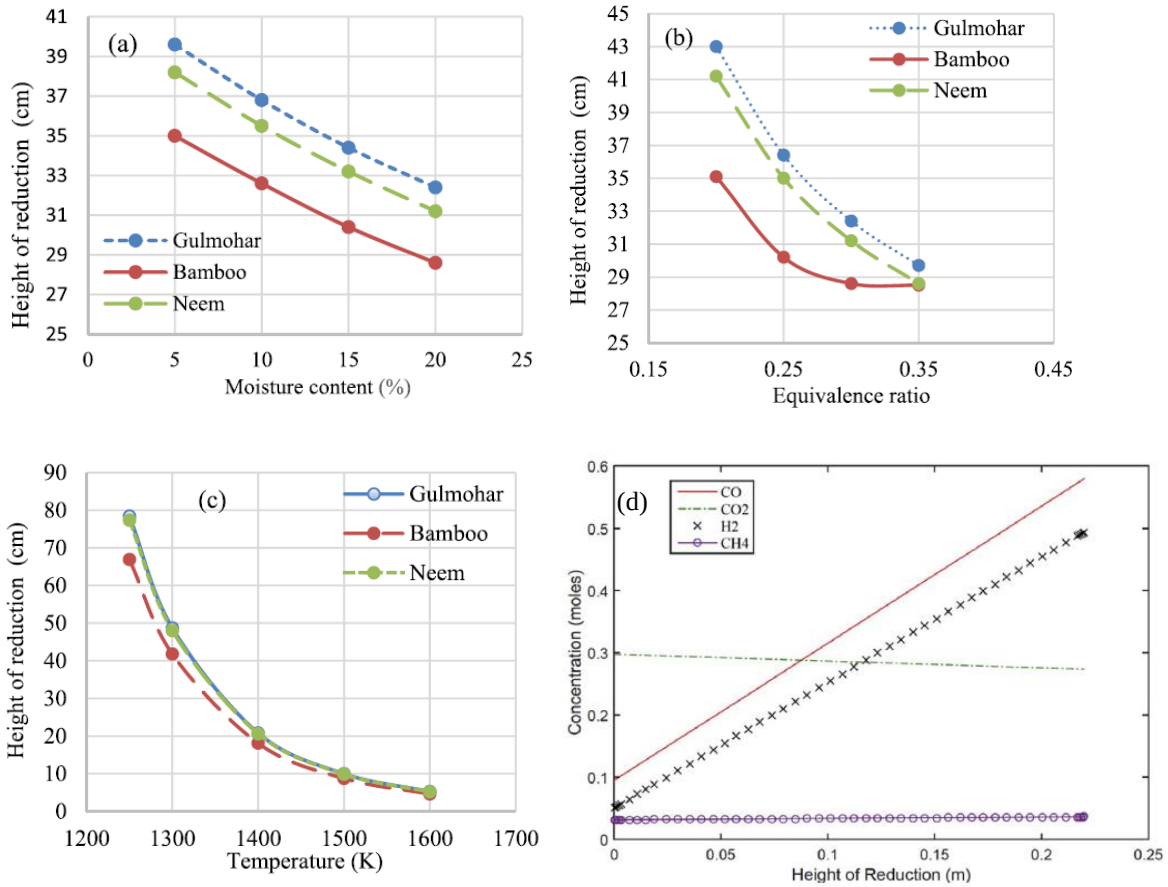

Figure 2-3: Variations in kinetic modelling results for (a-c) minimum reduction zone height for complete char conversion and (d) syngas composition based on reduction zone height [50]. Reprinted with permission from Elsevier.

Additionally, there is often significant disagreement in the values of kinetic parameters reported in the literature for the same chemical reactions or processes. The previously referenced CFD study of a downdraft gasifier [49] reported this effect when an initial set of kinetic parameters for oxidation and reduction reactions could not replicate the syngas composition from a reference validation case. Even though the same set of kinetic parameters had been validated on a separate model, they were ultimately unreliable when implemented in a new simulation. A different combination of kinetic parameters was then selected and used to successfully validate the model, however this demonstrates that kinetic models can often be unreliable.

Kumar and Paul further extended this investigation of how CFD models are sensitive to different kinetic rate parameters [51]. Their sensitivity investigation was limited to varying kinetic rate parameters of combustion reactions and included six different data sets for CO combustion, four different sets for H_2 combustion, and three different sets for CH_4 combustion all sourced from validated studies available in the literature. This range of contrasting parameters from the literature produced maximum temperatures that ranged

from 1730K to 2600K, compared to the validation experiment which had a maximum temperature of 1673K. Furthermore, all available kinetic data sets had difficulty replicating the CO and CH_4 content of the product syngas while significant variation in H_2 and CO_2 content was also observed. Although some of this discrepancy is due to differences in tar modelling, it remains an illustration of how sensitive all kinetic models are to input parameters for a chosen modelling case.

These aspects of kinetic models make them ideal analysis tools for the evaluation of specific gasifier design parameters. By relying on fundamental kinetics to determine the rates of the governing chemical reactions, kinetic models provide a robust method for determining the performance of a particular gasifier design under different operating conditions. Sensitivity of these models to gasifier dimensions and chosen kinetic rate parameters mean that each model is specific to one gasifier and cannot directly simulate the performance of a different gasifier without modification and possibly recalibration. In this way, kinetic models provide an excellent method for assessing a gasifier in particular but cannot directly simulate a range of gasification technologies without significant alteration to the configuration of the model.

2.2.3 Equilibrium models

Another method for determining the result of chemical reactions is based on the thermodynamics of the reacting species seeking a natural equilibrium point. Applied to a global gasification process, such an approach assumes that the gasification reactions will progress until the product and reactant species reach the point of chemical equilibrium for the given reaction conditions. Although the hydrodynamic conditions and chemical kinetics inside a real-life gasifier may prevent the gasification process from reaching its true equilibrium condition, this analysis remains convenient for assessing overall process performance. Predicted syngas composition from this model depends only on the elemental feedstock, operating conditions, and expected product species while remaining independent of the gasifier design [42]. These models can calculate one overall gasification equilibrium process or apply equilibrium modelling to individual steps like pyrolysis, oxidation, or reduction.

Equilibrium conditions exists at the point where the chemical potential, or Gibbs free energy, of a reacting system is minimised. For a given chemical reaction, the equilibrium condition is calculated from the fundamental thermodynamic relationships shown in

equations (2.3)-(2.5). The equilibrium coefficient, K_{eq}, is used to determine the ratio of products to reactants in terms of partial pressure, p_i, for a given chemical reaction at a specified reaction temperature.

$$0 = \Delta G_r^0 + R\,T\ \ln K_{eq} \tag{2.3}$$

$$\therefore\ K_{eq} = e^{\left(\frac{-\Delta G_r^{\ominus}}{R\,T}\right)} \tag{2.4}$$

$$K_{eq} = \frac{\prod_{products} {p_i}^{\upsilon_i}}{\prod_{reactants} {p_j}^{\upsilon_j}} \tag{2.5}$$

Stoichiometric equilibrium gasification models, e.g., [50], seek to establish the equilibrium conditions for a set of selected gasification reactions (e.g. Table 2-1). In each case, a reaction quotient, K_{eq} (eq(2.5)), is defined to relate the partial pressures of product, *i*, and reactant, *j*, species for the referenced reaction. Considering the known stoichiometry of the reaction, each species partial pressure is raised to the order of its stoichiometric coefficient, v_i. Combined with an elemental balance, proper selection of key gasification reactions create a system of equations that solve the equilibrium condition of the system. Commonly, a combination of char hydrogasification, water gas shift, primary water gas, Boudouard, and steam reforming reactions are chosen to evaluate the equilibrium condition [53]

Melgar, et al. [54] combine this approach with the known enthalpy changes of the specified reactions (Table 2-1) to complete an adiabatic energy balance across the gasifier model. By iterating between the calculated species concentrations at equilibrium and the system temperature changes due to reaction enthalpies, the model will eventually converge on an equilibrium temperature thus fixing the equilibrium reaction quotient and therefore the syngas composition.

A similar approach to equilibrium modelling can be adopted in such a way that stoichiometric considerations can be ignored [55]. An advantage of this non-stoichiometric method of gasification modelling is that no detailed knowledge of the precise reaction mechanisms is needed to complete the calculations. By specifying the elemental input to the gasifier from the feedstock and gasifying agent while assuming the expected syngas products, the equilibrium composition of syngas can be calculated directly by recognising that the total system Gibbs free energy of the syngas mixture will be minimised under equilibrium conditions. This fundamental thermodynamic foundation of this method is

equivalent to stoichiometric equilibrium models but rather than calculating reaction equilibrium constants from the zero Gibbs energy change (equation (2.3)), the Gibbs function of the resulting syngas mixture itself (equation (2.6)) is minimised.

$$G_{total} = \sum_i n_i \Delta G^0_{f,i} + \sum_i n_i \mathrm{R}T \ln\left(\frac{n_i}{\sum n_i}\right) \tag{2.6}$$

Of all modelling techniques, thermodynamic equilibrium models have the most robust phenomenological foundations, being derived from fundamental first principles. While the calculation of the thermodynamic conditions of gasification is deterministic, local conditions within a particular gasifier may not reach the equilibrium point. This causes some discrepancies between the calculated equilibrium syngas mixture and experimentally derived syngas. Due to the inherent minimisation of the Gibbs free energy as part of the model, thermodynamically unfavourable species tend to be under reported. This means that CH_4 and tars tend to be underpredicted while H_2 might be overpredicted.

To better match equilibrium models to experimental conditions, some modifications can be applied to the methodology. One method is to artificially restrict the equilibrium temperature, and thus the equilibrium constant, of select gasification reactions [56]. Tuning these temperatures, or temperature approaches, applies an empirical methodology to help correct the equilibrium conditions. Silva's method [53] similarly adjusted the equilibrium constants to modify the model outputs. Calibration factors were applied directly to the equilibrium constants to improve model agreement with known calibration cases. Biagini et al [57] show a mixed methodology that considers an explicitly empirical model for pyrolysis and then develop two parallel equilibrium models for gasification at different temperatures. By selectively choosing the ratio of pyrolysis products that go to which equilibrium model, the final syngas mixture is adjusted to better match known products.

Since equilibrium conditions are independent of gasifier dimensions, they cannot assess specific design features of an individual gasifier. Nevertheless, the rigorous derivation of the model allows for the best assessment of integration of gasification processes into highly coupled systems. The focus of the current work is on the system-level effects on the thermodynamic conditions of gasification rather than a detailed design analysis for specific gasifiers. Consequently, only a 0-dimensional equilibrium model is capable of such an analysis since empirical, kinetic, or CFD models will be dependent on the exact design and geometry of a chosen reactor [58]. Indeed, equilibrium models are often the preferred method for assessing complex systems with integrated gasification cycles [59, 60, 61, 62].

2.2.4 Modelling Summary

This section has explained in detail the principal methodologies used to determine the products of biomass conversion processes. Table 2-2 briefly summarises the general advantages and limitations inherent to each category of models.

Table 2-2: Comparison of gasification modelling techniques

Advantages	Limitations
Empirical Models	
• Based on real observations and empirical measurements • Simple to implement • Correlated models allow limited output variations for simulated conditions	• Outputs invariant to process conditions • Models biased to selection of reference data • Inherent uncertainties in correlated data • No direct phenomenological basis for model calculations
Kinetic and CFD Models	
• Strong conceptual framework based on detailed empirical measurements • Accounts for temperature and concentration gradients • Detailed information on individual chemical processes • Lumping chemical processes simplifies calculation routines	• Complex implementation • Extremely sensitive to gasifier design and geometry • Models require recalibration for novel design or operating conditions • Inconsistencies in reported empirical data cause uncertainties in selected kinetic rate expressions
Equilibrium models	
• Governing equations established from fundamental first principles • Fully describes thermodynamic conditions of chemical equilibrium • Detailed information on equilibrium conditions of individual chemical processes/reactions • Solution independent of intermediate reaction steps	• Deviates from real gasifier designs which do not achieve chemical equilibrium • Underpredicts chemical species with unfavourable thermodynamics

For the purposes of the current work, a thermodynamic model based on the chemical equilibrium of gasification products is the preferred methodology to study the conversion

process of biomass feedstock. While recognising that syngas from real gasifiers will differ from the chemical equilibrium mixture due to physical design features, analysis of the equilibrium condition remains the most technically rigorous approach to evaluate an integrated gasification system. This methodology is the only modelling technique derived from first principles rather than correlated to empirical data, meaning it is best suited to determine the potential performance of novel gasification processes.

Both empirical and kinetic based approaches introduce unintended influences that are not features of the fundamental cycle. Correlated empirical models, lacking phenomenological calculations, have very limited capacity to predict the performance of novel systems. Kinetic and CFD models incorporate sensitivities to kinetic rate data that may not be suitable for all modelling scenarios considered [51]. Furthermore, they are too dependent on particular gasifier designs to clearly distinguish system level effects from consequences of gasifier designs. Even minor variations in gasifier dimensions, flow rates, or temperature profiles can generate significantly different outputs [50]. As such, only equilibrium models can be used to minimise these sources of error and investigate novel gasification technologies on an integrated cycle basis independent of the specific design of one system component.

2.3 Potential impact of CDU and BECCS cycles

The principal advantages that make BECCS the anticipated CDR to lead negative emission efforts are that it generates a useful by-product in the form of mechanical power which can easily be converted into electricity, partially offsetting the costs of CO_2 sequestration. Additionally, the output power is a net-zero-carbon source of energy which can offset demand for fossil fuels, thus serving a double benefit in achieving net-zero emissions. In contrast, direct air capture (DACCS) requires an energy input to drive the process to capture carbon while afforestation and land use change (AFLOU) techniques require land areas to reduce or forgo otherwise productive uses to build-up and maintain a biogenic stock of carbon [63]. BECCS cycles with higher efficiencies would amplify these benefits since the output energy for a given amount of carbon sequestered would likewise increase.

In general terms, BECCS systems provide a CDR pathway comprising three main processes as shown in Figure 2-4; the natural fixation of atmospheric CO_2 into a biomass feedstock through photosynthesis, the conversion of the biomass feedstock into useful energy, and finally the capture and sequestration of CO_2 emitted from the conversion step

in long-term geologic storage [64]. While all BECCS systems rely on photosynthesis to absorb CO_2 from the atmosphere and geological formations to ultimately sequester the CO_2, several different technologies are capable of converting the biomass feedstock into energy and capturing the resulting emissions. Typically, energy conversion is achieved through either direct combustion or feedstock gasification while established CCS techniques include post-combustion capture, pre-combustion capture, and oxyfuel systems as illustrated in Figure 2-5 [65] . In short, post-combustion capture removes CO_2 from combustion exhaust, pre-combustion capture removes CO_2 from a syngas fuel prior to combustion, and oxyfuel combustion uses pure O_2 in combustion to produce an exhaust gas of only CO_2.

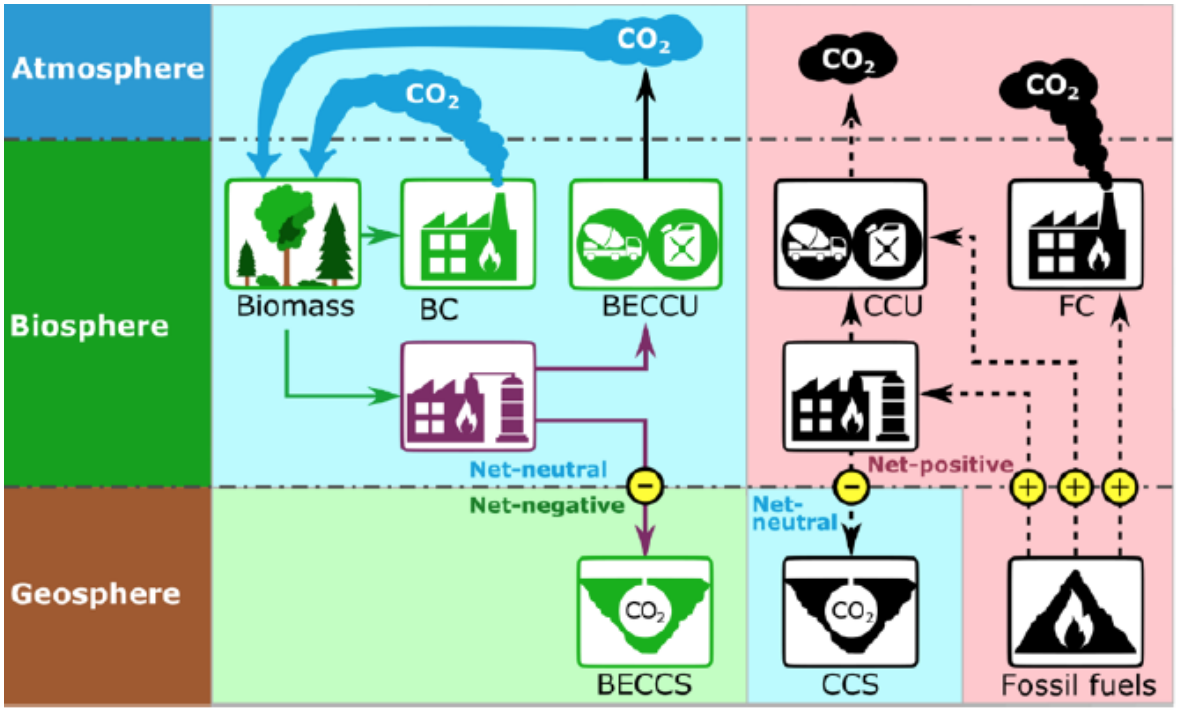

Figure 2-4: Carbon flows in biomass and fossil fuel power systems [66]. Shared under license CC BY 4.0.

The principal strategy of all CCS technologies is to ultimately separate any carbon containing species (i.e. CO_2) from other compounds within the cycle so that they can be removed and stored separately. Post-combustion technologies (Figure 2-5a) allow for both gasification-based or conventional methods of fuel combustion, producing an exhaust gas mixture consisting of CO_2, H_2O, N_2, and excess O_2. This exhaust is then treated to separate the CO_2 from the mixture. Several methods to achieve this separation are possible and generally involve absorption or adsorption of the CO_2 molecules into a sorbent material [65]. Treatment of the CO_2-saturated sorbent liberates a separate effluent stream of CO_2

from the system and regenerates the sorbent for continued use in removing CO_2 from the exhaust.

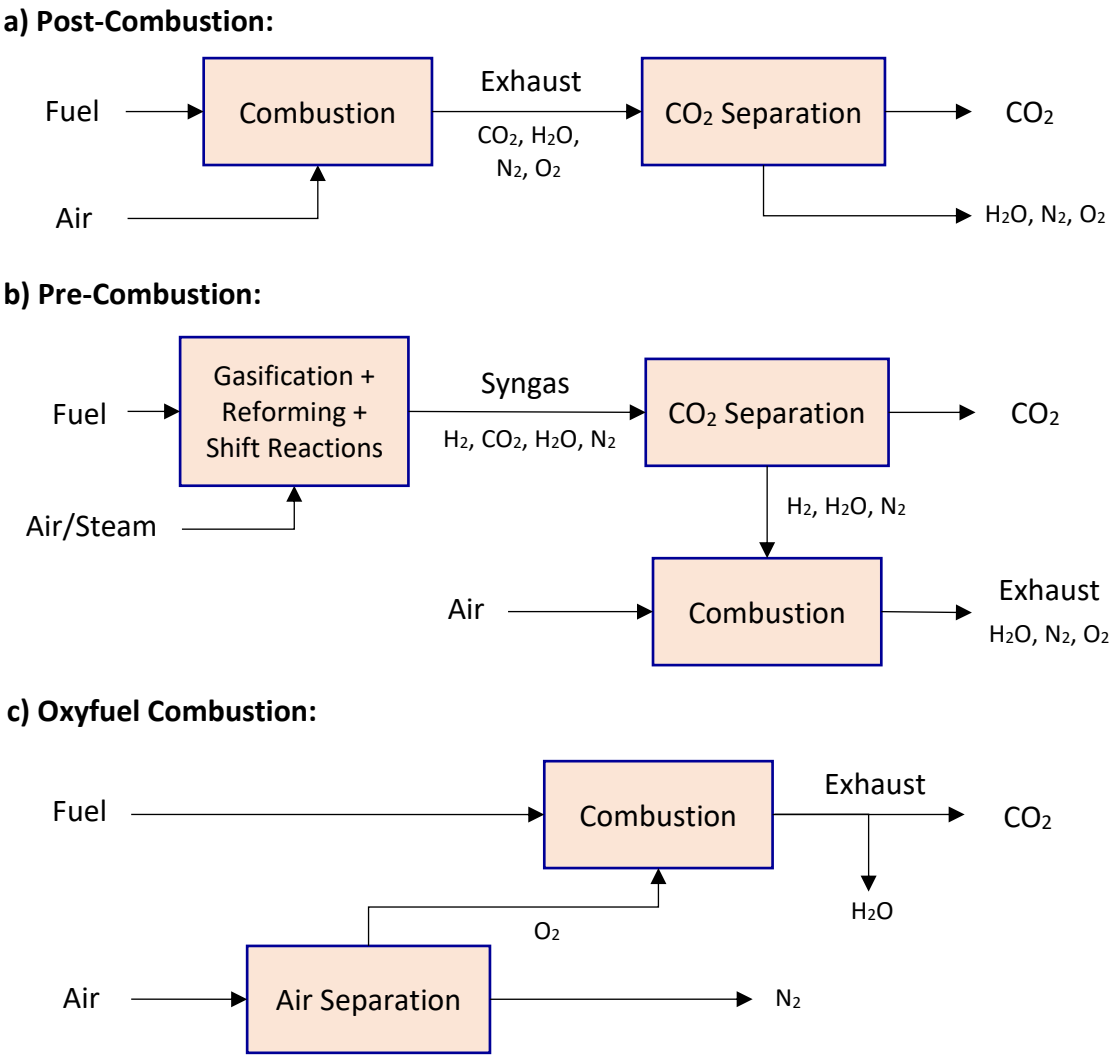

Figure 2-5: Schematics of CCS systems

Pre-combustion CCS systems adopt a slightly different approach for CO_2 separation that aims to separate any carbon out of the input feedstock through a series of chemical reactions. Instead of traditional combustion, the fuel is first gasified to produce a gaseous mixture of hydrocarbons, H_2, CO, and any residual reactants from the gasifying agents like N_2 or H_2O. To fully convert remaining carbonaceous compounds into CO_2, the syngas goes through steam injection to reform any hydrocarbons into CO and H_2 and then convert the CO to CO_2 through the water-gas shift reaction while generating additional H_2 (ref. Table 2-1). The final syngas mixture therefore has CO_2 as the only carbon-containing compound which can be separated using typical methods described previously. The remaining H_2 is the calorific species intended for combustion, producing a CO_2-free exhaust.

Rather than separating CO_2 from a mixture of other gases, oxyfuel combustion aims to make a combustion exhaust that itself consists only of CO_2. In this system, a stream of pure oxygen (O_2) is created by separating air in an air separation unit (ASU). Using pure O_2 as a oxidiser creates an exhaust mixture of only CO_2 and H_2O from the combustion of a hydrocarbon fuel. The water content is easily condensable, thus resulting in only CO_2 remaining in the flue gas. Chemical looping combustion systems (CLC) adopt the same overall strategy but rely on a metallic oxygen carrier to chemically separate oxygen from the air and bring it into the fuel combustion region [67].

Assessment models used in determining the costs of CO_2 removal using BECCS rely on fixed assumptions of the system's energy efficiency [68, 20, 69]. Such assumptions are based on historical operating data collected from coal fired and coal-biomass co-fired steam plants and then extrapolated for biomass firing scenarios. Additional efficiency penalties are applied to approximate the effect of incorporating CCS to these plants. Although this is a robust method for predicting the near-term costs of deploying BECCS, state of the art developments in BECCS system design which incorporate carbon dioxide utilisation technologies stand to improve the efficiency performance of these cycles well beyond these established assumptions.

Although some proposed BECCS technologies would produce fuels for the transportation sector rather than mechanical or electrical power directly [70, 71], only CO_2 sequestered during the production process constitutes a CDR pathway since any carbon contained in manufactured fuels is likely to return to the atmosphere when that fuel is consumed. This work maintains focus on the former case of BECCS for power production.

Based on the Global Change Assessment Model (GCAM), BECCS (and bioethanol and biomass FT liquid fuels) systems are shown to be more expensive than fossil fuel systems so long as CO_2 emissions remain unpriced. Under policy regimes where punitive costs are assigned to net-positive CO_2 emissions and CO_2 sequestration generates additional revenue of the same magnitude, BECCS systems become increasingly attractive as CO_2 costs increase. Simplified GCAM results predict BECCS and biofuels with CCS become economically competitive at carbon prices near 100\$/tCO_2 (2010 US dollars) and become the economically preferred technology as prices exceed 150\$/tCO_2 [72]. Increasing generating efficiencies of BECCS cycles beyond the current performance levels would therefore improve the economic performance of the system and allow for CO_2 capture at lower costs.

An additional benefit of CCS systems allows for deployment of firm (i.e. dispatchable), low-carbon intensity assets. Intermittent renewable energy sources (iRES) alone cannot reliably supply sufficient energy and require supplemental reserve capacity, largely provided by fossil fuel fired stations at present, to meet energy demands. Incorporating CCS into reserve generating stations allows an optimisable mix of generating assets that can best satisfy the energy trilemma of CO_2 reduction, cost minimisation, and energy security. Some modelling predicts traditional thermal generators with CCS technology will be able to outperform a wind iRES with thermal power reserve, achieving lower carbon intensities at lower marginal abatement costs [73]. These benefits are also realised for BECCS systems, which are dispatchable, with the added benefit of atmospheric CO_2 removal which is not possible for fossil-fuel fired CCS reserve generators.

Carbon dioxide utilisation (CDU) refers to any practice capable of benefitting from the use of CO_2 that would otherwise be released to the atmosphere or sequestered away. Such benefits might convert the CO_2 into useful products like fuels or could also provide a service like heat transfer or combustion dilution [21]. Beyond the particular CDU application, each CDU process affects the overall carbon cycle [74]. CDU pathways that result in long-term removal of CO_2 from the atmosphere are called “closed” pathways. CDU applications in BECCS technologies follow this scheme. CO_2 to fuel processes which return the CO_2 to the atmosphere over a short time scale are called “cycling” pathways. Other CDU technologies that store carbon in biological or soil stocks are “open” pathways. Although open pathways do not directly add CO_2 to the atmosphere, biological and soil systems exchange carbon with the atmosphere, so some amount of CO_2 added to these stocks is expected to reach the atmosphere over some time.

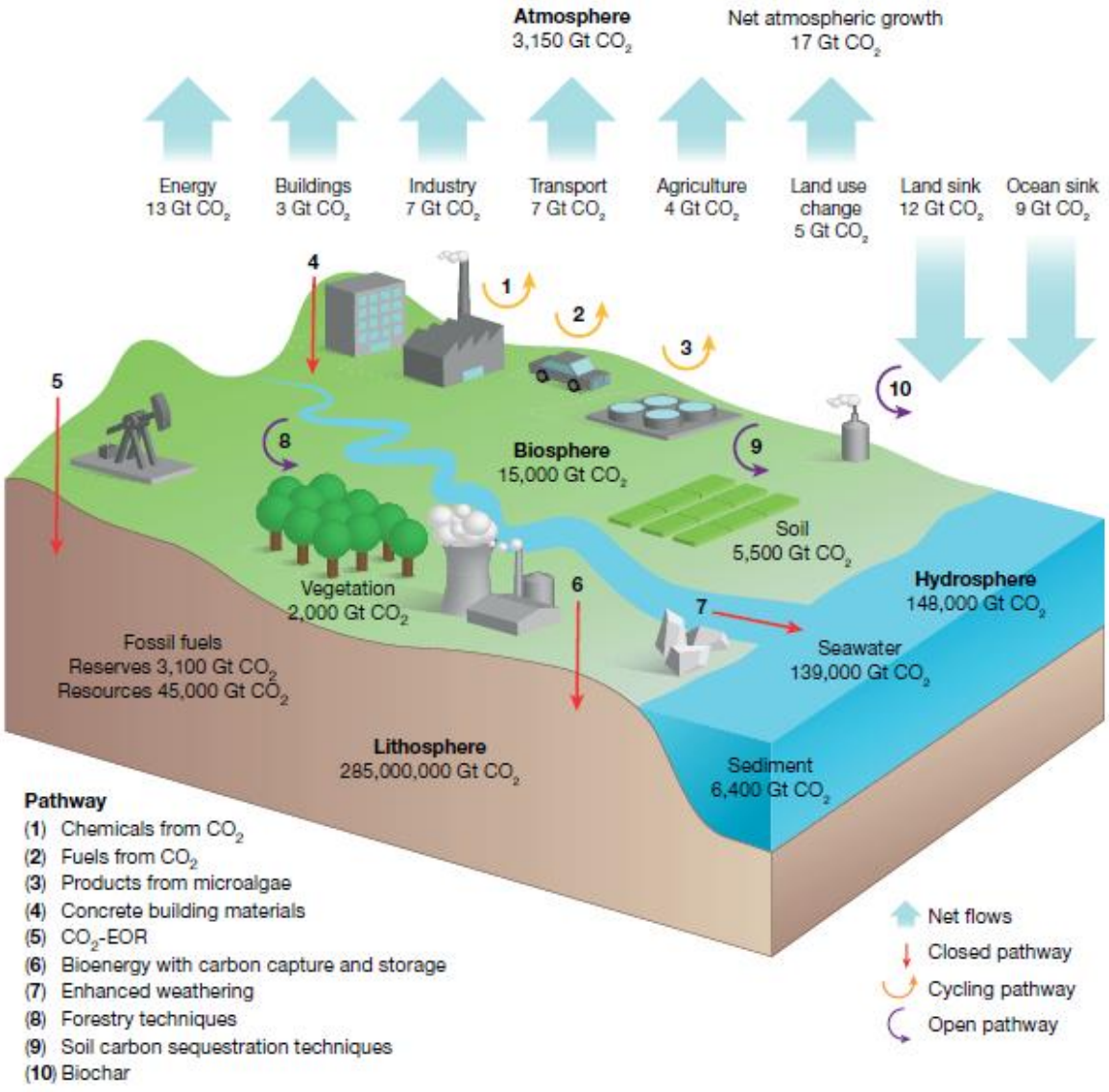

Figure 2-6: CO_2 utilisation pathways and annual net CO_2 fluxes (2008-2017) [74]. Reproduced with permission from Springer Nature.

Ahlström et al. [75] analyse cases of using waste CO_2 from biomass gasification as a feedstock to enhance product outputs. The base gasification cycle uses steam/O_2 to gasify wood residues while adding subsequent water-gas shift and methanation processes to clean the product syngas into a source of clean synthetic natural gas (SNG), rich in methane and CO_2 [76]. The high carbon to hydrogen content of the biomass feedstock, even considering the use of steam as a gasifying agent, means significant CO_2 will be present in the final SNG mixture. Using an additional source of hydrogen, the excess CO_2 can be converted to additional CH_4 through a Sabatier reaction (equation (2.7)). As a CO_2 to fuel pathway, it ultimately represents a "cycling" CDU pathway. This configuration integrates well with iRES to implement variation management strategies (VMS) where the biomass gasification unit can supply lower quality SNG to a local generator to supplement periods of low renewable electricity. When there is excess availability of electricity, electrolysers supply

the H_2 needed for the CDU upgrading process described above to upgrade the bio-SNG to a quality suitable for distribution to energy markets. Such a system has a clear CDU process, however it requires a complicated, multistep process to be implemented.

$$CO_2 + 4\,H_2 \rightarrow CH_4 + 2\,H_2O \tag{2.7}$$

2.4 Use of CO_2 as a gasifying agent

New techniques in system design for biomass fuelled, integrated gasification power cycles have shown promise in increasing the efficiency of power production through a direct CDU strategy unique to gasification applications [77, 62, 78]. In effect, using CO_2 as a gasifying agent to produce biosyngas has the potential to enhance the reverse Boudouard, reverse water-gas shift (rWGS), and methane dry reforming (DRM) reactions under high temperatures. Use of reactions like DRM and rWGS as CO_2 sinks appears technically attractive, although energy inputs are high. The stoichiometric ratios of H_2:CO of the resulting syngas does have a much higher CO content than syngas from other sources and may, however, restrict the usefulness of these chemical processes to only a few downstream applications [79]. Since combustion or direct energy applications are less sensitive to H2:CO ratios, this means direct CO_2 conversion into fuel gases is a potentially advantageous use of these reactions.

Recent avenues of research have focused on using CO_2 as a medium for gasifying solid fuels like biomass and char [80, 81, 82, 83, 84, 85]. Despite the slow, endothermic, energy intensive process of CO_2 gasification [86, 87], this technology provides a pathway for simultaneously utilising CO_2 produced during industrial processes while augmenting the output of syngas from the feedstock [88]. A CO_2 gasifiying agent also generates a more reactive char, is not as corrosive as steam, and provides versatility in syngas composition for desired applications [89]. Specifically, using CO_2 as a gasifying agent will enhance the reverse Boudouard reaction (eq(2.8)) by directly providing additional reactant to be converted into CO syngas.

$$C_s + CO_2 \rightarrow 2CO \tag{2.8}$$

$$\Delta h^0_{r\,Boud} = 2\left(\Delta h^0_{f\,CO}\right) - \left(\Delta h^0_{f\,C} + \Delta h^0_{f\,CO_2}\right) = 172.459\ \text{kJ/mol} \tag{2.9}$$

$$\Delta G^0_{r\,Boud} = 2\left(\Delta G^0_{f\,CO}\right) - \left(\Delta G^0_{f\,C} + \Delta G^0_{f\,CO_2}\right) = 120.07\,\text{kJ/mol} \quad (2.10)$$

$$\Delta G_{Boud} = \Delta h_{Boud} - T \cdot \Delta s_r = 172.459 - 0.1757\,T \quad (2.11)$$

Thermodynamic quantities of enthalpy and Gibbs free energy of the Bourouard equation are calculated in equations (2.9)-(2.10). Under standard conditions, the equilibrium of the reaction strongly favours the reactants. Higher temperatures are needed to shift the equilibrium condition toward the production of CO and away from the reactants. Changes in Gibbs free energy for the Boudouard reaction (eq(2.11)) to produce CO become negative (thus spontaneous) when the reaction temperature increases beyond ~980 K. Regardless of reaction spontaneity, the production of CO from char and CO_2 is highly endothermic; requiring 172.5 kJ/mol at standard conditions.

Despite CO_2 gasification reactions being generally slow, highly endothermic, and energy intensive compared to other fuel reforming processes [86], recycling of industrial CO_2 streams in a carbon capture and utilisation scheme is an appealing method for reducing greenhouse gas intensity of industrial processes. Bui et al [84] evaluated several reaction models (volumetric reaction, shrinking core, random pore, and traditional n^{th}-order kinetic) and determined that the traditional kinetic power-law model best matched experimental results for CO_2 gasification of wood charcoals produced at different pyrolysis pressures. This model considered only the Boudouard gasification reaction, but this simplification is reasonable since the experimental setup used charcoals high in carbon and oxygen content gasified in a stream of pure CO_2. Gasification in this experiment was performed at a temperature of 850°C.

Using an equilibrium model similar to Melgar et al [54], Chaiwatanodom et al [90] investigated a gasification cycle to separate CO_2 gasses from the product gas stream and return it to the gasifier. The model featured both steam and oxygen options as primary gasifying agents mixed with the CO_2 return from syngas stream and considered six key gasification reactions. Further model control allowed for metering of the CO_2 into the gasifier to adjust the ratio of CO_2 to C present in the biomass sample. In this study, the anticipated use of the syngas was for future upgrading as a chemical feedstock so the model used steam injection to control the syngas H_2:CO ratios. Increasing concentrations of CO_2 in the gasifier shifted the composition of the product gas toward higher levels of CO and lower amounts of CH_4 and H_2 as Boudouard, water-gas shift, and methane steam

reforming reactions are enhanced to favour CO production. Although the chemical conversion efficiency (CGE) of the gasifier was enhanced with increasing CO_2/C in the gasifier, the total system efficiency decreased as increased energy demands were required for steam generation and CO_2 separation [90].

Other computational studies of these CO_2 reactions have illustrated how this phenomenon influences the gasification process of carbonaceous feedstocks and depends on the thermodynamic conditions of the system, as shown in Figure 2-7 [91]. Under equilibrium conditions, syngas compositions in these studies show an increase in CO content from <10%vol to 60%vol as the reaction temperature increases from 500°C to 1000°C while the CO_2 content decreased from >90%vol to 10%vol over the same temperature interval. Under isothermal conditions of 850°C, different mixtures of O_2/CO_2 showed complete carbon conversion occurring between 0.3 – 0.04 molCO_2/molC_{feed} for mixtures ranging from 100%v - 20%v CO_2 in O_2. While the increase in O_2 content did improve the carbon conversion calculated in these simulations, it lowered the maximum CO_2 conversion rate from 80% to <40% and the maximum CGE from 120% to 105%. The co-gasification case also reported decreases in syngas CO content at the carbon boundary point since the O_2 will compete with CO_2 to react with the feedstock, forming CO_2 rather than CO. Additionally, the use of O_2 alongside the CO_2 gasifying agent has a positive effect on the heat inputs required to fully convert the feedstock carbon content. While pure CO_2 required between 5 – 20 MJ/kg_{feed} to convert the feedstock depending on temperature, use of 80% O_2 in the gasifying mixture lowered the heat requirements by ~3 MJ/kg_{feed} for equilibrium temperatures over 800°C [91].

Thermodynamic simulations of this process in an integrated cycle further reinforce both the potential for gasification enhancement and the increased thermal demands of using CO_2 as a gasification agent [61]. These increased thermal demands are due to the high endothermicity of the chemical reactions that convert CO_2 into a syngas species (e.g. Table 2-1). Under steam/CO_2 co-gasification scenarios, the syngas concentrations of CO increased from 32 – 50 %vol at the expense of H_2 and CH_4 products as the CO_2/C ratio was increased from 0 – 1 at 800°C isothermal conditions. While the CGE of gasification increased slightly, the extra heat inputs required due to the enhancement of the endothermic reactions caused the energy efficiency of the total system to actually decrease by 10-15%. Both these modelling scenarios have detailed the anticipated benefits of CO_2 gasification while highlighting the significant thermodynamic challenges inherent in developing such a system.

Similar computational studies also investigated CO_2 gasification equilibrium properties [92, 91, 61, 93]. Overall trends from these investigations highlight the capacity for enhanced char reduction, increased CO production, and potential for net-consumption of CO_2 while showing the increased endothermicity of the reaction mechanism and temperature dependency of the process. CO_2 conversion at the carbon boundary point increases with temperature, approaching 100% as the equilibrium temperature passes 1000°C although the minimum specific heat input for carbon conversion is reached at 850°C. Co-gasification with oxygen and steam can improve char conversion and reduce the required energy inputs for gasification but this also reduces the CO_2 conversion of the process since the additional gasifying agents will be reacting with the feedstock [91]. There are some limitations to this effect under the integrated system conditions of Chaiwatanodom et al. [61] where gasification under a CO_2/C ratio of 1 decreased the system efficiency by 10-15% due to the high thermal inputs required in the gasifier, although the corresponding cold gas efficiency (CGE) increased by a similar margin. These studies nevertheless indicate CO_2 is an effective gasifying agent, potentially improving the performance of a biomass gasifier.

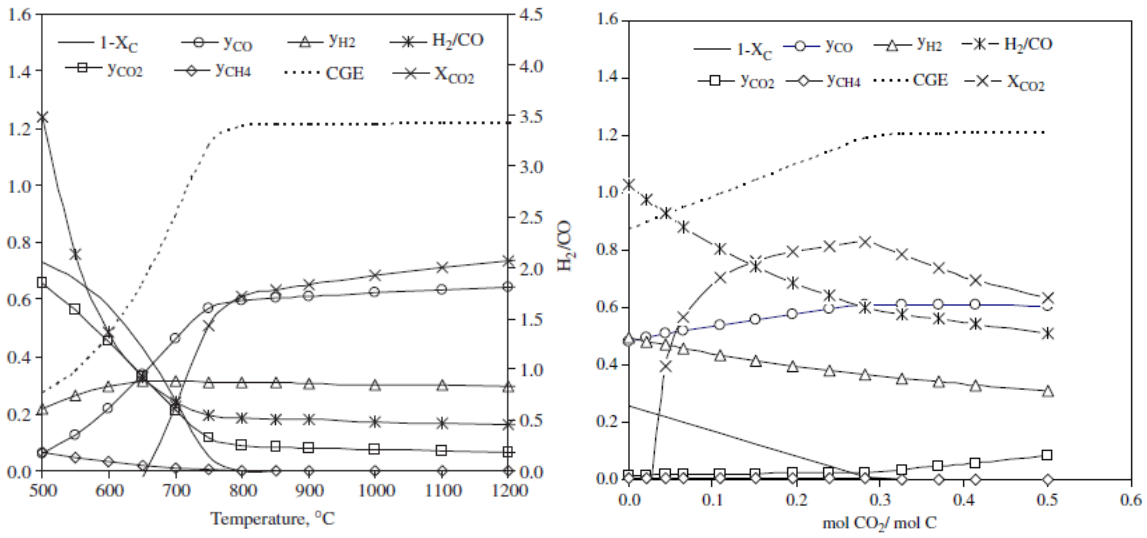

Figure 2-7: Equilibrium CO_2 gasification of a carbonaceous feedstock (left) under a CO_2/C ratio of 0.5 and (right) under isothermal conditions at 850°C [91]. Reprinted with permission from Elsevier.

Several experiments have also shown how CO_2 can enhance biomass gasification. While having little influence on the pyrolysis of biomass, CO_2 acts to enhance the reduction of biochar produced during the pyrolysis process [83]. Under a CO_2 atmosphere, gasifier CO production increased by roughly 2.5 times and CO_2 conversion increased by a factor of 3 as carbonaceous feedstocks were gasified under increasing temperatures from 800°C to 1000°C [86]. Even in O_2/CO_2 mixtures, addition of CO_2 as a gasifying agent enhanced CO

production by 130% [94] and improved char reduction from 20% to 95% while reducing the O_2 required in the system [95]. These results confirm the theoretical simulation predictions that CO_2 gasification will enhance the feedstock conversion into syngas. Experimental studies of this CO_2 conversion phenomenon have been conducted on biomass samples gasified with CO_2 as the only gasification agent [86, 83] or with CO_2 used in gasifying mixtures with H_2O [87, 96] or O_2 [95, 94]. Under isothermal conditions, use of CO_2 as a gasifying agent primarily influences char reduction while having negligible effects on the pyrolysis of a biomass sample [83].

Measurements during char reduction under CO_2 atmospheres show the enhancement of the reverse Boudouard reaction since CO is produced while CO_2 is consumed. Consistent with the endothermicity of the reaction, this effect is temperature dependent with CO_2 conversion increasing threefold and CO production increasing by a factor of 2.5 as the reaction temperature increases from 800°C to 1000°C [86]. Likewise, observations of autothermal gasification using O_2/CO_2 mixtures show the yield of CO increased by 130% when additional CO_2 was supplied [94]. CO_2/O_2 gasification also promoted CO_2 and char conversion compared to reference cases using N_2/O_2 gasification mixtures. For example, a mixture of 40%v O_2 in CO_2 resulted in 95% char conversion while a 40%v O_2 in N_2 mixture converted only 20% of the char sample. Additionally, higher concentrations of CO_2 in the gasifying mixture allowed for complete char conversion at lower oxygen fluxes with a 25% v O_2 in CO_2 mixture requiring only 35 g_{O2}/m^2s while the 40%v O_2 in CO_2 mixture required nearly 80 g_{O2}/m^2s for 95% char conversion [95].

Applying the CO_2 gasification principle to an integrated power cycle provides a way to effectively realise a carbon dioxide utilisation (CDU) method. In the context of a BECCS power cycle, this becomes a “closed” CDU pathway [74] since the CO_2 supplied to the gasifier system will ultimately end up in long term sequestration following the power production cycle. By recycling some CO_2 from the power plant’s exhaust for use in the gasifier, this system becomes a method of direct CDU since the production and consumption of the CO_2 happens within the same cycle. Enhancing a BECCS cycle with this CDU strategy is likely to improve the performance of the system and might also be considered a BECCUS cycle.

2.5 Knowledge gaps in existing literature

Current work on direct CDU strategies used in integrated biomass gasification cycles is limited. More in-depth investigations are needed to better comprehend the interactions of system parameters that influence both the overall system performance and the fundamental thermodynamics of the gasification process specifically. The high thermodynamic loads of CO_2 utilisation reactions suggest gasification performance would be sensitive to reaction temperatures, supplied allothermal heat, and any other effect that changes thermal conditions of the gasifier. Consequently, integration of CO_2 gasification into biomass energy cycles could introduce coupled interdependencies of component operations such that numerous factors can influence the system as a whole, however this has yet to be investigated in detail within an integrated system. Particularly, an assessment of the specific benefits and limitations of implementing a CDU strategy in a gasification power cycle is needed to inform future system designs to optimally implement CO_2 gasification.

Incorporating CCS into cycles using CO_2 gasification represents another area for further research. Any studies that have analysed this topic have so far been limited to simply examining the overall system outputs and efficiencies without in-depth investigation into the particular effects on the gasification process. These brief analyses do indicate some efficiency improvements of 1.68-4.86% for coal-fired Rankine cycles [97], 6-7% for coal-fired IGCCs [98], 5% for chemical-looping-combustion in a Rankine-based BECCS cycle [99], 6.1% for an Otto-cycle BECCS model [77], and 7.57% for a Brayton-cycle based BECCS system [62] when CO_2 recycling is implemented. In order to better understand this phenomenon, underlying thermodynamic conditions of the processes of gasification must be closely examined and aspects of CO_2 utilisation must be evaluated.

2.6 Summary

Deployment of bioenergy and BECCS systems is currently assessed based on empirical assumptions to determine the near-term costs of CO_2 sequestration. Development of innovative cycle technologies will be key to improving the efficiency of BECCS as a CDR technology, however existing tools are insufficient to predict the performance of such advances. Innovation in BECCS technology to improve efficiency is crucial to successfully implementing CDR capacities required to meet national and international emissions targets in the near future.

A variety of modelling techniques are available to assess gasification processes. To best determine the system-level effects of combining CDU applications into a biomass energy cycle, an equilibrium model should be chosen. This will ensure the true thermodynamic effects of system parameters on gasification conditions will be analysed. Use of any other gasification model would implicitly constrain the model to gasifier specific limitations which may not be representative of the fundamental thermodynamic conditions of gasification.

Direct exhaust CO_2 recycling in biomass gasification and BECCS cycles could be an effective method for increasing cycle efficiencies by using a CDU strategy. Locally circulating CO_2 in a traditional biomass energy cycle creates a “cycling” CDU pathway while the same approach in a BECCS cycle qualifies as a “closed” carbon pathway. Specifically, using waste CO_2 from the power cycle as a gasifying agent could enhance several CO_2 based gasification reactions to improve feedstock conversion and generate more CO, but clear evidence of these conversion processes is needed. Incorporating this technology in power cycles using an internal combustion engine (ICE) as the energy conversion system is particularly interesting.

Chapter 3 Derivation and Validation of Numerical Models and Methods

3.1 Fundamental Thermodynamic and Physical Properties

Models developed to analyse the thermodynamic conditions of the systems presented in this work are derived from known fundamental relationships between the system's properties. These foundational concepts are well described in relevant chemistry and engineering texts (e.g. [100, 101, 102]) and are very briefly summarized here to inform the development of numerical methods to simulate representative systems.

3.1.1 Gibbs Free Energy Methods

System energy changes are quantified through the thermodynamic potentials of enthalpy, *H*, and internal energy, *U*. The relationship between enthalpy and internal energy provides a means of assessing energetic changes in thermodynamic systems under constant pressure and constant volume regimes, and therefore under open or closed system boundaries. Applying standard experimental conditions of constant pressure and temperature, Hess' law (equation (3.1)) determines the net change in the system energy resulting from a chemical change in the thermodynamic system.

$$\Delta H_r^0 = \sum_{products} \nu_i \Delta H_{f,i}^0 \quad - \sum_{reactants} \nu_j \Delta H_{f,j}^0 \tag{3.1}$$

Kirchoff's equation (equation (3.2)) evaluates the enthalpy of a system at any temperature by accounting for sensible heating. This same principle can also be used to assess the change in a constant pressure system's thermodynamic potential from a chemical reaction at temperatures other than the reference state (equation (3.3)).

$$H = H^0 + \int_{T^0}^{T} C_P \; dT \tag{3.2}$$

$$\Delta H_r|_T = \Delta H_r^0 + \int_{T^0}^{T} \Delta\overline{C_P}\, dT \tag{3.3}$$

Considering the second law of thermodynamics, the entropy change of a system during a reversible process follows equation (3.4). This relationship is further developed using the

ideal gas equation of state and the thermodynamic identities shown in Appendix A to quantify the changes of entropy in constant pressure (equation (3.5)) and constant volume processes (equation (3.6)).

$$\delta S = \frac{\delta Q}{T} = -\delta S_{env} \tag{3.4}$$

$$\delta S = \frac{\delta H_r}{T} = C_V \frac{\delta T}{T} + R \frac{\delta V}{V} \tag{3.5}$$

$$\delta S = C_P \frac{\delta T}{T} - R \frac{\delta P}{P} \tag{3.6}$$

The change in a system's entropy reflects a dispersal of energy into the environment surrounding the system boundary, causing a corresponding change in the entropy of the environment, δS_{env}. For a chemical process, the overall entropy generated would therefore be the sum of the entropy change within the reaction and the entropy dispersed to the environment (equation (3.7)).

$$dS_{tot} = dS_r + dS_{env} \tag{3.7}$$

Under standard reference conditions of temperature and pressure, the calculation of overall entropy generated is modified through substitution of a thermodynamic identity. The resulting expression (equation (3.8)) becomes the change in standard Gibbs free energy for the reaction, dG_r^0.

$$\begin{gathered} -T \cdot dS_{tot}^0 = dH_r^0 - T \cdot dS_r^0 = dG_r^0 \\ \text{or} \\ dU_r^0 + \mathrm{P}^0 \cdot \mathrm{dV} - T \cdot dS_r^0 = dG_r^0 \end{gathered} \tag{3.8}$$

Because the second law of thermodynamics requires the total entropy of a process to increase, any process with a spontaneous thermodynamic potential will have a negative ΔG_r while processes with positive valued changes in Gibbs free energy are non-spontaneous, or rather are spontaneous in the reverse direction. This also shows that the Gibbs free energy of a system is a state function and can be evaluated based on a reaction's products and reactants (equation (3.9)).

$$\Delta G_r^0 = \sum_{products} \nu_i \Delta G_i^0 \quad - \sum_{reactants} \nu_j \Delta G_j^0 \tag{3.9}$$

As a state function, the system's Gibbs free energy equation is valid at non-standard conditions and is described in terms of state variables for entropy, enthalpy, temperature, and volume (equation (3.10)).

$$\begin{gathered} dG = dH - d(T \cdot S) \\ \text{or} \\ dG = V \cdot dP - S \cdot dT \end{gathered} \tag{3.10}$$

Completing the integration of these state variable differentials gives useful expressions for the isothermal change in Gibbs free energy of an ideal gas system between two states at constant pressure (equation (3.11)) or at constant volume (equation (3.12)).

$$\Delta G = \Delta H - T \cdot \Delta S \tag{3.11}$$

$$\Delta G = nRT \ln\left(\frac{P}{P^0}\right) \tag{3.12}$$

Equation (3.12) is particularly significant for multi-component systems undergoing chemical reactions since the partial pressure of the reactant and product species is likely to vary throughout the process and is unlikely to remain at standard conditions of 1 atm. Accounting for these concentration changes across the reactants and products yields the following equation (3.13) for a chemical reaction in a gas mixture at constant reaction pressure, P_r (see Appendix B for details of derivation).

$$\Delta G_r = \Delta G_r^o + RT \ln\left(\frac{\prod_{prod} {x_i}^{\upsilon_i}}{\prod_{react} {x_j}^{\upsilon_j}}\right) + (\Delta n_r) RT \ln\left(\frac{P_r}{P^0}\right) \tag{3.13}$$

For convenience, a system's extensive Gibbs free energy can be normalised by the molar extent of the system to determine the intensive chemical potential, μ_c, simplifying equation (3.12). Thus, the Gibbs free energy change of a system with N chemical species becomes further dependant on any changes to the composition of the system (equation (3.15)).

$$\mu_c = \frac{G}{n} = \mu_c^0 + RT \ln\left(\frac{P}{P^0}\right) \tag{3.14}$$

$$dG = V \cdot dP - S \cdot dT + \sum_{i}^{N} \mu_i \cdot dn_i \tag{3.15}$$

3.1.2 Chemical Equilibrium

Any system property reaches an equilibrium state when forces influencing that system property become balanced, resulting in no net change for that particular attribute. This can be a thermal equilibrium where heat flows balance to create steady temperature gradients or a kinematic equilibrium where momentum flows balance to create steady pressure fields. Equilibrium conditions also exist for chemical processes where the composition of a reacting mixture maintains a steady distribution of constituent species.

The change in Gibbs free energy, ΔG, or chemical potential, $\Delta\mu_c$, represents the thermodynamic impetus of a particular chemical reaction under given system conditions of concentration, temperature, and pressure. For a system at standard pressure with components *A* and *B* which can reversibly react to form species *C* and *D* (equation (3.16)), the change in Gibbs free energy is calculated from equation (3.17) where the change in standard Gibbs free energy, ΔG^0, is determined from equation (3.9).

$$\nu_A A + \nu_B B \leftrightarrow \nu_C C + \nu_D D \tag{3.16}$$

$$\Delta G_r = \Delta G_r^o + RT \ln\left(\frac{{x_C}^{\upsilon_C} \cdot {x_D}^{\upsilon_D}}{{x_A}^{\upsilon_A} \cdot {x_B}^{\upsilon_B}}\right) \tag{3.17}$$

At equilibrium, neither the forward nor the reverse direction of this reaction is spontaneous meaning the associated change in Gibbs free energy will be zero. Applying this condition to equation (3.17) allows for an expression giving the relative ratios of product and reactant species at equilibrium (equation (3.18)).

$$\frac{{x_C}^{\upsilon_C} \cdot {x_D}^{\upsilon_D}}{{x_A}^{\upsilon_A} \cdot {x_B}^{\upsilon_B}} = \exp\left(\frac{-\Delta G_r^o}{RT}\right) = K_P \tag{3.18}$$

For given process conditions of temperature and pressure, this stoichiometric ratio of species will remain constant following Le Châtelier's principle and defines the reaction's equilibrium constant, K_P. As a general simplification, higher values of the equilibrium constant imply the products of the reaction are thermodynamically preferred and will therefore represent a larger fraction of the mixture. The opposite case is equally true for

small valued equilibrium constants where conversion of the reactants is not favourable and thus the reactants remain as more significant components in the equilibrium mixture.

Reaction equilibrium constants are temperature dependant parameters thus the reaction temperature will influence the distribution of mixture species at equilibrium. Chemical reactions listed in Table 3-1 are relevant to a gasification process. Figure 3-1 shows equilibrium constants, K_p, of these reactions calculated using the fundamental equation previously derived (equation (3.18)) across a range of temperatures. Behaviour of these equilibrium constants is typical for endothermic reactions where higher temperatures generate larger equilibrium constants.

Although not shown in Figure 3-1, the equilibrium constants for combustion and partial oxidation reactions are several orders of magnitude greater than the reactions in Table 3-1 for all temperatures shown. This means these reactions can be considered irreversible and will proceed to completion. Since these oxidation reactions will not be thermodynamically limited under typical gasification temperatures, control of these processes is achieved through limiting the availability of free oxygen in the reacting mixture.

Table 3-1: Selected reactions relevant to biomass gasification [42]

Reverse Boudouard	$\mathrm{C} + \mathrm{CO_2} \leftrightarrow 2\ \mathrm{CO};\ \ \Delta h^0 = +172\ \mathrm{kJ/mol}$	(R1)
Reverse WGS	$\mathrm{H_2} + \mathrm{CO_2} \leftrightarrow \mathrm{CO} + \mathrm{H_2O};\ \ \Delta h^0 = +41.2\ \mathrm{kJ/mol}$	(R2)
Dry reforming (CH_4)	$\mathrm{CH_4} + \mathrm{CO_2} \leftrightarrow 2\ \mathrm{CO} + 2\ \mathrm{H_2};\ \ \Delta h^0 = +247\ \mathrm{kJ/mol}$	(R3)
Steam reforming (CH_4)	$\mathrm{CH_4} + \mathrm{H_2O} \leftrightarrow \mathrm{CO} + 3\ \mathrm{H_2};\ \ \Delta h^0 = +206\ \mathrm{kJ/mol}$	(R4)
Primary Water-Gas	$\mathrm{C} + \mathrm{H_2O} \leftrightarrow \mathrm{CO} + \mathrm{H_2};\ \ \Delta h^0 = +131\ \mathrm{kJ/mol}$	(R5)

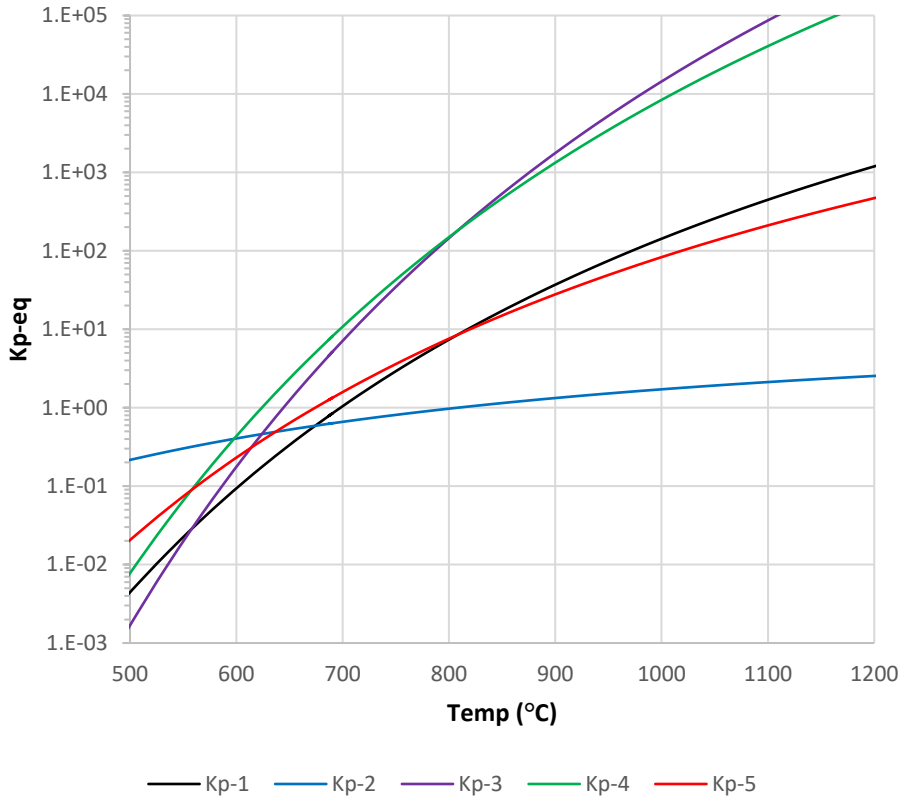

Figure 3-1: Equilibrium constants of selected gasification reactions

3.1.3 Physical Properties

As implied above, calculation of the thermodynamic state of a system requires knowledge of the fundamental state variables of that system. Such parameters depend on both the operating conditions and the chemical components which make up the system.

3.1.3.1 Pure component properties

Empirically derived polynomials are used to calculate the thermophysical properties of pure gas species as a function of temperature. Coefficients from NASA's set of polynomials [103] are published for key species across the temperature range from 0 K up to 5000 K.

Thermodynamic quantities of heat capacity (C_p), enthalpy (H), and entropy (S) are related through the defined equations (3.19) and (3.20).

$$H = H_0 + \int_{T0}^{T} C_p \, \mathrm{d}T \tag{3.19}$$

$$S = S_0 + \int_{T0}^{T} \frac{C_p}{T}\,\mathrm{d}T \tag{3.20}$$

Quantities of enthalpy and entropy are therefore calculated from the same set of polynomial coefficients (a_n) as heat capacity with additional terms (b_n) for integration constants. Polynomials are normalized by the gas constant and temperature.

$$\frac{C_p}{R} = a_1 + a_2T + a_3T^2 + a_4T^3 + a_5T^4 \tag{3.21}$$

$$\frac{H}{RT} = a_1 + \frac{a_2T}{2} + \frac{a_3T^2}{3} + \frac{a_4T^3}{4} + \frac{a_5T^4}{5} + \frac{b_1}{T} \tag{3.22}$$

$$\frac{S}{R} = a_1\ln(T) + a_2T + \frac{a_3T^2}{2} + \frac{a_4T^3}{3} + \frac{a_5T^4}{4} + b_2 \tag{3.23}$$

Viscosity and thermal conductivity transport properties of these species are also calculated from polynomials with coefficients V_n and C_n. The published polynomials represent the logarithm of the calculated property.

$$\ln\mu = V_A\ln(T) + \frac{V_B}{T} + \frac{V_C}{T^2} + V_D \tag{3.24}$$

$$\ln k = C_A\ln(T) + \frac{C_B}{T} + \frac{C_C}{T^2} + C_D \tag{3.25}$$

3.1.3.2 Mixture properties

The working fluid of the model is a mixture of gaseous species where the overall fluid properties are dependent on both the properties of the constituent components and on interactions between these components [104]. Thermodynamic and transport properties of this mixture are calculated based on the individual properties of each species and the amount of each species in the mixture. Thermodynamic properties of the mixture are the weighted averages of the properties of the constituent species (equations (3.26) to (3.28)).

$$C_{p,m} = \frac{\Sigma_{i=1}^{N}(n_i \times C_{p,i})}{\Sigma_{i=1}^{N} n_i} = \Sigma_{i=1}^{N}(x_i \times C_{p,i}) \tag{3.26}$$

$$H_m = \frac{\Sigma_{i=1}^{N}(n_i \times H_i)}{\Sigma_{i=1}^{N} n_i} = \Sigma_{i=1}^{N}(x_i \times H_i) \tag{3.27}$$

$$S_m = \frac{\Sigma_{i=1}^{N}(n_i \times S_i)}{\Sigma_{i=1}^{N} n_i} = \Sigma_{i=1}^{N}(x_i \times H_i) \tag{3.28}$$

Transport properties, however, involve interactions between species and require a more detailed model to account for this phenomenon. Wilke's equation [105] is used to determine the mixture viscosity from the partial viscosities of the constituent species and molar masses (equations (3.29) and (3.30)).

$$\mu_m = \sum_{i=1}^{N}\left(\frac{x_i \cdot \mu_i}{x_i + \sum_{(j=1)(j\neq i)}^{N} x_j \phi_{ij}}\right) \tag{3.29}$$

Where ϕ_{ij} is a dimensionless interaction parameter between species *i* and species *j*.

$$\phi_{ij} = \frac{\left[1 + \left(\frac{\mu_i}{\mu_j}\right)^{\frac{1}{2}} \cdot \left(\frac{M_j}{M_i}\right)^{\frac{1}{4}}\right]^2}{\frac{4}{\sqrt{2}} \cdot \left[1 + \frac{M_i}{M_j}\right]^{\frac{1}{2}}} \tag{3.30}$$

Cheung et al. [106] used a similar method to calculate the thermal conductivity of a gas mixture from specific conductivities, viscosities, heat capacities, and molar masses.

$$k_m = \sum_{i=1}^{N} \frac{x_i \cdot k_{c,i}}{x_i + \sum_{(j=1)(j\neq i)}^{N} x_j \phi_{ij} \left(\frac{M_{ij}}{M_i}\right)^{\frac{1}{8}}} + \sum_{i=1}^{N} \frac{x_i \cdot k_{d,i}}{x_i + \sum_{(j=1)(j\neq i)}^{N} x_j \phi_{ij}} \tag{3.31}$$

The interaction parameter, ϕ_{ij}, is the same as before (equation (3.30)) while the average molar mass of an interacting pair is given in equation (3.32).

$$M_{ij} = \frac{M_i + M_j}{2} \tag{3.32}$$

Individual modes of heat conduction for collision, $k_{c,i}$, and diffusion, $k_{d,i}$, are calculated based on the overall thermal conductivity of the particular species.

$$\text{collision: } k_{c,i} = \frac{2.5\, c_{v,t} + 1.0 c_r}{2.5 c_{v,t} + 1.0 c_r + 1.32(c_{vb} + c_{ir})} \cdot k_i \tag{3.33}$$

$$\text{diffusion: } k_{d,i} = k_i - k_{c,i} \tag{3.34}$$

The modal heat capacities are the translational ($c_{v,t}$), rotational (c_r), vibrational (c_{vb}), and internal rotational (c_{ir}). These are determined from kinetic theory and calculated from equations (3.35)-(3.38).

$$C_v = C_p - R \tag{3.35}$$

$$c_{v,t} = \frac{3}{2} R \tag{3.36}$$

$$c_r = \begin{cases} 0 & \text{monatomic molecule} \\ R & \text{linear molecule} \\ \left(\frac{3}{2}\right) R & \text{non} - \text{linear molecule} \end{cases} \tag{3.37}$$

$$(c_{vb} + c_{ir}) = C_v - (c_{v,t} + c_r) \tag{3.38}$$

3.2 Equilibrium Modelling of Gasification Processes

Biomass gasification is simulated using a non-stoichiometric, thermodynamic equilibrium method [61]. As explained in Chapter 2, only a thermodynamic chemical equilibrium model is capable of adequately assessing the novel system-level features of a fully integrated gasification cycle. Since the current analysis aims to investigate the thermodynamic conditions underlying the gasification process, this approach is particularly useful. The fundamental basis of this model is that under equilibrium conditions, the Gibbs free energy of the syngas mixture is minimized. This is a consequence of the equilibrium condition spontaneously achieving the highest possible entropy as a condition of stability.

To establish this methodology, consider the total Gibbs free energy in the product syngas as a function of the temperature and amount of each syngas species, *i* (equation (3.39)). The syngas is assumed to be an ideal gas, allowing the Gibbs free energy to be expressed in terms of the mole fraction of each constituent component. This same concept can also be represented in terms of the chemical potential of each species, $\mu_{c,i}$.

$$G_{total} = \sum_i n_i \Delta G^0_{f,i} + \sum_i n_i \bar{R} T \ln\left(\frac{n_i}{\sum n_i} \cdot \frac{P}{P^0}\right) = \sum_i n_i \cdot \mu_{c,i} \tag{3.39}$$

The task now remains to minimise this Gibbs free energy function within the bounds of a mass balance between the reactants (feedstock and gasifying medium) and products (syngas species). More formally, the balance of each element, *j*, would constrain the total amount of that element present across all syngas species, *i*, to be equal to the total amount of element *j* input to the gasifier from the feedstock and gasifying agent, n_j.

$$n_j = \sum_i a_{ij} n_i = \sum_k a_{kj} n_k \tag{3.40}$$

Here, the coefficient a_{ij} signifies the number of atoms of element *j* present in syngas species *i* and a_{kj} signifies the number of atoms of element *j* present in the gasifier input species *k*. By prescribing both the expected syngas chemical products and the reaction conditions along with the inputs of feedstock and gasifying agents, the model solves a system of equations describing the minimisation of the syngas Gibbs free energy (equation (3.39)) constrained by the elemental mass balance (equation (3.40)).

For the resulting system of equations to be tractable, the set of product molecular species must be prescribed *a priori*. In these studies, syngas species of H_2, CO, CH_4, CO_2, H_2O, N_2, and solid carbon char residues are considered as the possible outputs of the gasifier. Indeed, larger hydrocarbon molecules could be added to the model however the standard Gibbs free energy of formation for these compounds is prohibitively large compared to the simple compounds used here. Such a result means that the larger molecules are not thermodynamically favourable under typical gasification conditions and will not be present in an equilibrium syngas mixture.

Such an approach to equilibrium modelling maintains the same fundamentals as a stoichiometric equilibrium model which would analyse the gasification process using a representative set of chemical reactions. While the stoichiometric approach would evaluate individual reaction equilibrium constants based on equation (3.18), this non-stoichiometric

method effectively combines these into one single process and evaluates the equilibrium condition simultaneously. This simplifies the operation and makes for a robust solution which is always linearly independent.

3.2.1 Method of Lagrange Multipliers

Equations (3.39) and (3.40) form the basis of a mathematical optimisation problem that can be solved using the well-known method of Lagrange multipliers [107]. Basu [42] presents a general application of this mathematical method to the problem of Gibbs free energy minimisation by defining the Lagrange function, $L(x_i)$, with equation (3.39) as $f(x_i)$ and equation (3.40) as $g(x_i)$.

$$\mathrm{L}(n_i, \lambda_j) = \sum_i n_i \Delta G^0_{f,i} + \sum_i n_i \bar{R} T \ln(x_i) - \sum_j \lambda_j \left(\sum_i a_{ij} n_i - n_j \right) \tag{3.41}$$

Minimisation of this Lagrange function (equation (3.41)) is the basis for a system of equations ((3.42) and (3.43)) which will solve for the set of moles of each chemical species in the syngas, n_i, that feasibly minimises the Gibbs free energy of that mixture thus representing the equilibrium output of the gasification reaction.

$$\nabla L(n_i, \lambda_j) = 0;$$

$$\therefore \frac{\partial L}{\partial n_i} = \Delta G^0_{f,i} + \bar{R} T \ln(x_i) - \sum_j \lambda_j a_{ij} = 0; \tag{3.42}$$

$$\therefore \frac{\partial L}{\partial \lambda_j} = -\left(\sum_i a_{ij} n_i - n_j \right) = 0 \tag{3.43}$$

3.2.2 Gasification Temperature and Heating

Additional thermodynamic aspects are calculated when an energy balance across the gasifier is considered (equation (3.44)). When a known equilibrium temperature is specified, the indirect allothermal heat required can be calculated from the difference in enthalpy across the products (syngas) and reactants (feedstock/gasifying agents). Under autothermal or adiabatic conditions, the gasifier energy balance (equation (3.44)) becomes coupled to the Gibbs free energy (equation (3.39)) since enthalpy is a temperature-dependant quantity (equation (3.45))). The solution of the resulting system of equations

will provide the equilibrium gasifier temperature in addition to the quantities of syngas species produced.

$$\sum_k n_k \cdot h_k + Q_{indirect} = \sum_i n_i \cdot h_i \tag{3.44}$$

$$h_i = h_{f,i}^0 + \int_{T_0}^{T} C_{p,i}\ dT \tag{3.45}$$

For the systems presented in later chapters, the gasifier is assumed to be adiabatic and is directly heated by using air or oxygen as the primary gasification agent. Additional allothermal heat is introduced only through the recycled exhaust mass flow, thus indirect heating is neglected. Gasification is specified to occur under atmospheric pressure while the reaction temperature is a dependent parameter, calculated as described above.

Gasifying agent supply is quantified in terms of the gasification air equivalence ratio, λ, for air or O_2 and a CO_2 recycling ratio for engine exhaust. The former compares the air supplied to the amount required for complete combustion of the biomass feedstock while the latter is a molar ratio of the recycled CO_2 to carbon supplied in the feedstock.

$$\lambda = \frac{\dot{n}_{O_2,supplied}\left(\mathrm{mol}/_{s}\right)}{\dot{n}_{O_2,stoichiometric}\left(\mathrm{mol}/_{\mathrm{s}}\right)} \tag{3.46}$$

$$\mathrm{CO_2\ recycling\ ratio} = \frac{\mathrm{CO_2\ recycled}\left(\mathrm{mol}/_{\mathrm{s}}\right)}{\mathrm{C\ in\ biomass}\left(\mathrm{mol}/_{\mathrm{kg}_b}\right) \times \dot{m}_b\left(\mathrm{kg}/_{\mathrm{s}}\right)} \tag{3.47}$$

3.2.3 Gasification model validation

Gasification is a complex process, sensitive to many operational and design parameters. The focus of the current work is on the system-level effects of CO_2 recycling on the thermodynamic conditions of gasification rather than a detailed design analysis for specific gasifiers. Consequently, only a 0-dimensional equilibrium model is capable of such an analysis since empirical, kinetic, or CFD models will be dependent on the exact design and geometry of a chosen reactor [42]. Indeed, equilibrium models are often the preferred method for assessing complex systems with integrated gasifcation cycles since they report

the true thermodynamic equilibrium conditions of the gasification process rather than the specific outputs of one chosen gasifier design [59, 60, 61, 62].

To ensure the correct implementation of this model, validation simulations were performed to match predictions from comparable thermodynamic simulations in the literature. Equilibrium temperatures, carbon conversion, and syngas species distributions showed excellent fit with the existing data. Figure 3-2 further highlights the agreement between this model and a range of published thermodynamic equilibrium models for gasification.

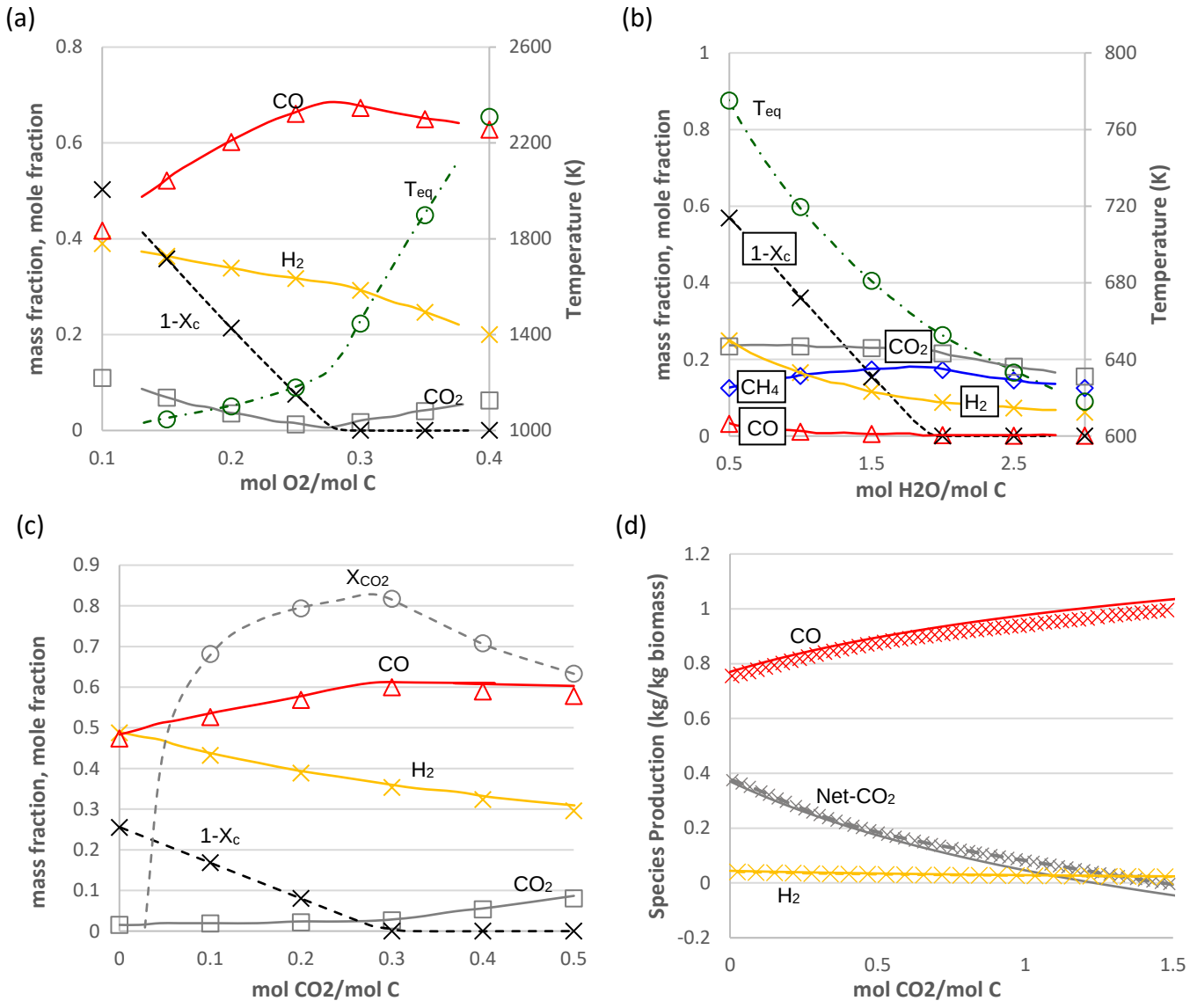

Figure 3-2: Comparisons of the developed gasifier model with numerical results showing key syngas species, carbon conversion, CO_2 conversion, and equilibrium temperature as appropriate from a) oxygen & b) steam adiabatic gasification of Ravikiran et al. [14], c) isothermal CO_2 gasification of Renganathan et al. [15], and d) adiabatic gasification with recycled CO_2 of Prabowo et al. [13]. Lines represent published results while markers signify current simulation outputs.

Thermodynamic studies of Ravikiran et al. [92] and Renganathan et al. [91] used this modelling approach to study gasification conditions across a range of simulated feedstock

H/C/O compositions. Relevant parameters of these studies were the volumetric composition of H_2, CO, CO_2, and CH_4 in the dry syngas, the carbon residual (1-X_C), and the equilibrium temperature. The model developed for the present study shows strong agreement with these simulations for oxygen and steam gasification of a feedstock of $CH_{0.9}O_{0.45}$ under adiabatic conditions (Figure 3-2 a & b). Similarly, the current model matches the results for pure CO_2 gasification of a simulated feedstock with relative mass composition of 46% C, 6% H, and 48% O under isothermal conditions at 850°C. This study also reported the relative conversion of CO_2 (X_{CO2}) alongside the volumetric composition of the dry syngas (Figure 3-2 c).

Non-stoichiometric thermodynamic gasification models have also been incorporated into integrated cycle simulations, as in the work of Prabowo et al. [62]. Here, a simulated feedstock representative of coconut shells (49.3% C, 5.5% H, 45.0% O) drives an integrated power cycle where it is gasified with O_2 and recycled CO_2 to generate syngas. Again, the current model generates similar gasification results to those reported in the referenced study for a gasifier temperature of 850°C (Figure 3-2 d). This configuration assumes an adiabatic gasification model while controlling the supply of O_2 gasifying agent to maintain the desired reaction equilibrium temperature.

Although the focus of the current work is to analyse the thermodynamic conditions of gasification within the integrated system, this approach can also approximate specific gasification tests. Additional validation data from Table 3-2 confirms the model can replicate experimental, downdraft gasification conditions [108]. The feedstock for this study is a wood sawdust while the gasifier was a pilot scale unit designed for a nominal 200 kW thermal input with a 0.3 m diameter throat. Under steady state conditions, the temperature profile ranged from 334°C above the air inlet to peak temperatures of 1100°C in the throat's combustion zone before dropping across the reduction zone to reach an outlet temperature of 350°C. While the equilibrium model is zero-dimensional and thus will not reproduce a temperature gradient, the calculated equilibrium temperature of 625°C is nevertheless representative of the reduction zone temperature partway between the combustion zone and the outlet.

Table 3-2: Comparison of syngas composition as predicted by the developed Aspen equilibrium model and measured experimentally by Simone et al [108] for wood sawdust pellets in air at an air ratio $\lambda = 0.3$

Experiment		Gas Composition (%vol)				
		H_2	CO	CO_2	CH_4	N_2
Current model		19.73	19.97	12.66	2.44	39.91
Simone et al. [103]	Test 1	17.5	21.3	13.3	3.1	44.2
	Test 2	17.6	21.6	12.0	2.3	46.0
	Test 3	16.3	21.3	12.4	2.3	47.2

Comparing the syngas compositions illustrates common limitations of a purely thermodynamic assessment of gasification conditions. Slight overpredictions in the H_2 content and under predictions of the CO content are evident here. This is ultimately a consequence of the gasifier design where temperature gradients and hydrodynamic conditions created conditions different from equilibrium predictions. Although these minor errors are generally expected in real gasifiers, thermodynamic models remain the preferred methodology for comparing general, system-level performance of an integrated gasification system, as described in Chapter 2.

While simulated methane production appears to closely match the experimental results in this instance, methane is generally not a thermodynamically favourable product under typical gasification conditions and equilibrium models tend to under predict methane content in syngas. Similarly, higher carbon compounds like tars are not thermodynamically favoured and will not be accurately modelled under equilibrium conditions. Tar formation and subsequent cracking is understood to be a kinetic phenomenon of gasification [109] and is highly variable based on operating conditions, reactor geometry, and gasifier design. Even though syngas tar content is an important, practical consideration of integrated gasification power cycles, evaluation of tars is best suited to detailed design studies of specific gasification reactors and is not within the scope of this thermodynamic assessment.

3.3 Engine model

The systems presented in this work focus on integrated cycles using internal combustion engines (ICEs) as the prime mover to convert the syngas fuel into useful work. IC engines are highly scalable between the kW to MW output range, with larger sized engines usually

boasting higher conversion efficiencies. These engines also demonstrate a fairly consistent conversion efficiency across a variety of off-design operating points making them ideal for meeting any variability in output requirements [110]. Coupled with low capital costs and good reliability, ICEs are identified as having great potential for use with syngas applications [111]. Although other power conversion cycles are possible, ICEs are a proven technology with some tolerance for any residual tar content in the syngas [112]. Tar abrasion and fouling concerns make gas turbine powerplants, like those modelled in some previous integrated gasification cycles [62], unfavourable candidates for inclusion into biomass gasification cycles.

Analysing the engine as an idealised Otto cycle (Figure 3-3) assesses the power conversion performance independent of specific engine design components like piston geometry and rotational speed. This is convenient for an approximation of the energy converted by the engine, however this approach won't consider combustion dynamics or heat losses which have an effect on both the power developed in the engine and the thermodynamic properties of the exhaust gases. More detailed ICE modelling techniques addressing these concerns are derived and used in some modelling cases. Figure 3-3 qualitatively compares the idealised processes considered in the Otto cycle with a more detailed model. While this shows the general trends of the Otto cycle processes can be seen in the detailed model, the smoother transitions between these processes and the differences in rates of pressure change are indicative that this model accounts for heat losses and combustion dynamics.

3.3.1 Ideal Otto Cycle

Ideal thermodynamic engine cycles approximate each stroke of the engine cycle as a distinct, quasi-steady thermodynamic process. System properties of pressure, volume, and temperature are calculated at the end of each process and summed over the total cycle to determine the thermodynamic performance of the engine. A traditional Otto cycle is used here to approximate an idealised internal combustion engine. Figure 3-3 illustrates a typical Otto cycle P-V diagram with each process labelled.

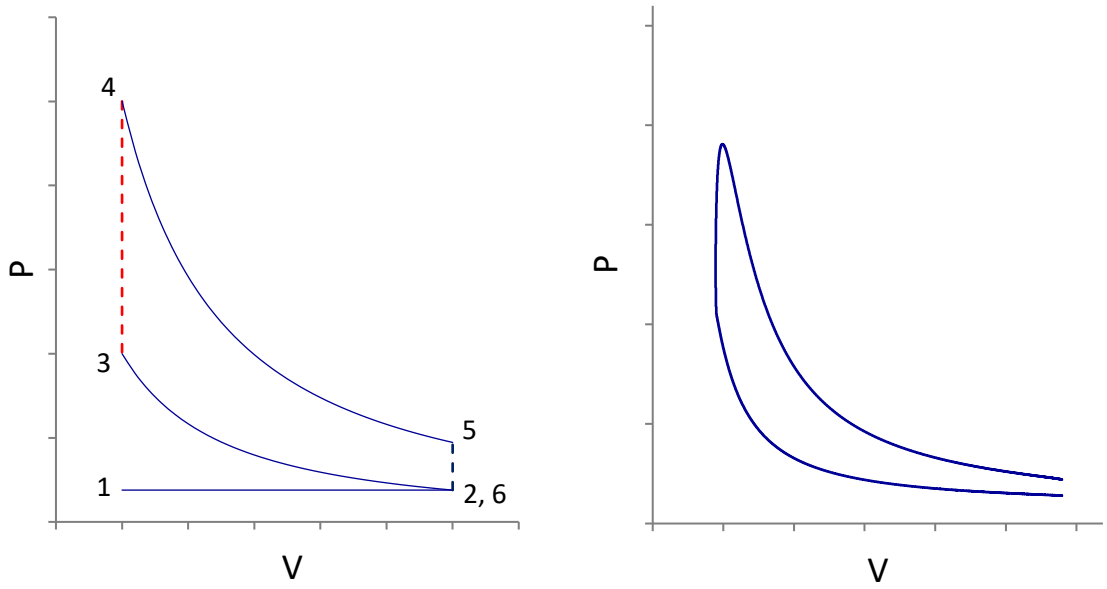

Figure 3-3: Illustrative Pressure-Volume diagrams for the ideal Otto cycle (left) and detailed ICE model (right). Otto station numbers used in this analysis are labelled. Isobaric intake from 1-2, adiabatic compression from 2-3, isochoric combustion from 3-4, adiabatic expansion from 4-5, cylinder blowdown from 5-6, and isobaric exhaust from 6-1. Detailed model covers the compression and expansion strokes of the engine cycle.

3.3.1.1 Intake Stroke

The engine is assumed to be naturally aspirated so the intake from station 1 to station 2 is an isobaric filling process with volumetric efficiency of 100%. Intake pressure is assumed to be 100 kPa.

3.3.1.2 Compression *Stroke*

Otto cycle compression stroke from station 2 to station 3 is modelled as the adiabatic compression of the ideal gas fuel/air mixture through the specified volume compression ratio, r_c.

$$P_3 = P_2(r_c)^{\gamma} \; ; \;\; T_3 = T_2(r_c)^{\gamma-1} \tag{3.48a;b}$$

The work required for this compression process is determined from the first-law analysis of the adiabatic process.

$$\dot{W}_c = \; \dot{n}_t \; C_v(T_3 - T_2) \tag{3.49}$$

3.3.1.3 Combustion and Power Stroke

The power stroke model includes an initial, instantaneous isochoric heating process between station 3 and station 4 followed by an adiabatic expansion process from station 4

to station 5. Isochoric heat addition from the combustion reactions causes a temperature and pressure rise in the system.

$$T_4 = T_3 + \frac{\dot{Q}_{comb}}{\dot{n}_t\, C_v}\ ;\ \ P_4 = P_3 \frac{T_4}{T_3} \tag{3.50a;b}$$

Power stroke motion is modelled as the adiabatic expansion of the ideal gas fuel/air mixture through the specified volume compression ratio, r_c (equations (3.51)).

$$P_5 = P_4(r_c)^{-\gamma}\ ;\ \ T_5 = T_4(r_c)^{1-\gamma} \tag{3.51a;b}$$

Power generated from the expansion stroke is determined from a first-law analysis of the adiabatic process.

$$\dot{W}_p = \dot{n}_t\, C_v(T_5 - T_4) \tag{3.52}$$

The indicated power output from the ideal Otto cycle is the sum of work required by the compression stroke and work created in the expansion stroke.

3.3.1.4 Blowdown

At the end of the power stroke, cylinder pressure is released through an adiabatic expansion until the working fluid pressure returns to the exhaust pressure, P_6, at 100 kPa while the cylinder remains at bottom dead centre (BDC). This process also cools the gas charge as a consequence of the blowdown expansion.

$$T_6 = T_5 \left(\frac{P_6}{P_5}\right)^{\frac{\gamma-1}{\gamma}} \tag{3.53}$$

3.3.1.5 Exhaust

Remaining exhaust gasses are released from the system isobarically at atmospheric pressure between station 6 and station 1. Since this ideal cycle is modelled as naturally aspirated, both the intake and exhaust strokes are assumed to take place at atmospheric pressure thus no net pumping work is included in the ideal cycle.

3.3.1.6 Residual Mass

Since the engine piston cannot sweep the whole cylinder volume to remove burned gases during the exhaust stroke, some residual gas remains trapped in the clearance volume. This means that the working fluid cylinder charge contains some fraction of exhaust gases during the intake and compression strokes. The mass fraction of exhaust in the working fluid is calculated by considering the density of the exhaust gases and cylinder volume at the end of the exhaust stroke compared to the density of the cylinder charge and cylinder volume at the end of the intake stroke.

$$\frac{m_r}{m_t} = x_r = \frac{P_6}{T_6} \cdot \frac{T_2}{P_2} \cdot \frac{1}{r_c} \tag{3.54}$$

Calculation of the Otto cycle model is iterated until the residual fraction, x_r, converges.

3.3.2 Time-dependent engine model

Otto cycles represent an idealised model of the processes within reciprocating internal combustion engine cycles. They are 0-dimensional and time independent, providing a theoretical means of assessing maximum potential engine thermodynamic performance independent of particular design features of a specific engine. Such an approach is alike the analysis provided from sources in the literature using Rankine [97] and Joule/Brayton [62] cycles integrated with a CO_2 gasifier. While this model is convenient for a preliminary system analysis, ideal power cycles will tend to overpredict both the indicated work and exhaust temperatures compared to a real power plant.

A detailed, time-dependent engine model has also been developed to incorporate the combustion dynamics typical of syngas and account for heat losses from the working fluid during the engine cycle. Briefly, the basis of this model is a system of differential equations describing the pressure, volume, and work of the cylinder gas charge. Additional submodels are used to calculate other parameters relevant to these main system equations. This approach aligns with established methods of time-dependent engine simulation [113, 114].

3.3.2.1 Piston-cylinder geometry and kinematics

A piston-cylinder arrangement, shown in Figure 3-4, is the traditional configuration of common internal combustion engines running on either an Otto or Diesel power cycle.

Motion of the piston, *y(θ)*, is coupled to the motion of the crankshaft, *a*, through the connecting rod, *L*. At a crank angle of $\theta = 0°$ the piston is at its highest position within the cylinder, called Top Dead Centre (*TDC*), where the cylinder volume is minimised to the clearance volume, V_c. As the crank angle advances to $\theta = 180°$ the piston descends by a full stroke length, *S*, to the Bottom Dead Centre (*BDC*) position. Since the connecting rod length is fixed as the crankshaft radius rotates from the up position to the down position, the piston stroke length is therefore set to be twice the crank radius, or $S = 2a$.

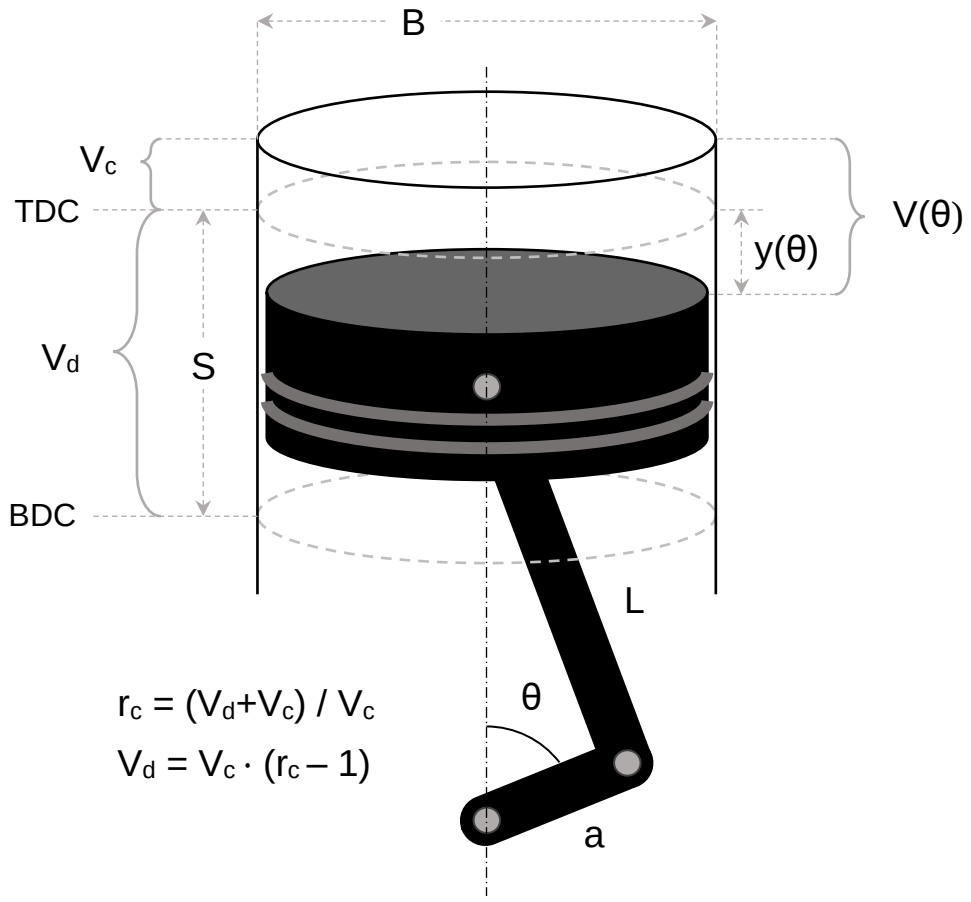

Figure 3-4: Schematic of an internal combustion engine piston-cylinder mechanism with relevant dimensions, stations, and relationships illustrated.

It is convenient to calculate the piston position below the TDC datum, as indicated in Figure 3-4, since this distance corresponds to an increase in cylinder volume due to piston motion. Because each component of this mechanism is considered rigid, the piston displacement is the same as the reduction in height of the crank-rod assembly at a given crank angle. Given this geometry, the maximum crank-rod height at TDC is the sum of each component length, $a + L$. The instantaneous crank-rod height is derived from the geometry by considering the trigonometry of the crank-rod mechanism at crank angle θ to derive the vertical components of the crank and rod displacement (eq(3.55)).

$$y(\theta) = L + a - \left(a \cdot \cos(\theta) + \sqrt{L^2 - a^2 \cdot \sin^2(\theta)}\right) \tag{3.55}$$

The vertical piston displacement can be normalised with respect to the stroke length to yield a function that returns 0 at TDC and maximises to 1 at BDC. Another useful simplification is to substitute in the ratio of crank radius to connecting rod length, $\epsilon = a/L$.

$$\tilde{y}(\theta) = \frac{L + a - \left(a \cdot \cos(\theta) + \sqrt{L^2 - a^2 \cdot \sin^2(\theta)}\right)}{S}$$

$$\therefore \ \tilde{y}(\theta) = \frac{1}{2}(1 - \cos(\theta)) + \frac{1}{2\epsilon} \cdot \left(1 - \sqrt{1 - \epsilon^2 \sin^2(\theta)}\right) \tag{3.56}$$

This formula can be further simplified by considering a Taylor series expansion for the $\sqrt{1 - \epsilon^2 \sin^2(\theta)}$ term with $x = \sin^2\theta$. Since the x value considered will remain small (i.e. ≤ 1) this series is calculated near the point $x_0 = 0$.

$$\sqrt{1 - \epsilon^2 \sin^2(\theta)} \approx 1 - \frac{\epsilon^2 \cdot \sin^2(\theta)}{2} \tag{3.57}$$

Substituting equation (3.57) into equation (3.56) gives a simplified expression for the piston displacement as a function of the crank angle.

$$\tilde{y}(\theta) = \frac{1}{2}(1 - \cos(\theta)) + \frac{\epsilon}{4} \cdot \sin^2(\theta) \tag{3.58}$$

The instantaneous volume of the cylinder is calculated by adding the volume swept by the piston through crank angle θ to the clearance volume. Due to the cylindrical geometry of the system, the piston swept volume is a function only of the cylinder bore and the instantaneous piston displacement.

$$V(\theta) = V_c + \pi \frac{b^2}{4} \cdot y(\theta)$$

$$\therefore V(\theta) = V_c + \frac{V_c}{2}(r_c - 1) \cdot \left(1 - \cos(\theta) + \frac{\epsilon}{2}\sin^2(\theta)\right) \tag{3.59}$$

This expression can be normalised with reference to the maximum cylinder volume at BDC to provide a function that varies from a maximum of 1 at BDC to $1/r_c$ at TDC, where r_c is the engine's compression ratio.

$$\tilde{V}(\theta) = \frac{V_c + \pi \frac{b^2}{4} \cdot y(\theta)}{V_c \cdot r_c}$$

$$\therefore \quad \tilde{V}(\theta) = \frac{1}{r_c} + \frac{r_c - 1}{2\, r_c} \cdot (1 - \cos(\theta)) + \frac{(r_c - 1)\epsilon}{4\, r_c} \sin^2(\theta) \tag{3.60}$$

Both piston position and cylinder volume can be differentiated with respect to crank angular displacement to provide the following rates of change.

$$\frac{d\tilde{y}}{d\theta} = \frac{1}{2} \sin(\theta) \cdot (1 + \epsilon \cos(\theta)) \tag{3.61}$$

$$\frac{d\tilde{V}}{d\theta} = \frac{r_c - 1}{2\, r_c} \sin(\theta) \cdot (1 + \epsilon \cos(\theta)) \tag{3.62}$$

As the crank rotates with angular velocity ω, both instantaneous piston velocity and time rate of volume change can be calculated as the product of ω and equations (3.61) and (3.62) respectively. Although this calculation provides a detailed analysis of the mechanism's kinematics, it is often convenient to consider the mean piston speed, $\overline{U}_p$, as averaged over one full crank rotation. Total distance travelled by the piston will be twice the stroke length, one up stroke and one down stroke, while the elapsed time will be the reciprocal of the engine rotational speed.

$$\overline{U}_p = \frac{\Delta d}{\Delta t} = \frac{2\, S}{\left({}^{2\,\pi}/_{\omega} \right)} = \frac{\omega\, S}{\pi} \tag{3.63}$$

3.3.2.2 Combustion heat release

For a better representation of fuel combustion, our model considers changes in the charge of gases in the cylinder over time. Initially, the charge consists of the unburnt mixture of fuel and oxidiser. As the combustion reaction progresses this mixture will be converted to the combustion products that make up the exhaust gases. A mass burned fraction (MBF) is

defined to quantify the progress of the combustion reaction as a mass ratio of burned gases in the combustion chamber to the total charge mass. Since the MBF is a representation of the progress of combustion, it also represents the fraction of total heat released into the cylinder from the enthalpy change of the combustion reaction (equation (3.64)).

$$X_b = \frac{m_b}{m_t} = \frac{\text{burned mass}}{\text{total charge mass}} = \frac{Q}{\Delta H_c} \tag{3.64}$$

During in-cylinder combustion, the MBF is expressed as a function of the crank angle by the Weibe function, as calculated by equation (3.65) [115]. Differentiating the Weibe function with respect to crank angle gives an expression for the rate of the combustion reaction in terms of the piston cycle. Furthermore, this provides a means of determining the rate of heat release into the combustion chamber (equation (3.67)). The heat release equation can also be normalised by the initial system conditions of pressure and volume taken at piston BDC between the intake and compression strokes (equation (3.68)).

$$X_b(\theta) = 1 - \exp^{-a\left(\frac{\theta-\theta_s}{\theta_d}\right)^m} \tag{3.65}$$

$$\frac{dX_b}{d\theta} = (1 - X_b) \cdot \frac{a\,m}{\theta_d} \cdot \left(\frac{\theta - \theta_s}{\theta_d}\right)^{m-1} \tag{3.66}$$

$$\frac{dQ}{d\theta} = \Delta H_c \cdot (1 - X_b) \cdot \frac{a\,m}{\theta_d} \cdot \left(\frac{\theta - \theta_s}{\theta_d}\right)^{m-1} \tag{3.67}$$

$$\frac{d}{d\theta}\left(\tilde{Q}\right) = \frac{\Delta H_c}{P_{\text{BDC}} \cdot V_{\text{BDC}}} \cdot \frac{dX_b}{d\theta} \tag{3.68}$$

Ignition starts from the crank angle θ_s and the combustion process proceeds over a duration of θ_d crank angle degrees (CAD). Weibe constants *a* and *m* are used to match the function output to empirical combustion profiles. The *a* parameter is also a measure of the combustion efficiency since it dominates the MBF function during the later part of the cycle at large CAD. In traditional applications for petrol fuelled engines, these are taken as $a = 5$ and $m = 3$ with good agreement to measured data. For engines fuelled by syngas mixtures of H_2, CO, and small amounts of CH_4, Weibe parameters vary from $a = 1.45 – 2.54$ and $m = 1.68 – 1.78$ based on data covering several engines over a range of loading conditions [108]. At engine loads greater than 40% the variability in parameters becomes less pronounced. Values of $a = 2.23$ and $m = 1.71$ are shown to give good results

for syngas fuelled engines across many configurations and operating points and are used for this present study.

Shivapuji and Dasappa [117, 116, 118] give a detailed discussion on the nature of syngas combustion in ICEs. Contrasted with traditional petrol fuels having C5-C8 aliphatic molecules as the primary fuel, the mixture of CO and H_2 in syngas has different combustion properties. While initial combustion profiles appear similar, syngas tends to have slower heat release profiles toward the end of combustion region. Since this heat release is the only injection of energy into the ICE system, this in turn influences the pressure and temperature profiles near TDC and during the initial period of the piston's power stroke. Ultimately, this combustion timing has an influence on the total torque, and thus power, produced by the engine.

In a spark-ignited engine it is the ignition system that initiates charge combustion. Ignition timing is varied or tuned to produce maximum brake torque (MBT). Although the crank angle at the start of combustion is ultimately governed by ignition lead, the kinetics of the combustion reaction determine the duration. Compared to combustion profiles for gasoline, the final 50% of syngas combustion takes longer. It is currently understood this is due to both the increased laminar flame velocity and thermal conductivity of syngas such that flame fronts quickly reach the cylinder walls thus conducting much of the heat generated in the final stages of combustion out of the combustion chamber [116]. Though both charge equivalence ratio and engine rotational speed appear to influence the combustion duration [119], this study uses combustion crank angle data for MBT tuning and stoichiometric combustion [117].

3.3.2.3 Cylinder heat loss

As previously mentioned, not all heat released during fuel combustion contributes to the pressure rise of the gas charge in the cylinder. Due to material limitations, the boundaries of the cylinder zone (i.e. the cylinder walls, cylinder head, and piston head) must be maintained below a critical temperature. Most engines use a dedicated liquid cooling system to remove excess heat from these engine components to prevent structural damage. Temperature gradients between the hot gases and the cylinder surfaces cause a transfer of energy out of the working fluid, reducing the available energy for power generation.

Although the system conditions allow for both radiation and convective heat transfer, traditional analysis techniques for spark ignition engines focus primarily on the role of

forced convection. Heat flux for convection follows a Newtonian cooling relationship (equation (3.69)). Non-dimensional analysis of this heat transfer regime establishes correlations between Nusselt, Prandtl, and Reynolds numbers (equation (3.70)) that allow for determination of the convective heat transfer coefficient.

$$\dot{q}" = \frac{\dot{Q}_{loss}}{A_{cyl}} = h_c\left(T_g - T_w\right) \tag{3.69}$$

$$Nu = C\ Re^x Pr^y \tag{3.70}$$

Annand [120] applied an empirical approach to calculate the instantaneous heat transfer coefficient directly from a Nusselt-Reynolds relationship (equation (3.71)) with the cylinder bore, *B*, and mean piston speed, $\overline{U}_p$, as the characteristic parameters.

$$Nu = \frac{h_c\ B}{k} = a\ Re^b \qquad \therefore\ h_c = a\ k\ B^{b-1}\left(\frac{\rho\ \overline{U}_p}{\mu}\right)^b \tag{3.71}$$

Both *a* and *b* are empirical constants determined from experimental data. Annand's analysis showed the parameter *b*=0.7 while parameter *a* varied from 0.35 – 0.8, depending on the degree of in-cylinder gas motion. Although this correlation requires retuning the coefficients *a* and *b* for a particular engine design and/or fuel mixture, known values can be used to simulate a variety of operating conditions for similar engines. When tuned for the thermophysical properties of a typical syngas of H_2, CO, CH_4, CO_2, and air mixtures in a 6-cylinder, 5.9 litre engine, the Annand heat transfer parameters were determined to be *a*=0.76 and *b*=0.71 [117].

The particular correlation parameters for this non-dimensional heat transfer relationship do fit within the general range expected of traditional ICEs [113] however Shivapuji and Dasappa [117, 118] note that the air to fuel ratio of the engine mixture is significantly lower under these cases than when petrol fuel is used. This change to the gas mixture will have an effect on the thermophysical properties of the working fluid and means the convective heat transfer condition in a syngas engine will be different than under a petrol fuelled regime. Although the non-dimensional nature of Annand's Nusselt-Reynolds relationship (equation (3.71)) should partially account for this, it must be noted that the Prandtl number is not directly considered here. In effect, the Prandtl number is absorbed into the correlation constant *a*. For applications with similar gas mixtures, this parameter

will not significantly change, however it does justify the derivation of a particular set of correlation parameters for syngas application since the working fluid mixture will be different from the traditional petrol combustion cases.

Having determined the instantaneous heat transfer coefficient, the time-rate of heat loss can be calculated. For consistency with the previously derived differential equations, this time-rate of heat transfer is converted to an angular-rate of heat transfer through the engine angular velocity (3.72).

$$\frac{dQ_L}{d\theta} = \frac{A_{cyl} h_c (T - T_w)}{\omega} \tag{3.72}$$

Cylinder wall temperatures may be variable depending on engine design and operating conditions, however an accepted range of 130-250°C is typical for spark-ignited engines [121].

3.3.2.4 Intake compressible flow and valve pressure drop

Even in a naturally aspirated engine, the cylinder pressure does not remain constant during mass exchanges as gas flow becomes partially restricted while passing through the cylinder valves. Analysing the flow through the intake valve allows an accurate estimation of the initial cylinder pressure and volumetric efficiency.

A first law analysis of adiabatic, reversible gas flow shows the conservation of energy between stagnation conditions and flow conditions at average velocity, *U*. From the definition of the gas heat capacity at constant pressure, C_p, this relationship can be expressed in terms of stagnation, T_0, and flow temperatures, *T*.

$$h + \frac{U^2}{2} = h_0 \quad \therefore \quad T_0 = T + \frac{U^2}{2\,C_p} \quad \therefore \quad \frac{T_0}{T} = 1 + \frac{U^2}{2\,T\,C_p} \tag{3.73}$$

For any fluid medium, the speed of sound, *a*, is a function of the ratio of specific heats, the gas constant, and the gas temperature. This means the flow Mach number, *Ma*, is expressed in terms of the gas properties.

$$a = \sqrt{\gamma RT} \;\; \therefore \;\; Ma = \frac{U}{\sqrt{\gamma RT}} \tag{3.74}$$

Combining equations (3.73) and (3.74) with the known adiabatic relationship for gas expansion relates the gas pressure to the local flow Mach number, *Ma*.

$$\frac{T_0}{T} = 1 + \frac{Ma^{\,2} * \gamma RT}{2\,T\,C_p} = 1 + \frac{\gamma - 1}{2}(Ma)^2 \;\; \therefore \;\; \frac{P_0}{P} = \left(1 + \frac{\gamma - 1}{2}(Ma)^2\right)^{\frac{\gamma}{\gamma - 1}} \tag{3.75}$$

For flow through a valve, the ideal gas mass flow rate depends on the cross-sectional valve area, A_v, the gas density, ρ, and the flow velocity.

$$\dot{m}_\iota = U\,\rho\,A_v \tag{3.76}$$

Combining the previous compressible flow equations with the ideal gas equation ($P = \rho RT$) can ultimately express the gas mass flow rate through a valve in terms of the gas stagnation properties, valve geometry, and flow velocity through the valve.

$$\therefore \quad \dot{m}_\iota = \frac{A_v\,Ma\,P_0\,\gamma}{a_0} * \left(1 + \frac{\gamma - 1}{2}(Ma)^2\right)^{\frac{-(1+\gamma)}{2(\gamma-1)}} \tag{3.77}$$

Due to the nature of this relationship, the maximum mass flow rate through a valve occurs when the flow velocity reaches Mach 1. The critical pressure ratio from stagnation to valve static pressure associated with this choked flow condition also corresponds to the flow Mach number of 1.

$$\frac{P^*}{P_0} = \left(\frac{2}{\gamma + 1}\right)^{\frac{\gamma}{\gamma - 1}} \tag{3.78}$$

From the above compressible flow equations, the gas mass flow rate can be expressed in terms of the ratio of the gas flow static pressure to the upstream stagnation pressure. In the context of intake valve flow, the stream static pressure at the inlet valve is understood to be the same as the static gas pressure within the cylinder while the intake manifold conditions are taken as the stagnation properties. The reverse of this assumption is equally applied to the exhaust valve for cylinder exhaust flow analysis.

$$\frac{P_0}{P} = \left(1 + \frac{\gamma - 1}{2}(Ma)^2\right)^{\frac{\gamma}{\gamma-1}} \tag{3.79}$$

$$\therefore \quad Ma = \sqrt{\left(\left(\frac{P}{P_0}\right)^{\frac{1-\gamma}{\gamma}} - 1\right)\frac{2}{\gamma - 1}} \tag{3.80}$$

$$\therefore \quad \dot{m}_\iota = \frac{A_v\, P_0\, \gamma}{a_0}\left(\frac{P}{P_0}\right)^{\frac{1}{\gamma}}\sqrt{\frac{2}{\gamma - 1}\left(1 - \left(\frac{P}{P_0}\right)^{\frac{\gamma-1}{\gamma}}\right)} \tag{3.81}$$

Under conditions where the valve pressure drop ratio falls below the critical pressure ratio for sonic flow the flow conditions are said to be choked, thus the choked mass flow, $\dot{m}^*$, through the valve is determined only by the critical mass flow at Mach 1.

$$\therefore \quad \dot{m}_i{}^* = \frac{A_v\, P_0\, \gamma}{a_0}\left(\frac{2}{1+\gamma}\right)^{\frac{(1+\gamma)}{2(\gamma-1)}} \tag{3.82}$$

Since the idealised mass flow calculation is based on a uniform flow assumption, there will be some discrepancy between ideal and real flow rates through the intake valve. To account for the difference between these flow rates, an empirically determined discharge coefficient is defined. For common engine applications, a discharge coefficient between 0.7-0.8 can be assumed [113].

$$C_D = \frac{\dot{m}_{real}}{\dot{m}_i} \tag{3.83}$$

$$\therefore \quad \dot{m}_{real} = \frac{C_D\, A_v\, P_0\, \gamma}{a_0}\left(\frac{P}{P_0}\right)^{\frac{1}{\gamma}}\sqrt{\frac{2}{\gamma - 1}\left(1 - \left(\frac{P}{P_0}\right)^{\frac{\gamma-1}{\gamma}}\right)} \tag{3.84}$$

To assess the degree of influence restricted valve flow has on the overall performance of a time-dependent engine model, a reference case was studied using the dimensions of a typical 6 cylinder spark ignited engine [116]. A simulated mixture of syngas (20% H_2, 20% CO, 20 CO_2, 40% N_2) and air at intake conditions of 320 K (47°C) temperature and 100 kPa pressure is used as a filling gas. Figure 3-5 illustrates the calculated pressure in the cylinder during the intake stroke at engine speeds ranging from 1500 RPM to 5500 RPM.

Flow resistance as the intake mixture of syngas and air passes through the restricted valve opening causes incomplete cylinder filling mid-stroke which in turn reduces the pressure in the cylinder.

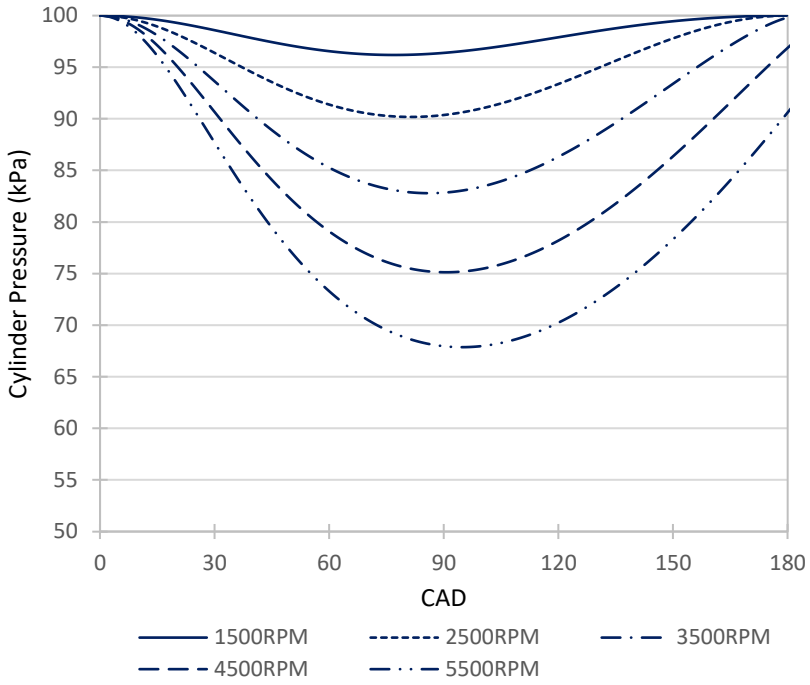

Figure 3-5: Cylinder pressure during intake of a syngas/air mixture at various engine speeds.

Despite a minor reduction in pressure mid-stroke, low speed conditions show that the cylinder pressure returns to the inlet pressure by the end of the filling process. At higher engine speeds, the restricted flow prevents the complete filling of the cylinder and leaves the cylinder pressure below the desired intake pressure at the bottom of the piston stroke. In all cases, incomplete filling of the cylinder reduces the volumetric efficiency of the intake stroke, however this more significant for faster engine speeds.

Engine speeds 4000 RPM and lower have volumetric efficiencies exceeding 97% while reaching a final pressure above 98.9 kPa and thus have negligible effect on the performance of the syngas fuelled engine. Higher speeds cause further reduction in filling performance with an engine speed of 5500 RPM achieving only 87% volumetric efficiency and finishing with a cylinder pressure of 90.6 kPa at BDC. Although valve timing strategies can be used to compensate for this effect at high speeds, the focus of this work is not on engine parameters or control strategies thus the volumetric efficiency and BDC pressure calculated are used as the initial point for further cycle analysis. By limiting the engine speeds considered to below 4000 RPM, the negative effects of valve restrictions are largely avoided.

3.3.2.5 Engine cylinder 1st law analysis

A more complete description of the in-cylinder, finite-time process during the intake, compression, combustion, power, and exhaust strokes of our internal combustion engine requires calculation of the working fluid state variables. Thermodynamic quantities of pressure, temperature, and volume are related to the system mass using the ideal gas equation (shown in differential form in eq (3.89)) and combined with the fundamental definition of work (equation (3.86)), enthalpy (equation (3.88)), and internal energy (equation (3.87)) to provide an analysis of the piston-cylinder system according to the first law of thermodynamics (3.85). This approach will neglect the effects of kinetic and gravitational potential energy changes on the piston-cylinder system.

$$\delta Q_{net} - \delta W + \delta H_{i/e} = \delta U \tag{3.85}$$

$$\delta W = P \cdot \delta V \tag{3.86}$$

$$\delta U = m\, C_v\, \delta T + T\, C_v\, \delta m \tag{3.87}$$

$$\delta H_{i/e} = T_0\, C_{p,0}\, \delta m \tag{3.88}$$

$$\delta T = \frac{P\, \delta V + V\, \delta P - \frac{PV}{m}\, \delta m}{m\, R} \tag{3.89}$$

Combining these differential relationships together allows for a description of the first law analysis in differential form. Constant parameters of heat capacity and gas constant are simplified though the known relationships of the gas constant, $R = C_p - C_v$, and the adiabatic index, $\gamma = C_p/C_v$. Net heat flow to the system is the difference between the heat released from combustion and the heat lost to the cylinder walls, Q_L. For mass exchange terms, the reference variables are taken as the inlet stagnation properties during the intake stroke but are the cylinder properties during the exhaust stroke. The mass flow rate is calculated from the isentropic, compressible gas flow pressure drop across either the intake or exhaust valve (equation (3.84)).

Expressing this differential equation in terms of the crank angle displacement becomes a convenient way of coupling this governing equation to the previously derived equations of heat release and system volume. A final rearrangement of the terms provides the explicit, first-order, ordinary differential equation that describes the pressure of the piston-cylinder

system in terms of crank angle position (equation (3.90)). This is the primary differential equation to simulate the operation of the model engine.

$$\frac{dP}{d\theta} = \frac{\gamma - 1}{V} \cdot \left(\Delta H_c \cdot \frac{dX_b}{d\theta} - \frac{dQ_L}{d\theta} \right) - \frac{\gamma \cdot P}{V} \cdot \frac{dV}{d\theta} + \frac{\gamma - 1}{V} \left(\frac{\gamma_0 \, T_0 \, R}{\gamma_0 - 1} \right) \cdot \frac{dm}{d\theta} \tag{3.90}$$

3.3.2.6 Engine mechanical losses

So far, extensive consideration of geometry, kinematics, and thermodynamics has produced a suite of differential equations that describe the state of the cylinder gas charge during the engine cycle. Integrating the pressure differential equation with respect to the cylinder volume over the engine cycle calculates the thermodynamic work performed by the gas charge per cycle. This is called the indicated work, W_i.

Not all this indicated work is available at the engine crankshaft for use in electricity generation. A percentage of the indicated work must be used to pump the working fluid into and out of the cylinder through the inlet and exhaust valve restrictions; this is called the pumping work, W_p. Some work is also harvested to run the auxiliary pumps, shafts, fans, generators, and other equipment needed for engine functionality; this is called the auxiliary work. Finally, some work is dissipated in the friction of the many moving components within the engine; this is called the rubbing friction work, W_{rf}. Collectively, the sum of all lost work is called the total friction work, W_{tf}. The net sum of the indicated work and total friction work is the brake work output from the crankshaft, W_b.

Expressing the engine cycle work and losses in terms of engine displacement gives a convenient measure for comparing the performance of engines of different sizes. This term, called the mean effective pressure, *mep* (equation (3.91)), represents the average cylinder pressure over an engine cycle.

$$\text{mep} = \frac{W_c}{n_c \cdot V_d} \tag{3.91}$$

As mentioned previously, the total friction work depends on a wide number of engine parameters. While increasingly detailed models can be used to precisely determine the rubbing friction, auxiliary work, and pumping work, using such models requires an

exhaustive list of variables to be input, including crankshaft and bearing dimensions, piston ring dimensions, lubricant viscosities, and valve sizes, lift profiles, and timings. In lieu of these data-intensive models, Heywood [113] provides an empirical correlation that relates engine speed, *N* in RPM, to the engine's total friction mean effective pressure, *tfmep* in bar.

$$\text{tfmep} = 0.97 + 0.15\left(\frac{N}{1000}\right) + 0.05\left(\frac{N}{1000}\right)^2 \tag{3.92}$$

With the *tfmep* approximated, the net engine brake mean effective pressure, *bmep*, can be determined and thus the brake engine power, $\dot{W}_b$.

$$\text{bmep} = \text{imep} - \text{tfmep} \tag{3.93}$$

$$\dot{W}_b = \text{bmep} * V_d * \frac{N}{n_r} \tag{3.94}$$

3.3.2.7 Model implementation

A custom Fortran subroutine has been written to interface with the AspenPlus simulation platform. An inlet stream of the fuel/oxidiser mixture is passed to the model along with relevant thermodynamic properties at engine intake conditions, modified by the calculated volumetric efficiency and filling pressure, as well as the combustion enthalpy. The subroutine steps through crank angles to simulate the compression, combustion, and expansion processes. The differential equations shown below (equations (3.95)-(3.97)) are solved using a 4th order Runge-Kutta method for each crank angle step. Exhaust blowdown and residual mass fraction are calculated as detailed previously.

$$\frac{dP}{d\theta} = \frac{\gamma - 1}{V} \cdot \left(\Delta H_c \cdot \frac{dX_b}{d\theta} - \frac{dQ_L}{d\theta}\right) - \frac{\gamma \cdot P}{V} \cdot \frac{dV}{d\theta} + \left[\frac{\gamma - 1}{V}\left(\frac{\gamma_0\, T_0\, \text{R}}{\gamma_0 - 1}\right) \cdot \frac{dm}{d\theta}\right] \tag{3.95}$$

$$\frac{dV}{d\theta} = \frac{V_c \cdot (r_c - 1)}{2} \sin(\theta) \cdot (1 + \epsilon \cos(\theta)) \tag{3.96}$$

$$\frac{dW}{d\theta} = P \cdot \frac{dV}{d\theta} \tag{3.97}$$

Calculation of the Fortran program is iterated using new inputs based on the calculated residual mass fraction until the exhaust stream reaches 0.01% convergence of pressure,

temperature, and flowrate. Results of the time-dependent engine simulation are integrated over one complete four-stroke cycle and scaled by the engine size and speed to provide the overall flow rates of intake and exhaust streams and the indicated output power and heat loss rate. The exhaust gas stream along with calculated cycle power and heat loss rate are returned to the main Aspen flowsheet.

For a small, distributed generator, the dimensions of a typical four stroke, 6-cylinder, 5.9 litre, spark ignited (SI) engine is chosen for the model. When run on natural gas, the engine has a rated brake output of 50 kW. Specifications of the engine simulated are provided in Table 3-3. The engine air/fuel ratio was set for complete stoichiometric combustion of the supplied syngas. While a detailed engine model is central to the work at hand, the present analysis focuses on the system-level integration of CO_2 gasification. As such, variations of engine parameters, including combustion equivalence ratio, were not considered.

Table 3-3: Simulated engine specifications

Cylinders	6	-
Bore	102	mm
Stroke	120	mm
Connecting rod	192	mm
Compression ratio	10.5	-
Engine cycle	4	stroke

3.3.3 Engine model validation

Validation cases using syngas (19% H_2, 18% CO, 1.8% CH_4, 12% CO_2, 49.2% N_2) at an A/F ratio of 1.27 and inlet pressure of 78.9 kPa were compared to experimental data available in the literature [116]. Power control of the experimental naturally aspirated engine is achieved by throttling the air/fuel mixture supplied to the engine, reducing both the mass flow and intake pressure. While the mass flow of fuel and A/F ratio were specified from experimental conditions, actual intake pressure was estimated from the volumetric flowrate specified through the given engine speed and displacement combined with the assumed intake temperature.

Table 3-4 summarises the experimental flow rates of air and syngas reported by Dasappa et al [122] and the calculated throttled intake pressure. Indicated power calculated by the simulation was converted to brake power by approximating the fmep based on the engine speed (equation (3.92)) and determining the bmep from the imep calculated by the in-cylinder simulation.

Table 3-4: Validation case parameters and results

Syngas flow	0.0275	kg/s
Air flow	0.0351	kg/s
Total intake flow	0.0626	kg/s
A/F ratio	1.27	-
Mixture gas constant	307.4	J/kg-K
Volumetric flow	0.0735	m^3/s
Intake temperature	300	K
Intake pressure	78.5	kPa
Model indicated power	46.48	kW
Model fmep	130.75	kPa
Model brake power	**27.25**	**kW**
Reported brake power	**27.32**	**kW**

Reported engine brake power is compared to the brake power calculated by the engine model, showing good agreement with <1% relative error. Model outputs of indicated power and total friction mean effective pressure are also reported. Experimental, in-cylinder pressure measurements from Shivapuji and Dasappa [116] are compared to calculated model outputs for three engine power settings ranging from 5 kW to 27 kW in Figure 3-6 and Table 3-5. Results indicate good overall model agreement on both the predicted brake power and cylinder pressure profiles with better results achieved for higher power settings. Furthermore, the heat release profiles for the in-cylinder syngas combustion are also compared.

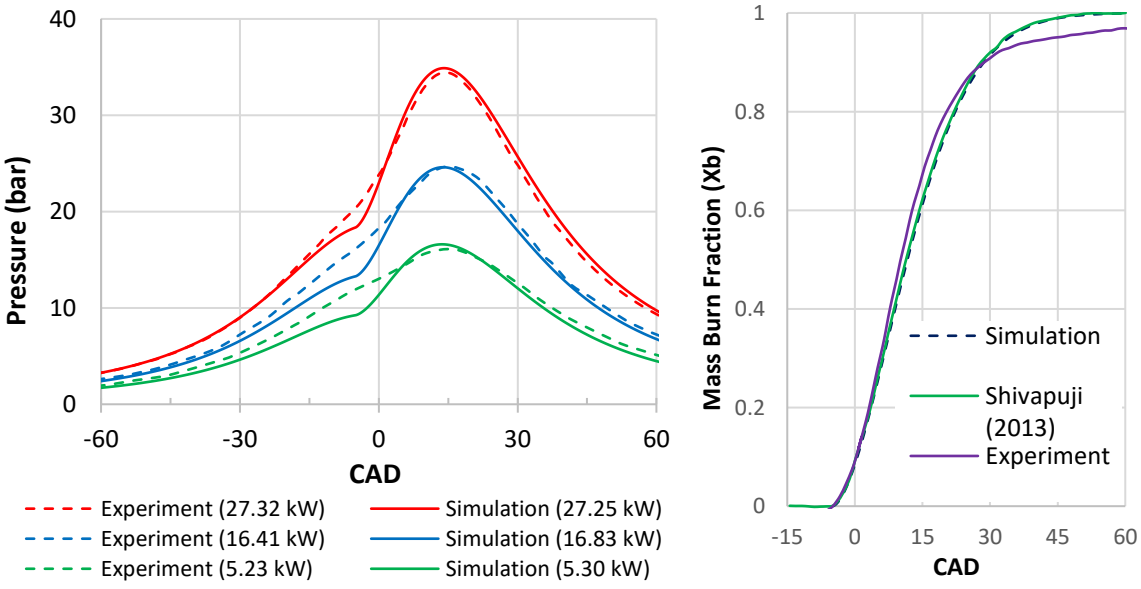

Figure 3-6: Validation of the simulated engine model and empirical engine performance for (left) cylinder pressure traces and shown brake power outputs at different power settings and (right) calculated combustion profiles for the current simulation and reference model compared to experimental data [117].

Table 3-5: Validation brake power outputs

	High Power	Medium Power	Low Power
Simulated Power	27.25 kW	16.83 kW	5.30 kW
Experimental Power	27.32 kW	16.41 kW	5.23 kW

A separate validation case was evaluated to establish the overall energy balance of the engine model. Using a specified thermal energy input of 123.5 kW [123], model brake power, jacket cooling load/cylinder heat loss, and exhaust sensible heat were compared to reported experimental results. As shown in Figure 3-7, the model predicts the overall energy outputs from the system with close agreement to the experimental measurements. The largest difference in results is the sensible thermal energy of the exhaust gasses. Since the experimental setup determined the exhaust heat load by temperature measurement of the exhaust gasses in the exhaust manifold, any heat conducted/radiated away from the manifold piping and exhaust valves will not be accounted for in the experimental data. This is in contrast to the numerical model which directly calculates the exhaust gas temperature adiabatically. Any heat losses from the exhaust manifold would cause the experimental exhaust sensible load to appear lower than the modelling case.

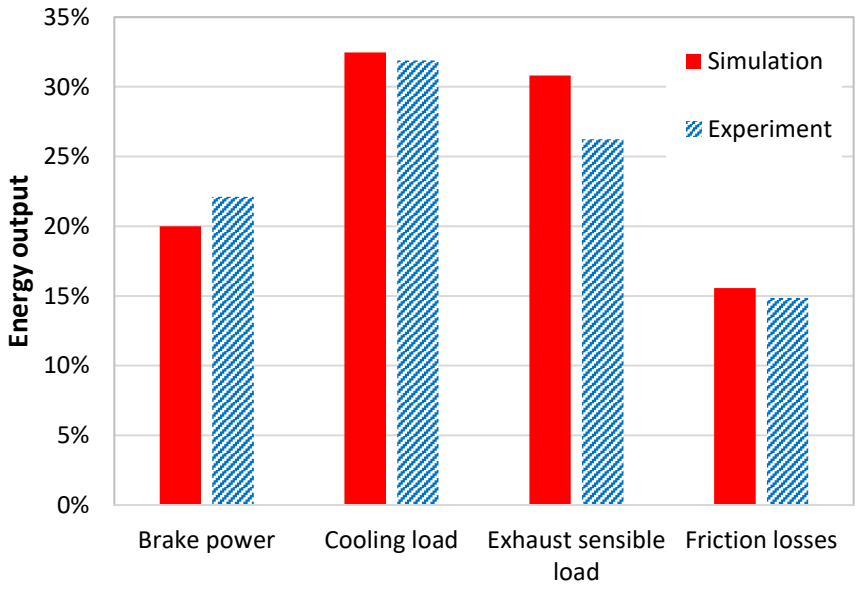

Figure 3-7: Distribution of energy output from experimental data and simulated engine model.

For added confidence in the accuracy of the engine model, an additional validation case [124] for an engine with different geometry run on a different syngas blend (50% H_2, 50%

CO) was evaluated. The specifications of this smaller engine with a larger compression ratio are provided in Table 3-6.

Table 3-6: Additional validation engine specifications

Cylinders	1	-
Bore	76.0	mm
Stroke	88.0	mm
Compression ratio	14	-
Engine cycle	4	stroke

Engine performance was evaluated for two operating conditions at different engine speeds and combustion excess air ratios. Overall performance results are reported in Table 3-7. Both cases showed the model was effective at predicting IMEP and engine power. The low-speed case also showed particularly good agreement for the maximum cylinder pressure however the combustion phasing had a minor difference of 3.7 CAD with the model pressure peak leading the experimental engine. Data from the high speed case indicates the simulation slightly overpredicted the maximum cylinder pressure by approximately 7 bar, however the timing of the pressure peak was very similar.

Table 3-7: Engine performance and model results for two validation cases.

	RPM	λ	IMEP (bar)	$\dot{W}$ (kW)	P_{max} (bar)	P_{max} -CAD (ATDC)
Simulation	1500	1.5	8.01	4.00	62.25	11.3
	2100	1.97	6.24	4.36	52.41	10.7
Experiment	1500	1.5	7.9	3.94	61.44	14
	2100	1.97	6.4	4.47	45.46	11

Cylinder pressure traces for these validation cases also support the accuracy of the derived engine model. Both the pressure profiles and the heat release curves calculated by the engine simulation follow the same trends shown in the experimental data. There is a slight difference in the low-speed combustion profile beyond CAD50, however this minor deviation seems to have a negligible effect on the overall pressure profile and derived engine performance. Although the combustion profile in the high-speed case is very well matched between the experimental and simulated data, the pressure profile calculated by

the model is slightly higher than what is observed in the experimental case. Despite this apparent overprediction in the pressure time-series, the calculated IMEP of the model is slightly lower than what was reported experimentally. Regardless of this slight difference in scale of the pressure curve, the trends match well and the curves converge as the expansion stroke progresses. The derived model therefore appears well suited to approximate the performance of an internal combustion engine run on syngas.

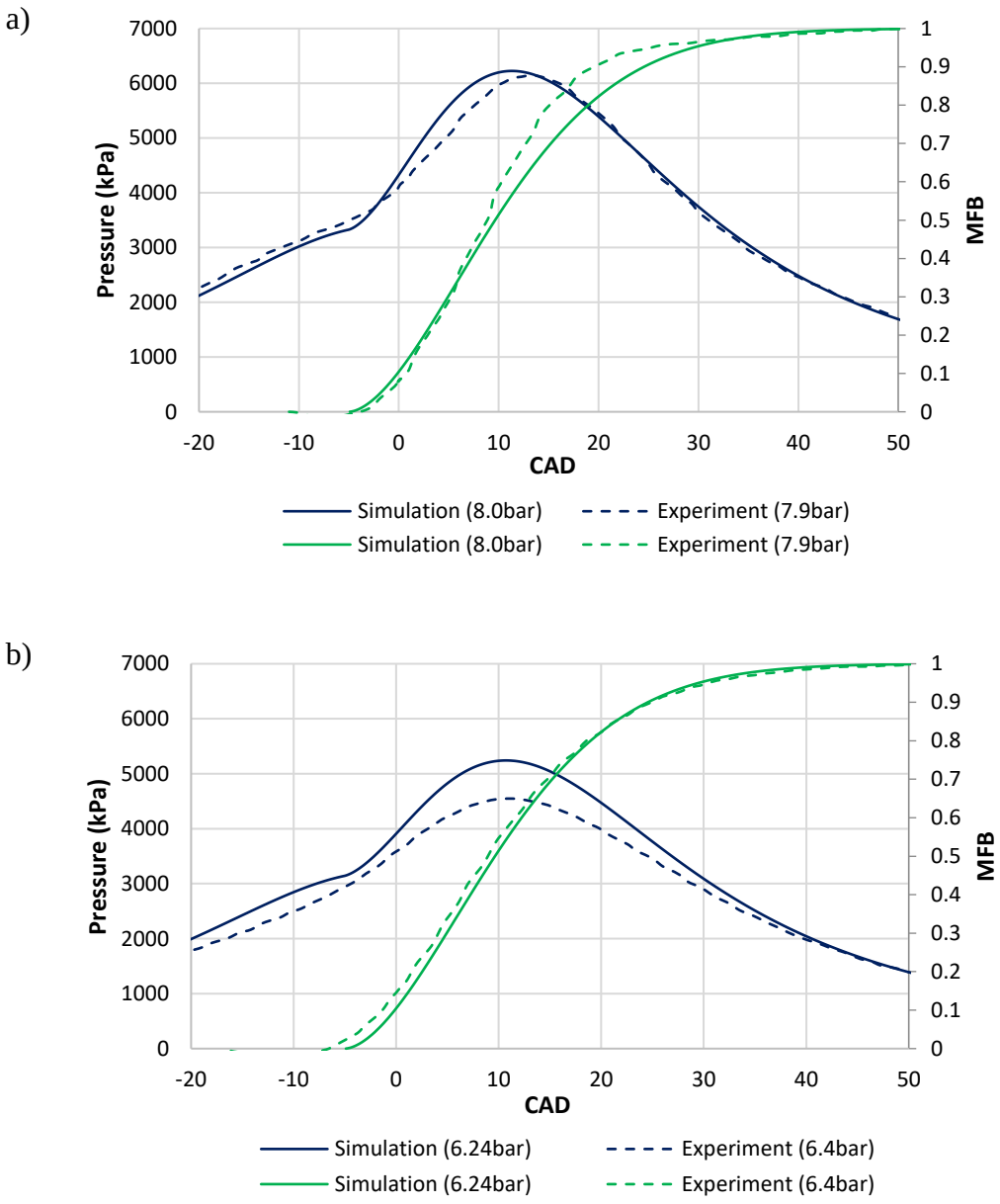

Figure 3-8: Comparison of cylinder pressure (blue) and MFB (green) between a simulation and experiment [124] of an engine run on syngas at a) 1500 RPM and b) 2100 RPM.

3.4 Summary

A set of phenomenological models have been developed to simulate an integrated gasification power cycle. Non-stoichiometric equilibrium models are selected to determine the gasification conditions. This modelling approach has a robust foundation on fundamental thermodynamics and is preferred for applications where system-level interactions are analysed. The implementation of this model was successfully verified against other, established numerical models. Further comparison of modelling results to known syngas from a downdraft gasification was discussed to assess the limitations of the model.

Calculations for a standard Otto cycle are presented to describe an idealised internal combustion engine cycle. A detailed, time dependent engine model is also derived from established principles. Particular parameters controlling the rate of combustion are tuned to values representative of in-cylinder syngas charge combustion. Additional parameters governing the heat transfer correlation were also tuned for syngas operation. The resulting model was validated against published data from experiments of internal combustion engines run on syngas.

Chapter 4 CO_2 Recycling in Traditional Integrated Gasification Power Cycles

Contents of this chapter have previously been published in **Greencorn, MJ** et al. (2022) *Thermodynamic Limitations to Direct CO_2 Utilisation within a Small-scale Integrated Biomass Power Cycle*, Energy Conversion and Management, 269, DOI: 10.1016/j.enconman.2022.116144. and in **Greencorn, MJ** et al. (2020) *Modelling the performance of a syngas fuelled engine: Effect of excess air and CO_2 as combustion diluents*, Low-Carbon Combustion: Joint Meeting of the British and French Sections of the Combustion Institute.

4.1 Introduction

There have been only limited investigations to date on direct CDU strategies used in integrated gasification cycles. The in-depth investigation presented here is needed to fully understand how system parameters interact to influence both the overall system performance and the fundamental thermodynamics of the gasification process specifically. Complexities of such integrated systems and the coupled interdependency of component operations mean that many factors can influence the system as a whole. Additionally, the high endothermicity of the CO_2 utilisation reactions suggests gasification performance would be sensitive to any effect that changes the thermal conditions of the gasifier either through temperature or supplied allothermal heat, however this has yet to be investigated in detail within an integrated system. Particularly, an assessment of the specific benefits and limitations of implementing such a CDU strategy in a gasification power cycle is needed to inform future system designs to optimally implement exhaust gas recycling (EGR) gasification. This is of interest in the context of small-scale distributed generation systems and internal combustion engines where gasification-based direct CDU technologies have not been explored.

In this work, the thermodynamic gasification conditions in a model representative of a small-scale, internal combustion engine-based biomass power cycle using EGR-enhanced gasification as a CDU strategy are analysed. System outputs of indicated power, efficiency, and specific emissions are studied along with resulting thermodynamic gasification parameters. This analysis focuses on the thermodynamic equilibrium conditions for gasification so that system-level effects of CO_2 recycling can be studied separate from the performance of any individual gasifier design. Specifically, the potential for carbon

utilisation in the system is investigated independently of carbon capture and storage technologies to determine benefits to system efficiency and reductions to specific emissions. System parameters that influence the thermodynamics of CO_2 conversion into syngas are also highlighted. Particular focus is given to the effects of N_2 dilution within the system.

4.2 Proposed System

The integrated gasification cycle (IGC) is illustrated in Figure 4-1. The aim of this system is to efficiently generate power from a feedstock of biomass fuel at the scale of a small, modular, distributed power generation unit. Critically, this system incorporates a recycling line from the engine exhaust to the gasifier to implement an EGR-enhanced gasification scheme for direct CDU within the system, a practice not currently used in any piston-engine based IGC. A variable fraction of the exhaust stream can be recycled in such a manner while temperatures, flow rates, and chemical composition for each line are monitored to gain detailed information on system component interactions. This allows for detailed analysis of the system response to exhaust recycling.

In the proposed system, biomass is converted to syngas in an air-blown gasifier operated at atmospheric pressure. Hot syngas is used to preheat the supplied gasification air (PRE-HEAT) to within 20°C of the gasifier temperature. The product syngas then undergoes cyclone separation of ash and char and subsequent cooling to 40°C (GASCOOL) to remove condensed species (DRAIN). Sufficient air for stoichiometric combustion is mixed with the syngas (CARB) and burned in an internal combustion engine to generate power (ENGINE). Exhaust gases from the engine are at high temperature and contain both CO_2 and H_2O. A portion of the flue gases are returned to the gasifier (FGR) as a source of both allothermal heat and additional gasifying agents CO_2 and H_2O, thus providing a method of using exhaust CO_2 to enhance the gasification process. Residual flue gasses are released to the atmosphere (OUT).

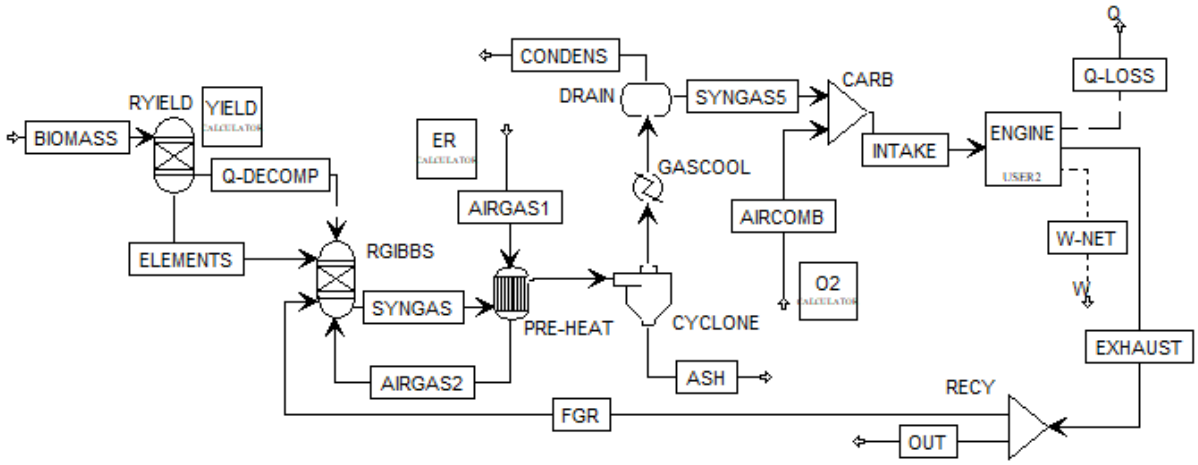

Figure 4-1: Schematic of simulated biomass IGC with recycled exhaust

The proposed system is modelled based on the methods described in Chapter 3 using Aspen Plus chemical process simulation software. Custom program scripts written in Fortran are also integrated within the simulation. In summary, the input biomass feed is interpreted in a Fortran script (RYIELD) based on its ultimate and proximate analyses along with its calorific value and then combined with gasifying agents for the gasification sub model (RGIBBS) to determine the chemical equilibrium mixture of the gasification process. After product gas cooling (PRE-HEAT) and separation of solid (CYCLONE) and condensed (DRAIN) species, a Fortran script (O2) controls airflow (AIRCOMB) to create a stoichiometric mixture of syngas and air for intake (INTAKE) into a Fortran based engine model (ENGINE), as described in Chapter 3. This detailed engine model incorporates heat transfer and combustion dynamics specific to syngas fuel, as extensively detailed in Chapter 3. Engine simulation is iterated until the exhaust stream properties of pressure, temperature, and composition satisfy relative convergence criteria of 0.01%. The recycled exhaust stream is specified on a mass fraction basis (RECY) and returned to the gasifier as an additional input (FGR). Overall system simulation is iterated until the syngas stream properties satisfy relative convergence criteria of 0.01%.

4.2.1 Feedstock

To simulate a small generating unit, the biomass feed rate is set to 50 kg/h to give a steady input of 230 kW in terms of biomass lower heating value (LHV). This corresponds to an anticipated generator system output of 50 kW assuming approximate conversion efficiencies of 80% for the gasifier and 30% for the engine. A model representative of industrial wood residues (sawdust) is approximated in terms of a proximate and ultimate analysis [108], as shown in Table 4-1.

Table 4-1: Proximate and ultimate analyses of wood sawdust pellets [108]

Proximate Analysis (wt%)				
Moisture	Volatile Matter	Fixed Carbon	Ash	LHV (MJ/kg)
9.5% (ar)	80.63% (dry)	17.27% (dry)	2.10% (dry)	18.43 (dry)
Ultimate Analysis (wt%)				
C	H	N	O	
48.91% (daf)	5.80% (daf)	0.18% (daf)	45.11% (daf)	

** (ar: as received, daf: dry, ash free)*

4.2.2 Exhaust gas recycling

The exhaust gas stream leaving the engine model is split with one branch returning to the gasifier as stream FGR in Figure 4-1. Parameters of the FGR stream are identical to the exhaust stream leaving the engine in terms of component mole fractions, pressure, and temperature while the total stream mass flow is a specified fraction of the exhaust stream. This stream becomes an additional gasifying agent input to the gasification sub model. To study the effects of FGR enhanced gasification, successive iterations of the system model vary the mass fraction of exhaust gases recycled to the gasifier from this point. The range of CO_2 recycling ratios is set to encompass a baseline where no exhaust is recycled to the gasifier and extend to recycling ratios slightly beyond the 1.6 molCO_2/molC ratio reported in the experiments of Prabowo et al. [94]. Remaining flue gases are released from the system through a flue stack, stream OUT in Figure 4-1.

4.3 Results and Discussion

A preliminary case of the simulated IGC at a gasification air equivalence ratio of $\lambda = 0.3$ without any exhaust recycling provides a baseline for the system performance. Syngas generated under these conditions is typical of the products of air gasification. The gaseous products were 22.24% H_2, 28.89% CO, 7.42% CO_2, and 41.45% N_2 by volume with negligible CH_4, having a LHV of 6.19 MJ/Nm^3 (6.08 MJ/kg) while the equilibrium gasification temperature was 972°C. This results in a gasifier cold gas efficiency (CGE) of 82.13%.

Engine performance under these conditions generated 65.18 kW of indicated power with a cylinder cooling load of 61.93 kW, giving an engine thermal efficiency, η_{eng}, of 34.80% and an exhaust temperature of 604°C. Compared to the total thermal energy input from the biomass feeding rate, the overall IGC system has an indicated efficiency, η_{sys}, of 28.14%.

$$\mathrm{CGE} = \frac{\dot{n}_{syn} \cdot LHV_{syn}}{\dot{m}_{bio} \cdot LHV_{bio}} \times 100\% \tag{4.1}$$

$$\eta_{eng} = \frac{\dot{W}_{net}}{\dot{n}_{syn} \cdot LHV_{syn}} \times 100\% \tag{4.2}$$

$$\eta_{sys} = \frac{\dot{W}_{net}}{\dot{m}_{bio} \cdot LHV_{bio}} \times 100\% \tag{4.3}$$

4.3.1 Effect of exhaust recycling

4.3.1.1 Effect of excess CO_2 in an internal combustion engine

Before considering the consequences of exhaust recycling on the overall system performance or on the thermodynamic conditions of gasification, the effect of adding CO_2 to the working fluid of the ICE should be considered directly. It has previously been shown that a limited increase in engine performance is observed simply from replacing excess air with excess CO_2 in the power cycle [125]. This case, analysed separately from the fully integrated model, is seen in Figure 4-2. For comparison to excess air cases, an equivalent λ-parameter is calculated for the CO_2 cases (equation (4.4)) such that the mass flow of air remains at the stoichiometric flow rate while the CO_2 mass flow substitutes the equivalent mass flow of excess air.

$$\lambda_{eq} = \left(1 + \frac{\dot{m}_{CO_2}}{\dot{m}_{air,st}}\right) \tag{4.4}$$

As shown in Figure 4-2, adding excess air or CO_2 effectively lowers the cylinder IMEP as the relative composition of fuel species in the gas charge is displaced by the additional inert compounds. While diluting the gas charge with excess air or CO_2 produces similar trends, CO_2 dilution cases retain a marginally higher IMEP than the excess air cases. In part, this can be attributed to favourable changes in the heat capacity, heat conductivity,

and adiabatic index of the working fluid by increasing the CO_2 content and limiting the N_2 content. By substituting CO_2 for excess air as the engine diluent gas, the indicated mean effective pressure at high λ ratios remains slightly higher, indicating more available work per engine cycle. For $\lambda_{(eq)}$=1.50, this translates to a 1% increase in IMEP with a trend that rises to 2% for $\lambda_{(eq)}$=2.15.

This also results in lower combustion temperatures. Under stoichiometric combustion conditions, the peak cylinder temperature is calculated to be 1941.4 K. For engine operation at excess air of λ=2.0, peak temperature is limited to 1519.1 K. This falls to a peak temperature of 1470.3 K for an equivalent CO_2 dilution of λ_{eq}=2.0. Additionally, lower cylinder cooling loads are required and exhaust gas temperatures remain higher under the CO_2 diluent regime. For example, at $\lambda_{(eq)}$=2.0 the cooling load reduces from 37.48 kW in excess air to 36.56 kW in CO_2 while exhaust temperatures are 629.7 K and 688.2 K, respectively. This is attributable to the increased heat capacity of the exhaust gases since they have a higher CO_2:N_2 ratio. Such an effect is beneficial for potential downstream processes like removal of pollutants or combined heat and power (CHP) applications. Table 4-2 summarises these findings and further highlights the effects of using only O_2 and CO_2 as the working fluid in the combustion system.

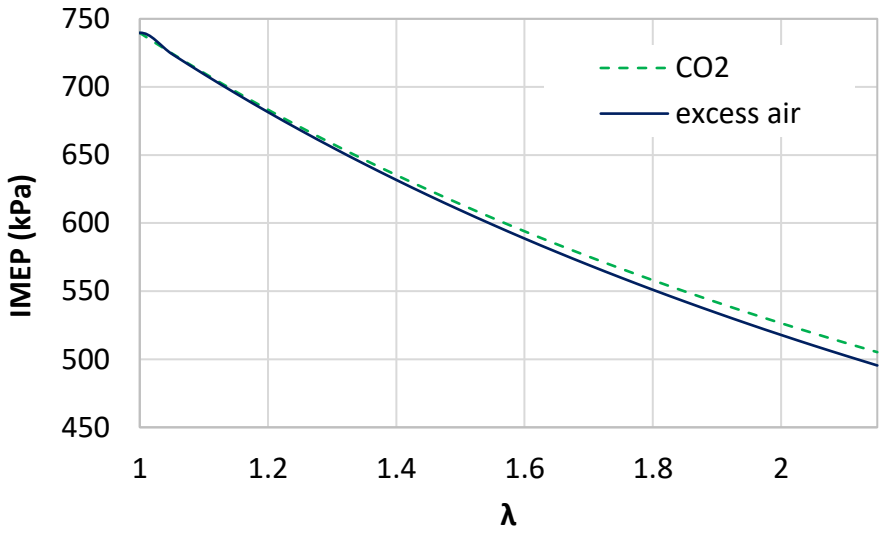

Figure 4-2: Engine IMEP performance under excess air and air/CO_2 combustion regimes

The overall effect seen in this study explains the trend in engine thermodynamic efficiency illustrated in the fully integrated cases discussed later (e.g. Figure 4-4). It should be noted that, while the effect is positive and increases engine efficiency, it is small in magnitude.

As discussed later, the benefit of exhaust recycling to the engine efficiency is minor compared to the changes in gasification efficiency and is mentioned here for clarity.

Table 4-2:Results summary of select model cases for excess air, air/CO_2, and O_2/CO_2 combustion regimes

Case	IMEP (kPa)	Peak T (K)	Cooling load (kW)	Exhaust T (K)
Stoic. Air	739.4	1891	42.13	782
Excess air (λ=2)	517.8	1519	37.48	630
Air/CO_2 (λ=2)	526.5	1470	36.56	624
Stoic. O_2	1109.4	2678	49.31	1108
O_2/CO_2 (λ=2)	681.2	1709	40.12	844

4.3.1.2 Constant air ratio cases

To examine the potential use of exhaust gases in a CO_2 utilisation scheme to enhance gasification performance, the model is adapted to recycle a portion of the engine exhaust to the gasifier. Recycled exhaust is quantified by the amount of CO_2 returned to the gasifier through the molar recycling ratio (equation (4.6)). While this ratio is defined in terms of CO_2 recycling, the exhaust gases returned to the gasifier will also contain some water vapour as a co-product of the engine's combustion reaction.

$$\lambda = \frac{\dot{n}_{air,supplied}\left(\mathrm{mol}/_{s}\right)}{\dot{n}_{air,stoichiometric}\left(\mathrm{mol}/_{\mathrm{s}}\right)} \tag{4.5}$$

$$\mathrm{CO_2/C} = \frac{\dot{n}_{CO_2,supplied}\left(\mathrm{mol}/_{\mathrm{s}}\right)}{\mathrm{C\ in\ biomass}\left(\mathrm{mol}/_{\mathrm{kg}_b}\right) \times \dot{m}_b\left(\mathrm{kg}/_{\mathrm{s}}\right)} \tag{4.6}$$

An integrated exhaust recycling gasifier represents a complex gasification system since flowrates of gasifying agents, supplied allothermal heat, and equilibrium temperatures are all coupled with the contents of the produced syngas. Figure 4-3 presents data for the syngas generated under various amounts of exhaust recycling while the gasification air

flow, and thus air ratio, is held constant at $\lambda = 0.3$. As more exhaust gases are returned to the gasifier the total volume of syngas increases accordingly. Despite a modest increase in the total H_2 production from 0.348 mol/s to a maximum of 0.396 mol/s at a recycling ratio of 0.923 molCO_2/molC, the higher total volume of produced gas decreases the fraction of H_2 in the syngas as the recycling ratio goes up. Furthermore, a slight decrease in the total production of CO from 0.399 mol/s to 0.248 mol/s over the same range of recycling ratios contributes to an increase in the H_2/CO ratio. Both H_2 and CO production drop off dramatically as the recycling ratio passes 1.0 molCO_2/molC. A minor increase to the CH_4 content is also evident as the recycling ratio rises, reaching 0.063 mol/s at the maximum recycling ratio. Additionally, there are significant increases in the N_2 and CO_2 content as exhaust gases are recycled. This dilution of the syngas with N_2 and CO_2 has the consequence of decreasing the syngas LHV with increased exhaust recycling. Sources of these diluents within the gasifier system are the N_2 introduced with the gasification air stream and the N_2 contained in the recycled exhaust gas since air is also used as the oxidizer in the combustion engine. The CO_2 diluent is generated from both the gasification and combustion processes.

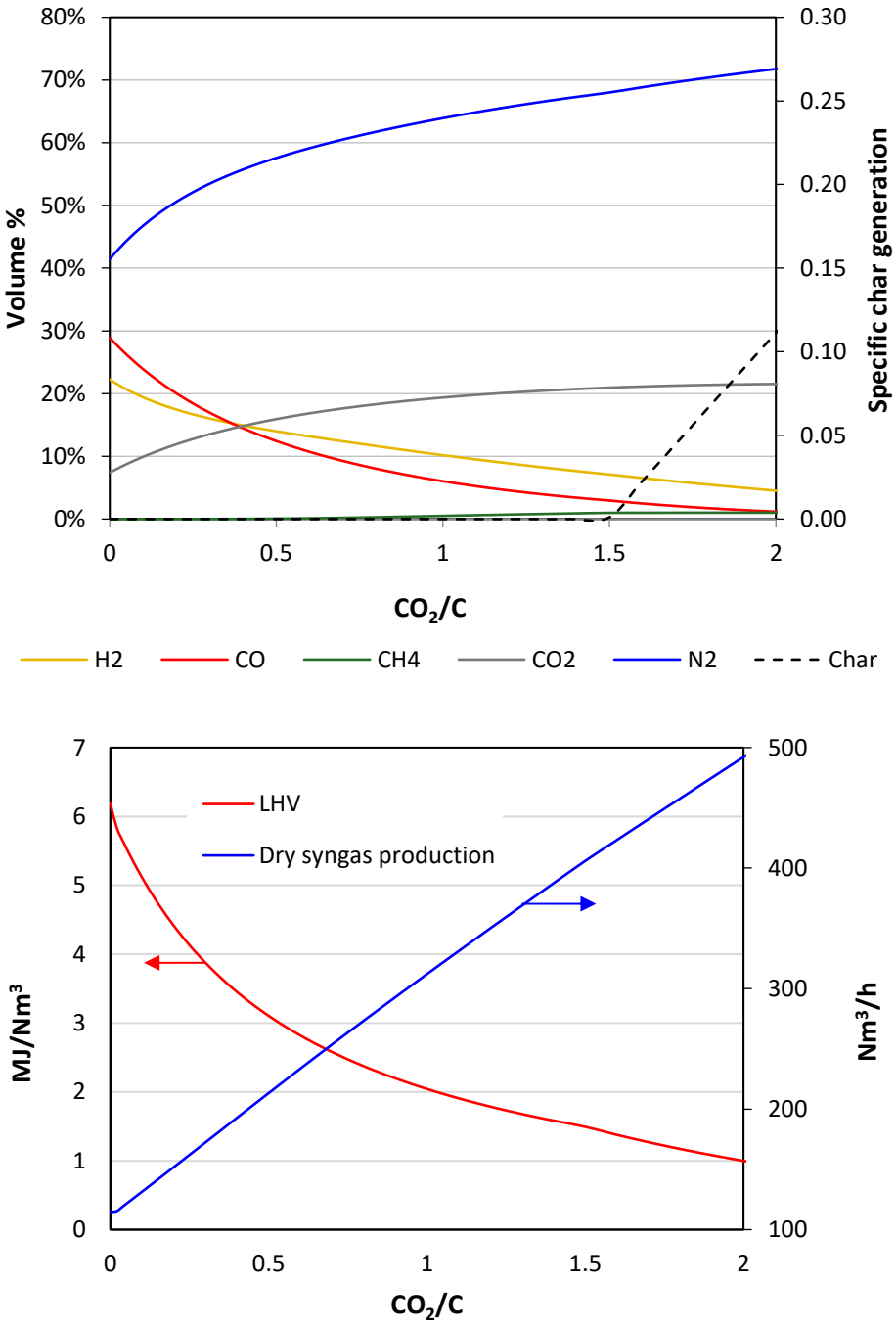

Figure 4-3: Dry syngas composition and unconverted char residual (top) and dry syngas LHV and production rate (bottom) for air gasification at λ=0.300 enhanced with recycled engine exhaust gases.

Under this system configuration, gasifier temperatures decrease with increasing exhaust recycling (Figure 4-4), creating thermodynamic conditions less favourable to endothermic reactions. As the recycling ratio exceeds 1.5 mol CO_2/mol C, the gasifier equilibrium condition can no longer convert all the carbon contained in the biomass feed into gases and char residues are produced. This behaviour is also reflected in the observed cold gas efficiency (CGE) where initial efficiency losses due to declining syngas LHV are moderate but significantly drop off beyond the carbon boundary point noted above. In principle, this

gasifier performance agrees with previous thermodynamic studies of CO_2 gasification [91] where lower gasification temperatures, incomplete carbon conversion, and poor CGE were observed with increased supply of a CO_2 gasifying agent. Increases in the H_2:CO ratio and syngas dilution were also associated with lower gasification temperatures.

Despite the decreasing quality of the syngas, engine performance (Figure 4-4) shows a marginal improvement in indicated power of 170 W for low levels of exhaust recycling. Since gasifier performance decreased under these same conditions, this phenomenon is attributable to the excess N_2 and CO_2 acting as a combustion diluent within the engine, lowering the average cylinder temperatures. With lower combustion temperatures, less charge energy is lost to the engine coolant so a higher proportion of the available energy can be transferred to useful work. Furthermore, higher CO_2 concentrations in the cylinder working fluid have previously shown limited improvement to engine performance due to changes in thermal properties, as shown above (Figure 4-2) [125]. This has diminishing returns, however, since the specific LHV of the fuel is decreasing overall as the recycling ratio increases.

Moreover, the lower combustion temperatures from the lower LHV fuel produce lower exhaust temperatures. In this coupled system, these exhaust gas temperatures (EGTs) have an effect on the gasification process since the recycled exhaust gases also act as a source of allothermal heat in the gasifier. The conditions of this case produced EGTs that were always cooler than the corresponding gasification temperature, limiting this benefit to the gasifier. High EGR can also lower the gasification temperature by encouraging endothermic reactions since higher concentrations of CO_2 and H_2O will tend to push the equilibrium point of the reverse Boudouard and primary water-gas char reduction reactions. Lower equilibrium temperatures however will tend to favour the exothermic water-gas shift reaction, hence the increasing H_2:CO ratio. In total, EGR gasification for this case showed minimal benefit, increasing the system efficiency to only 28.21% at a recycling ratio of 0.219 molCO_2/molC.

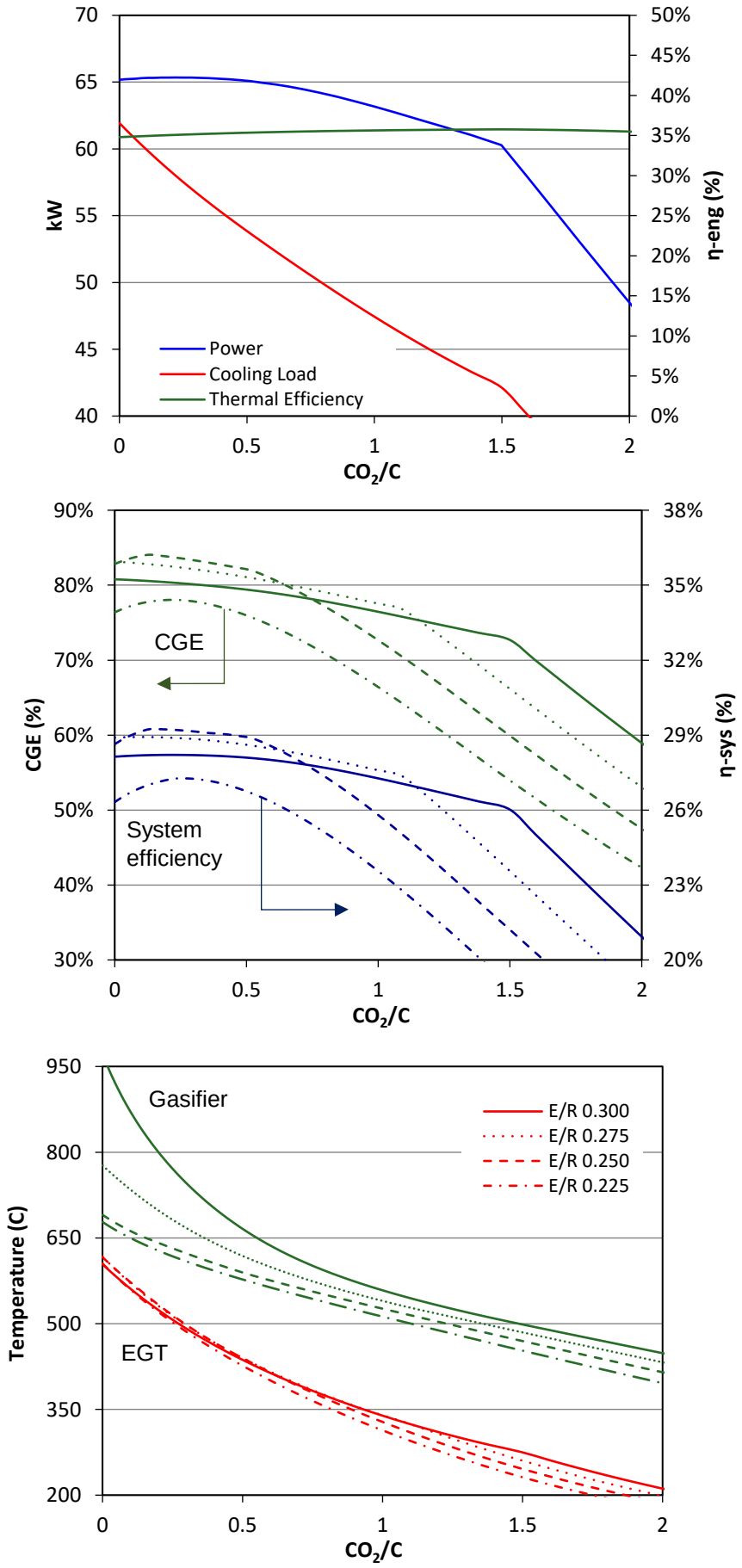

Figure 4-4: System performance parameters under varying degrees of exhaust recycling showing (top) engine performance, (middle) CGE in green and total system efficiency in blue for different E/R, and (bottom) EGT in red and gasification temperature in green at different E/R

4.3.1.3 Varying gasifier air ratio

Although the previous case demonstrated only minor system benefits for recycling engine exhaust, CO_2 gasification is known to enhance char conversion [95], potentially improving gasification conditions under lower air ratios. The initial air ratio of $\lambda = 0.300$ was capable of generating a good quality syngas and completely converting the biomass carbon content to syngas. However, higher air ratios would actually decrease the quality of syngas since additional oxygen would promote more combustion, generating higher temperatures and more CO_2 and H_2O rather than fuel species. On the other hand, an air equivalence ratio too low would produce temperatures too cold for effective gasification and cause low carbon conversion, as can be seen for the extreme low λ cases studied below.

To further investigate the interaction of exhaust gas enhanced gasification and air ratio, four different air ratio cases are studied while varying amounts of exhaust gases are recycled to the gasifier. Equivalence ratios were chosen to cover a range of simulations where carbon conversion varied depending on CO_2 recycling. The baseline $\lambda = 0.300$ showed complete carbon conversion without the need for any CO_2 recycling while the extreme rich condition of $\lambda = 0.225$ was not capable of complete carbon conversion at any recycling ratio. Figure 4-5 illustrates the syngas composition for these cases. Trends in gaseous species concentration remain similar across all the studied air ratios, with N_2 and CO_2 dilution remaining as a significant feature of increased recycling. However, notable differences in char production highlight a remarkable feature of EGR enhanced gasification. While $\lambda = 0.275$ appears to be sufficient to fully convert the biomass carbon without EGR, a lower $\lambda = 0.250$ can only achieve full carbon conversion with some exhaust recycling. Finally, no amount of exhaust recycling is capable of complete carbon conversion for the lowest $\lambda = 0.225$ case in this system configuration.

Gasifier CGEs for these cases (Figure 4-4) highlight the benefit of full carbon conversion at the lowest possible air ratio, as the peak CGE of 84.06% and system efficiency of 29.24% correspond to the $\lambda = 0.250$ case with a recycling ratio of 0.136 molCO_2/molC. The $\lambda = 0.275$ case showed trends in efficiencies similar to the original case of $\lambda = 0.300$ with initial efficiencies slightly higher, indicating the original air ratio was higher than thermodynamically necessary. Finally, the $\lambda = 0.225$ case demonstrates some of the limitations of air ratio reductions as its efficiencies were lower than the base case regardless of amount of exhaust recycling.

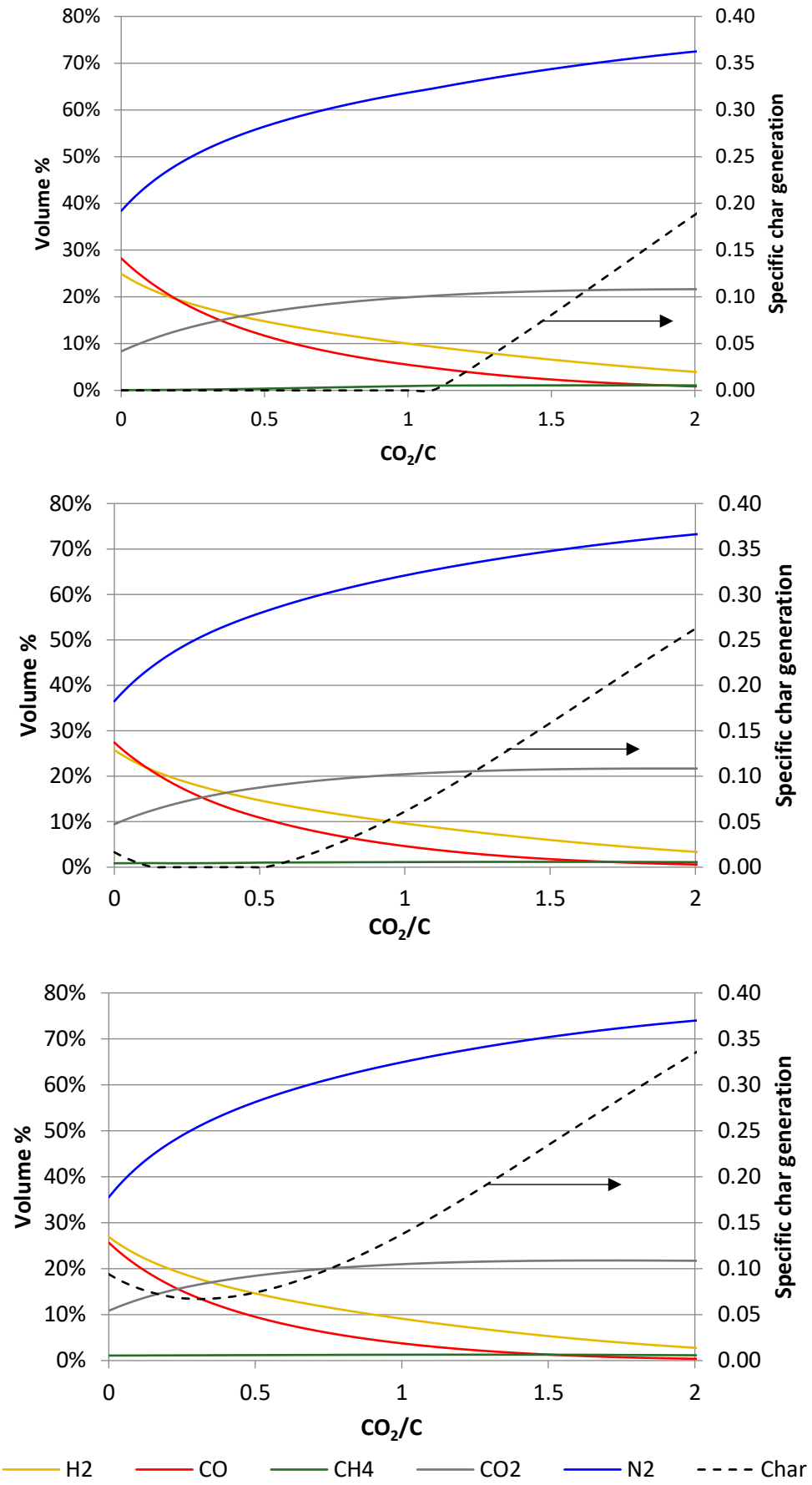

Figure 4-5: Dry syngas composition and unconverted char residual for air gasification enhanced with recycled engine exhaust gases at λ=0.275 (top), λ=0.250 (centre), and λ=0.225 (bottom).

One reason for the incomplete carbon conversion at low air ratios is the lower gasification temperatures. Supplying air is what allows for partial oxidation of some of the feedstock, providing the needed energy to drive the gasification reactions. Although the $\lambda = 0.250$ case was successfully able to supplement some autothermal heat with recycled exhaust heat, the exhaust temperatures in the $\lambda = 0.225$ case were not hot enough to compensate for the low air ratio, despite the recycled exhaust heat.

4.3.1.4 Constant temperature gasification

The previous simulations showed that equilibrium temperatures were influenced by exhaust recycling when gasification air supply remained fixed. Since the air ratio in the gasifier has the strongest influence over the gasification temperature, control of the air flow can effectively set the gasification temperature. By manipulating the airflow into the adiabatic gasifier model, three additional simulations for constant gasifier temperatures of 650°C, 700°C, and 750°C were analysed for system performance.

For these cases, equilibrium temperatures over 700°C caused full char conversion without any exhaust recycling while only the 650°C gasification case required EGR of at least 0.163 mol CO_2/mol C for complete carbon conversion. This latter case also had the highest efficiencies of 83.94% for CGE and 29.23% for the overall system efficiency occurring at the carbon boundary point (Figure 4-6). Recycled gas temperatures significantly limit EGR benefits in these cases since EGTs become increasingly colder than the target gasifier temperature. This has the effect of requiring additional sensible heat to bring these reactants up to temperature, forcing ever higher air ratios in the gasifier to maintain the desired equilibrium temperature (Figure 4-6 c).

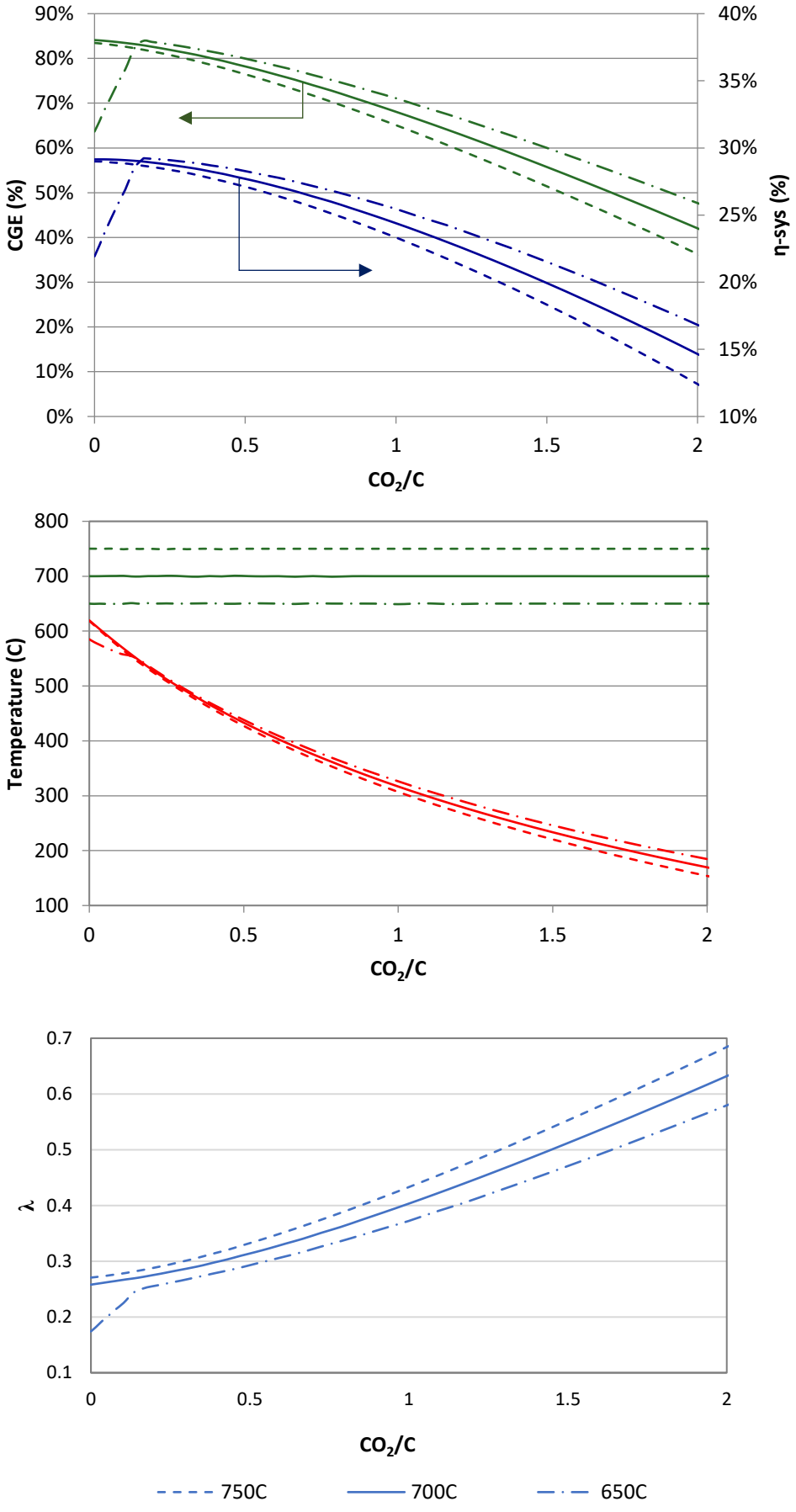

Figure 4-6: CGE in green and system efficiency in blue (top), EGT in red and gasifier temperature in green (centre), and required air ratio (bottom) for constant gasifier temperatures.

4.3.1.5 Summary of exhaust recycling cases

The range of model conditions for the simulated cases are presented in Table 4-3 below. The engine geometry used for this model has been discussed in Chapter 3 and given in Table 3-3 while the feedstock details have been clearly listed in Table 4-1.

Table 4-3: Summary of simulation parameters

Model Parameters	**Values**
Feed stock feeding rate:	50 kg/h
Air equivalence ratio* (λ):	0.225 – 0.300
Gasification temperature*:	650°C - 750°C
Exhaust recycling ratio (CO_2/C):	0.0 – 2.0

*n.b. Range of independent input variables given, when calculated as a dependant variable the value may fall outwith the given range

4.3.2 Effect of excess diluents

From the previous analyses, it is evident that temperature differences between the recycled exhaust and the gasifier cause limitations to the benefits of EGR gasification. It was also shown that the dilution of the syngas with N_2 contributes to the low EGT that exacerbates this issue. In order to quantitatively examine this aspect of the integrated gasification system, two separate modelling cases are considered where N_2 is artificially removed from the modelled system; one where N_2 is eliminated from the syngas stream and another where it is instead removed from the recycled exhaust stream. Both cases remove the diluent downstream from one of the two sources where it originates: in the gasifier air or the combustion air. Of course, the reference cases without N_2 removal are identical to the cases fully described above with system efficiencies shown in Figure 4-4 for the different air equivalence ratios indicated.

Under constant air ratio configurations, Figure 4-7 indicates removal of N_2 from the syngas stream prior to combustion in the engine has the strongest impact on overall system efficiency. Less diluent during combustion results in higher combustion temperatures and, consequently, an initial EGT roughly 100°C higher than the baseline case (Figure 4-8), a trend which continues to improve across all recycling ratios. In turn, these higher exhaust temperatures improve the thermodynamic conditions of gasification by returning more

allothermal heat to the gasifier in the recycled exhaust. This beneficial influence on the total system efficiency demonstrates the improved allothermal heating supplied by the recycled exhaust gases at higher temperatures. For the $\lambda = 0.250$ case the EGT actually exceeds the gasifier temperature for low recycling ratios and increases the overall system efficiency to a maximum of 31.02% at a recycling ratio of 0.220 mol CO_2/mol C. Nevertheless, the precombustion cases tend to require some amount of exhaust recycling to achieve full char conversion for the $\lambda = 0.275$ and $\lambda = 0.250$ equivalence ratios, as evidenced by the efficiency peaks in the data.

Both scenarios of N_2 removal demonstrate the effect of diluent build up within the exhaust recycling system. The rates of change in system efficiency for both removal scenarios are approximately identical after any local efficiency peak, showing the effect of CO_2 build up when isolated from the long-term build-up of N_2 within the system. Interestingly, both of these cases maintain gasifier temperatures sufficiently high to allow full char conversion even at high recycling ratios since the build-up of combustion diluents is limited by removal of the N_2. Similarly, the offset between the efficiency curves indicates the impact of pre-combustion versus post-combustion diluent removal which causes a temperature difference in the recycled exhaust stream, affecting the allothermal heat returned to the gasifier. For the $\lambda = 0.300$ air equivalence ratio, this difference was ~1.5% and rose to ~2.5% for the $\lambda = 0.250$ case.

Removal of N_2 from the exhaust stream before recirculation to the gasifier actually has a slightly negative effect on system performance compared to the original simulation for low to moderate amounts of exhaust recycling. This highlights the importance of the exhaust gases in reusing waste heat. Since the N_2 species is inert in the gasifier, we can see here the effect of supplying additional heat to the gasifier through the mass flow of exhaust N_2 compared to the case where it is removed from the exhaust. It appears that the lower temperature of the N_2 diluted exhaust is offset by the increased mass flow of the exhaust stream to the gasifier, thus carrying more thermal energy into the gasifier. This result is eventually negated at higher recycling ratios as the continuous build-up of N_2 diluent causes a rapid decrease in EGT as the recycling ratio accumulates.

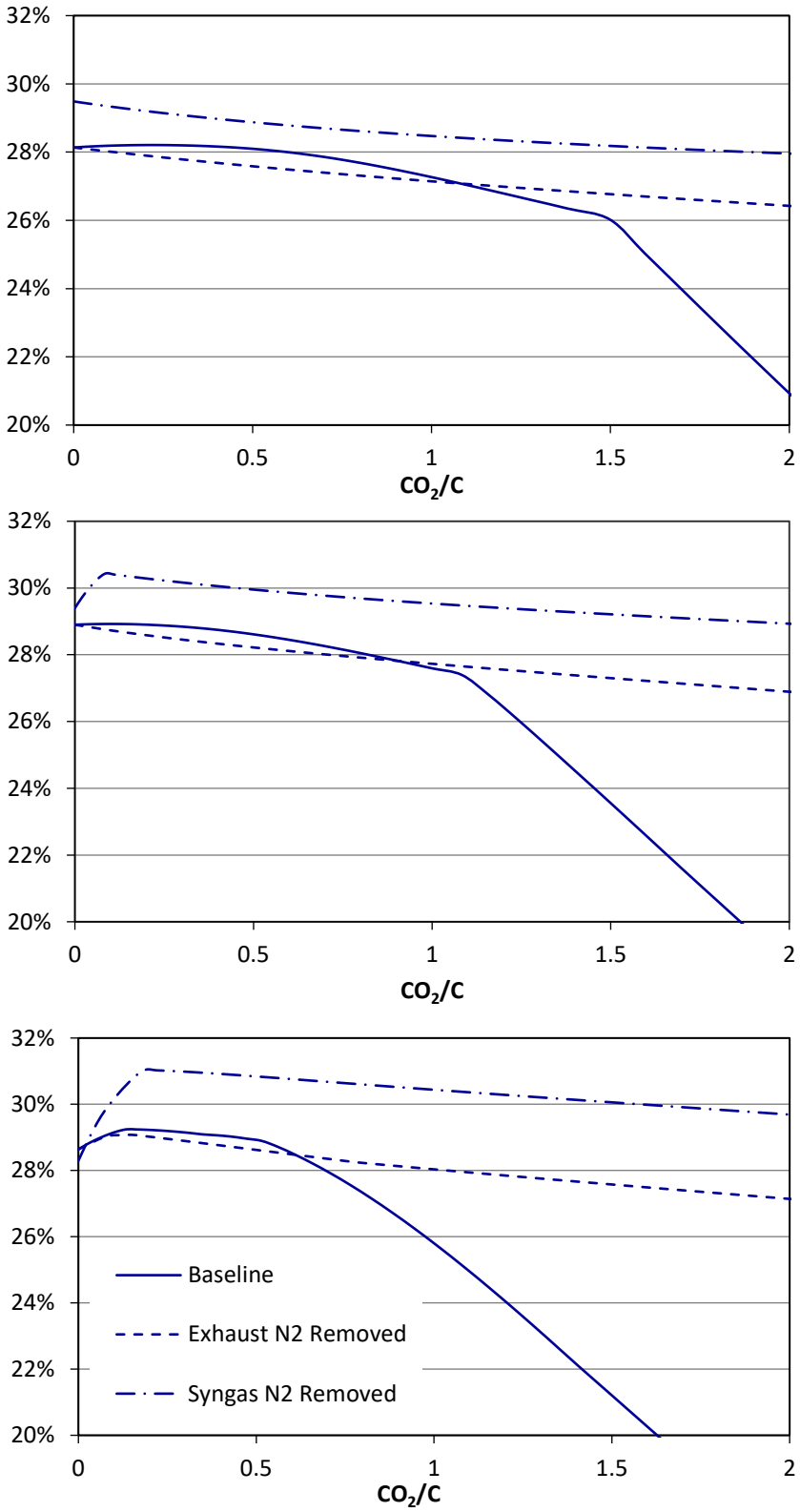

Figure 4-7: System efficiencies at λ=0.300 (top), λ=0.275 (centre), and λ=0.250 (bottom) for different diluent removal strategies.

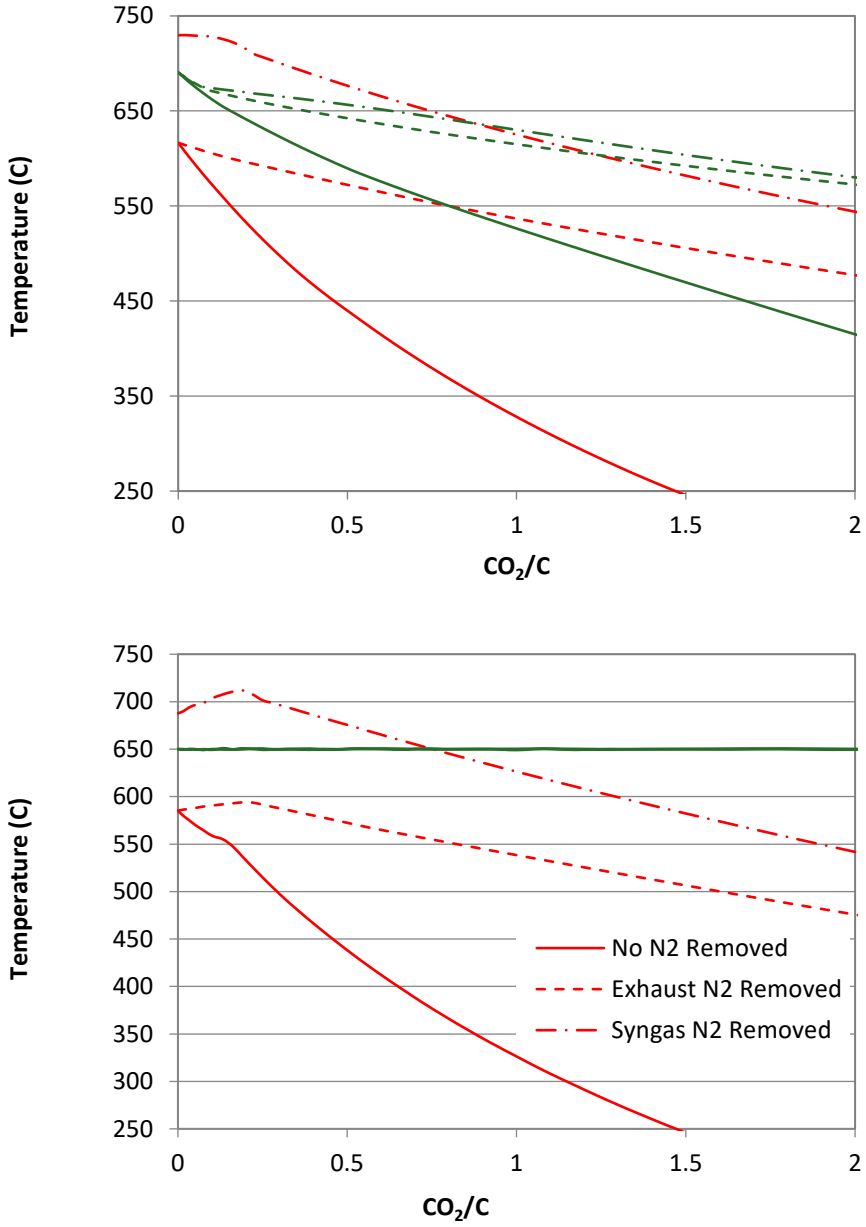

Figure 4-8: Effect of nitrogen removal on EGT in red and gasifier temperature in green for λ=0.250 (top) and constant temperature 650°C (bottom)

Precombustion diluent removal also improves the performance when constant temperature gasification is used. Figure 4-9 demonstrates this effect is most pronounced for lower gasifier temperatures since the higher EGTs will have a greater allothermal heating effect, particularly for the 650°C and 700°C gasifier temperature cases at low recycling ratios when EGTs are above the gasifier equilibrium temperature. The causes of these trends are attributable to similar processes as described above for constant air ratio cases. Again, the removal of diluent from the exhaust stream in the second case has a marginally negative impact on overall system performance for the same reasons highlighted above. Peak system efficiencies of 31.17% and 30.84% were reported at recycling ratios of 0.220 and

0.163 mol CO_2/ mol C for pre-combustion N_2 removal at the constant gasifier temperatures of 650°C and 700°C, respectively.

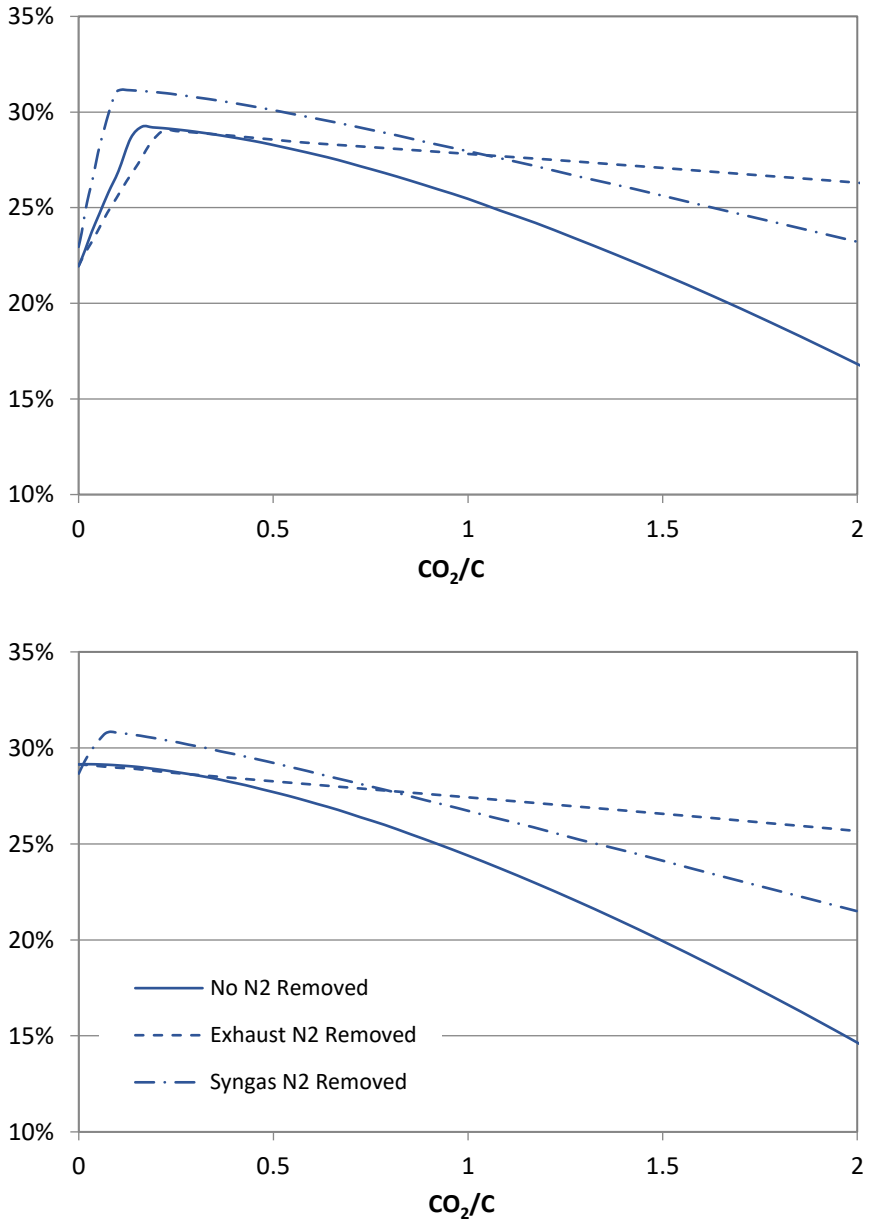

Figure 4-9: System efficiency for constant gasifier temperatures of 650 °C (top) and 700 °C (bottom)

4.3.3 Assessment of CO_2 utilisation and emissions

Analysis has so far focused on the overall system performance and thermal integration of the gasifier and engine exhaust. Assessment of the CO_2 utilisation within the system also provides insight on the most effective CDU aspects of EGR enhanced gasification. To determine the actual generation rate of CO_2 from gasification, the gasifier's net CO_2 production is calculated as the difference between the CO_2 content in the syngas and the

amount of CO_2 supplied to the gasifier as a gasifying agent (Equation (4.7)). In this way the CO_2 generated during gasification is distinguished from the CO_2 recycled to the gasifier from the engine exhaust.

$$CO_{2,net} = CO_{2,syngas} - CO_{2,EGR} \tag{4.7}$$

Figure 4-10 shows a trend that, in general, net CO_2 increases with recycling ratio, indicating that recycled CO_2 is not being consumed in the gasifier. This is due to the lower gasifier temperatures (see Figure 4-4) which will not favour the endothermic reactions that convert CO_2 to syngas. As examples of this situation, the equilibrium constants (see Table 4-4) of the reverse Boudouard (K_{p1}), reverse WGS (K_{p2}), and methane dry-reforming (K_{p3}) reactions demonstrate a marked downward shift for temperatures corresponding to increased recycling ratios, often in orders of magnitude. Such changes mean the reactants (including CO_2) become thermodynamically favoured over the products of those reactions. Mathematically, this behaviour is predictable from the calculation of the equilibrium constant from fundamental thermodynamic principles as $K_p = \exp(-\Delta G/RT)$. This effect is further evidenced by the corresponding reductions in CO production discussed previously in Figure 4-3 and Figure 4-5 due to these same temperature-induced equilibrium shifts in the WGS and dry-reforming reactions that favour CO_2 over CO. Higher recycling ratios at constant air ratios indicate an eventual benefit of concentration-based shifts to the CO_2 equilibrium in the gasifier, however the corresponding syngas is very dilute, carbon conversion is poor, and the equilibrium temperature is so low that gasification may not be achievable in practise.

Table 4-4: Equilibrium constants for reverse Boudouard (1), reverse water-gas shift (2), and methane dry-reforming (3) reactions under exhaust recycling ratios at corresponding gasifier temperatures

CO_2/C	**Temp (°C)**	**$K_{p,1}$**	**$K_{p,2}$**	**$K_{p,3}$**
0	690.5	8.50×10^{-1}	6.33×10^{-1}	5.19×10^{0}
0.508	524.7	1.01×10^{-2}	2.56×10^{-1}	5.88×10^{-3}
1.034	408.4	1.22×10^{-3}	1.01×10^{-1}	7.25×10^{-6}

For the 650°C constant gasifier temperature case, the continuous increase in air ratio required to maintain the gasification temperature will favour the oxidation reactions, thus increasing the net production of CO_2 in a nearly linear fashion beyond the carbon boundary. This is not simply a modelling feature, real autothermal gasification processes

do actually control reaction temperatures by modulating the air intake, and thus equivalence ratio, of the gasifier causing a higher degree of feedstock combustion. Although reaction equilibrium constants will remain the same at the constant gasification temperature, the increase in O_2 supply to the gasifier promotes the formation of CO_2 through combustion reactions. While partial char oxidation reactions would generate some CO due to the increase in O_2 supply up to the carbon boundary, CO_2 remains the thermodynamically favoured product given the significant difference in equilibrium constants since $K_{p,comb} >> K_{p,p\text{-}ox}$. Additionally, CO combustion reactions will contribute to a decrease in CO and a corresponding increase in CO_2 as additional O_2 is supplied beyond the carbon boundary.

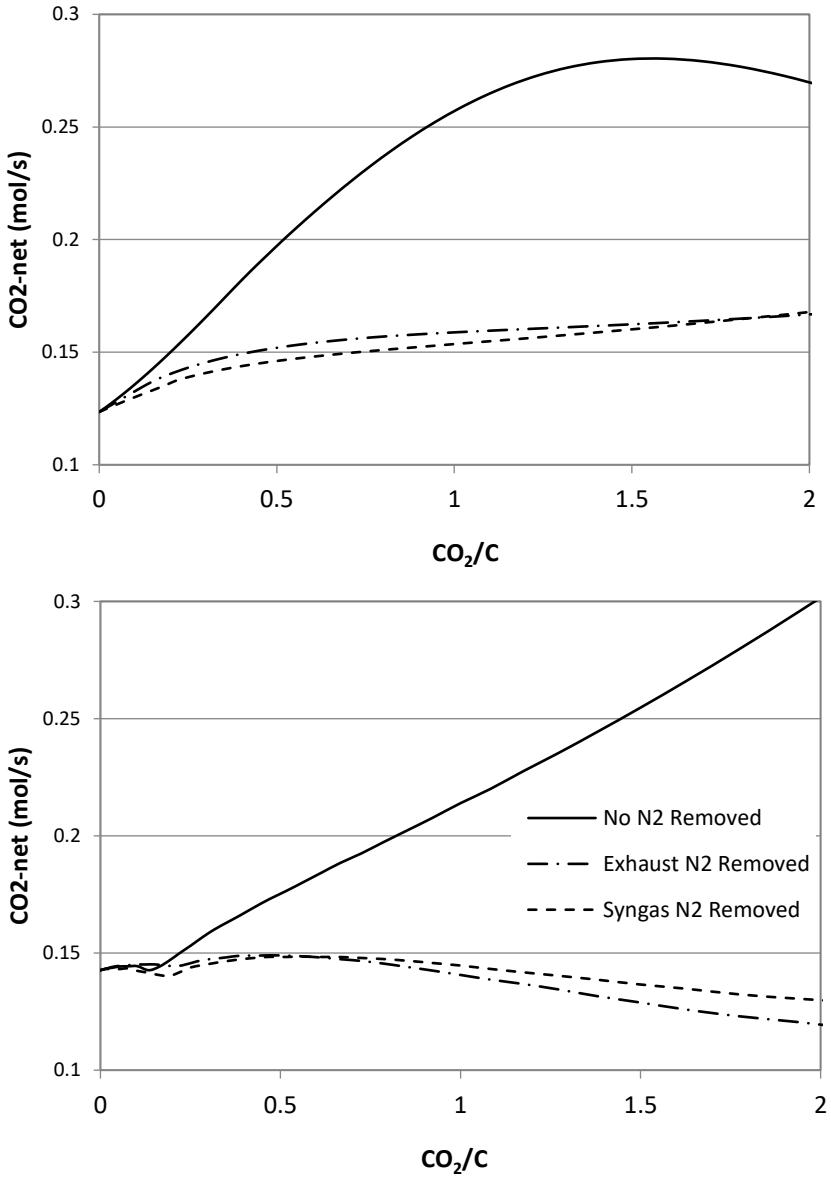

Figure 4-10: Net CO_2 production in the gasifier for (top) constant λ=0.25 and (bottom) constant gasifier temperature of 650°C

A minor improvement in CO_2 conversion occurs for low amounts of exhaust recycling in the constant temperature gasifier. However, net CO_2 production only decreased by approximately 1.00% from initial conditions up to the point of full char conversion while O_2 input increases by 44.04% further indicating the gasification thermodynamic conditions favour char oxidation reactions over the reverse Boudouard reaction. Despite the limited CO_2 conversion for the constant temperature case up to the carbon boundary, it appears that the recycled CO_2 is not active in any chemical reactions to produce fuel since the net CO_2 production from the gasifier continues to increase. In this instance the increase in system performance is attributable to CO_2 and other exhaust gases acting primarily as a heat transfer medium to recycle heat rejected from the engine cycle to the gasifier.

N_2 dilution in the system has a significant, negative impact on these CO_2 utilisation trends. For the cases where N_2 is removed from the syngas or exhaust gases, dramatic reductions in gasifier CO_2 generation are evident over the same recycling ratios. In the first instance, removal of excess N_2 effectively increases the concentration of CO_2 in the gasifier as exhaust gases are recycled, even though the total amount of CO_2 supplied to the gasifier is the same as before. This is in contrast to the original cases where N_2 concentrations in the syngas were typically above 40% by volume and tended to approach 80% at very high recycling ratios. Additionally, the increases in EGT when N_2 is removed allowed for higher gasifier temperatures, making favourable conditions for endothermic reactions to consume CO_2. In fact, a 1.74% improvement in CO_2 conversion occurs at the carbon boundary for the 650°C constant temperature gasifier before a moderate increase in net CO_2 production. This operating point is near the peak EGT condition. Additionally, the higher temperature recycled exhaust heat minimised the required air flow to maintain the constant gasifier temperature, allowing for net CO_2 production to once again decrease at higher recycling ratios. This is consistent with experimental results that indicate best CO_2 conversion conditions exists at the highest temperatures [95].

Although the chemical utilisation of CO_2 as a gasifying reagent tends to be poor, the modest improvements to indicated power and system efficiency from exhaust recycling will affect specific emissions released from the power cycle. Under all system configurations, the local minima of indicated specific CO_2 emissions occur at the best efficiency points, highlighting the importance of gasifier equilibrium conditions on the overall system performance. In the context of biomass energy, this aspect becomes important due to the delay between CO_2 emissions from the power cycle and the reabsorption of the carbon into the next generation of feedstock required to make the cycle

carbon neutral. While there is considerable variability in the extent of this "carbon debt" [17, 16] it stands to reason that any improvement in bioenergy specific emissions will be beneficial in reducing the carbon debt for a given rate of bioenergy generation.

Although it seems there are marginal benefits in the gasifier's CO_2 consumption at higher recycling ratios, the dilute, low-quality syngas produced under these conditions drastically reduces both the CGE and the engine's indicated power output. Regardless of the gasifier's CO_2 conversion conditions, use of EGR enhanced gasification successfully reduced the indicated specific CO_2 emissions at the optimal efficiency operation points. Table 4-5 summarises the system efficiencies and CO_2 emissions for these key cases, underscoring the combined effect of air ratio and recycling ratio on the overall system performance. Although the increase to system efficiency is minor, EGR gasification at an air ratio of λ = 0.250 would reduce the specific CO_2 emissions by 46.2 g/kWh, a 3.79% decrease from the original system configuration at λ = 0.300.

Significant emissions improvement would be achieved if inert diluents could be removed from the syngas or if gasification temperatures could be increased. In addition to the efficiency benefits previously discussed, pre-combustion N_2 removal would decrease indicated CO_2 emissions by 9.73%, emitting 118.5 g/kWh less than the basic system.

Table 4-5: Summary of combined system efficiency and specific CO_2 emissions for select system configurations

Air Ratio, λ	**Gasification Temperature**	**N_2 Removal**	**Recycling Ratio (CO_2/C)**	**Combined System Efficiency**	**Specific CO_2 Emissions (g-CO_2/kWh)**
0.300	(972°C)	-	-	28.14 %	1218.5
0.300	(788°C)	-	0.219	28.21 %	1215.4
0.250	(654°C)	-	0.136	29.24 %	1172.3
(0.251)	650°C	-	0.163	29.23 %	1172.4
(0.260)	700°C	-	0.020	29.15 %	1176.1
0.250	(669°C)	from Syngas	0.220	31.02 %	1104.3
(0.241)	650°C	from Syngas	0.220	31.17 %	1100.0
(0.260)	700°C	from Syngas	0.163	30.84 %	1111.6

*Dependent gasification variable indicated in parentheses

4.4 Conclusions

Analysis of a representative numerical model has quantified the capacity for direct CDU in a small-scale, air-blown, biomass gasification power cycle using EGR enhanced gasification. While these observed trends in system performance are likely generalisable to exhaust recycling for systems of any scale, the specific values calculated here are a result of the particular system that includes a given engine geometry. Naturally, ICEs are a very modular technology and simply adding additional cylinders could scale-up these results to any desired extent. By maintaining a thermodynamic focus on the equilibrium conditions of gasification, the performance of the gasifier is therefore independent of geometry or scale but is nevertheless partially dependent on the conditions of the engine. Key conclusions relating to thermodynamic gasification conditions and system responses are as follows:

- Marginal improvements in indicated output power, system efficiency, and specific emissions are observed under modest exhaust recycling conditions.
- Over certain ranges, EGR supply to the gasifier can lower the air ratio required in the gasifier to maintain full carbon conversion, thus increasing CGE.
- Recycling 0.136 mol-CO_2/mol-C to a gasifier with an air-ratio of $\lambda = 0.250$ increased overall system efficiency by 1.1% and reduced the specific CO_2 emissions by 46.2 g-CO_2/kWh compared to the reference system configuration.
- Exhaust recycling dilutes the syngas with excess N_2 and CO_2, resulting in a lower LHV, lower EGT, and thus lower equilibrium temperatures. High amounts of EGR limits gasifier thermodynamic performance since lower equilibrium temperatures cause lower CO_2 conversion and thus lower syngas quality.
- Gasification equilibrium temperatures dropped by 318°C from the reference case when the gasifier had 0.136 mol-CO_2/mol-C of exhaust recycled and the air-ratio reduced to $\lambda = 0.250$. The net-CO_2 utilisation decreases and the H_2:CO ratio tends to increase with exhaust recycling due to lower equilibrium temperatures.
- Modelling techniques revealed the impact of N_2 dilution is most prevalent in the engine exhaust temperatures. In total, syngas N_2 dilution lowers the overall system efficiency by 2.5 percentage points and increases specific emissions by 72.4 g-kWh, or 6.16%, compared to a N_2-free syngas. This suggests CDU aspects of the system could be further enhanced if additional syngas upgrading or diluent removal is implemented.

- Due to unfavourable thermodynamic conditions in the gasifier, most cases studied showed poor CO_2 conversion to syngas. This indicates the primary use of recycled CO_2 under these conditions is as a heat transfer medium and engine diluent rather than a chemically active reagent. Evidence of enhanced CO_2 chemical conversion to CO is limited to the point of full char conversion in 650°C gasifiers, with N_2 dilution of the syngas also diminishing this effect.

This technical assessment has highlighted the thermodynamic benefits and limitations of EGR enhanced gasification as a direct CDU strategy for a biomass IGC, leading to a detailed understanding of the system thermodynamic conditions under different operating points. It provides a system-level understanding of how EGR influences an IGC and serves as a baseline for future detailed analysis including specific gasifier designs. The key observation that excess N_2 diluent has a significant, detrimental effect on the system thermodynamics indicates that applications of this technology are best suited to low-nitrogen systems.

Chapter 5 CO_2 Recycling in Oxyfuel BECCS Power Cycles

Contents of this chapter have previously been published in **Greencorn, MJ**, et al. (2023) *Enhancement of Gasification in Oxyfuel BECCS Cycles Employing a Direct Recycling CO_2 Utilisation Process*, Energy Conversion and Management, 277, DOI: 10.1016/j.enconman.2022.116601. and **Greencorn, MJ**, et al (2019) *A Novel BECCS Power Cycle Using CO_2 Exhaust Gas Recycling to Enhance Biomass Gasification*, Energy Proceedings, 3, DOI: 10.46855/energy-proceedings-1956.

5.1 Introduction

Results from Chapter 4 have indicated that there may be some limited benefit to the thermodynamics of gasification in a cycle that integrates engine exhaust recycling with biomass gasification. Building from that knowledge base, it must now be investigated whether this effect is possible in BECCS systems that incorporate some method of separating and removing CO_2 from this cycle. Chapter 2 included extensive details on aspects of CCS that may be used to this end. While several hypothetical CCS cycles using CO_2 gasification have been proposed, the system analyses have so far been limited to a discussion simply on the overall system outputs and efficiencies without in-depth investigation into the particular effects on the gasification process. Nevertheless, these systems do show the potential for efficiency improvements of 1.68-4.86% for coal-fired Rankine cycles [97], 6-7% for coal-fired IGCCs [98], 5% for chemical-looping-combustion in a Rankine-based BECCS cycle [99], 6.1% for an Otto-cycle BECCS model [77], and 7.57% for a Brayton-cycle based BECCS system [62] when CO_2 recycling is implemented. Additionally, these models implement idealised power cycle models to simplify the analysis by adopting adiabatic and steady-state approximations of the fundamental cycle processes, discounting effects of heat loss from the cycle and neglecting dynamic aspects of combustion. Furthermore, although the thermodynamic modelling remains insightful, major practical challenges in integrating biomass gasification with gas turbines in particular currently prevent mainstream adoption of this technology. Reciprocating internal combustion engines (ICE) remain preferred over gas turbines since they can accept syngas tar concentrations roughly 100 times higher without failure [112].

While several CCS technologies can be used to remove CO_2 either before or after combustion, detailed results from Chapter 4 have clearly shown excess inert N_2 from air-

based combustion and gasification has a significant, negative impact on the performance of these power cycles. Accordingly, an oxyfuel system is selected as the basis for the BECCS cycle considered in this work. Since the effects of exhaust recycling on the gasification process in a BECCS system using an integrated oxyfuel gasification cycle (IOGC) are as yet unknown, this study investigates in detail the outcome that exhaust recycling has on the thermodynamic equilibrium conditions of the gasification reactions in a representative integrated system. Key cycle measurements of this study are the gasification temperatures and syngas compositions as well as the gasification cold gas efficiency. Engine exhaust temperatures and integrated cycle indicated efficiencies are also calculated to provide insight on the overall performance of the cycle operating conditions studied. Furthermore, system level effects contributing to these thermodynamic conditions are illustrated through comparisons of different modelling cases to further highlight the importance of detailed power cycle models that account for heat losses and fuel combustion dynamics for integrated system analysis. This is particularly important due to the known endothermic nature of the CO_2 gasification reactions. Accurate energy balances of the recycling and gasification processes are critical to understanding the system response to exhaust recycling.

Chapter 3 has also explained some consequences of adopting simplified engine modelling approaches like the idealised Otto cycle. The effect of using such an idealised cycle is compared to cases where the engine is modelled with a more detailed set of time-dependent equations to account for combustion dynamics and heat losses. Additional operational limitations typical of oxyfuel systems and ICEs are also explored to compare the impact of these measures on the cycle performance and gasification thermodynamics.

To address these research gaps, this analysis extends beyond a comparison of indicated cycle energy efficiencies to encompass an in-depth assessment of the gasification thermodynamic conditions by evaluating reaction temperatures, cold gas efficiencies, syngas chemical compositions, and the extent of feedstock carbon conversion. Aspects of local CDU acting within the system are also highlighted and discussed. System responses show this is a complex system with a high degree of thermodynamic coupling between the gasification process and the power generation cycle. These aspects are explained through a series of modelling cases to illustrate how each detail of the model influences the gasification reactions. Finally, extrema of the system are probed to determine the thermodynamic limitations of the observed phenomena.

5.2 Integrated Oxyfuel Gasification Cycle

The system illustrated in Figure 5-1 represents an IOGC suitable for use in a BECCS system. Boundaries of the cycle are limited to the energy conversion and CO_2 separation processes since upstream biomass production and downstream CO_2 sequestration aspects of this BECCS system would be identical to other BECCS systems and are therefore omitted from the studies conducted here. Renewable biomass fuel is fed into the system where it is gasified and the resultant syngas is directly used in a thermal power cycle to generate useful work. By selecting an oxyfuel-type CCS strategy that uses oxygen as the gasifying agent and combustion oxidiser, the resulting cycle exhaust is suitable for CO_2 sequestration without any further need for chemical processing. Furthermore, this cycle uses the novel feature of recycling a portion of the engine exhaust to the gasifier, realising a direct CDU technique to enhance gasification with CO_2 derived from within the system.

Syngas is generated from the biomass feed in an oxygen supplied gasifier at atmospheric pressure (GASIFIER). The modelled feedstock for these simulations is identical to that used for the traditional bioenergy system analysis performed in Chapter 4. Details are given in Table 4-1. Biomass feedstocks and oxygen gasifying agents are input to the system at standard temperature and pressure of 25°C and 1 bar. Supplied oxygen is then pre-heated to within 20°C of the gasification temperature (GAS-HX) while ash and char are separated (CYCLONE) and the syngas is cooled (GASCOOL) and condensed liquids are removed (DRAIN). A stoichiometric mixture of the resultant syngas and oxygen is formed (CARB) and burned in an internal combustion engine (ENGINE) to generate power (W-IND). An ICE is selected as the power conversion method here since this technology has been reliably proven to work well with biosyngas as a fuel. Hot engine exhaust gases are recycled within the system in two locations (ENG-EGR and GAS-EGR). One branch of the exhaust is returned to the gasifier (EGR-G) to supply CO_2 and H_2O gasifying agents as well as allothermal heat to the gasification model, influencing the thermodynamic conditions therein. Other exhaust gases can be recycled locally to the engine model (EGR-E) to act as a combustion diluent and limit the maximum combustion temperatures. Remaining exhaust gasses are ready for CO_2 sequestration and are passed to a CCS stream (TO-CCS) where they are cooled, dried, and compressed. Relevant temperature and gas composition data from these streams are presented throughout section 5.3 and discussed to illustrate the performance of the cycle under different modelling conditions and amounts of exhaust recycling.

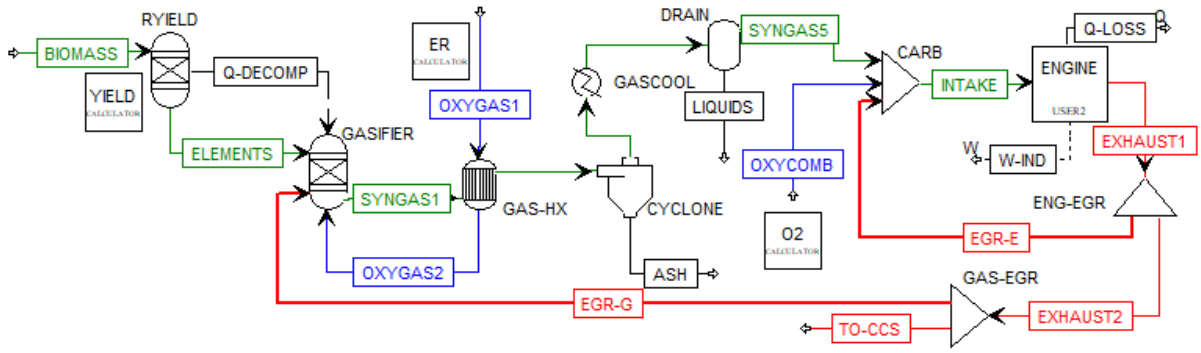

Figure 5-1: Schematic of simulated BECCS cycle with recycled exhaust. Biomass feed and syngas streams shown in green, oxygen streams shown in blue, and exhaust streams shown in red.

The proposed system is modelled according to the fundamental principles discussed in Chapter 3 using Aspen Plus chemical process simulation software. It is also very similar to the model explained in Chapter 4 with differences in gasification agent, combustion oxidiser, and engine exhaust recycling as detailed above. Custom program scripts written in Fortran are also integrated within the simulation. In summary, the input biomass feed is interpreted in a Fortran script based on its ultimate and proximate analyses along with its calorific value and then combined with gasifying agents for the gasification sub model. After product gas cooling and separation of solid and condensed species, a Fortran script controls airflow to create a stoichiometric mixture of syngas and air for intake into a Fortran based engine model. Both Otto cycle and time-dependant engine models as described in Chapter 3 are used for different simulation cases. Engine simulation is iterated until the exhaust stream properties of pressure, temperature, and composition satisfy relative convergence criteria of 0.01%. The recycled exhaust stream is specified on a mass fraction basis and returned to the gasifier as an additional input. Overall system simulation is iterated until the syngas stream properties satisfy relative convergence criteria of 0.01%.

5.3 Results and Discussion

A series of simulations covering a range of gasification O_2 equivalence ratios, exhaust recycling ratios, gasification equilibrium temperatures, and engine combustion temperatures are run to determine the system performance. Thermodynamic conditions of the gasification process are reported by the equilibrium temperature, the syngas composition, and the cold gas efficiency (CGE). Engine performance is evaluated in terms of the indicated thermal efficiency, η_{eng}, while the overall system performance is described through the system's indicated efficiency, η_{sys}.

$$\mathrm{CGE} = \frac{\dot{n}_{syn} \cdot LHV_{syn}}{\dot{m}_{bio} \cdot LHV_{bio}} \times 100\% \quad (5.1)$$

$$\eta_{eng} = \frac{\dot{W}_{net}}{\dot{n}_{syn} \cdot LHV_{syn}} \times 100\% \quad (5.2)$$

$$\eta_{sys} = \frac{\dot{W}_{net}}{\dot{m}_{bio} \cdot LHV_{bio}} \times 100\% \quad (5.3)$$

5.3.1 Ideal Otto cycle analysis

As a preliminary study of the effect of CO_2 exhaust recycling on the integrated cycle, the idealised cycle was run with a constant gasification O_2 equivalence ratio of $\lambda = 0.30$ while increasing fractions of the Otto cycle exhaust gas stream were recirculated to the gasifier. Y-intercepts in Figure 5-2, Figure 5-3, and Figure 5-4 show the baseline simulation without exhaust recycling achieved an equilibrium gasification temperature of 772°C, yielding a syngas of 39.6% H_2, 44.5% CO, and 15.6% CO_2 with trace amounts of CH_4 having a LHV of 223.45 kJ/mol (9.98 MJ/Nm^3 or 11.07 MJ/kg). This initial configuration shows the O_2 equivalence ratio is sufficient to fully convert all the biogenic carbon to syngas species since no char residuals are present. The CGE and indicated system efficiencies corresponding to this reference case are 80.1% and 37.7%, respectively.

Recycling hot exhaust gases from the Otto cycle to the gasifier influences the syngas composition, as shown in Figure 5-2a. In this case, the initial increase in relative CO content at the expense of H2 content appears to be due predominantly to the corresponding increase in equilibrium temperature shifting the equilibrium point of the reverse water-gas shift reaction. This endothermic reaction will thermodynamically favour the products of CO and H_2O as the equilibrium temperature increases. As the CO content of the syngas reaches its maximum of 54.31%, the thermodynamic equilibrium temperature is increasing past 1475°C (see Figure 5-4).

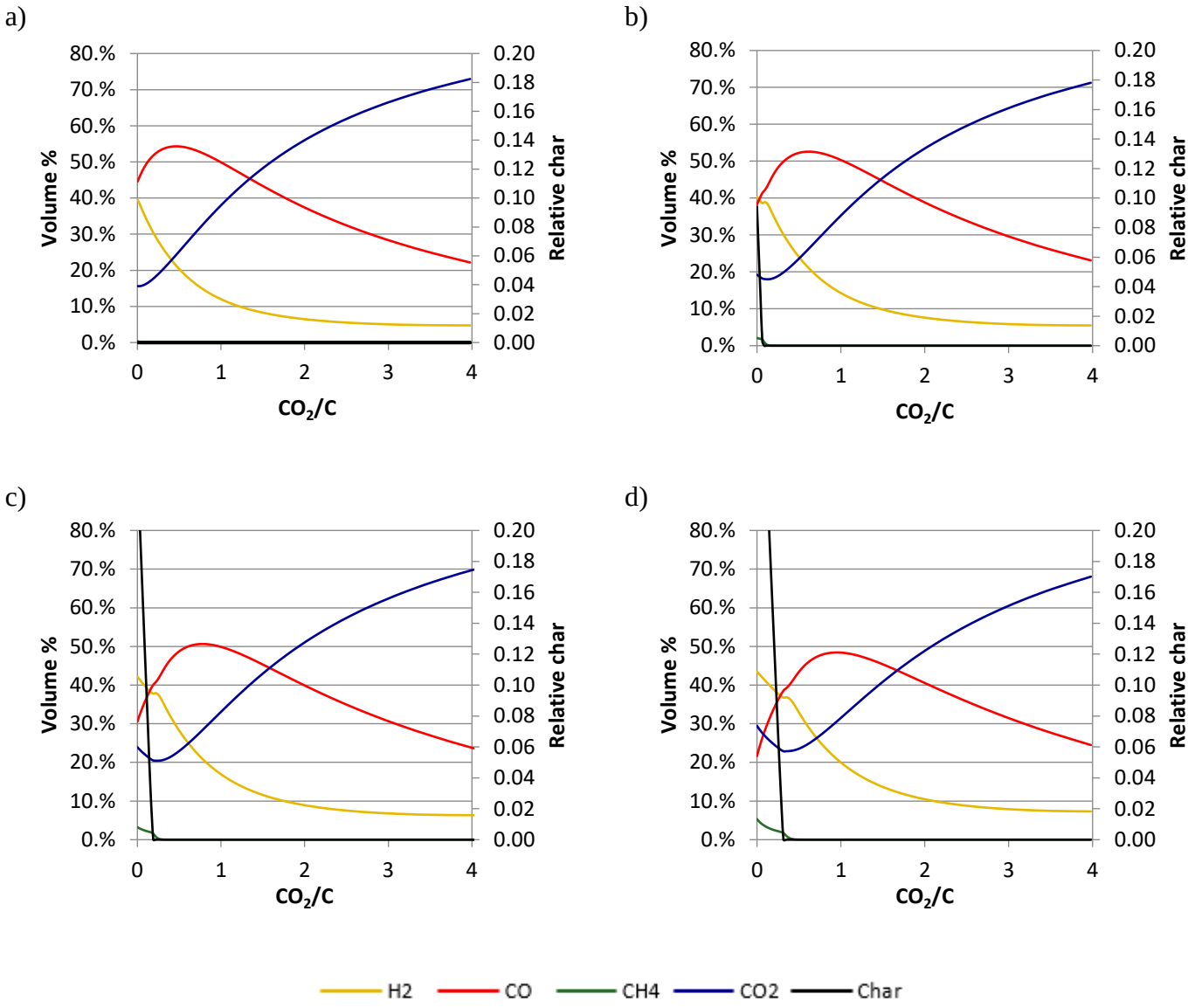

Figure 5-2: Dry syngas composition and residual char for gasification with oxygen and recycled exhaust gases at O_2 equivalence ratios of (a) λ=0.30, (b) λ=0.25, (c) λ=0.20, and (d) λ=0.15 in an ideal IOGC.

Although the cycle model determines the peak equilibrium temperature reaches 1560°C at a recycling ratio of CO_2/C=0.850, syngas dilution with excess CO_2 limits the relative percentage of CO content in the syngas to 51.69% at this point. Regardless of this dilution effect, the total amount of CO produced through gasification continues to increase due to concentration-based shifts, even as the equilibrium temperature cools slightly (see Figure 5-5). In effect, the amount of CO produced increases from an initial 0.737 moles CO/mole of biomass carbon (molCO/molC_{bio}) without CO_2 recycling to a maximum of 1.204 molCO/molC_{bio} at a recycling ratio of CO_2/C=2.322 (see Figure 5-5). Since this means more CO is produced from the gasifier than carbon is supplied through the feedstock, it must be concluded a portion of the recycled CO_2 is being converted to CO through the reverse Boudouard, reverse water-gas shift, and reforming reactions. As further evidence of the enhancement of the reverse water-gas shift reaction, total H_2 production sees an

associated decrease from 0.656 molH_2/molC_{bio} to 0.205 molH_2/molC_{bio} over the corresponding range of exhaust recycling ratios. Indeed, the trends of H_2 and CO production shown in Figure 5-5 are clearly indicative of the combined temperature and concentration effects of exhaust recycling on the gasifier. This includes a distinct inflection of species production at the carbon boundary for lower equivalence ratio cases. Leading up to the carbon boundary, exhaust recycling yields increased feedstock conversion which generates more of each species. Beyond the carbon boundary, the temperature (Figure 5-4) and CO_2 concentration changes explained above contribute to the decreasing H_2 and increasing CO trend until the CO_2 dilution in the system creates colder gasification temperatures that then reverse these trends as the gasification thermodynamics change.

Previous studies have shown CO_2 gasification enhances feedstock carbon conversion at lower equivalence ratios [83, 95, 78]. Figure 5-2 shows that this is also evident here for several additional cases at lower O_2 equivalence ratios. While other trends in species production are similar to the reference $\lambda = 0.30$ case, lower equivalence ratios initially resulted in lower CO content, higher H_2 and CH_4 content, and residual chars when CO_2 was not recycled to the gasifier. As exhaust is recycled to the gasifier, the char content drops very quickly due to the thermodynamic enhancement of the reverse Boudouard reaction. Both increasing equilibrium temperatures and increasing amount of CO_2 present in the system contribute to this char reduction effect. Of course, some differences from this thermodynamic case may exists in real gasification systems. Chapters 2 and 3 clearly discuss this aspect of thermodynamic modelling. Although a real gasification system under these exhaust recycling conditions may experience some char residual, this study shows there is a sufficient thermodynamic potential to influence the chemical equilibrium conditions to make residual char production an unfavourable product when a certain amount of exhaust recycling is provided to the gasifier.

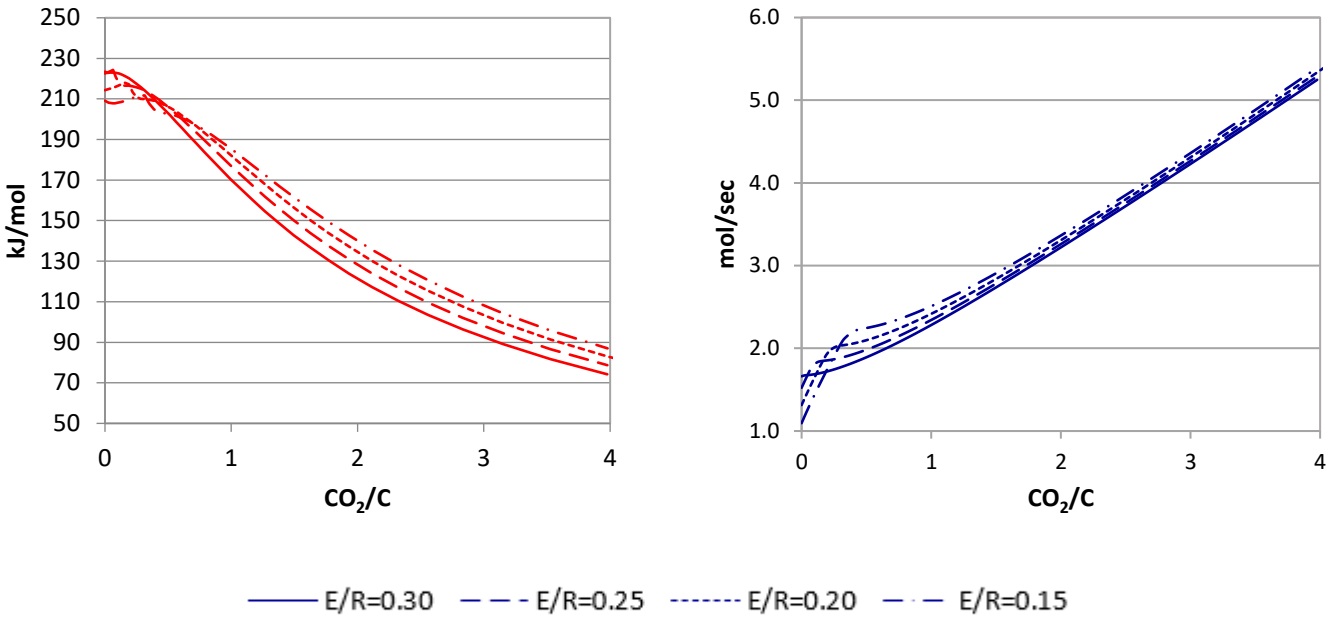

Figure 5-3: LHV (left) and total production (right) of dry syngas at different equivalence ratios in an ideal IOGC.

Trends in total syngas production and LHV (Figure 5-3) reflect the previously discussed developments in molecular composition. In general, recycling exhaust CO_2 increases the total molar yield of syngas while reducing the LHV due to the aforementioned dilution effect caused by the addition of more CO_2 gasifying agent to the gasifier. At lower recycling ratios, small increases to LHV are caused by the enhancement of CO production. This effect is most evident for low equivalence ratios due to the increased char conversion explained earlier, although the dilution effect dominates beyond the carbon boundary point. Similarly, the enhanced char conversion is shown by higher increases in gas production rates leading up to the carbon boundary. Effectively, the combination of syngas production rate and LHV constitutes the combustion energy available in the gas output from the gasifier. This quantity is reflected in the gasifier CGE (Figure 5-6).

Temperature profiles of the engine exhaust and gasification equilibrium condition (Figure 5-4) show the contribution of waste heat recycling within the system. Since exhaust temperatures are maintained above the gasifier temperature for these scenarios, recycling exhaust gases contributes a net source of sensible heat to increase the gasifier equilibrium temperature. This effect is particularly beneficial for gasification at lower equivalence ratios. Under these conditions, the initial exhaust recycling has sufficient available heat content to allow for a modest increase in equilibrium temperatures even as the thermal energy requirements of gasification intensify from the promotion of the highly endothermic reverse Boudouard reaction. Beyond the point of complete char conversion, the heat from recycled exhaust continues to drive augmentation of the equilibrium

temperature for moderate amounts of exhaust recycling. Eventually, CO_2 dilution of the syngas causes the combustion and exhaust temperatures to fall, leading to a corresponding decrease in the equilibrium temperatures. This effect also emphasises the thermodynamic coupling between the engine and gasifier within the complex system since the syngas equilibrium point is sensitive to the exhaust temperature which in turn is dependent on the properties of the syngas.

While these observations hold across all equilibrium ratio cases considered, lower equivalence ratios nevertheless lead to lower equilibrium temperatures for the same amount of exhaust recycling. This effect is due to the restricted availability of oxygen within the gasifier which limits the formation of low (or negative) enthalpy species like CO_2 and H_2O, causing the thermodynamic energy balance to settle on a milder temperature. However, once sufficient exhaust is recycled to fully convert the fuel's carbon content then the resulting exhaust temperatures for the low equivalence ratio cases remain hotter than for higher equivalence ratio cases at the same recycling ratio. Effectively, by using the exhaust waste heat in the gasifier to enhance the carbon conversion process instead of supplying additional oxygen, more calorific species are produced than in the higher equivalence ratio cases (see Figure 5-5), allowing for comparatively higher combustion and exhaust temperatures.

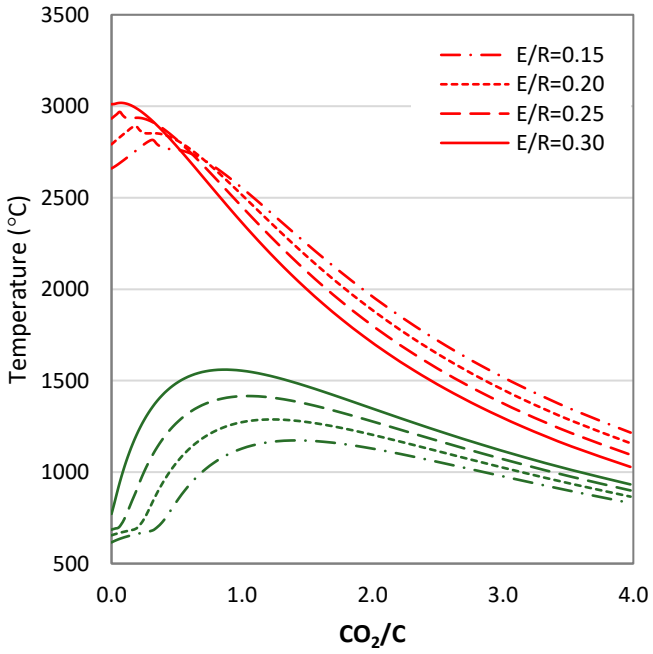

Figure 5-4: Exhaust (red) and gasifier (green) temperatures for different O_2 equivalence ratios in an idealised cycle

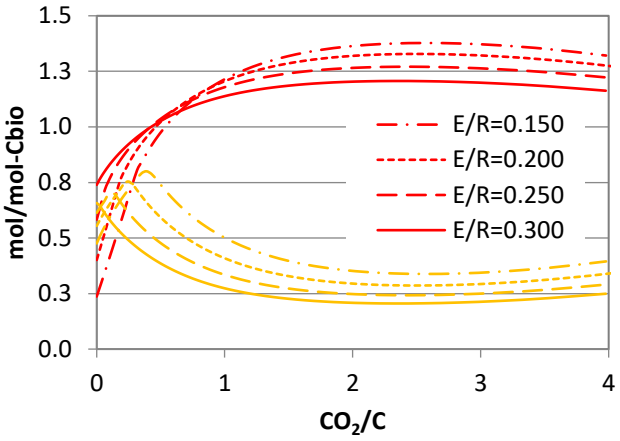

Figure 5-5: Equilibrium production of CO (red) and H_2 (yellow) species in mol/mol-C_{bio} at different equivalence ratios.

Considering the overall impact of exhaust recycling and equivalence ratios studied, Figure 5-6 illustrates the trends in cold gas efficiency (CGE) and indicated system efficiency determined from the model. For the reasons previously discussed, all cases show recycling exhaust gases has a beneficial effect on the CGE due to both the conversion of some recycled CO_2 into additional CO as well as the addition of allothermal heat. This effect becomes even more pronounced for low equivalence ratios that use the additional heat to supplement the lower O_2 inputs, allowing for further production of calorific species. Under some conditions, conversion of recycled CO_2 into CO results in CGE values exceeding 100%, further indicating the formerly inert species are converted into a useful fuel thanks to the high equilibrium temperatures enhancing the CO_2 conversion reactions. As the CO_2 gasifying agent is converted into a combustible fuel, the available combustion heat content of the syngas increases accordingly. When this additional fuel augments the total available energy content of the syngas to be greater than the original combustion energy content of the feedstock, the calculated CGE would exceed 100%. This may seem counter-intuitive, however the CGE calculation does not account for the additional allothermal heat that drives these CO_2 conversion reactions. In this way, the CGE is not a true efficiency but rather a simple comparison of syngas heating potential to the biomass heating potential at standard temperature. Thermodynamic simulations with CGE values exceeding 100% have previously been reported in the literature [61, 91].

A further explanation of how this gasification case contributes to a syngas with higher heating potential than the supplied feedstock arises from comparing the combustion heat of each elemental component of the feedstock to the corresponding products of gasification. Considering the feedstock carbon content could generate up to 393.5 kJ/mol of heat upon combustion at standard conditions, when it instead is used with recycled CO_2 in the reverse

Boudouard reaction, two moles of CO are produced. Together, they are capable of a combined heat release of 566 kJ upon combustion (i.e. 283 kJ/mol for each of these two moles), increasing the potential heat release by 172.5 kJ for each mole of biomass carbon converted in this way. Similarly, the reverse WGS reaction has a small benefit to increasing the energy content of the syngas beyond the potential heat content of the feedstock by allowing some of the biomass hydrogen to convert the recycled CO_2 into CO. This causes a net increase in combustion heat of 41.2 kJ for each mole of biomass H_2 consumed. Again, the thermodynamic heat requirements to drive these endothermic reactions is partially supplied by the allothermal heat recycled from the engine in the exhaust gases, a phenomenon not captured in the standard calculation of CGE.

These CGE trends are also evident in the indicated system efficiency, however some thermodynamic limitations in the power cycle realise diminishing returns at higher degrees of exhaust recycling. Since syngas produced at higher recycling ratios becomes diluted with a build-up of CO_2, lower combustion temperatures and thus peak Otto cycle pressures are achieved. Expansion across a fixed volumetric compression ratio starting from a lower pressure will generate less indicated work, reducing the overall efficiency of the Otto cycle. Nevertheless, peaks in overall indicated system efficiencies show the thermodynamic conditions where the interrelated gasification equilibrium conditions, engine combustion conditions, and exhaust conditions are optimised. While exhaust recycling for the reference $\lambda = 0.30$ case with an indicated system efficiency of 37.7% only modestly improved the indicated system efficiency to 38.7% when 0.723 molCO_2/molC are recycled to the gasifier, a marked increase in indicated system efficiency up to 46.6% at a recycling ratio of 1.171 molCO_2/molC is observed for the $\lambda = 0.15$ case. By combining the cycle efficiency with the known LHV of the feedstock, reported in Table 4-1, the system outputs can be compared in terms of specific work output. The effect of exhaust recycling increased the specific cycle work from 1.746 kWh/kg_{feed} for the reference case to 2.158 kWh/kg_{feed} for the peak efficiency case discussed above.

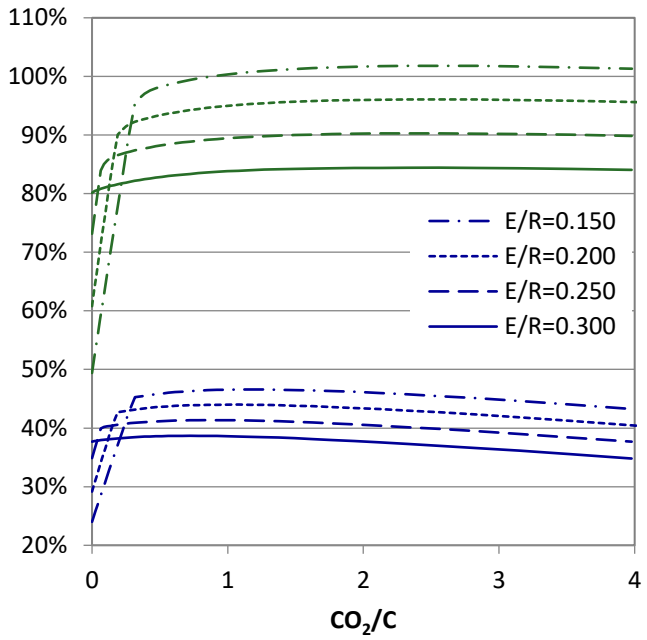

Figure 5-6: CGE (green) comparing syngas heat content to feedstock heat content and indicated system efficiency (blue) comparing indicated cycle work to feedstock heat content for different O_2 equivalence ratios in an idealised cycle

5.3.2 Limiting Combustion Temperature

While the previous analysis has described the overall processes leading to thermodynamic enhancements of biomass gasification using recycled exhaust gases, some consequences of assuming an ideal model will impact the thermodynamic conditions of the simulation. Of particular importance to oxyfuel combustion systems, the combustion temperatures under stoichiometric conditions are unrealistically high for many of the modelling cases considered. For example, the adiabatic flame temperature of a stoichiometric oxyfuel mixture of H_2 and CO at atmospheric pressure exceeds 4300°C. Under the conditions analysed for the Otto cycle, this combustion temperature is calculated to exceed 6000°C for low recycling ratios, well beyond the material limits for conventional engine mechanical components.

Typical engine operating conditions do experience combustion temperatures that are often above the thermal limits of their mechanical components, however these peak conditions are present only over short time intervals and engine coolant systems are designed to remove excess heat to maintain material temperatures within a safe tolerance. Nevertheless, stoichiometric oxyfuel combustion is understood to be impractical for this reason. A lower combustion temperature is therefore specified for the system model. While an exact temperature specification would depend on detailed engine cylinder design criteria, a reasonable assumption of a 1927°C (2200K) limit is implemented based on a

conservative approximation of the adiabatic flame temperatures of stoichiometric syngas and air mixtures which can exceed 2000°C. Although somewhat arbitrary, adoption of this fixed combustion temperature limit will nonetheless provide a useful system-level comparison to the original analysis of the ideal system with an unrestricted combustion process.

Control of the combustion temperature in the model is provided by using local engine exhaust gas recycling to dilute the stoichiometric oxyfuel intake mixture. This is achieved by diverting a fraction of the exhaust stream to the intake mixture using line EGR-E, shown in the system schematic presented in Figure 5-1. An iterative Fortran loop adjusts the recycled fraction of the engine exhaust until the desired combustion temperature is achieved.

While Figure 5-7 shows the general trends in H_2 and CO_2 concentrations are similar to the original scenarios (cf. Figure 5-2), syngas CO content is markedly different under the limited combustion temperature regime. Concentrations of CO always decrease, regardless of exhaust recycling. CO_2 content is also comparatively higher for low recycling ratios than in the previous cases, indicating the CO_2 conversion reactions are not as effective under these operating conditions.

The principal effect driving these composition changes is the reaction temperatures calculated under the new combustion dilution modelling regime, as shown in Figure 5-8. By limiting the combustion temperature, the engine exhaust temperatures do not have the variation as in the previous case (cf. Figure 5-4). Exhaust recycling to the gasifier only causes moderate changes in the exhaust temperatures, rising from ~875°C – 925°C. Correspondingly, the gasification equilibrium temperatures are cooler under this modelling condition since less heat is returned to the gasifier in the exhaust stream. Although the numerical methods controlling peak combustion temperature have induced small amounts of variability in the exhaust temperatures, these artifacts have limited effect on the resulting gasification temperature. The principal trends in gasification temperature are predominantly influenced by the recycled allothermal heat and the enhancement of the endothermic char reactions leading up to the carbon boundary in the lower equivalence ratio cases.

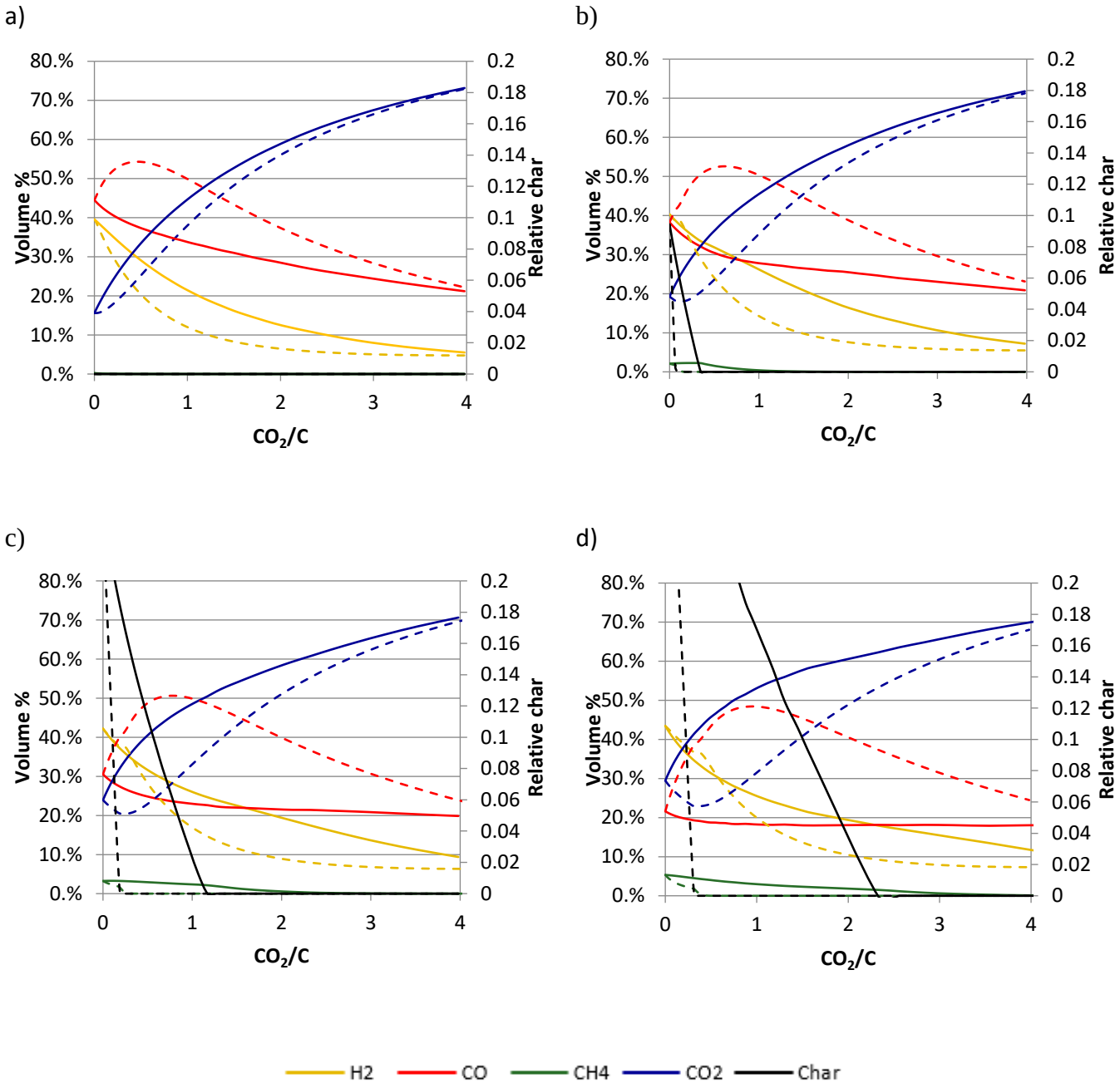

Figure 5-7: Dry syngas composition and residual char for gasification with oxygen and recycled exhaust gases at O_2 equivalence ratios of (a) λ=0.300, (b) λ=0.250, (c) λ=0.200, and (d) λ=0.150 in an ideal IOGC using local engine EGR to limit combustion temperatures to 2200K. Dashed lines represent previous data from the ideal IOGC without combustion temperature controls for comparison (c.f. Figure 5-2).

These comparatively lower reaction temperatures will induce shifts in the gasification equilibrium conditions that limit the achievable extent of the reactions that convert CO_2 into syngas species. Table 5-1 demonstrates this effect for several selected scenarios by comparing the equilibrium constants of the reverse Boudouard ($K_{p.1}$), reverse WGS ($K_{p,2}$), and methane dry-reforming ($K_{p.3}$) reactions calculated at the corresponding equilibrium temperatures determined based on equivalence and recycling ratios. The equilibrium constants highlight how sensitive these reactions are to the gasifier temperature and are calculated from fundamental thermodynamic principles as $K_p = \exp(-\Delta G_r/RT)$. For

reference, equilibrium constants calculated at 1000°C are also given since most simulations under the previous, ideal modelling conditions resulted in equilibrium temperatures above 1000°C. Because the reactions are endothermic, the equilibrium constants will be larger at higher temperatures and vice versa for the lower temperature conditions. Variations in equilibrium temperature across these cases range from ~580°C - 850°C but the resultant equilibrium constants range across orders of magnitude. As the equilibrium constants decrease, reactant species are thermodynamically favoured over the product species. Considering this temperature shift in equilibrium constants for the reverse Boudouard reaction explains the difference in CO, CO_2, and char residuals compared to the original suite of simulations. Similarly, the temperature effect on the equilibrium constants of the reverse water-gas reaction also influences the CO and H_2 content of the syngas. Although the dry reforming reaction remains favourable for most conditions, under the cooler reaction conditions at low equivalence ratios the small equilibrium constants contribute to the presence of CH_4 in the syngas, albeit at low concentrations.

Table 5-1: Equilibrium constants for reverse Boudouard (1), reverse water-gas shift (2), and methane dry-reforming (3) reactions under exhaust recycling ratios at corresponding gasifier temperatures for an ideal IOGC using local engine EGR to limit combustion temperatures to 2200K.

λ	CO_2/C	Temp (°C)	$K_{p,1}$	$K_{p,2}$	$K_{p,3}$
0.30	0	771.7	4.42×10^{0}	8.79×10^{-1}	6.56×10^{1}
0.30	1.08	809.5	8.72×10^{0}	1.00×10^{0}	1.88×10^{2}
0.30	3.15	847.5	1.65×10^{1}	1.14×10^{0}	5.03×10^{2}
0.25	0	685.8	7.66×10^{-1}	6.21×10^{-1}	4.42×10^{0}
0.25	1.00	660.3	4.27×10^{-1}	5.52×10^{-1}	1.80×10^{0}
0.25	3.16	746.2	2.71×10^{0}	7.98×10^{-1}	3.09×10^{1}
0.20	0	654.7	3.74×10^{-1}	5.37×10^{-1}	1.47×10^{0}
0.20	0.97	603.2	1.02×10^{-1}	4.13×10^{-1}	2.00×10^{-1}
0.20	3.15	657.2	3.97×10^{-1}	5.44×10^{-1}	1.61×10^{0}
0.15	0	616.0	1.43×10^{-1}	4.42×10^{-1}	3.36×10^{-1}
0.15	1.07	580.8	5.51×10^{-2}	3.64×10^{-1}	7.82×10^{-2}
0.15	3.15	593.9	7.93×10^{-2}	3.92×10^{-1}	1.36×10^{-1}
		1000	1.43×10^{2}	1.72×10^{0}	1.44×10^{4}

Despite the temperature-based influence on the equilibrium conditions, the addition of excess CO_2 from the recycled exhaust still contributes to concentration-based shifts to the

gasification reactions. As before, this phenomenon allows for full carbon conversion to occur in the low equivalence ratio gasification cases. The previously noted temperature effects do reduce the effectiveness of the char reduction process since higher recycling ratios are required in these cases compared to the previous modelling conditions, with the $\lambda = 0.15$ condition requiring at least 2.325 molCO_2/molC recycled to fully convert the biomass carbon content. Further consequences of these concentration-based effects are seen as the initial equilibrium temperature decreases for low equivalence ratio cases. Even though sensible exhaust heat is introduced to the gasifier from the recycled exhaust, the excess CO_2 driving the endothermic reverse Boudouard reaction dominates the equilibrium condition and forces this slight decrease in temperature.

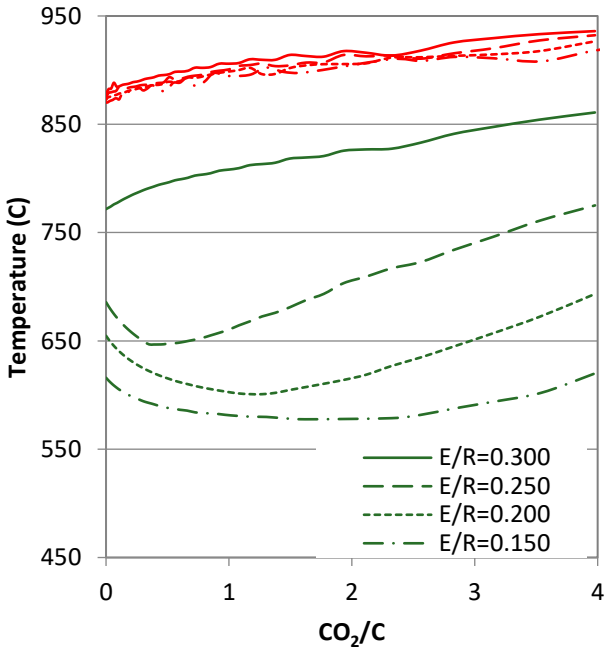

Figure 5-8: EGT (red) and gasifier equilibrium temperature (green) for different O_2 equivalence ratios in an idealised cycle with local engine EGR to limit combustion temperature to 2200K.

Indicated system efficiencies (Figure 5-9) have similar characteristics to the previous cases (cf. Figure 5-6) but with an observed stretch to the right, demonstrating that the equilibrium conditions are more strongly influenced by the concentration-based shifts requiring higher recycling ratios. The efficiencies are also lower than in the previous cases due to the lower exhaust temperatures not contributing as much allothermal heat to the gasifier. Regardless, gasification enhancements from recycling exhaust gases led to a peak indicated efficiency of 41.29% for the $\lambda = 0.15$ equivalence ratio case with an exhaust recycling ratio of 3.541 molCO_2/molC. This is an improvement over the $\lambda = 0.30$ case which had an indicated system efficiency of 29.18% without exhaust recycling and 35.03% at a recycling ratio of 2.560 molCO_2/molC.

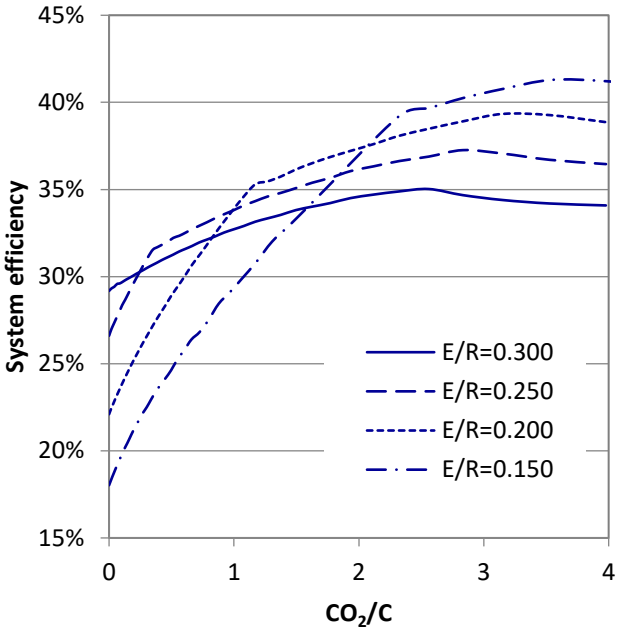

Figure 5-9: Indicated system efficiency for different O_2 equivalence ratios in an idealised cycle using local engine EGR to limit combustion temperature to 2200K.

5.3.3 Detailed engine model analysis

So far, the system analysis has demonstrated the temperature and allothermal heat available in the recycled exhaust gases have a significant impact on the thermodynamic conditions of gasification and thus on the overall system performance. This was particularly evident from the changes observed by limiting the combustion temperature. Given the importance of the exhaust condition, further refinement of modelling methods is required to ensure the engine processes more accurately reflect physical and chemical changes in the working fluid during the power cycle. Additionally, the use of a detailed engine model accounts for heat losses from the engine working fluid.

The IOGC model is adapted with the detailed, time dependent engine model described in Chapter 3 to determine the effect of syngas combustion dynamics and engine heat losses on the system. Combustion temperature control EGR is maintained as before for a maximum combustion temperature of 2200K. Since the focus of this study is to investigate the system-level effects of exhaust recycling rather than a detailed evaluation of the specific engine design, engine parameters of intake temperature and pressure, engine speed, combustion equivalence ratio, and cylinder geometry are fixed for all simulation cases. To maintain these conditions, an iterative Fortran script was used to vary the biomass feed rate to maintain the desired engine operating speed and intake conditions of 2000RPM and 100kPa, respectively.

Syngas mixtures at the calculated equilibrium conditions under these modelling terms are illustrated in Figure 5-10 while the corresponding equilibrium and exhaust temperatures are shown in Figure 5-11. Exhaust temperature range is typically in the 900-950°C range for low to moderate recycling ratios since the peak combustion temperature is held constant using local EGR. As recycling ratios increase beyond ~1 molCO_2/molC, the exhaust temperature tends to drop due to heat losses during the expansion stroke. Beyond a recycling ratio of ~2.5 molCO_2/molC the CO_2 content of the syngas from the gasifier is sufficiently dilute that combustion temperatures no longer reach the specified limit. Local engine EGR is no longer used and the combustion temperatures decrease as the recycling ratio increases further, causing corresponding exhaust temperatures to be cooler.

Low recycling ratios display similar equilibrium properties as shown in the ideal Otto cycle cases, however the decreasing exhaust temperatures limit the available heat supplied in the recycled exhaust as the recycling ratio increases. Char conversion is again enhanced for the low equivalence ratio cases as additional CO_2 and allothermal heat are supplied to the gasifier, however limitations to this effect become apparent at the lowest equivalence ratio. For the λ = 0.15 equivalence ratio case, recycling ratios above 3.155 molCO_2/molC are no longer capable of complete carbon conversion. Since the carbon conversion is primarily dependent on the extent of the reverse Boudouard reaction in this situation, we can attribute this incomplete conversion phenomenon to the low equilibrium temperatures causing a shift to favour the carbon and CO_2 reactants. Syngas produced at these high recycling ratios becomes diluted with excess CO_2, causing low combustion and subsequent exhaust temperatures which limits the degree of allothermal heating in the gasifier from the recycled exhaust. For the secondary carbon boundary here, the exhaust temperature is 755°C and the corresponding equilibrium temperature is 566°C which results in an equilibrium constant of K_p=0.037 for the reverse Boudouard reaction. In concentration-based terms, this means the thermodynamic driving force of the reaction will be neutral when the concentration of CO is 20% that of the concentration of CO_2. While increasing the recycling ratio would increase the concentration of CO_2 in the gasifier, this would not sufficiently compensate for the associated equilibrium temperature drop caused by the high degree of temperature coupling within this system. As previously mentioned in the analysis provided in section 5.3.1, these aspects of syngas production and char conversion indicate the thermodynamic potential of the system configuration studied. An actual gasification system may not be capable of fully achieving these equilibrium conditions and some trace residuals of char may remain.

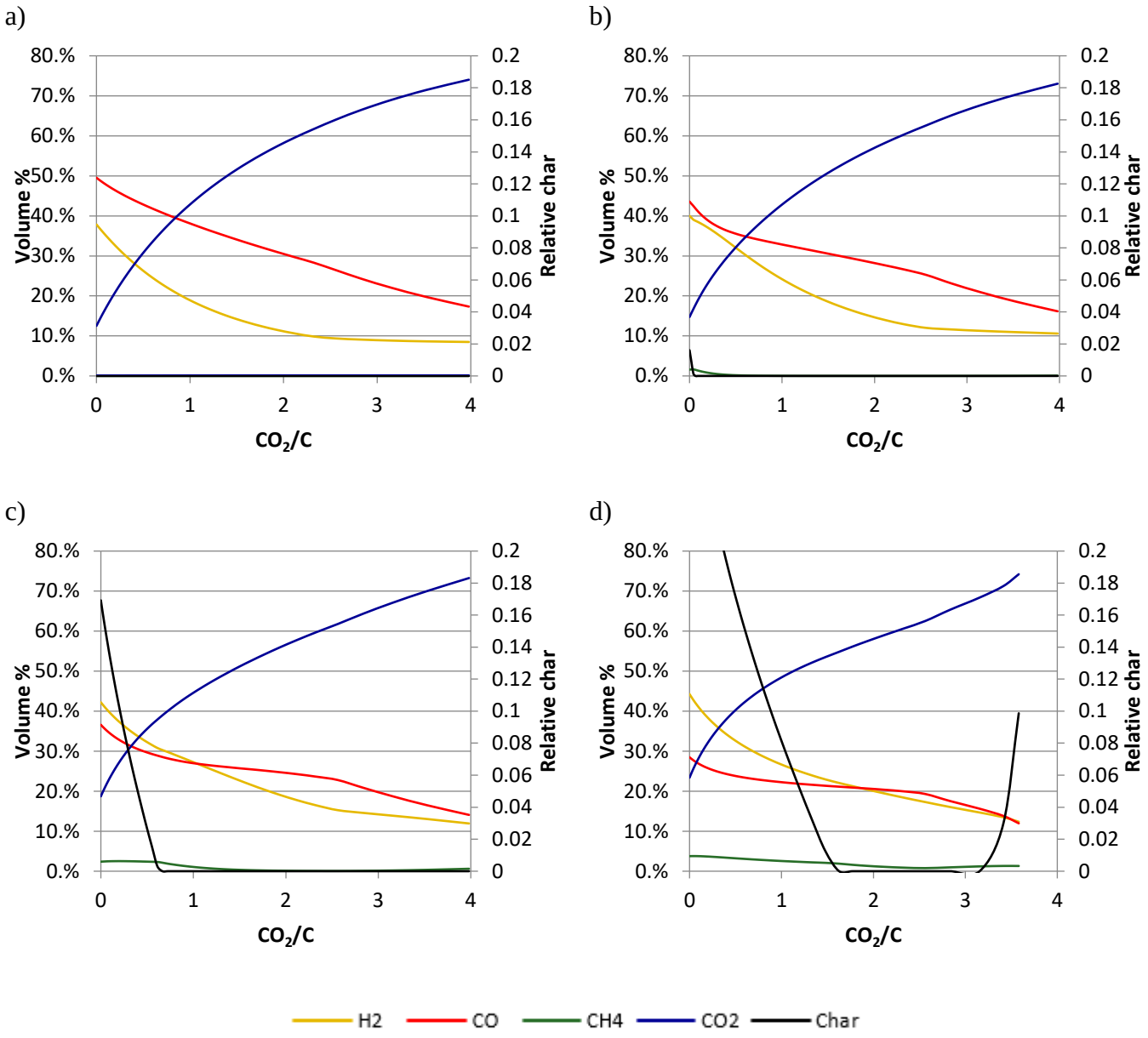

Figure 5-10: Dry syngas composition and residual char for gasification with oxygen and recycled exhaust gases at O_2 equivalence ratios of (a) λ=0.300, (b) λ=0.250, (c) λ=0.200, and (d) λ=0.150 in a detailed IOGC using local engine EGR to limit combustion temperatures to 2200K.

These thermal effects on the gasification equilibrium performance are also reflected in the calculated CGEs shown in Figure 5-12. The typical initial increase in CGE due to enhanced char conversion remains present, though slightly lower efficiencies are observed compared to the ideal case (cf. Figure 5-6). Conditions of incomplete char conversion for the λ = 0.15 equivalence ratio case at recycling ratios above 3.155 molCO_2/molC are also evident from the dramatic decline in CGE. Even in cases where complete carbon conversion is achievable across the range of recycling ratios studied, maximum CGEs are observed in the data. Such points represent the optimum trade off in equilibrium temperatures, allothermal heating, and gasifying agent supply in effectively converting the feedstock to fuel gases.

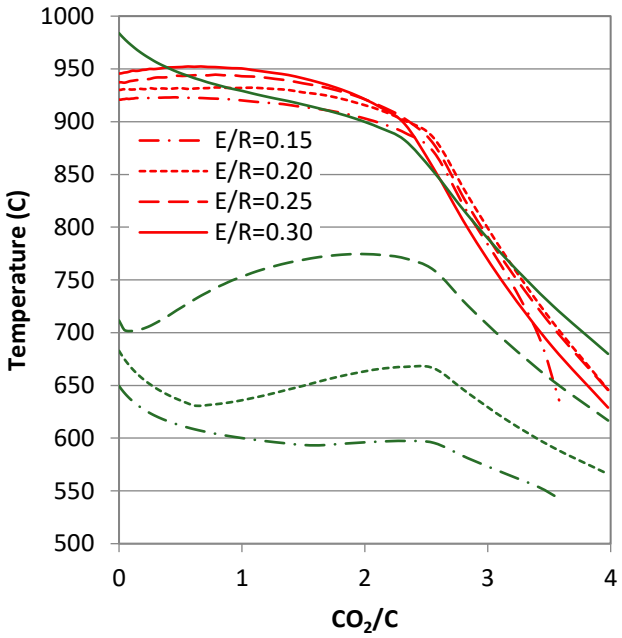

Figure 5-11: EGT (red) and gasifier equilibrium temperature (green) for different O_2 equivalence ratios in a detailed IOGC model with local engine EGR to limit combustion temperature to 2200K.

Similarly, the indicated system efficiencies display corresponding behaviour across the simulated recycling ratios. Efficiency peaks occur at the same recycling ratios that generated the associated CGE maxima. The effect of engine cycle heat losses is pronounced when comparing these efficiencies to the previous ideal cases. For the reference case of an equivalence ratio of $\lambda = 0.30$ without exhaust recycling, the indicated efficiency was merely 16.60%, however recycling 2.560 molCO_2/molC of exhaust to the gasifier increased this efficiency to 23.35%. Again, the ability to use lower equivalence ratios because of exhaust recycling results in even higher indicated efficiencies, reaching 26.89% at an equivalence ratio of $\lambda = 0.15$ and recycling ratio of 2.562 for the cases presented here. In all of these cases it is evident that the use of a detailed model capable of calculating cycle heat losses dramatically reduces the indicated efficiency as a significant portion of the energy supplied in the syngas fuel is lost to the engine coolant.

Another interesting observation is that the points of maximum system efficiency arise under the conditions where local engine EGR is no longer necessary for combustion temperature control. Put another way, CO_2 is useful in these scenarios as both a combustion diluent and gasifying agent but the best system performance is achieved when CO_2 dilution is provided directly in the gasifier rather than separately in an engine EGR loop. This condition arises because the additional high temperature CO_2 diverted to the

gasifier means that more allothermal heat is supplied while simultaneously increasing the CO_2 present in the gasifier to further contribute to concentration-based equilibrium shifts. CO_2 supplied directly to the engine as a diluent will not contribute to these beneficial effects in the gasifier.

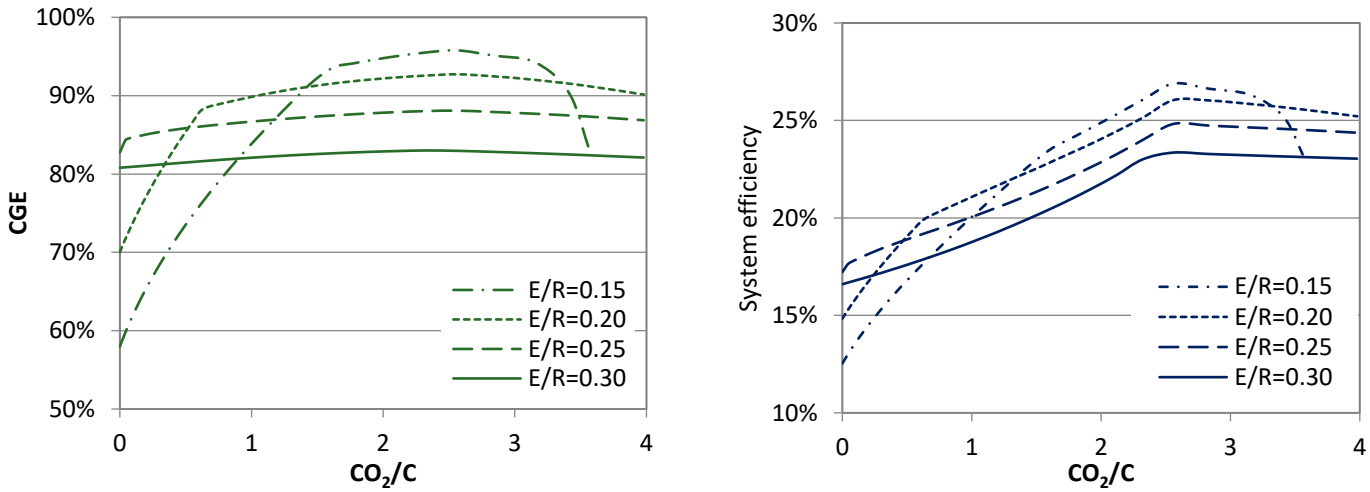

Figure 5-12: Gasification CGE (left) and indicated system efficiency (right) for different O_2 equivalence ratios in a detailed IOGC using local engine EGR to limit combustion temperature to 2200K.

5.3.4 Constant temperature gasification

Given the importance of equilibrium temperatures on the thermodynamic performance of the gasification reactions, additional studies highlight the consequences of operating under isothermal gasification conditions. Thermodynamically, the supply of O_2 to the gasifier has a dominant influence on the equilibrium temperature by allowing for increased formation of low enthalpy gas species products through oxidation reactions. For these following cases, a Fortran script controls the flow of O_2 into the gasifier to provide sufficient direct heating for a desired adiabatic thermodynamic equilibrium temperature. No indirect heat is supplied to the gasifier, only the allothermal heat from the recycled exhaust and the enthalpy changes due to the gasification reactions cause the desired gasifier temperature rise. Detailed engine modelling techniques are again used to simulate the power generation cycle, as previously discussed.

The equilibrium syngas products again show common trends of H_2 and CO production, CO_2 dilution, and improved carbon conversion with increasing exhaust recycling (see Figure 5-13). The general trends are quite similar to the previous constant equivalence ratio cases while showing the same differences compared to the idealised systems presented earlier, particularly the CO content of the syngas. One distinct feature of the constant temperature cases compared to the constant equivalence ratio cases is the increase in CO

concentration for low equivalence ratio cases at recycling ratios below the carbon boundary. Due to the isothermal conditions, the equilibrium constants of the gasification reactions will remain unchanged thus all changes to the syngas mixture are due to the concentration-based shifts caused by the varying amounts of gasifying agents supplied. In the incomplete carbon conversion regions, increasing the CO_2 supply will push the equilibrium concentrations of the reverse Boudouard reaction to generate the higher CO concentrations observed. Although the temperatures remain constant during this process, the O_2 requirements (Figure 5-14) of the gasifier display a sharp increase in demand to satisfy the higher thermodynamic inputs demanded by this enhanced endothermic reverse Boudouard reaction.

A clear representation of the thermodynamic needs of the gasification reactions is shown in the equivalence ratios required to maintain the reaction temperatures, as illustrated in Figure 5-14. As previously discussed, the additional CO_2 introduced in the recycled exhaust enhances the endothermic char conversion reactions which creates a stronger thermodynamic load on the system. Allothermal heat recycled in the exhaust stream is not sufficient to meet this thermodynamic requirement since the combustion temperatures, and therefore the exhaust temperatures in turn, are limited. To compensate for the increased thermal demand, additional O_2 is supplied which increases the equivalence ratio in the gasifier. Beyond the carbon boundary, allothermal exhaust heating increases with recycling ratio, acting to supplement the thermal requirements of gasification and allowing for a modest decrease in the equivalence ratio needed to maintain the equilibrium temperature. This condition continues until the syngas dilution under larger recycling ratios lowers the exhaust temperatures, reducing the sensible heat available in the recycled exhaust stream. To compensate for the loss in allothermal heat in these cases, the equivalence ratio must therefore rise as additional O_2 is supplied to maintain the desired reaction temperature.

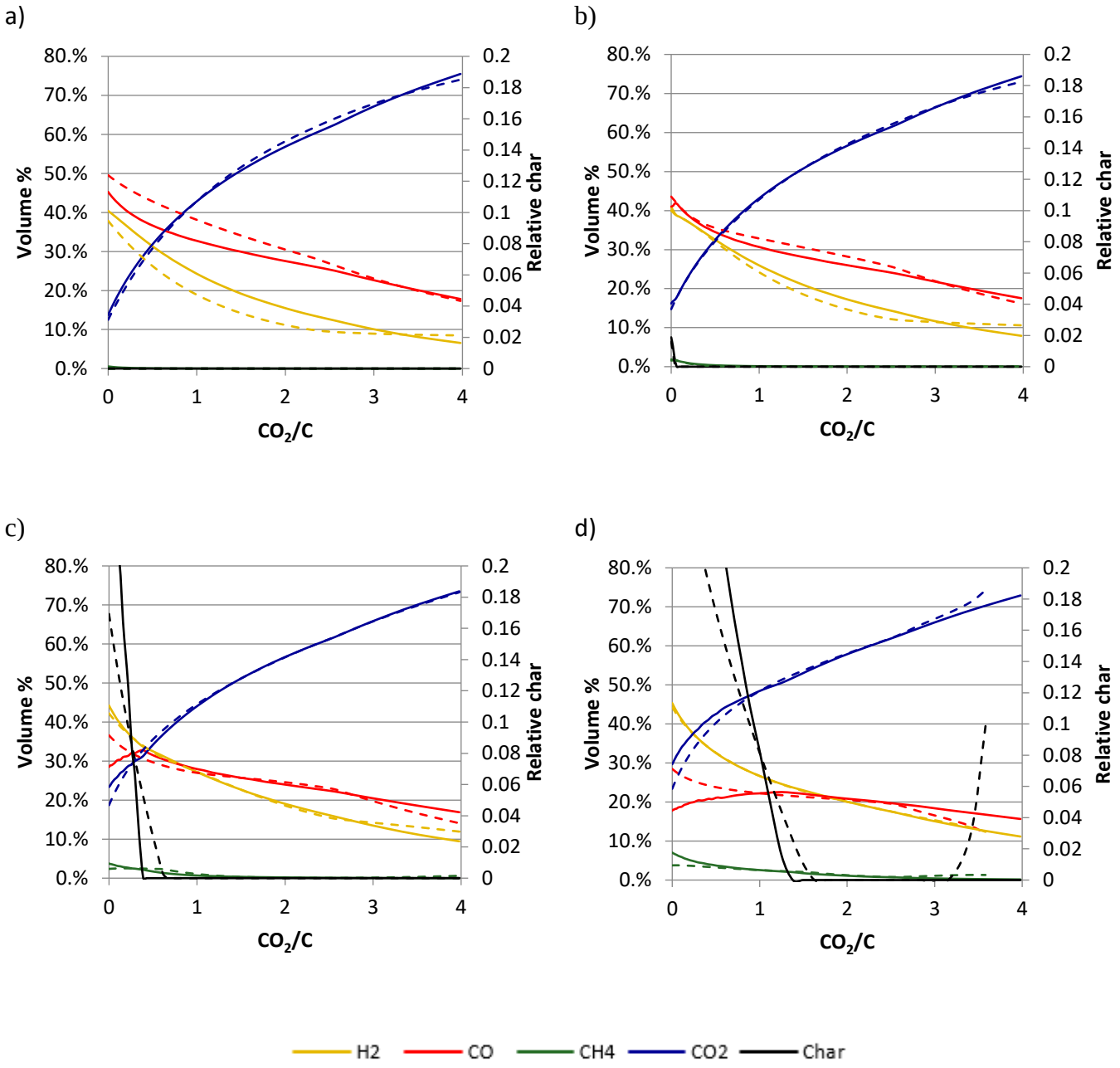

Figure 5-13: Dry syngas composition and residual char for gasification with oxygen and recycled exhaust gases at equilibrium temperatures of (a) 750°C, (b) 700°C, (c) 650°C, and (d) 600°C in a detailed IOGC using local engine EGR to limit combustion temperatures to 2200K. Dashed lines represent previous constant equivalence ratios for comparison at a) E/R=0.30, b) E/R=0.25, c) E/R=0.20, and d) E/R=0.15.

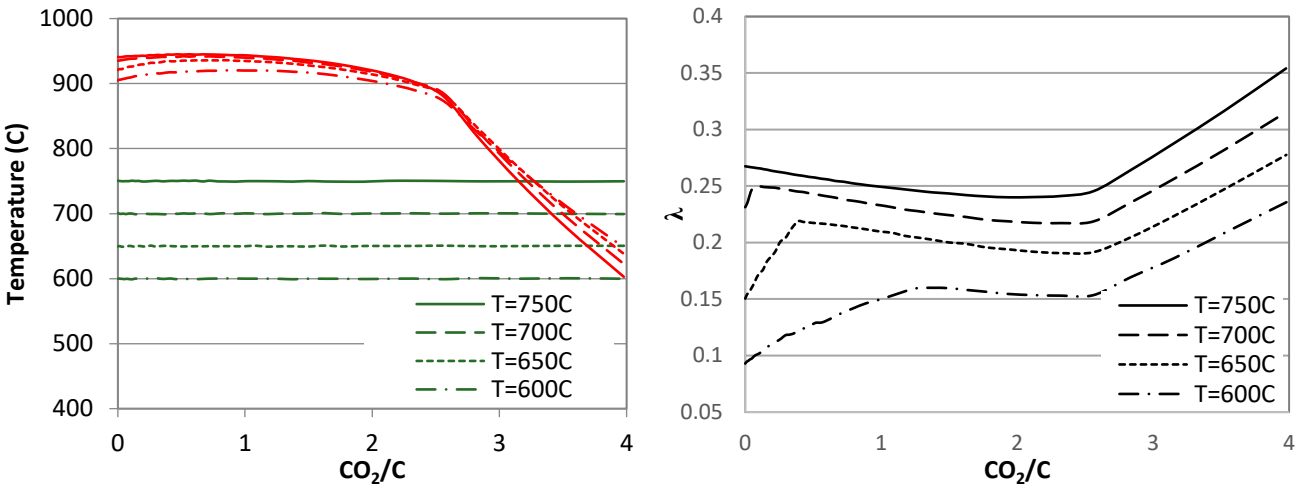

Figure 5-14: EGT (red) and gasifier equilibrium temperature (green) alongside required equivalence ratio (black) for selected gasification equilibrium temperatures in a detailed IOGC model with local engine EGR to limit combustion temperature to 2200K.

System efficiencies for the isothermal cases display similar qualitative features as the constant equivalence ratio cases, as seen in Figure 5-15. Again, the best system performance is achieved when the required syngas dilution for combustion temperature control is achieved in the gasifier rather than using a local EGR loop in the engine cycle. This ultimately results in the system efficiency of a 750°C gasification process rising from 17.35% to 24.97% when 2.561 molCO_2/molC are recycled to the gasifier. Lower temperature gasification at 600°C produced an indicated system efficiency of 26.88% at a recycling ratio of 2.562 molCO_2/molC. While it is obvious that the similar trends in the efficiencies of these isothermal cases are caused by the same processes discussed in the constant equivalence ratio cases, some minor distinctions offer insight to the consequences of the isothermal gasification cases. Interestingly, we can see the decreasing system efficiencies beyond the maxima appear more pronounced than in the constant equivalence ratio cases. Rather than the temperature-driven changes that caused this behaviour in the previous cases, this efficiency loss is due to the higher O_2 levels required to maintain the equilibrium temperature in the gasifier. Effectively, a larger percentage of the feedstock is converted into non-calorific CO_2 and H_2O due to these increased O_2 levels which lower the CGE and thus the overall efficiency.

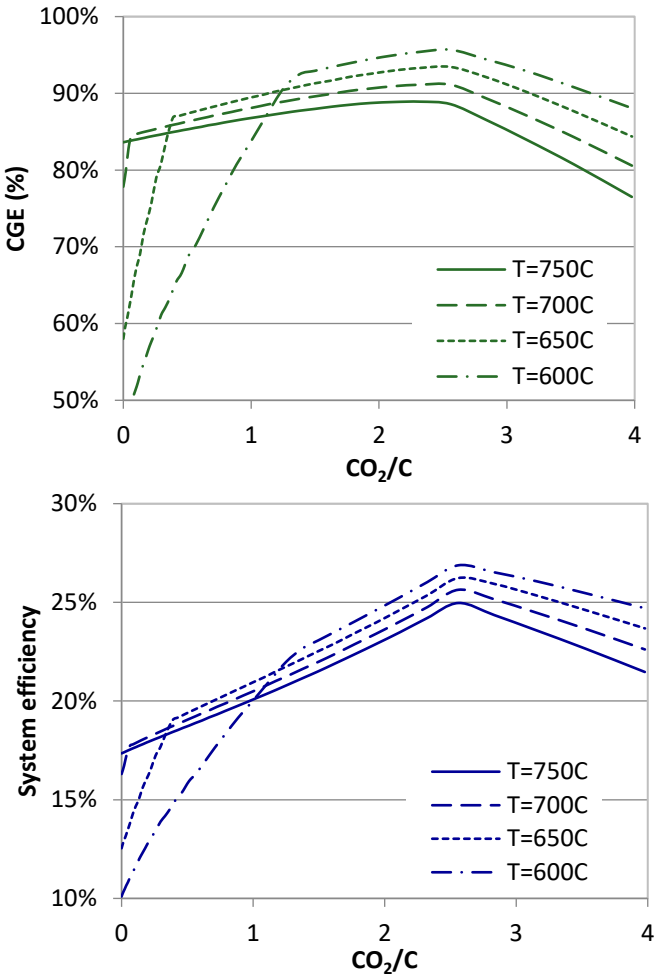

Figure 5-15: Gasifier CGE (top) and indicated system efficiency (bottom) for selected gasification equilibrium temperatures in a detailed IOGC model with local engine EGR to limit combustion temperature to 2200K.

5.3.5 Limiting Thermodynamic Conditions

The importance of exhaust temperatures, allothermal heating, equivalence ratios, and recycled CO_2 has been demonstrated for the systems studied. Observed trends indicate the systems capable of fully converting the feedstock carbon content at the lowest possible temperature and lowest possible equivalence ratio allow the greatest proportion of the biomass to be converted into fuel species in the syngas. This is what contributes to the best CGE and indicated system efficiency. Indeed, the trade-offs between reaction temperature, recycling ratio, and equivalence ratio suggests a thermodynamically limited case exists that will minimize the O_2 requirements and equilibrium temperature.

To highlight this condition, two simulations are analysed to illustrate the limits of equivalence ratio and reaction temperature (see Figure 5-16). For a constant equivalence ratio of $\lambda = 0.130$, full carbon conversion is only possible as recycling ratios range from

2.325 – 2.562 molCO$_2$/molC. Below this recycling ratio, there is insufficient gasifying agents to drive the conversion reaction at the calculated equilibrium temperatures while higher recycling ratios will cause the equilibrium temperature to fall too low to allow for full conversion, below 576°C in this case. Similarly, an isothermal gasification case that maintains the gasification equilibrium temperature at 576°C requires a minimum 2.562 molCO$_2$/molC of recycled exhaust to achieve complete carbon conversion. Beyond this point, increasing the recycling ratio requires increasingly greater equivalence ratios to maintain the desired equilibrium temperature.

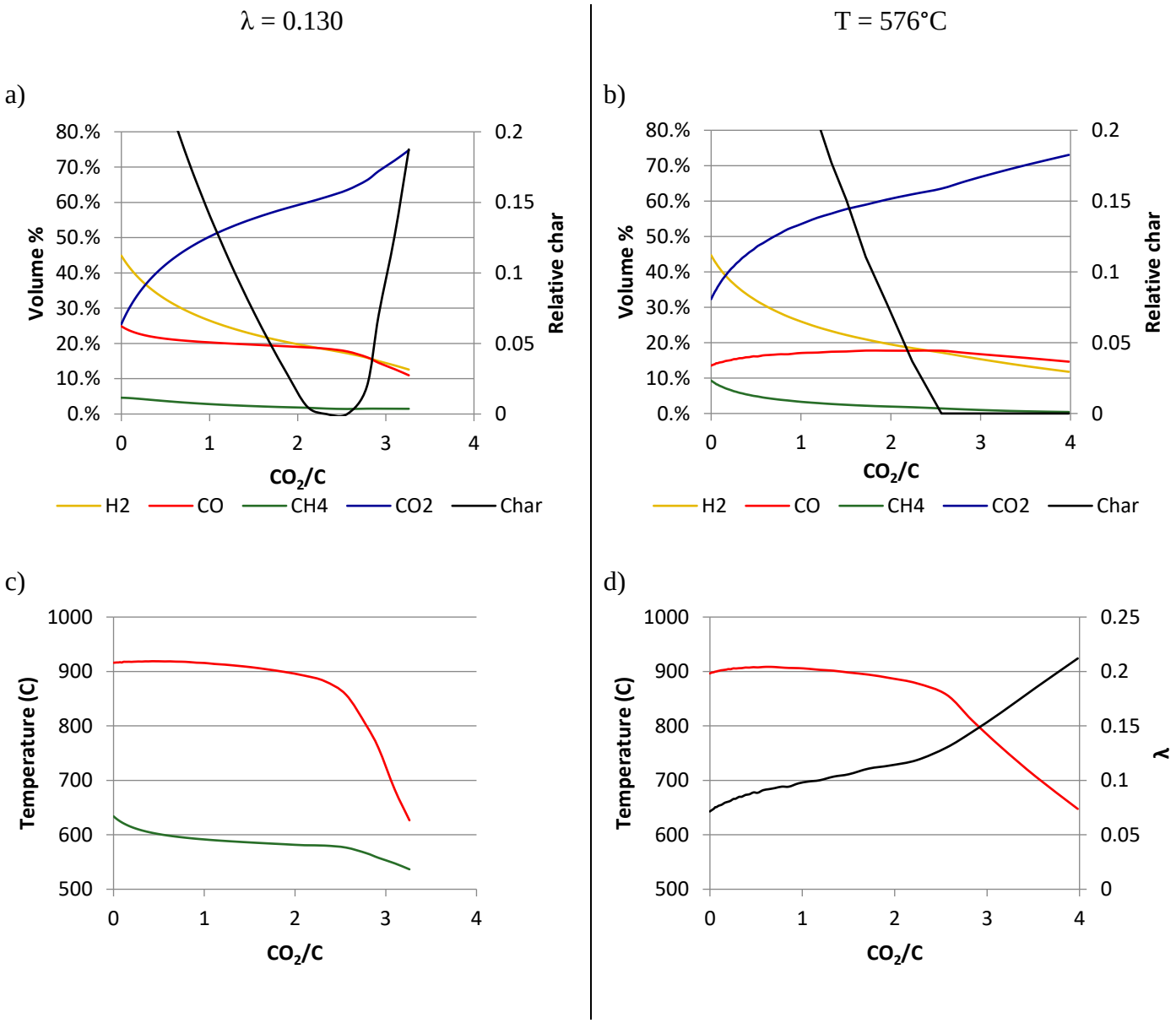

Figure 5-16: Equilibrium conditions for thermodynamically limited gasification with oxygen and recycled exhaust gases showing dry syngas composition and residual char at a) equivalnce ratio of λ=0.130 and b) isothermal temperature 576°C with c) exhaust temperature (red) and equilibrium temperature (green) for the equivalnce ratio of λ=0.130 case and (d) exhaust temperature (red) and equivalence ratio (black) for the isothermal temperature 576°C case.

Since these cases represent the thermodynamic limit of the gasification process for the system configuration studied, the CGE and indicated system efficiency maxima occur at the same recycling conditions of 2.562 molCO_2/molC for both. At this point, both models calculated an indicated cycle efficiency of 26.92%.

The low oxygen equivalence ratio of $\lambda = 0.13$ associated with this limit is remarkable when compared to traditional methods of air/oxygen gasification which typically require an equivalence ratio between 0.2 – 0.3 [42]. However, an important distinction to make here is that this integrated system uses a co-gasification process of both oxygen and CO_2, thus the lower oxygen content of the gasifying mixture is offset by the introduction of additional CO_2 gasifying agent to react with the feedstock. Furthermore, many air/oxygen gasification systems leverage the inherent exothermicity of the oxidation reactions to create a locally autothermal gasification process. Analysis of this integrated recycling system shows that waste heat contained in the engine exhaust returned to the gasifier provides sufficient allothermal heat to satisfy the thermodynamic requirements for complete gasification. Nevertheless, these simulations represent a system-level assessment of theoretical thermodynamic equilibrium gasification conditions. There are additional design-specific aspects of a real gasifier like heat losses, geometry, and chemical kinetic effects which may cause deviations from the equilibrium case.

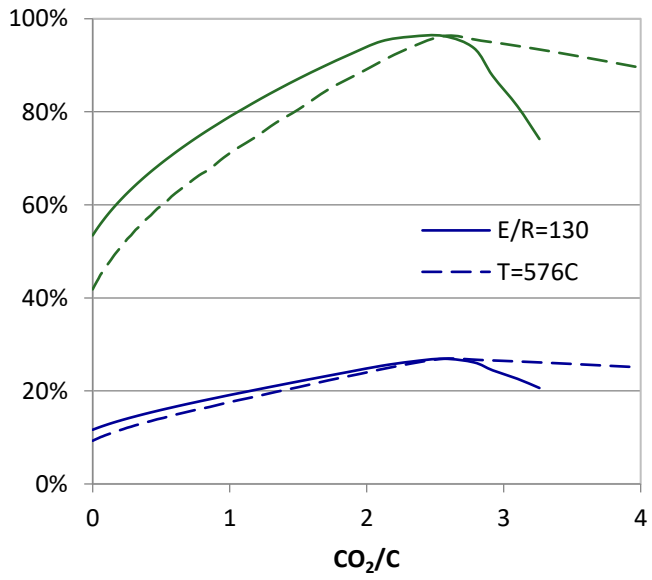

Figure 5-17: CGE (green) and indicated system efficiency for thermodynamically limited cases of constant equivalence ratio (λ=0.130) and isothermal (T=576°C) gasification conditions.

5.3.6 Summary of exhaust recycling cases

The range of model conditions for the cases simulated with the detailed engine model are presented in Table 5-2 below. The detailed engine geometry used for this model has been discussed in Chapter 3 and given in Table 3-3 while the feedstock details have been listed previously in Table 4-1.

Table 5-2: Summary of simulation parameters

Model Parameters	**Values**
Engine rotational speed:	2000 RPM
Peak combustion temperature	2200 K
O_2 equivalence ratio* (λ):	0.130 – 0.300
Gasification temperature*:	576°C - 750°C
Exhaust recycling ratio (CO_2/C):	0.0 – 4.0

*n.b. Range of independent input variables given, when calculated as a dependant variable the value may fall outwith the given range

5.3.7 CO_2 Conversion Performance

Evidence of both the conversion and non-conversion CDU characteristics of this exhaust recycling system has been seen throughout the simulation data studied. Previous analysis of EGT and gasification temperatures has clearly illustrated the thermodynamic benefit derived from the recycled CO_2 acting as both a combustion diluent and, more importantly, as a heat transfer medium to return waste engine heat to the gasifier. Changes in syngas composition and CGE have also suggested that the recycled CO_2 is being consumed by the gasification reactions and generating additional CO.

Considering the gasification system, recycled exhaust contributes an input of CO_2 while the CO_2 content of the syngas is an output. Within the system boundary, some CO_2 is consumed by a few gasification reactions while some CO_2 is produced by others. Calculating the net-CO_2 production of gasification assesses the difference in consumption and production of CO_2 within the gasifier. Equation (5.4) evaluates this measure in terms of net CO_2 production per kg of biomass feedstock. The difference in total CO_2 content in

the syngas product, $\dot{n}_{syn}$, and the CO_2 recycled in the exhaust gases, $\dot{n}_{EGR}$, shows the generation of CO_2 from the gasification process in net terms, that is the amount of CO_2 generated from the gasification reactions less the amount of exhaust CO_2 converted into fuel.

$$n_{CO_2,net} = \frac{\dot{n}_{syn} - \dot{n}_{EGR}}{\dot{m}_{bio}} \tag{5.4}$$

Figure 5-18 illustrates the net CO_2 production from gasification for the different modelling conditions studied. Trends in this data show the effect of gasification temperature and CO_2 concentration on the conversion of CO_2 into fuel species. Some regions of these plots show instances of net-negative CO_2 production from the gasification process where the syngas actually contains less CO_2 than was introduced into the gasifier through the recycled exhaust. While this is a very clear example of the CO_2 conversion within the system, even instances where the production of CO_2 is net-positive can still indicate some degree of exhaust CO_2 conversion. Since the gasification reaction itself will generate some amount of CO_2, as evidenced by the y-intercepts in these graphs, any decreasing trend in net-CO_2 production indicates at least some degree of exhaust CO_2 conversion that offsets the original CO_2 produced through gasification.

Due to the high EGTs seen in the ideal IOGC model, the corresponding gasification temperatures become very hot as exhaust gases are recycled (cf. Figure 5-4), often exceeding 1000℃. The thermodynamics of CO_2 gasification reactions cause equilibrium shifts under these high temperatures to favour the conversion of CO_2 into CO. These equilibrium shifts are often sufficient to make the gasification system on the whole a net sink of CO_2, generating less CO_2 in the syngas than was introduced in the recycled exhaust.

Given the high temperatures provide sufficient thermal energy to drive the CO_2 gasification reactions, variations in CO_2 conversion between operating conditions is largely due to changes in the relative concentrations of O_2 and CO_2 in the gasifying agent mixture. For each constant equivalence ratio case, the point of lowest CO_2 production occurs at recycling ratios beyond the peak gasification temperature, indicating the higher CO_2 content in the gasifying mixture also induces concentration-based equilibrium shifts that enhance net-CO_2 consumption. Further to this point, variation between equivalence ratios shows that temperature is not the primary factor influencing CO_2 conversion in this case. Despite having comparatively lower equilibrium temperatures, the $\lambda = 0.15$ equivalence

ratio case shows the strongest CO_2 conversion effect for this model setup. This is due to the lower amount of O_2 available in the gasification system which would compete with CO_2 to react with the feedstock.

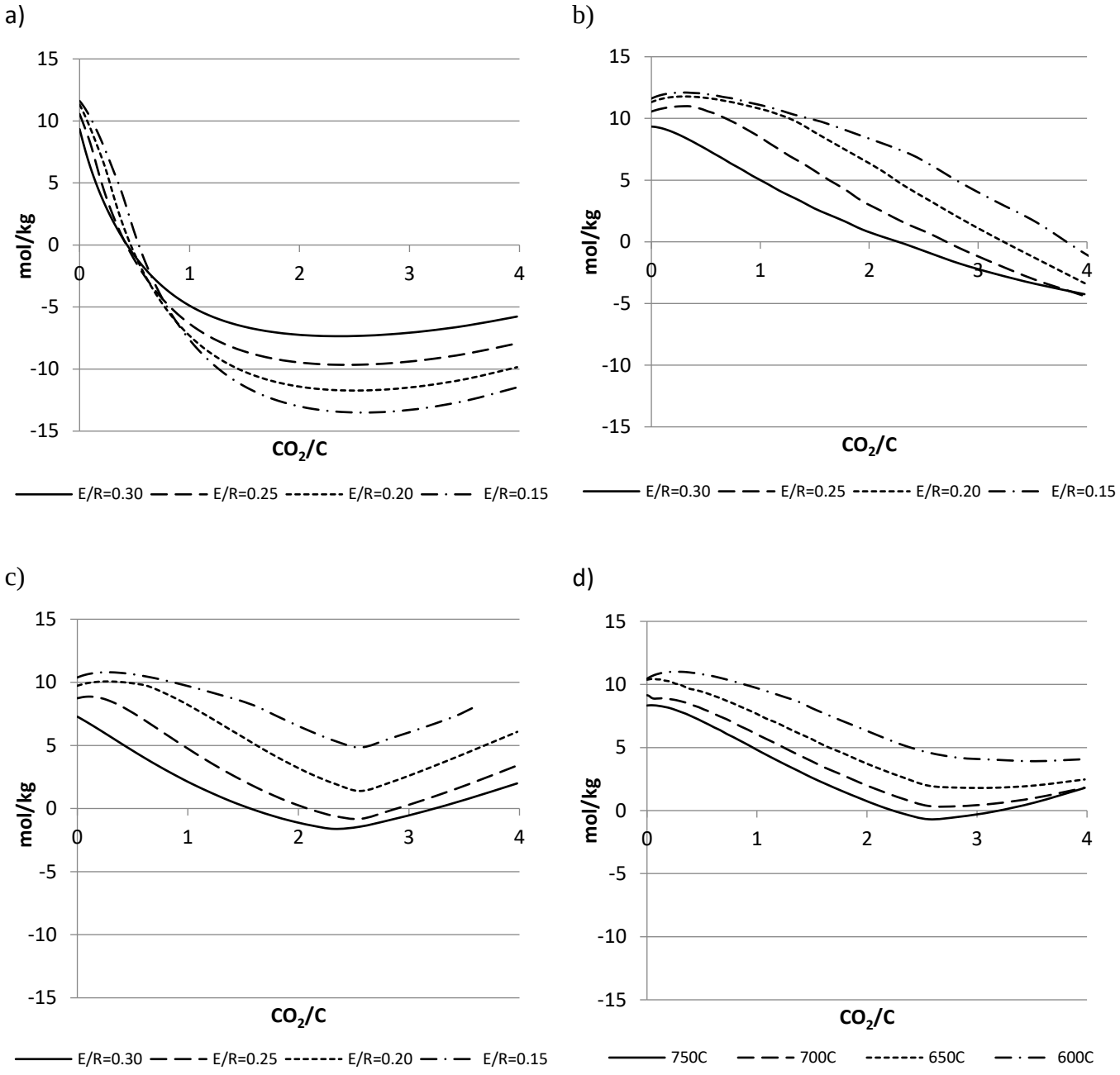

Figure 5-18: Net CO_2 production per mass of feedstock from equilibrium gasification reactions at various oxygen equivalence ratios or equilibrium temperatures for a) an ideal IOGC, b) an ideal IOGC with combustion temperature limited to 2200K, c) a detailed IOGC with combustion temperatures limited to 2200K and (d) a detailed IOGC with combustion temperatures limited to 2200K under isothermal gasification conditions.

Even when the combustion temperature is limited to 2200K in the ideal IOGC model, recycling exhaust generally contributes to a decreasing trend in net-CO2 production from gasification, as shown in Figure 5-18b. At low recycling ratios, net-CO2 production briefly increases for low equivalence ratio cases. This demonstrates that the reaction temperature

(cf. Figure 5-8) dominates the CO2 conversion process under these conditions as the reaction temperatures initially decrease with exhaust recycling for all cases except for λ = 0.30. Since the reaction temperatures have an increasing trend at high recycling ratios for this model case, both the increased reaction temperature and higher concentration of CO_2 in the system contribute to decreases in net-CO_2 production. This eventually leads to net-negative CO_2 production for high exhaust recycling ratios. Further evidence that reaction temperature is the primary factor governing CO_2 for this scenario is that lower equivalence ratio cases generate more net-CO_2 than the higher equivalence ratio cases. This means that, despite having less O_2 available to generate CO_2 through oxidation reactions, the colder reaction temperatures limit the extent of CO_2 gasification.

Both isothermal (Figure 5-18d) and constant equivalence ratio (Figure 5-18c) configurations of the detailed IOGC model display similar trends in net-CO2 production. Constant equivalence ratio cases demonstrate typical temperature dependence (cf. Figure 5-11) as seen in the previous examples, particularly for low equivalence ratio cases. Despite the decreasing reaction temperatures for the λ = 0.30 case, this equivalence ratio was capable of maintaining a sufficiently high reaction temperature that CO_2 concentration shifts were capable of reducing the net-CO_2 production of gasification. The other equivalence ratio cases show a net-CO_2 production rate that closely follows the reaction temperature trends as they rise and fall with different amounts of exhaust recycling. For all these cases, the minimum net-CO_2 production occurs around the point where syngas dilution causes a significant drop in EGTs. The corresponding temperature drop in the gasifier leads to an increase in net-CO_2 production.

These trends in the isothermal cases, while similar, have a slightly different explanation behind them. By definition, these cases will not experience any equilibrium temperature changes as the exhaust recycling ratio varies. However, the oxygen demands (cf. Figure 5-14) to maintain the desired reaction temperature can affect the net-CO_2 production. At low recycling ratios, any increasing O_2 supply seems to mostly be offset by the similarly increasing exhaust supply, leading to better CO_2 conversion. Once the syngas becomes critically diluted and the EGTs begin to fall the corresponding increase in equivalence ratio introduces more oxygen to the gasifier and generates increasing net-CO_2 production rates.

For a given equivalence ratio or equilibrium temperature, the best system indicated efficiency and lowest gasification net-CO_2 production tend to occur at similar recycling ratios, as reported in Table 4-5 for the detailed IGOC modelling cases. This indicates that

the direct conversion of exhaust CO_2 into syngas fuel is a CDU feature that benefits the system performance. Interestingly, the comparison of cases across different equivalence ratios or equilibrium temperatures indicates better efficiencies for lower equivalence ratio or temperature cases which do not have as strong a CO_2 conversion effect during gasification. Such a result suggests that the non-conversion CDU function of exhaust gas as a heat transfer medium has a more significant impact on system performance than as a chemically active reagent in the gasification process, although this analysis has clearly shown both aspects of this CDU strategy are contributing to the overall cycle improvement.

Table 5-3: Summary of indicated system efficiency and gasifier specific net-CO_2 for select configurations of the detailed IOGC model with limited combustion temperature.

Oxygen Equivalence Ratio, λ	**Recycling Ratio ($molCO_2/molC_{bio}$)**	**Gasification Temperature**	**Indicated System Efficiency**	**Net-CO_2 (mol/kg)**
0.300	0	(983°C)	16.60 %	7.279
0.300	2.232	(883°C)	23.01 %	-1.615
0.300	2.559	(853°C)	23.35 %	-1.436
0.250	0	(712°C)	17.22 %	8.735
0.250	2.562	(759°C)	24.82 %	-0.818
(0.267)	0	750°C	17.35 %	8.330
(0.245)	2.561	750°C	24.54 %	-0.687
(0.231)	0	700°C	23.13%	9.146
(0.219)	2.561	700°C	25.64 %	0.365
(0.235)	2.834	700°C	25.15 %	0.348
0.200	0	(683°C)	14.84 %	9.727
0.200	2.562	(666°C)	26.05 %	1.392
(0.151)	0	650°C	12.54 %	10.375
(0.192)	2.562	650°C	26.26 %	1.970
(0.223)	3.153	650°C	25.35 %	1.809
0.150	0	(649°C)	12.53 %	10.381
0.150	2.562	(596°C)	26.89 %	4.840
(0.093)	0	600°C	10.10 %	10.452
(0.153)	2.562	600°C	26.88 %	4.594
(0.209)	3.529	600°C	25.46 %	3.916
0.130	2.562	576°C	26.92 %	6.286

*Dependent gasification variable indicated in parentheses

5.4 Conclusions

A series of simulations using models representative of an IOGC tested the thermodynamic and system-level effects of recycling exhaust gases to enhance the gasification process. Variations in process parameters and modelling techniques illustrate the degree of coupling within the system and highlight sensitivities in gasification and power generation. Particularly, the following principal conclusions regarding the gasification chemical equilibrium and system response are determined:

- Recycled exhaust gases are an effective gasifying agent for converting biomass feedstocks into syngas fuel, however the integration of recycling in a gasification power system is complex due to thermodynamic coupling of the gasification and power generation processes.
- Exhaust recycling improves the thermodynamic conditions of gasification through concentration and temperature-based equilibrium shifts, increasing the CGE and consequently improving the indicated energy efficiency of the cycle.
- Exhaust recycling enhances the reverse Boudouard reaction thermodynamics such that lower equivalence ratios can be used while still fully converting the feedstock carbon content.
- Use of idealised power cycle models over predict the work output and exhaust temperatures compared to detailed models that account for combustion dynamics and heat losses. This can cause indicated efficiencies in the ideal models to exceed the efficiency of a detailed model by nearly 20%.
- Compared to a reference IOGC cycle without exhaust recycling at an equivalence ratio $\lambda = 0.300$, recycling 2.562 molCO_2/molC at an equivalence ratio $\lambda = 0.150$ improved the indicated cycle efficiency by 10.29%
- Exhaust gases are best used in excess as a gasifying agent rather than in an isolated EGR loop within the engine to control combustion temperatures. The resulting syngas will contain sufficient CO_2 concentrations to limit the peak cylinder temperature while simultaneously improving the thermodynamics of the conversion reactions to enhance syngas production in the gasifier.
- Gasification in this recycling IOGC is thermodynamically limited to equilibrium temperatures above 576°C and equivalence ratios above $\lambda = 0.130$. Conditions below these limits will not be capable of fully converting the carbon content in the feedstock. This condition also corresponds to the maximum indicated cycle efficiency of 26.92% for the configurations studied.

- Exhaust recycling leverages both conversion and non-conversion CDU features within the cycle. While conversion of exhaust CO_2 into useful syngas is apparent in all exhaust recycling studies, the role of CO_2 as a heat transfer medium to return waste heat to the gasifier has a predominant effect on gasification thermodynamics and overall cycle efficiency.

Although the specific values of cycle efficiency calculated here are likely associated with the particular design and operating conditions for the cycle used in this analysis, the comparison of these modelling cases reveals that exhaust recycling techniques are an effective method to enhance the thermodynamic conditions of gasification on a system level. Notwithstanding these important observations, technical challenges in biomass conversion processes remain. A clearer understanding of how exhaust recycling will affect these processes is needed.

Chapter 6 Experimental Investigation of CO_2 Gasification

6.1 Introduction

Results from integrated thermodynamic system modelling in Chapters 4 and 5 have indicated using recycled CO_2 as a gasifying agent can improve gasification performance. Particular benefit to gasification efficiency was observed for cases using mild equilibrium temperatures in the gasifier of approximately 600°C. These simulations further indicated the consumed CO_2 gasifying agent was converted into excess CO in the syngas while lowering the production of H_2 and CH_4 and enhancing char conversion. These simulation results also suggested the principal pathways for CO_2 conversion were through the reverse Boudouard, reverse water-gas shift (rWGS), and methane dry reforming (DRM) reactions.

While the novel analyses of those chapters clearly describe the thermodynamic benefit of employing an exhaust gas recycling CDU in the integrated gasification cycles studied, discussion throughout this thesis has pointed out that real gasification systems sometimes fail to achieve chemical equilibrium conditions. Although a complete experimental validation of the studied system is impractical, gasification of a sample of biomass can still provide insights detailing how the process evolves under conditions similar to those examined in the previous chapters. The thermodynamic calculations used in the simulations are time invariant so a detailed examination of how the biomass sample gasifies over time provides useful information about which processes may contribute to a syngas that differs from the equilibrium mixture.

Previous published gasification studies generally operate at standard gasifying temperatures of 800°C-1000°C but have shown the potential to convert CO_2 into CO and aid in char reduction (e.g. [86, 94, 95, 83]). This experiment investigates the performance of biomass gasification to determine the effect of using CO_2 as a gasifying agent at mild temperatures. Insights are gained by comparing pyrolysis, air gasification, and CO_2 gasification to record differences in syngas production over time. This approach highlights underlying conversion processes to show which are most influenced by the presence of CO_2 as a gasifying agent. Preliminary observations on the benefit of CO_2 for use as a supplementary gasifying agent for oxyfuel applications are also recorded.

6.2 Materials, methods, and experimental procedure

6.2.1 Setup and equipment

This experiment investigates the thermochemical conversion of biomass to syngas under different gasifying and inert atmospheres at ambient pressure. The equipment setup detailed in Figure 6-1 consists of a calibrated gas inlet plenum to supply the desired experimental atmosphere, a quartz reactor to contain the biomass sample, an electric furnace to supply the process heat, a tar condensation and filtration system to remove non-gaseous species, and a suite of detection instruments to measure the product gas stream.

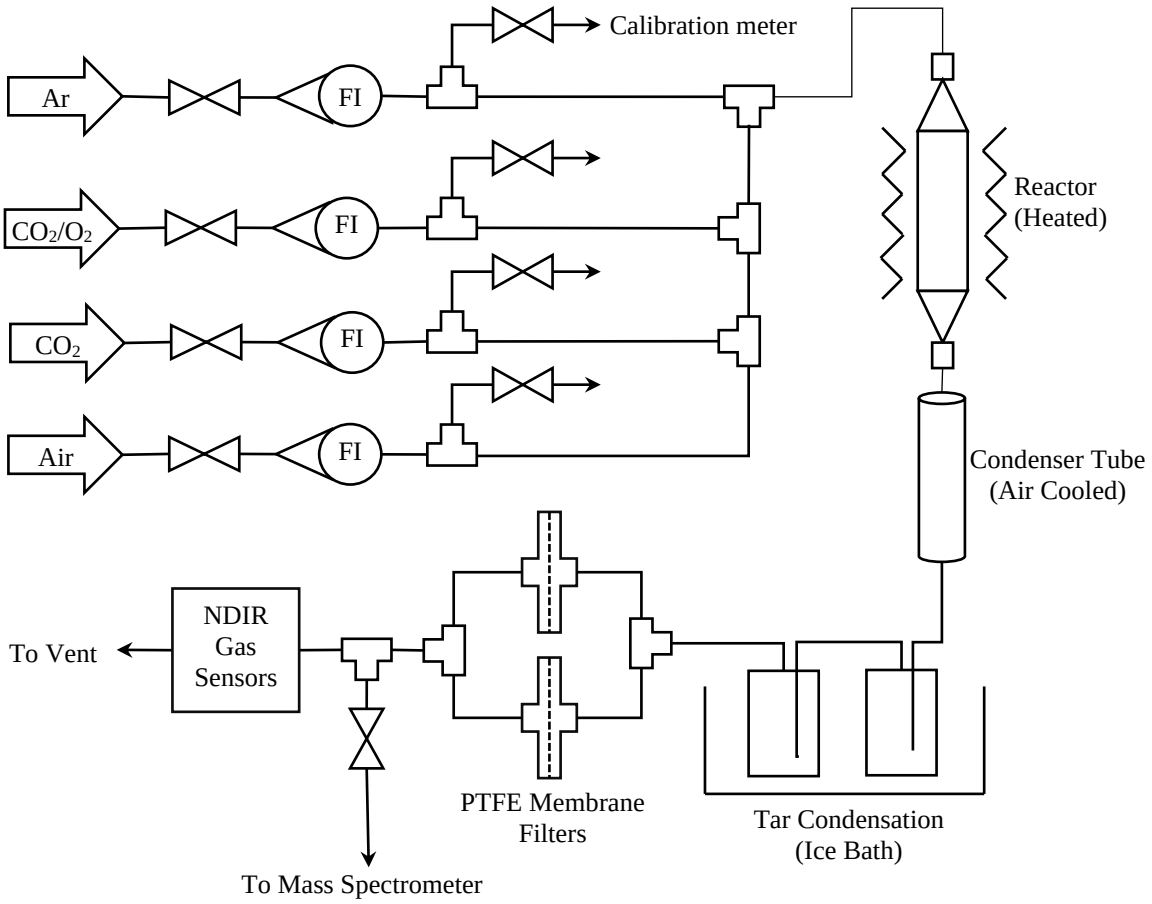

Figure 6-1: Schematic of experimental setup

Gas supply is controlled by inlet valves and variable area rotameters. The rotameter for the inlet air was supplied as a pre-calibrated unit while calibration tests for other gases/gas mixtures were performed to determine true gas flowrates. Calibration was determined by timing the gas flow through a 25±0.5 mL bubble flow meter to calculate the true volumetric flowrate. Each rotameter reading was set and measured four times at an ambient temperature of 25±2°C. A linear interpolation of the resulting data points

established the conversion from indicated to true volume flowrates for each gas and meter (Figure 6-3).

Figure 6-2: Heated reactor and tar removal components of the experimental setup. From left to right the heater and reactor, the straight condenser tube, the ice bath and condenser flasks, PTFE filters, and temperature controller.

The reactor is a quartz tube of 25mm diameter connected to steel tubing via removable endcaps fitted with 24/29 conical joints. Sample feedstock material was loaded into the quarts reactor and supported on a 75 μm porous glass frit. Thus, this reactor contains a single batch sample of biomass for each test while a continuous flow of gas is passed through the reactor. An electric heating furnace was placed around the quartz reactor and a West 4400 control unit was used to set the reaction temperature to 600℃ and heating rate to 10℃/min. The reactor was installed in a vertical direction with gasflow from the bottom of the reactor through to the top (Figure 6-2).

Product syngas was passed through a 25mm diameter, straight-tube, air-cooled glass condenser and then through a series of condensing flasks immersed in an ice bath to remove condensable species from the gas flow. Finally, the syngas was cleaned through 0.45μm PTFE filters to ensure all particulates and condensed droplets are captured before

gas sampling. Effluent flow from gas sampling instruments was collected and vented to a fume cupboard.

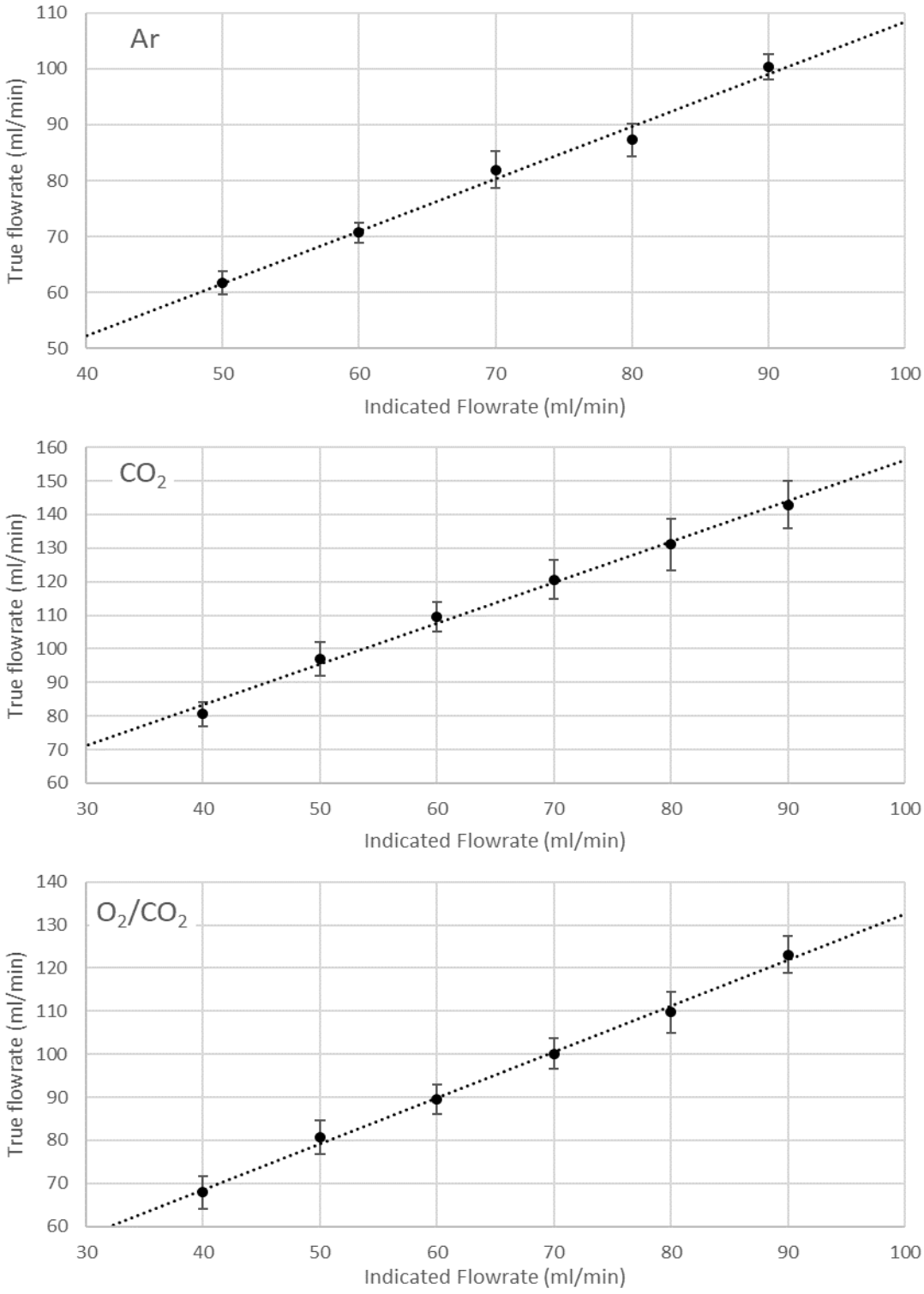

Figure 6-3: Calibration curves for rotameters used in this experiment.

6.2.2 Instrumentation

6.2.2.1 Temperature detection

An N-type thermocouple is situated in a thermal well built into the reactor and positioned to lie within the bed of lignin material. Additional thermocouples are located at the heater surface and in the ambient air at the lab bench. Thermocouple outputs are collected with a temperature logger (Picolog-TC08) and stored on a computer hard drive.

6.2.2.2 Mass Spectrometry (MS)

Primary gas species detection is achieved using a quadrupole mass spectrometer (European Spectrometry Systems Ltd. GeneSys Evolution QMS400). This instrument detects the relative molecular mass of each chemical species present in the effluent syngas sample [126]. As a gas sample enters the spectrometer, each gas molecule is ionised by an electron beam to form a positively charged ion. Generally, the electron beam provides sufficient energy for a first ionisation of the sample molecules, creating cations with an electric charge of +1 and thus having a mass to charge (*m/z*) ratio equal to the molecular mass of the sample. While the intention of this electron ionisation process is the formation of +1 charged molecular ions, higher order ionisation events occur occasionally giving ions with larger charges. Furthermore, the electron beam causes fragmentation of some molecular ions, creating smaller daughter ions with lower *m/z* ratios. Nevertheless, higher order ionisation and sample fragmentation are predictable occurrences that create a known distribution of *m/z* for a given species (ref. Appendix C) [127]. These sample ions are accelerated across a voltage potential into the quadrupole mass analyser.

In the mass analyser, an array of electrodes with both direct current and radio frequency voltage potentials creates an electric field orthogonal to the transit path of the sample ions. As the charged sample particles move through this electric field, they experience an electrostatic force which deflects their path of motion. Sample ions experience this electrostatic force as a centripetal force which causes an instantaneous arc of path deflection. This means the amount of path deflection is dependent on the magnitude of the ion's charge and on the mass inertia of the ion. By tuning the ratio of DC and RF voltages across electrode pairs, the resulting electric field becomes dynamically stable for sample ions of a particular mass to charge (*m/z*) ratio to complete the longitudinal transit of the analyser to reach the detector element. Paths of other ions through this electric field are not

stable and they will be ejected from the core of the mass analyser without impinging on the detector.

Ions meeting the detector are passed through a secondary electron multiplier (SEM) to amplify the incident signal. The result is an output of current, $I_{(m/z)}$, from the instrument proportional in magnitude to the number of ions detected at a given *m/z*. For samples of uniform volume and pressure, this provides a measure of the partial pressure of molecules of a particular *m/z* present in sample mixture [128].

6.2.2.3 Non-dispersive Infrared Spectrometry (NDIR)

Additional detectors are used to verify concentrations of selected gases of interest in the product stream, namely CO, CO_2, and CH_4. A series of three NDIR gas sensors (Edinburgh Instruments ND GasCards) were supplied and calibrated by a commercial vendor. These sensors measure the attenuation of an infrared light signal passed through the product gas sample. Each sensor uses an optical filter to select a unique bandwidth of low transmittance for the particular gas it is calibrated to detect (ref. Appendix C). A photometer detects the intensity of light across a known volume of gas. When this intensity is compared to a calibrated light intensity passed through a reference gas sample, the resulting volume fraction of the desired gas species is calculated once temperature and pressure variations are accounted for.

6.2.3 Data Calculation

The QMS provides rapid and accurate readings for each *m/z* of interest that can serve as a qualitative analysis of trends in species concentrations, however this analysis requires interpretation to quantitatively determine those concentrations. Such methods include determining relative sensitivity coefficients, C_i, and using inert reference standards [129]. Le et al. [130] show a method for online syngas QMS analysis based on these principles. Calibration of their method was based on a sample gasification experiment with the QMS results compared to syngas mole fractions measured using gas chromatography to determine the relative sensitivity coefficients. A similar method is used here, however calibration is determined during experiment initialisation and confirmed for several species using NDIR data. In this way, each set of experimental data is internally calibrated to ensure the accuracy of calculated syngas mole fractions.

Calibrated readings of inlet gas volume flowrates recorded by the rotameters allow precise calculation of the species partial pressures at initial conditions. This information is used to determine the relative sensitivity coefficients for the reference standard, Ar, and any gasifying agents used in the experiment, as shown in equations (6.1)-(6.4).

$$p_{Ar} = C_{Ar} * I_{40} \tag{6.1}$$

$$p_{O_2} = C_{O_2} * I_{32} \tag{6.2}$$

$$p_{N_2} = C_{N_2} * (I_{14} - 0.2 * I_{15}) \tag{6.3}$$

$$p_{CO_2} = C_{CO_2} * I_{44} \tag{6.4}$$

Both N_2 and CO gas species have *m/z* ratios of 28 so calculation of the N_2 component of the syngas is based on the *m/z* = 14 signal, instead. This still has some overlap with a known fragment of CH_4, however this is accounted for using the fragmentation distribution of CH_4. Furthermore, when CO_2 is not supplied as a gasifying agent, its relative sensitivity coefficient is determined from the measured volume fraction reported by the NDIR meters at local concentration peaks or during periods of stable production.

Partial pressures of CH_4 and CO are determined from the calculated CO_2 fraction and scaled by the CH_4/CO_2 and CO/CO_2 molar ratios measured by the NDIR spectrometers (equations (6.5)&(6.6)). This method reduces potential errors introduced through misinterpretation of isobaric ions of equal *m/z* ratios. NDIR outputs are temporally aligned using QMS peaks to account for system lag using *m/z* 15, 29, and 44 to coordinate the NDIR outputs for CH_4, CO, and CO_2 respectively.

$$p_{CH_4} = p_{CO_2} * \frac{x_{CH_4}}{x_{CO_2}} \tag{6.5}$$

$$p_{CO} = p_{CO_2} * \frac{x_{CO}}{x_{CO_2}} \tag{6.6}$$

Hydrogen partial pressure is determined from the *m/z* = 2 signal. The H_2 sensitivity coefficient was calibrated using a reference gas standard of 75% H_2 in Ar supplied to the QMS at 1 barg.

$$p_{H_2} = C_{H_2} * I_2 \tag{6.7}$$

Calculated partial pressures are converted to mole fractions by normalising over the sum of all recorded partial pressures.

$$x_i = \frac{p_i}{\sum_i p_i} \tag{6.8}$$

Using Ar as an inert reference standard with a known flowrate through the system, relative flowrates of other syngas components are determined from the ratio of mole fractions. These flowrates are integrated over the duration of the experiment (equation (6.9)) to determine the total molar production.

$$n_i = \int \frac{x_i}{x_{Ar}} * \dot{n}_{Ar}\ dt \tag{6.9}$$

Similarly, differences between known input flowrates and measured syngas content of a particular species determines net production or consumption.

$$n_{O_2} = \int \dot{n}_{O_2,ref} - \frac{x_{O_2}}{x_{Ar}} * \dot{n}_{Ar}\ dt \tag{6.10}$$

6.3 Results

6.3.1 Analysis of feedstock, char, and tar residues

6.3.1.1 Lignin Feedstock

Samples of a commercially available lignin feedstock (Protobind1000 soda lignin) are used as a biomass source for these experiments. The elemental composition of a sample of this material was determined by combustion analysis in an Exeter CE-440 Elemental Analyser and is presented in Table 6-1. Analysis consists of completely oxidizing the sample in a stream of O_2 gas to generate a full set of sample combustion products. These combustion products are carried through the instrument with a reference flow of He gas. First, the products enter a reducing chamber to reduce any NO_x compounds to elemental N_2. Since the resulting gas mixture now consists of only N_2, H_2O, CO_2, and He the gas flows through selective absorbents successively to remove any H_2O and then any CO_2. By measuring and

comparing the thermal conductivity of the gas mixture before and after each absorbent section, the hydrogen and carbon content of the original sample is deduced. Finally, the remaining mixture of He and N_2 has its thermal conductivity compared to a reference sample of pure He to determine the nitrogen content of the original sample. Based on this analysis, the lignin has an empirical chemical formula of $CH_{1.086}N_{0.001}O_{0.406}$ which corresponds to a molar mass of 19.75 g/mol.

Table 6-1: Lignin feedstock elemental mass composition

Element	Sample 1	Sample 2	Mean
C	60.74%	60.90%	60.82%
H	5.49%	5.60%	5.56%
N	0.70%	0.71%	0.71%
O (difference)	33.07%	32.79%	32.93%

This elemental makeup is similar to other known lignin components. Ranzi et al [43] identified three typical sub monomers present in lignin; an H-unit of hydroxyphenyl $C_9H_{10}O_2$ ($CH_{1.111}O_{0.222}$), a G-unit of guaiacyl $C_{10}H_{12}O_3$ ($CH_{1.2}O_{0.3}$), and an S-unit of syringyl $C_{11}H_{14}O_4$ ($CH_{1.273}O_{0.364}$). Dussan et al [131] considered slightly larger pseudo-component dimers of crosslinked monolignols (H, G, and S units) with H/C ratios ranging from 1.100 – 1.238 and O/C ratios ranging from 0.286 – 0.500. Lignin samples analysed in this experiment have slightly lower H/C ratios than reported in these typical subgroups while the O/C ratio falls toward the high end of the pseudo-components used by Dussan et al [131].

6.3.1.2 Char residues

Char samples were collected and weighed following pyrolysis and CO_2 gasification tests. Some of the collected samples were sent for elemental analysis, as described above, to establish the average composition of the char produced in this experiment. Data presented in Table 6-2 and Figure 6-4 shows the average empirical chemical formula of the chars to be $CH_{0.198}N_{0.019}O_{0.189}$.

Table 6-2: Elemental mass analysis of recovered char

Element	Sample 1	Sample 2	Sample 3	Sample 4	Mean
C	71.62%	73.71%	81.86%	82.86%	77.51%
H	0.80%	0.74%	1.80%	1.81%	1.29%
N	1.90%	1.83%	0.95%	2.14%	1.71%
O (diff.)	25.68%	23.72%	15.39%	13.19%	19.49%

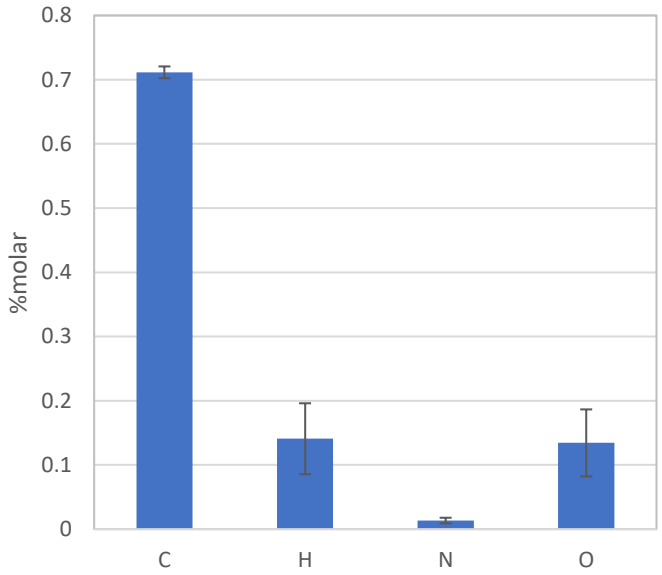

Figure 6-4: Molar composition of recovered chars

6.3.1.3 Tar condensates

Heavier compounds released during high temperature pyrolysis of the feedstock condense to leave oily and waxy residues in the reactor and condensing vessels as the product gas cools. These tar compounds were dissolved in dichloromethane (DCM) CH_2Cl_2, collected in a beaker, and left to stand for at least 48h to allow for evaporation of the solvent. Elemental analysis of tar samples was performed as previously described and is presented in Table 6-3 and Figure 6-5 showing the average empirical chemical formula of tar is $CH_{1.236}N_{0.018}O_{0.266}$ with a corresponding molar mass of 17.76 g/mol.

Table 6-3: Elemental mass composition of collected tar compounds.

Element	Sample 1	Sample 2	Sample 3	Sample 4	Mean
C	68.93%	68.11%	64.68%	68.77%	67.62%
H	7.33%	7.17%	6.75%	6.82%	7.02%
N	1.99%	1.66%	1.04%	1.08%	1.44%
O (diff.)	21.75%	23.06%	27.53%	23.33%	23.92%

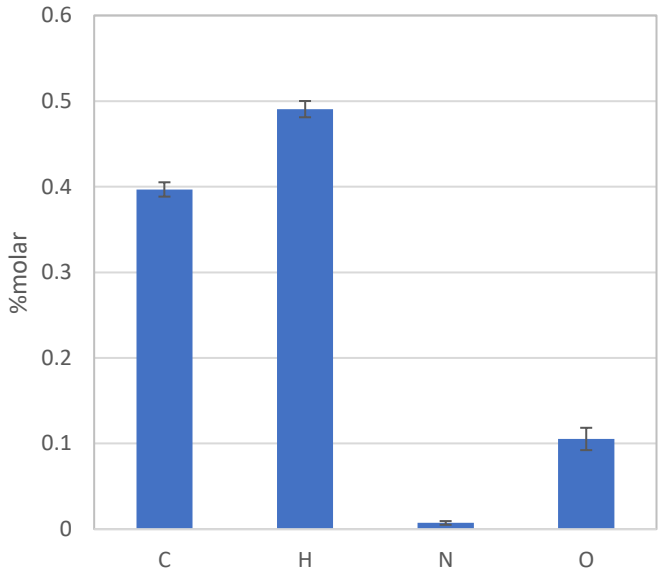

Figure 6-5: Molar composition of collected tar compounds.

Detailed studies of biomass derived tars have identified many distinct organic compounds including aromatics, phenolics, acids, and alcohols. For example, one experiment identified tars produced from the air gasification of wood consisted mainly of phenol, toluene, benzene, and naphthalene while also finding pyrenes, xylenes, cresols, and xylenols [109].

While the elemental analysis performed here does not identify individual components, the average composition of H/C and O/C ratios for the tars sampled in this experiment is typical of heavier condensable species. Indeed, any lighter aromatics like benzene, toluene, and phenol are likely to have evaporated concurrently with the DCM during the 48h drying period and will not be present in the sample. Measured elemental ratios could be representative of some methoxylated phenolic compounds known to originate from lignin during pyrolysis. For example, G-unit lignin monomers often decompose into compounds like coniferol ($C_{10}H_{12}O_3$) and guaiacol ($C_7H_8O_2$) [131]. These common pyrolysis tars have

a range of H/C 1.143 – 1.2 and O/C 0.285 – 0.3 which approximate the findings of this experiment.

6.3.1.4 Ash residues

Ash combustion analysis reported no mass fractions of H and only 1.2% C, indicating the presence of inorganic material in the ash residues. To illustrate possible inorganic components of the ash, samples were sent for powder X-ray diffraction (XRD) analysis. Figure 6-6 shows the resulting sample diffraction patterns compared to characteristic intensity peaks of inorganic crystal structures from the Inorganic Crystal Structure Database (ICSD) [132]. The illustrative inorganic components, while not quantified, are typical of the elements expected in the ash of biomass fuels. For comparison, inorganic elements in ashes from various biomass fuels measured by Sieradzka et al [133] using X-ray fluorescence are reported in Table 6-4. This shows the likely compounds inferred from the XRD analysis are also consistent with the elements typically present in biomass ash samples.

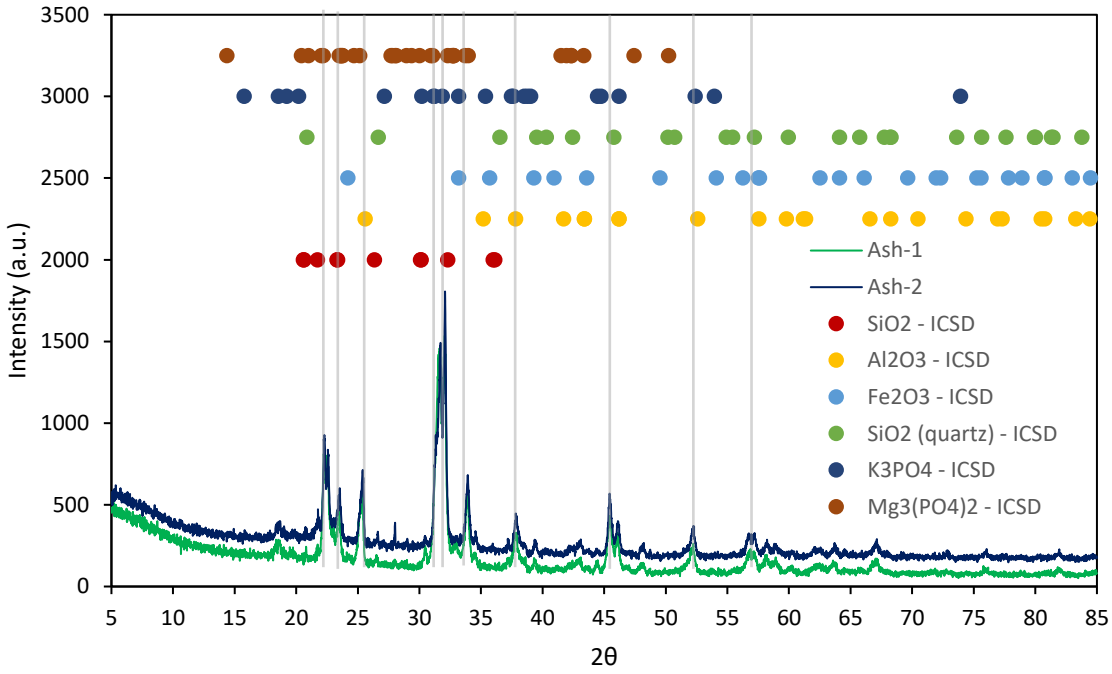

Figure 6-6: XRD patterns of ash samples and reference materials

Table 6-4: Elemental inorganic content of ash residues from various biomass feedstocks measured using x-ray fluorescence [123].

Element	Sample			
	Brewing Spent Grain	Wheat Straw	Pine Sawdust	Hay
Na	0.23%	0.13%	0.29%	0.52%
Mg	7.04%	3.33%	7.51%	1.01%
Al	0.12%	0.37%	0.53%	3.58%
Si	15.38%	13.64%	0.77%	31.44%
P	16.11%	5.60%	1.00%	1.34%
S	0.02%	1.53%	1.48%	0.73%
Cl	0.00%	1.92%	0.93%	2.01%
K	7.29%	32.00%	15.83%	8.49%
Ca	4.33%	4.55%	38.82%	2.73%
Ti	0.02%	0.05%	0.00%	0.31%
Fe	1.81%	0.29%	0.45%	1.26%

6.3.2 Pyrolysis under argon

Using Test P3 as an example for pyrolysis analysis, a 1.5007 g sample of lignin was heated up to 600℃ at a rate of 10℃/min under a carrier gas flow of 99 mL/min of Ar.

The initial phase of pyrolysis starts at a sample temperature above 250℃ and is marked by production of CO_2 from the lignin sample, occurring around 15:23 for the Test P3 experiment shown in Figure 6-7. In comparison, other TGA analyses of lignin samples also indicated devolatilisation mass loss tends to begin near this temperature and peaks beyond 300℃ [133, 134, 135]. This CO_2 production leads CH_4 and CO pyrolytic fractions by approximately 12 minutes. Although an early product of pyrolysis, CO_2 concentration peaks and then diminishes as other species become more prevalent in the gas mixture. CH_4 appears to be the predominant gaseous product of pyrolysis, causing a major peak approximately 25 minutes into the pyrolysis process as the sample temperature rises beyond 500℃. Production of CO happens simultaneously with the CH_4 peak, although the maximum concentration of this species is below 2%v and occurs approximately four minutes after the CH_4 peak. Hydrogen is the final product of pyrolysis to be generated from the sample, peaking roughly 45 minutes into the process once the temperature is established at 600℃ before diminishing to trace emissions. At the conclusion of the experiment, 0.5303g of char was recovered from the reactor. Although not directly

measured, the moisture content of the lignin sample appears to be low since there is no obvious reduction in the rate of temperature change of the sample that would indicate the evaporation of water from a drying process.

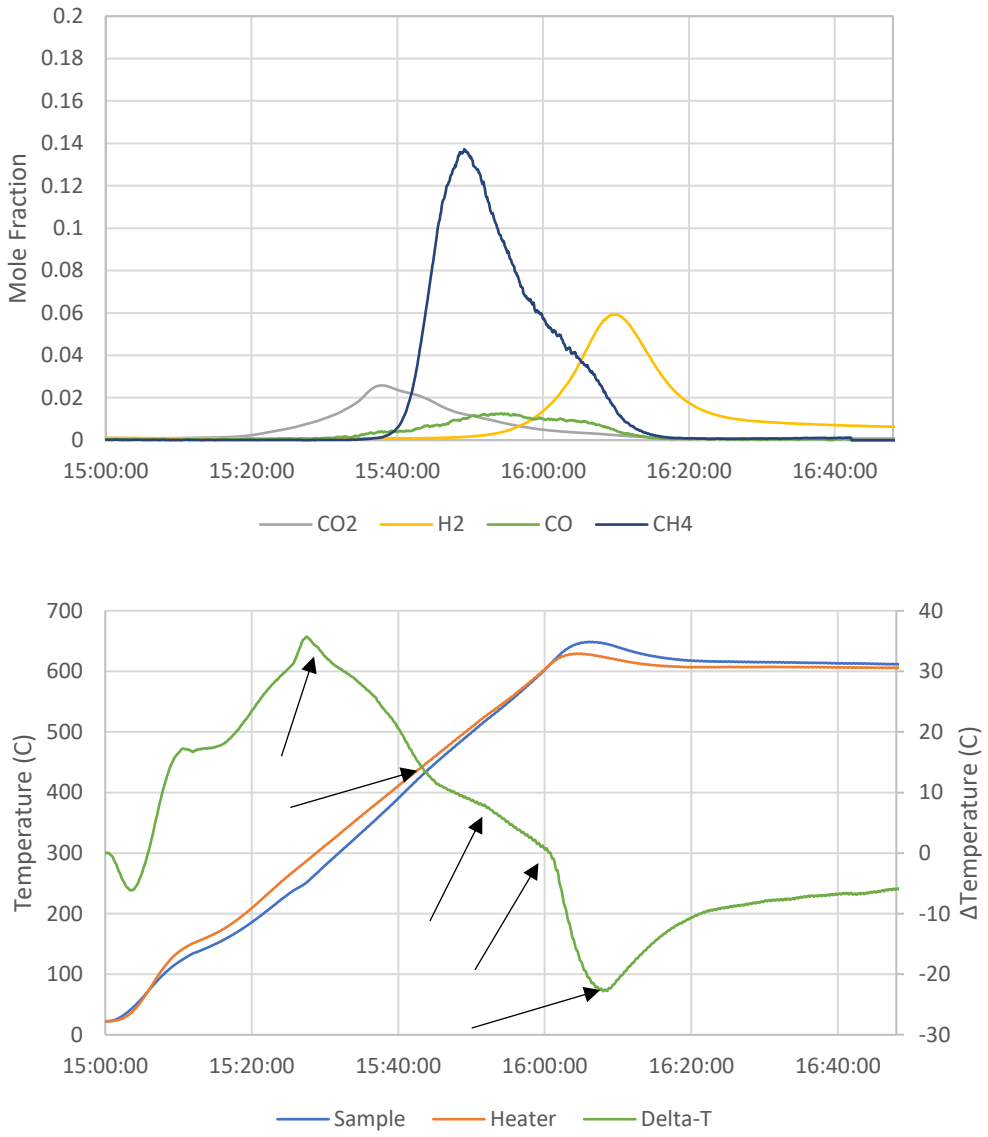

Figure 6-7: Product species (top) and temperature profiles (bottom) over time for 600°C pyrolysis of lignin. (Test P3)

Temperature profiles of the sample and heating element also show the largely endothermic nature of the pyrolysis process. Sample temperatures tend to lag behind the heater. This is most prominent at the onset of pyrolysis where the sample temperature stagnates, causing an abrupt spike in the temperature differential. Over time, the sample temperature converges to the heater temperature as the lignin devolatilises, leaving the char residues at 600°C. Examining the temperature and concentration profiles simultaneously indicates five regions or stages where unique process events seem to occur, as highlighted in Figure 6-7. The difference between the heater and sample temperature (i.e. the delta-T) gives some

information about the devolatilisation processes happening within the sample. Each process will have an effect on both the heat release and mass change of the sample, creating identifiable regions where the process is active. These are further described below.

First, the initial production of CO_2 is apparent in the temperature field near the peak temperature difference between the sample and heater. An inflection in the temperature profile after the peak CO_2 production also coincides with the start of CH_4 and CO production. Although both CH_4 and CO are generated in the following regions, the time difference in peak production and changes in the gradient of the temperature differential indicate each species comes from its own chemical event, the second and third processes observed. After each distinct peak in CO and CH_4, an extended region of moderate CO and CH_4 production continues for roughly 10 minutes and is likely due to a common process, event four. The final chemical event during pyrolysis is the H_2 production at the end of the process.

Since H_2 has a standard enthalpy of formation of 0 kJ/mol, chemical processes that form H_2 tend to be endothermic unless a co-product with a negative enthalpy of formation is also formed as in the WGS reaction. Interestingly, the temperature profile associated with the region of H_2 production shows a rapid increase in sample temperature. No CO_2 was present in the system leading up to this hydrogen event, so the temperature rise is unlikely a result of the WGS reaction, but it may yet be the result of a chemical process. That is to say some unknown intermediate process, perhaps associated with tar cracking or reforming, could be contributing to the temperature rise associated with this H_2 production although there is no clear indication of other product generation or reactant consumption shown in the data collected. Furthermore, since this represents the sample reaching the final temperature, this H_2 production may be associated with the end of the pyrolytic mass loss and the associated change in sample heat capacity. There is yet a possibility this temperature signal is due to the overshoot of the heater controller, however a similar trends in differential temperature are noted in all pyrolysis tests and also in CO_2 gasification tests, even under higher temperature conditions (ref. section 6.3.4.1 and Appendix D – Experimental Data), showing this is a repeatable occurrence in the pyrolysis process.

Table 6-5 records the sum of products derived during the pyrolysis experiments. In aggregate, CH_4 was the main gaseous pyrolytic product, representing over 53% of the dry syngas. H_2 production made up roughly 24% of the gas mixture while CO_2 contributed 14%. Due to the relatively low concentrations of CO generated during the experiment, this

species constitutes a mere 8% of the gas product. These dry syngas product concentrations are calculated based on the observed production rates of the species of interest and do not include the inert carrier gas in the calculation.

Table 6-5: Summary of pyrolysis experiments: Initial sample content, evolved gas products, char residues, estimated tar by-products, and calculated mass residuals shown.

			Test P1	Test P2	Test P3	Mean
Lignin Sample		(g)	1.5007	1.5002	1.5007	1.5005
	C	(mmol)	76.00	75.97	76.00	75.99
	H	(mmol)	82.55	82.53	82.55	82.54
	O	(mmol)	30.89	30.88	30.89	30.89
Dry Gas	CO_2	(mmol)	2.44	2.86	2.85	2.71
		(%v)	10.76%	17.56%	14.05%	14.12%
	CO	(mmol)	1.41	1.59	1.62	1.54
		(%v)	6.24%	9.78%	8.01%	8.01%
	CH_4	(mmol)	13.77	9.30	10.80	11.29
		(%v)	60.82	57.09%	53.34%	57.08%
	H_2	(mmol)	5.02	2.54	4.98	4.18
		(%v)	22.18%	15.57%	24.60%	20.79%
	Total gas	(g)	0.3779	0.3249	0.3540	0.3523
		(%m)	25.18%	21.66%	23.59%	23.48%
Char		(g)	0.5970	0.5890	0.5303	0.5721
		(%m)	39.78%	39.26%	35.34%	38.13%
	C	(mmol)	38.53	38.01	34.23	36.92
	H	(mmol)	7.28	7.18	6.46	6.97
	O	(mmol)	7.28	7.18	6.46	6.97
Estimated Tar		(g)	0.3524	0.4298	0.4707	0.417637
		(%m)	23.48%	28.65%	31.36%	27.83%
	C	(mmol)	19.80	24.20	26.50	23.52
	H	(mmol)	24.53	29.91	32.76	29.07
	O	(mmol)	5.27	6.43	7.04	6.24
Residuals		(g)	0.1734	0.1565	0.1457	0.1585
		(%m)	11.55%	10.43%	9.71%	10.57%
	C	(mmol)	-------	-------	-------	------
	H	(mmol)	-14.4	3.15	-9.84	-7.03
	O	(mmol)	12.06	9.96	10.08	10.70

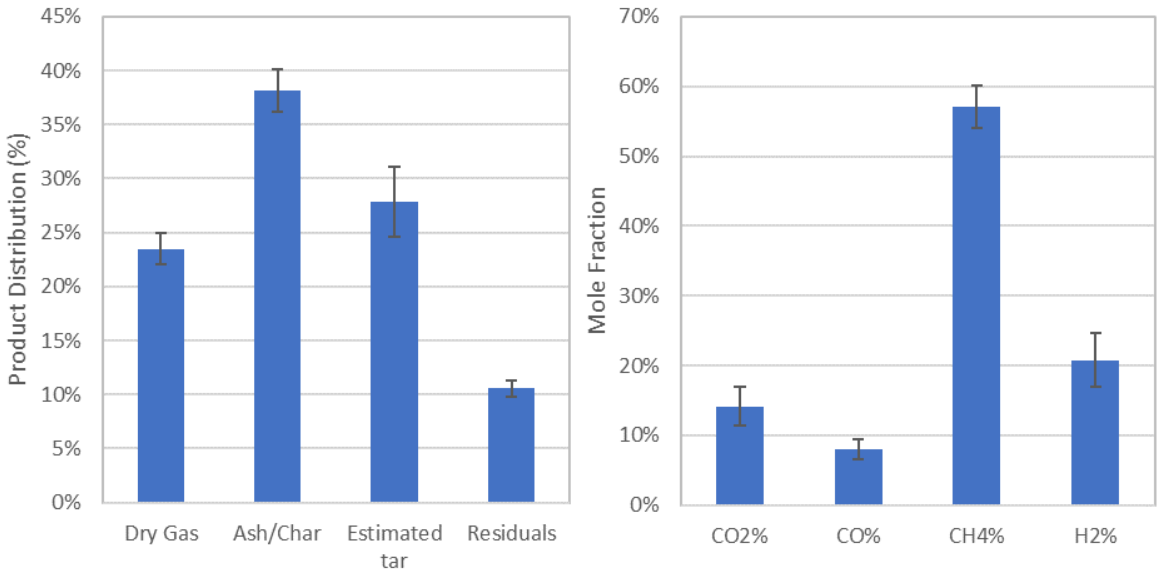

Figure 6-8: Product distribution and dry syngas mole fractions for lignin pyrolysis at 600°C

Analysis of the experiment mass balance shows that syngas and char account for 58.93% of the initial sample mass. Due to the setup of this experiment, condensable tar species were not directly measured and could represent a fraction of the mass deficit. Furthermore, tracking the elemental balance gives a breakdown of which elements from the original sample remain unaccounted for. As an estimate, tar production is assumed to make up the outstanding difference in carbon, 26.50 mmol or approximately one third of the initial sample carbon content for this experiment. This calculation improves the mass closure for the experiment to have a total residual of 9.71%, however the elemental balance does not hold for this condition as there is insufficient hydrogen to allow for this amount of tar production as indicated by the negative values in the elemental balance. Indeed, as described below, this is likely a shortcoming of the tar assumption applied to this caculation.

Since the detection of CO_2, CO, and CH_4 is confirmed by both mass and infrared spectrometry, calculated production of these species is taken to be accurate. Furthermore, H_2 production is calculated from an experimentally determined mass spectrum sensitivity coefficient and, although not doubly confirmed like the previous gases, is likewise understood to be acceptably accurate. Although there is some potential variation in the composition of collected char residues, particularly in the hydrogen content, the amount of carbon contained in the char is likely accurate to within ±1%.

The tar assumption applied above presumes that no other carbon containing products are generated from this experiment. This is unlikely a completely true assumption since other

light hydrocarbons of C_2-C_5 have been detected in other lignin pyrolysis experiments using gas chromatography [128, 129] that have not been included in the current analysis. Although these products make up only a small fraction of the final syngas composition, when combined with the tar assumption this would change the distribution of carbon and hydrogen across the products and could contribute to the imbalance in hydrogen.

General trends described above for Test P3 hold for the other pyrolysis experiments, as shown in Figure 6-9, indicating the reproducibility of these phenomena. Direct comparison of the mass spectra corresponding to H_2 (m/z = 2), CH_4 (m/z = 16), CO (m/z = 28), and CO_2 (m/z = 44) are quite well matched between experiments, particularly tests P1 and P3. This is useful since IR data for test P1 was corrupted and was unusable so relative sensitivity coefficients from test P3 were calculated and substituted into the calculations to quantify the mass spectra of test P1.

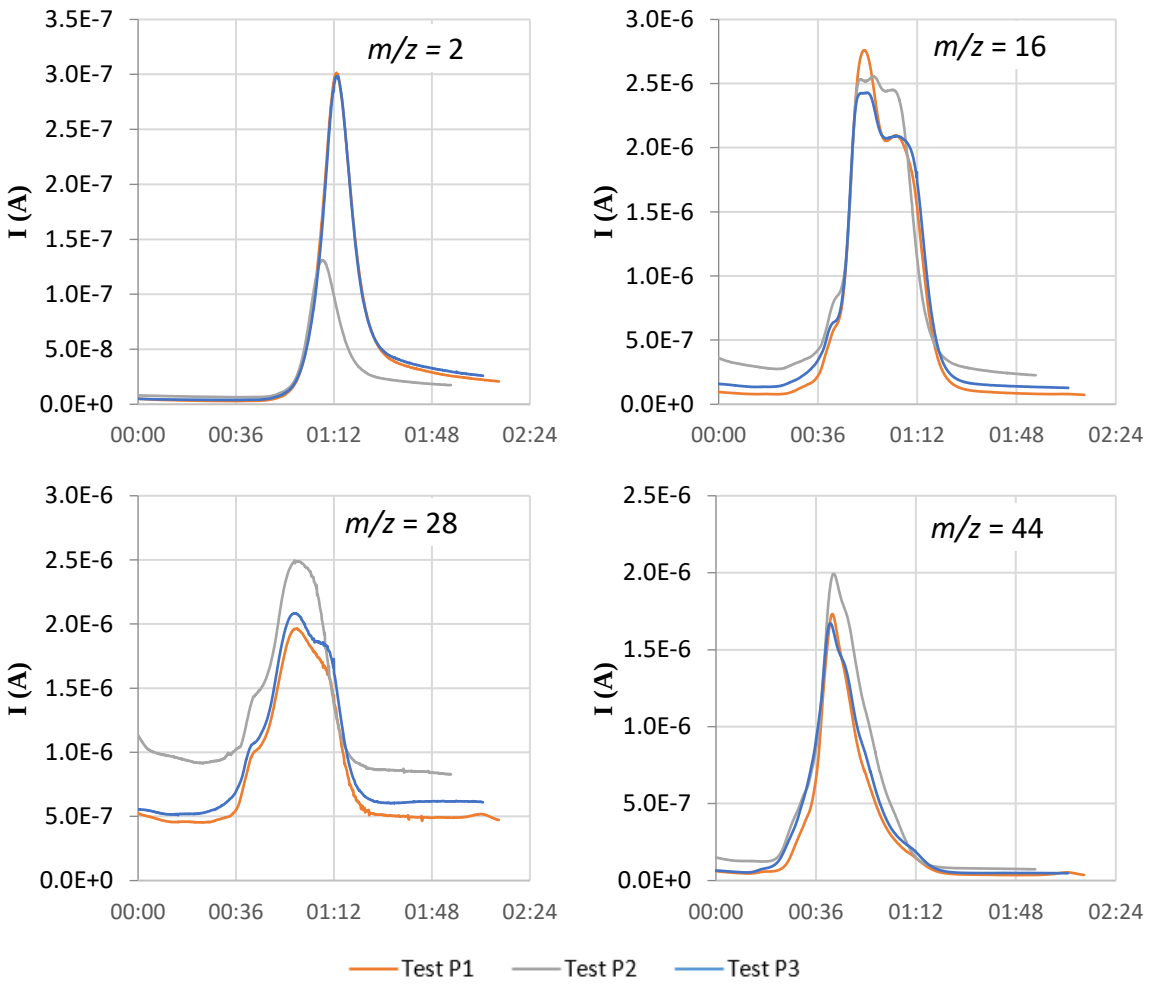

Figure 6-9: Comparison of mass spectra for key product species during three pyrolysis tests at 600°C

One noticeable deviation is the m/z = 2 data for test P2. While the MS data for tests P1 and P3 match very closely, the peak signal for test P2 is roughly half that observed for the other

two tests. This resulted in lower H_2 yields calculated for test P2 compared to the other pyrolysis tests, however since the other mass spectra appear closely matched to tests P1 and P3 and are further verified through the NDIR outputs, the test is taken to be valid.

Distributions of reaction products calculated in this experiment (Figure 6-8) agree in general with published literature [138, 139, 140] with char representing the largest fraction of products. Notably, a higher proportion of methane is observed in the current pyrolysis tests while comparatively lower amounts of H_2 and CO were released.

6.3.3 Gasification under air

A flow of 100-200 mL/min of air was used as a gasifying agent with 71 mL/min of Ar also included as a tracer gas. Early syngas development in these cases indicate the sample undergoes a devolatilisation process where some small amount of CO_2 is produced before the main release of pyrolysis gases CH_4 and CO. In contrast to the pyrolysis-only cases, the CO_2 content continued to rise throughout the devolatilisation region. This is attributable to the oxidation of some syngas, char or feedstock since the concentration of O_2 is simultaneously seen to diminish. The extended release of CH_4 and CO observed during pyrolysis is not evident in the data here due to the influence of O_2 which reacts with carbon containing compounds to create additional CO_2. H_2 production over the process appears to come from the end of the feedstock pyrolysis process, similar to the previous pyrolysis processes. Despite the presence of O_2 in the gasifying mixture, this initial process is clearly a result of pyrolysis rather than any other chemical process involving the gasifying agent. In the first place, the temperature profile shows the typical endothermic event associated with devolatilisation that previously observed for the cases under argon. Additionally, the O_2 content remains fairly constant during this initial event, only showing sings of consumption after the pyrolysis event begins to liberate volatile reactants. Also, the initial pyrolysis event occurs at a relatively low temperature of ~250°C while the sample is heating up. This temperature is too low for O_2 to react directly with the solid feedstock so devolatilisation must be the initial event, followed by O_2 reactions with the resulting pyrolysis products.

It is also notable that CO production in this case is significantly more prominent than under the inert atmosphere case. A prominent production peak during the early stages of the reaction is attributable to pyrolysis, however the rate of CO generation is higher than previously seen from pyrolysis. This signifies that O_2 is also being consumed in partial

oxidation reactions. As devolatilisation ends, char reduction dominates the syngas production. Here, O_2 from the gasifying air is reacting with the carbon in the char to generate CO_2 and CO as the prominent syngas species. The O_2 supplied to the reaction becomes fully consumed during the char reduction process and this appears to slightly overlap with the end of the pyrolysis process.

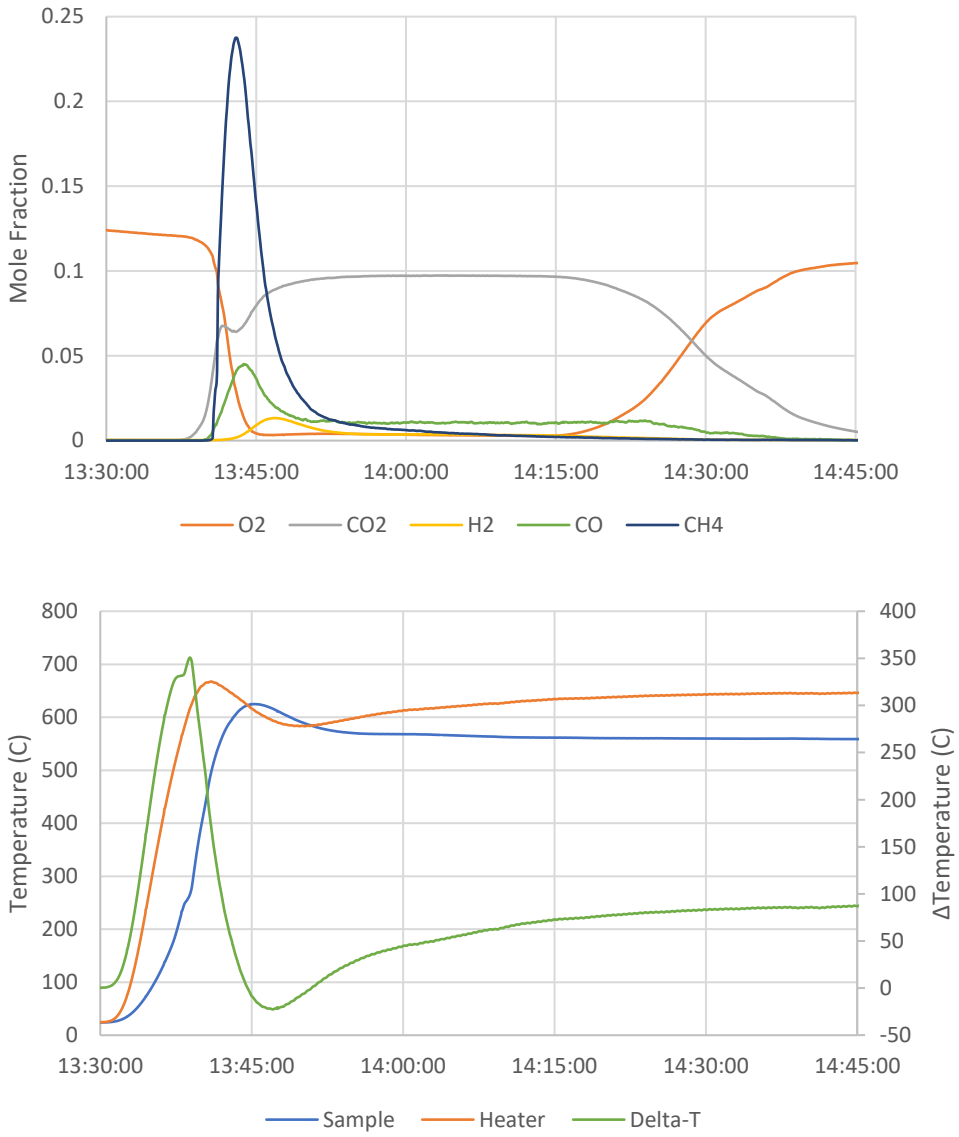

Figure 6-10: Product species (top) and temperature profiles (bottom) for 600°C air gasification of lignin. (Test A7)

Notably, the initiation of the endothermic pyrolysis process is again apparent in the temperature profile of the lignin sample and appears to initiate as the temperature reaches ~250°C. In contrast to the pyrolysis-only cases, the sample temperature exhibits exothermic behaviour just after the onset of pyrolysis as the temperature of the sample rapidly climbs. As this coincides with the apparent decrease in O_2 content, it is further evidence of the exothermic oxidation reactions. Except for the initial peak, the gradient

changes in the temperature differential that delineated the pyrolysis processes observed under the Ar atmosphere are not as apparent in this case due to the predominance of the exothermic oxidation reactions. Nevertheless, the H_2 production peak once again coincides with the minimum temperature differential.

The sum production of air gasification cases shows the use of oxygen in the gasifying agent mixture is effective at reducing the char within the system. Prevalence of oxidation reactions made a syngas rich in CO_2. Similarly, these air gasification cases produced 330% more CO than was generated from pyrolysis alone. Overall production of CO_2 was approximately five times greater than CO while CO_2 production during char reduction was nine times greater than for CO. A contributing factor to this situation is the relatively high consumption of O_2 in these experiments. On average, the air cases had an effective air equivalence ratio of 0.5, although there is some variation across the tests.

Despite the increase in both CO and CO_2 production, the total production of H_2 and CH_4 appears largely unaffected by the air gasification agent since total average yields are nearly the same as in the pyrolysis cases. Based on the profiles in Figure 6-10 it seems these products are mainly produced during pyrolysis and are somewhat invariant to the gasifying agent. Nevertheless, some limited oxidation of the hydrogen species may occur without detection since H_2O products are not detected in this analysis. Taken with the above observation, this suggests the O_2 introduced to the system preferentially reacts with feedstock carbon during both pyrolysis and char reduction.

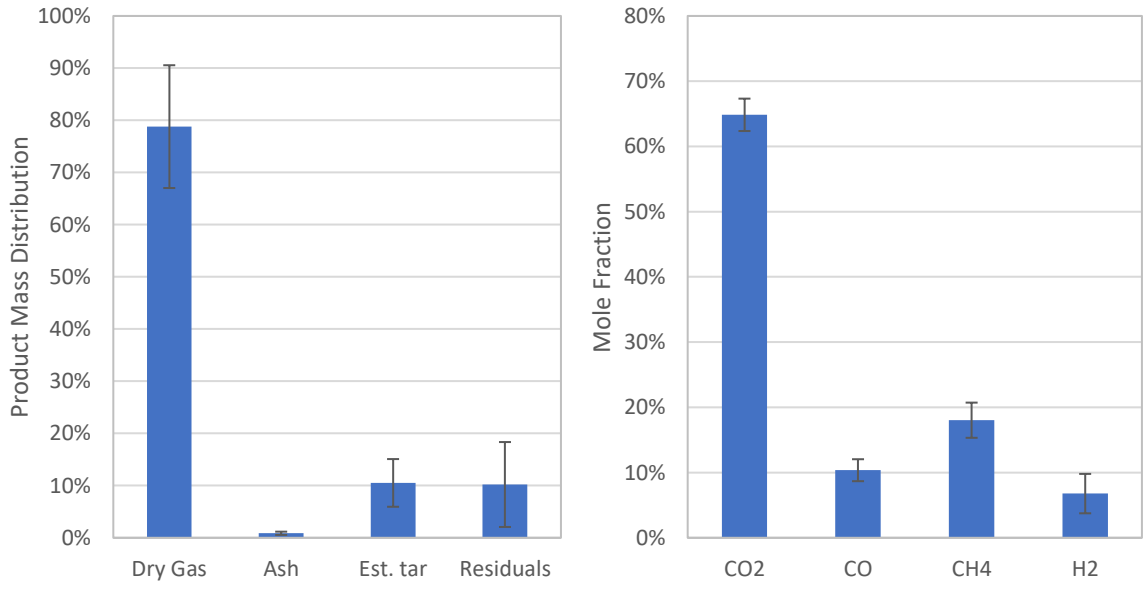

Figure 6-11: Product distribution and syngas mole fractions for air gasification at 600°C

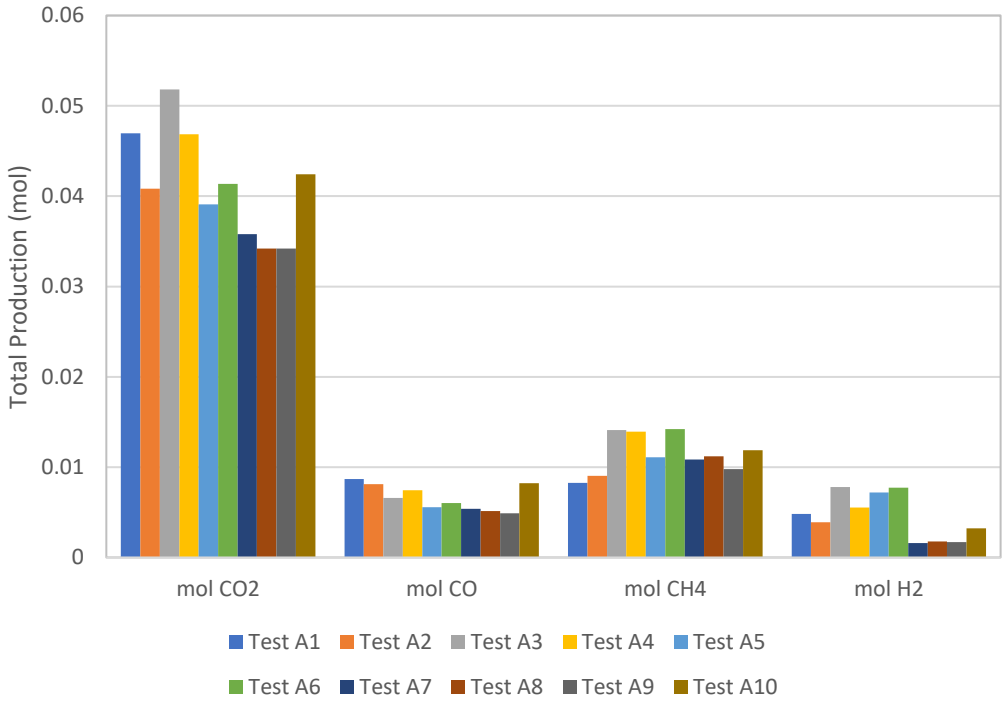

Figure 6-12: Total molar production of syngases during air gasification

Table 6-6: Summary of air gasification experiments: Initial sample content, evolved gas products, char residues, estimated tar by-products, and calculated mass residuals.

			Test A1	Test A2	Test A3	Test A4	Test A5	Test A6	Test A7	Test A8	Test A9	Test A10	Mean
Lignin Sample		g	1.504	1.504	1.501	1.500	1.500	1.501	1.500	1.501	1.500	1.500	1.5011
	C	mmol	76.16	76.16	76.01	75.96	75.96	76.01	75.96	76.00	75.96	75.96	76.02
	H	mmol	82.73	82.73	82.57	82.51	82.51	82.57	82.51	82.56	82.51	82.51	82.57
	O	mmol	30.96	30.96	30.89	30.87	30.87	30.89	30.87	30.89	30.87	30.87	30.90
O2 consumed		mmol	36.92	34.16	38.62	43.78	36.04	36.79	42.01	47.05	42.28	48.53	40.62
		g	1.181	1.093	1.236	1.401	1.153	1.177	1.344	1.505	1.353	1.553	1.2997
Equivalence ratio (λ)			0.454	0.420	0.475	0.539	0.444	0.453	0.518	0.579	0.521	0.598	0.500
Dry Gas:	CO2	mmol	46.96	40.81	51.82	46.85	39.11	41.37	35.79	34.20	34.19	42.43	41.35
		%v	68.31%	65.96%	64.53%	63.52%	62.12%	59.65%	66.78%	65.39%	67.66%	64.52%	64.84%
	CO	mmol	8.70	8.12	6.59	7.43	5.56	6.03	5.38	5.13	4.88	8.24	6.61
		%v	12.65%	13.12%	8.21%	10.07%	8.83%	8.69%	10.04%	9.81%	9.66%	12.53%	10.36%
	CH4	mmol	8.27	9.04	14.09	13.94	11.10	14.23	10.84	11.18	9.77	11.87	11.43
		%v	12.04%	14.62%	17.54%	18.90%	17.63%	20.52%	20.22%	21.38%	19.34%	18.05%	18.02%
	H2	mmol	4.81	3.91	7.80	5.54	7.19	7.73	1.58	1.79	1.69	3.22	4.53
		%v	7.00%	6.31%	9.72%	7.51%	11.42%	11.15%	2.95%	3.42%	3.35%	4.90%	6.77%
	Total gas	g	2.453	2.176	2.707	2.505	2.069	2.233	1.903	1.832	1.801	2.295	2.197
		%m	91.34%	83.80%	98.91%	86.33%	77.99%	83.38%	66.90%	60.93%	63.14%	75.17%	78.79%

			Test A1	Test A2	Test A3	Test A4	Test A5	Test A6	Test A7	Test A8	Test A9	Test A10	Mean
Ash/Char		g	0.014	0.026	0.016	0.021	0.022	0.012	0.022	0.042	0.030	0.040	0.025
		%m	0.52%	1.00%	0.57%	0.72%	0.84%	0.44%	0.78%	1.41%	1.05%	1.31%	0.86%
	C	mmol	0.01	0.03	0.02	0.02	0.02	0.01	0.02	0.04	0.03	0.04	0.024
Estimated tar		g	0.217	0.323	0.062	0.137	0.358	0.255	0.425	0.452	0.481	0.238	0.295
		%m	8.08%	12.42%	2.27%	4.73%	13.51%	9.53%	14.94%	15.03%	16.87%	7.79%	10.52%
	C	mmol	12.21	18.17	3.49	7.72	20.17	14.38	23.93	25.45	27.09	13.38	16.60
	H	mmol	15.10	22.45	4.32	9.55	24.94	17.77	29.58	31.45	33.49	16.54	20.52
	O	mmol	3.24	4.82	0.93	2.05	5.36	3.82	6.35	6.76	7.19	3.55	4.41
Residuals		g	0.002	0.002	0.072	-0.048	0.238	0.203	0.178	0.494	0.680	0.540	0.480
		%m	0.11%	2.77%	-3.18%	8.22%	7.67%	11.86%	17.38%	22.62%	18.94%	15.73%	10.21%
	C	mmol	0.00	0.00	0.00	0.00	0.00	0.00	0.00	0.00	0.00	0.00	0
	H	mmol	24.92	16.30	6.29	6.12	-1.19	-7.58	6.42	2.79	6.56	12.03	7.27
	O	mmol	-1.07	4.71	-3.03	15.27	13.82	11.90	31.58	44.70	34.99	31.28	18.41

6.3.4 CO_2 Gasification

Gasification tests using a flow of 120 mL/min of CO_2 as a gasifying agent mixed with 85 mL/min of argon as a carrying gas were also done on lignin samples heated to 600℃ at a rate of 10℃/min.

A pyrolytic event initiates around 13:10, as indicated by the prominent deviation in sample heating rate at that time as the sample temperature approaches ~250℃. Typical increases to syngas concentrations of CH_4, CO, and H_2 are seen in the data (Figure 6-13) during this devolatilisation process with peak CH_4 and CO production occurring before the H_2 peak. While not immediately evident in Figure 6-13, a slight increase to the net-CO_2 production indicates an initial release of CO_2 is again associated with the early pyrolysis of the sample, as shown in Figure 6-14. Trends in the temperature profile are again similar to the pyrolysis cases and indicate five distinct regions of species production, showing pyrolysis remains the dominant source of syngas products for this case.

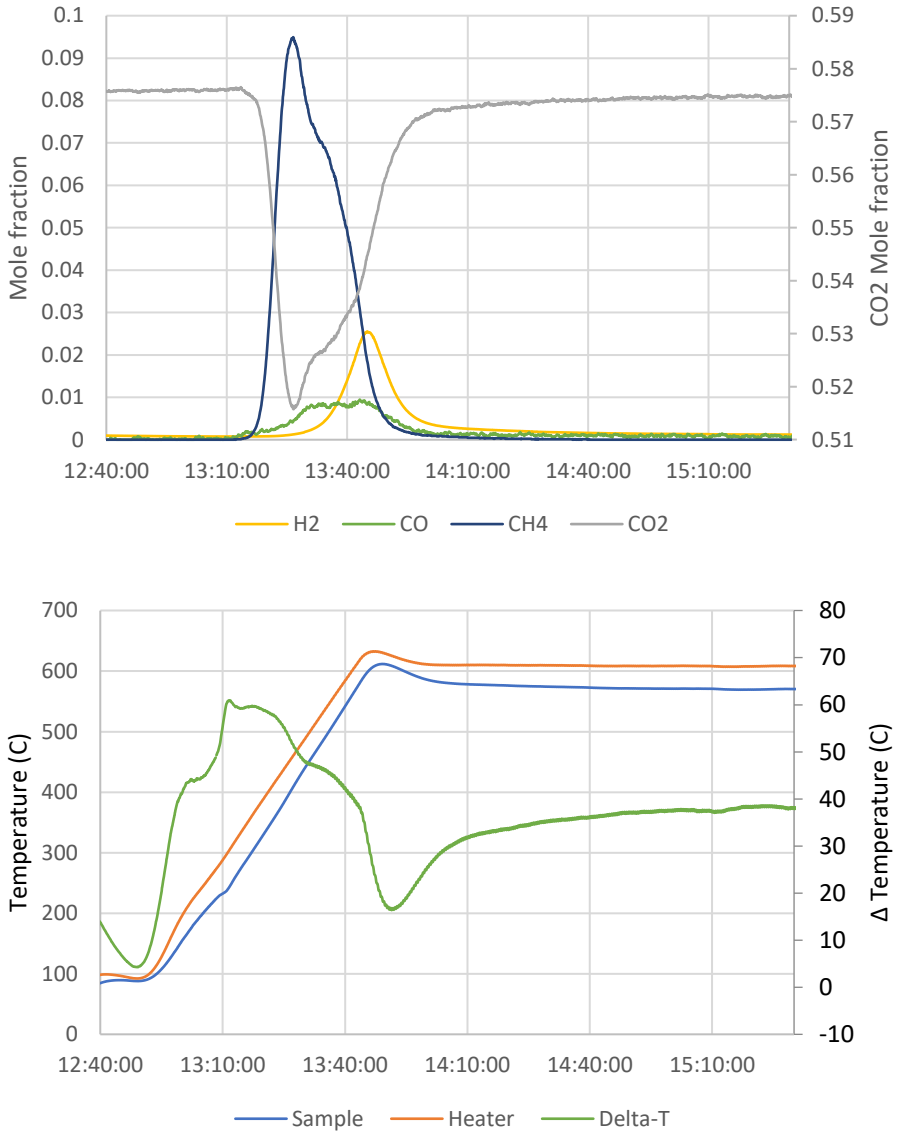

Figure 6-13: Product species (top) and temperature profiles (bottom) for CO_2 gasification of lignin 600°C. (Test C2)

To determine the net-CO_2 production of the process, the molar flowrate of supplied CO_2 was subtracted from the calculated flowrate of CO_2 in the syngas. Figure 6-14 illustrates how the net-CO_2 changes over the course of the gasification process. Initially, the net-CO_2 flowrate remains constant at ~0 mol/s as the sample warms up. A brief increase in net-CO_2 is indicative of the initial stages of pyrolysis before dropping into a negative flowrate regime, indicating more CO_2 is consumed in the process than is released through pyrolysis. Net-consumption rates of CO_2 are rather low under these conditions, representing approximately 0.44%v of the supplied CO_2 gasifying agent flowrate. Integration of the initial net-release of CO_2 is interpreted as the CO_2 produced by the process while the integral of subsequent region of net-negative CO_2 production calculates the assumed CO_2 consumption over the process. This region of net-consumption of CO_2 also coincides with slightly enhanced production of CO which remains noticeable, if minor, beyond the

pyrolysis of the sample. Such a result suggests the CO_2 supply interacts to some degree with char produced from feedstock pyrolysis.

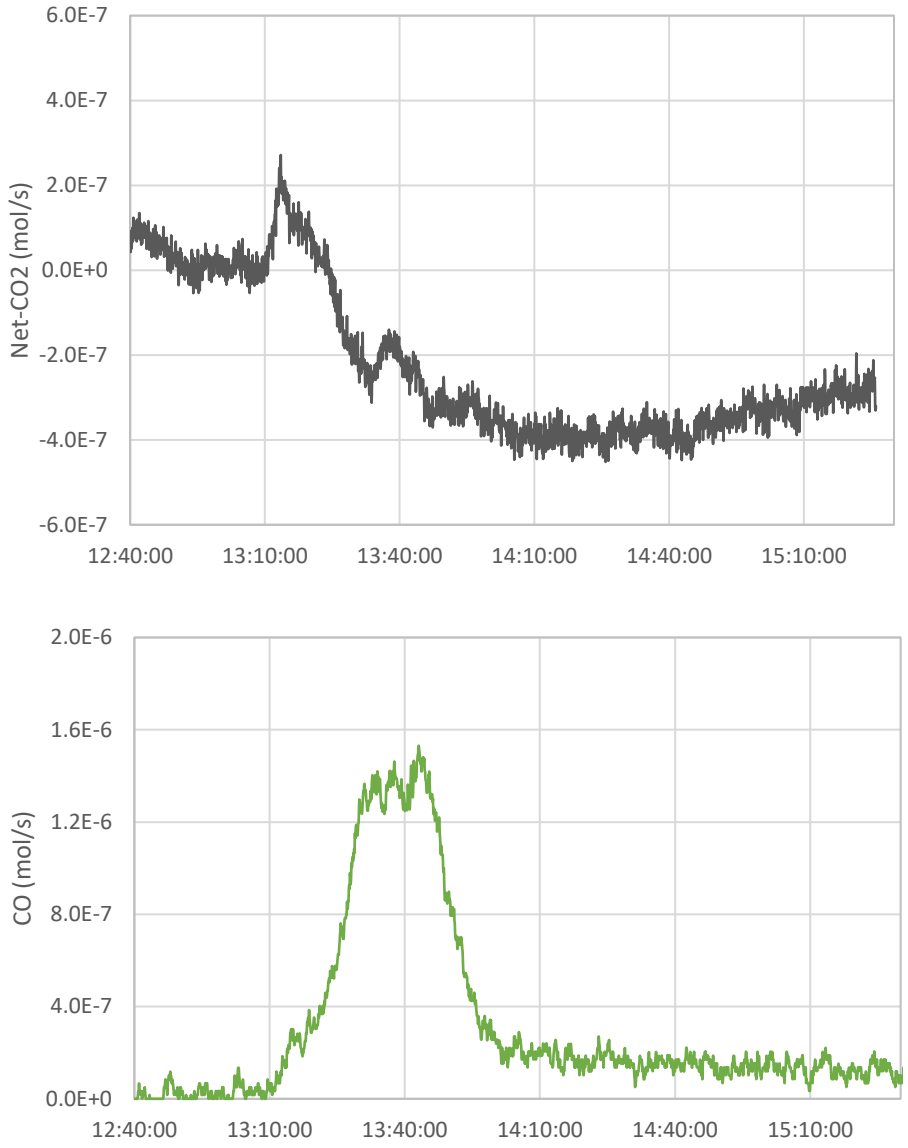

Figure 6-14: Net-CO_2 (top) and CO (bottom) production during CO_2 gasification of lignin (Test C2)

To better illustrate the impact CO_2 has as a gasifying agent, syngas production results from a CO_2 experiment and a pyrolysis experiment are compared in Figure 6-15. As previously mentioned, the production of CO_2 is generally negative in net-terms except for the initial release during event 1 at the beginning of the reaction. This initial net-CO_2 production still remains smaller in magnitude than under the pure pyrolysis conditions discussed in section 0. Although this initial period of the gasification reaction is still attributable to pyrolysis of the feedstock, it is likely that the CO_2 released in this way became reactive as the temperature increased and was consumed along with the supplied CO_2 gasifying agent. In

contrast, despite producing some CO_2 during the pyrolysis experiment, the concentration of CO_2 in the reactor remained less than 2.5%v (see Figure 6-7) and thus would be far less reactive with the char and other potential reactants than the CO_2 under the gasification conditions where CO_2 is supplied directly to the reactor at concentrations between 51-58%v. The higher concentration of CO_2 in this gasification case contributes to a concentration-based push to help drive CO_2 consumption reactions.

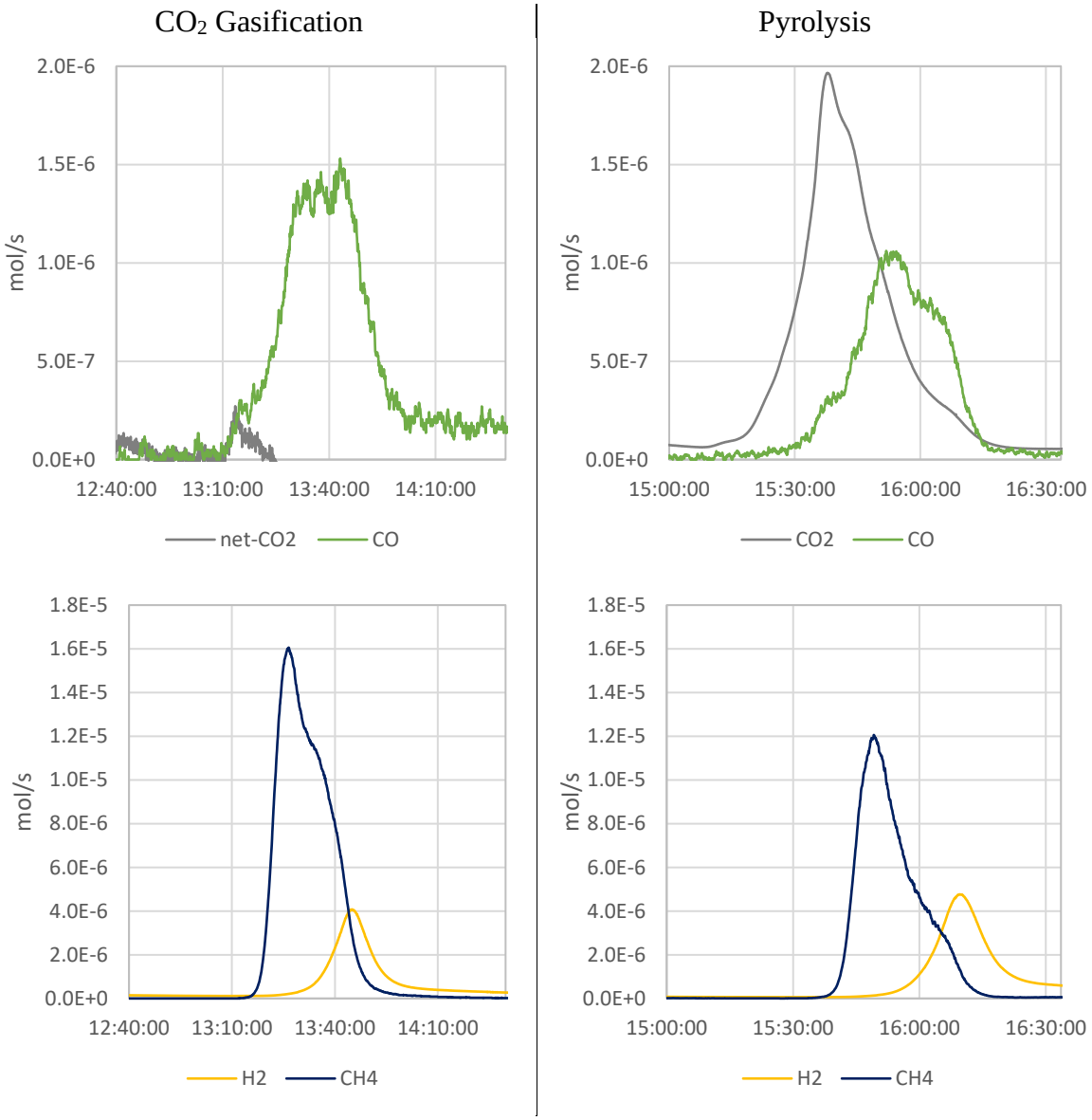

Figure 6-15: Molar flowrates of CO_2 gasification syngas (left, Test C2) compared to pyrolysis syngas (right, Test P3)

Correspondingly, CO production of event 3 for the gasification case was marginally higher than the comparable event under pyrolysis-only conditions. Peak CO production rates under CO_2 were nearly 50% higher compared to the peak production under only Ar. Furthermore, the decrease in CO at the end of pyrolysis (event 4 occurring around 16:00 in the pyrolysis test) is not evident in the CO_2 gasification case as CO production remains approximately constant during sample devolatilisation. Additionally, marginal CO

production continued well after feedstock devolatilisation while CO production under Ar was only observed during pyrolysis. On average, CO_2 gasification reactions produced 1.064 mmol more CO than pyrolysis-only over the course of the process, an increase of roughly 69%.

For the examples compared in Figure 6-15, the lignin sample produced higher amounts of CH_4 under CO_2 during events 2 and 4. The relative scales of primary and extended CH_4 production rates also differ under CO_2 gasification conditions with the late stage of pyrolysis maintaining CH_4 production rates roughly 2/3 of the peak rate measured during event 2. Under the Ar atmosphere example, the production rate during event 4 was only about 1/3 as much as the peak rate, although this effect varied between pyrolysis tests.

This comparison also shows slightly lower amounts of H_2 produced during event 5. While this particular change in H_2 production may indicate a comparative enhancement of the rWGS under CO_2 gasification conditions, this trend is not observed when all tests are compared in aggregate. Total production of CH_4 and H_2 tended to vary across CO_2 gasification tests and ranged from 11.642-16.580 mmol and 4.012-5.470 mmol, respectively. Although the mean production rates of CH_4 and H_2 remain slightly higher than under the pyrolysis-only conditions (Table 6-7, cf. Table 6-5), the variance in measurements overlaps with the mean production of CH_4 and H_2 during pyrolysis, ultimately leaving the effect of CO_2 on these gasification products uncertain. Similarly, mean char production in the CO_2 gasification tests is roughly the same as in the pyrolysis-only experiments.

While the measured net-CO_2 and CO indicate some potential conversion of CO_2 into CO, however slight, the apparent lack of variation in other gas and char products adds uncertainty to this observation. The conversion process would require some additional reactant which should be seen to vary between pyrolysis and CO_2 gasification. However, considering the low production rates of CO and consumption of CO_2 under these experimental conditions, it may be that any corresponding changes in other products, like H_2 or CH_4, were imperceivable. Altogether, the increase in CO production represents a mere 1.4% of the carbon input to the reaction through the feedstock and consumed gasifying agent. Furthermore, the CO_2 may be reacting with unaccounted for by-products that are not detected in this analysis, like some light alkanes or volatile tar species. For example, CO_2 can be consumed in an oxidative dehydrogenation reaction (ODH) to convert paraffins into olefins [141, 142] although these reaction typically require

heterogeneous catalysts to activate the CO_2 using an initial electron transfer from an active catalyst site to an adsorbed CO_2 molecule.

Table 6-7: Summary of CO_2 gasification experiments: Initial sample content, evolved gas products, char residues, estimated tar by-products, and calculated mass residuals shown.

			Test C1	Test C2	Test C3	Mean
Lignin Sample		g	1.5006	1.5001	1.5000	1.5005
	C	mmol	75.99	76.01	75.96	75.99
	H	mmol	82.55	82.57	82.51	82.54
	O	mmol	30.89	30.89	30.87	30.88
CO2 consumed		mmol	2.136	2.361	0.450	1.649
		g	0.0940	0.1039	0.0198	0.0725
CO2/C ratio (effective)			0.028	0.031	0.006	0.022
Dry Gas:	CO2	mmol	0.149	0.087	0.095	0.111
		%v	0.70%	0.35%	0.52%	0.52%
	CO	mmol	2.275	3.218	2.329	2.607
		%v	10.42%	12.86%	12.88%	12.05%
	CH4	mmol	13.941	16.580	11.642	14.054
		%v	63.86%	66.23%	64.40%	64.83%
	H2	mmol	5.470	5.150	4.012	4.88
		%v	25.03%	20.57%	22.19%	22.60%
	Total gas	g	0.305	0.370	0.264	0.313
		%m	19.23%	23.13%	17.43%	19.93%
Char		g	0.5703	0.5577	0.6325	0.587
		%m	35.96%	34.83%	41.73%	37.51%
	C	mmol	36.81	35.99	40.82	37.87
	H	mmol	7.28	7.12	8.08	7.50
	O	mmol	6.95	6.80	7.71	7.15
Estimated tar		g	0.440	0.398	0.381	0.406
		%m	27.73%	24.86%	25.11%	25.90%
	C	mmol	24.76	22.41	21.43	22.87
	H	mmol	30.61	27.69	26.49	28.26
	O	mmol	6.57	5.95	5.69	6.07
Residuals		g	0.2710	0.2750	0.2383	0.261
		%m	17.34%	17.18%	15.72%	16.75%
	C	mmol	0.00	0.00	0.00	0.00
	H	mmol	-22.05	-28.87	-6.64	-19.18
	O	mmol	18.67	19.30	15.67	17.88

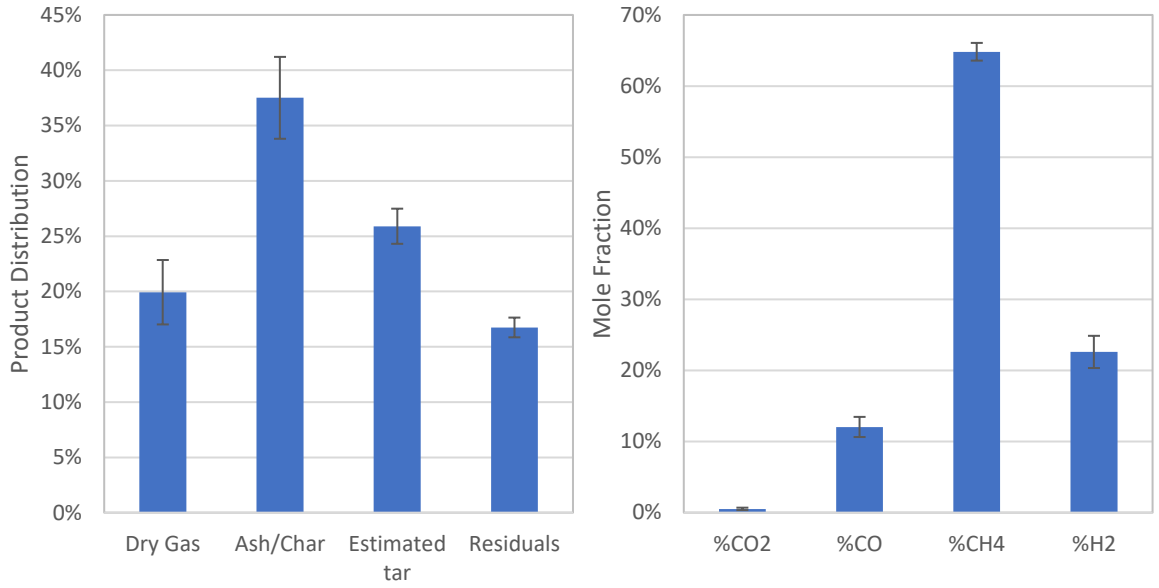

Figure 6-16: Product distribution and dry syngas mole fractions for CO_2 gasification at 600°C

There is also a noticeable difference in the calculated CO_2 consumed for test 15 compared to the other two gasification tests, as shown in Figure 6-17. It appears the process net-CO_2 production initially displays the same patterns as the other experimental runs until 1:20 of elapsed time when the net-CO_2 production of test 15 begins to increase while the other tests continue to consume CO_2. Despite this apparent difference, test 15 produced an amount of CO comparable to the other tests, although the total CH_4 and H_2 production were the lowest of all the CO_2 gasification tests. Notwithstanding the apparent variation in duration of the CO_2 consumption for this test, the overall trends and initial conditions indicate the net-conversion of CO_2 into CO was still achieved during this test as peak CO production rates exceeded 1.2×10^{-6} mol/s during feedstock devolatilisation and remained detectable after pyrolysis.

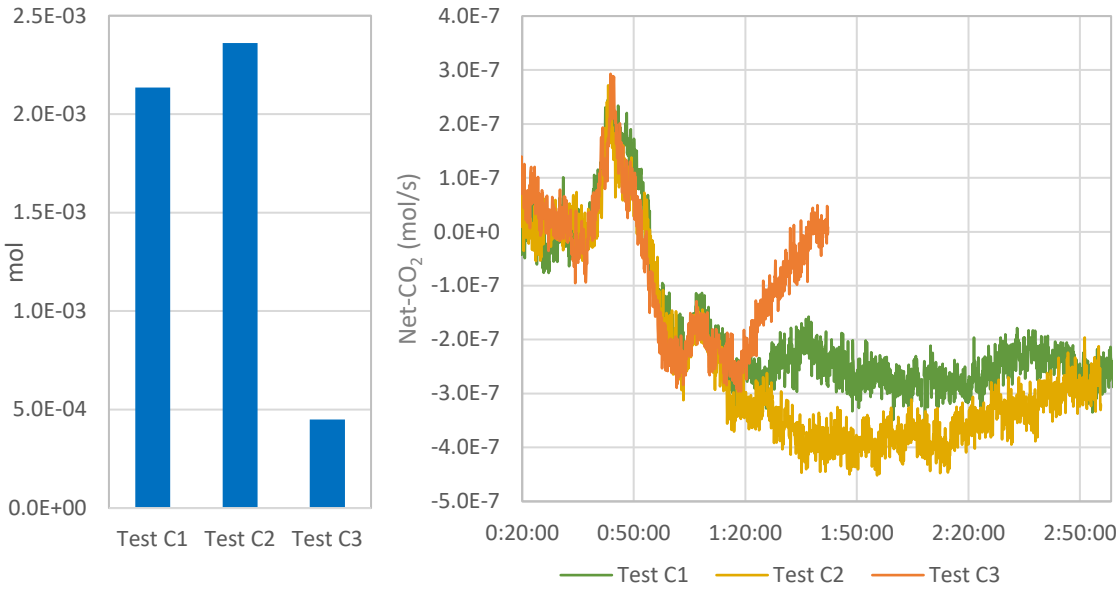

Figure 6-17: Total CO_2 consumption (left) and the net-CO_2 production rate (right) of each CO_2 gasification test.

6.3.4.1 Increased temperature CO_2 gasification

While the data clearly demonstrate CO_2 conversion to CO at mild temperature, the question of exact duration of this process raised by test C3 illustrates some potential variability in the achievable performance of this process for a sample of biomass. Considering this uncertainty remaining in the degree of CO_2 conversion previously observed, a further test of CO_2 gasification conditions at higher temperatures was performed to better illustrate the mechanisms of CO_2 conversion. Using the same flowrates of CO_2 and Ar from the earlier tests, a 1.5003g lignin sample was heated at 10°C/min up to a maximum temperature of 900°C.

Initial progress of the reaction (Figure 6-18) resembles the previous tests with a change in sample heating rate and a minor net-production of CO_2 at the beginning of sample devolatilisation. The temperature differential again shows five pyrolytic events and CH_4 and H_2 similarly follow the same trends in production, although the peak H_2 production is marginally higher than for the lower temperature CO_2 tests (8.76×10^{-6} mol/s, cf. 4.28×10^{-6} mol/s). Preliminary production of CO during pyrolysis is comparable to the low temperature cases, however CO production remains approximately constant at 1.2-1.4 $\times10^{-6}$ mol/s without peaking and then decreasing like happened under earlier low temperature cases.

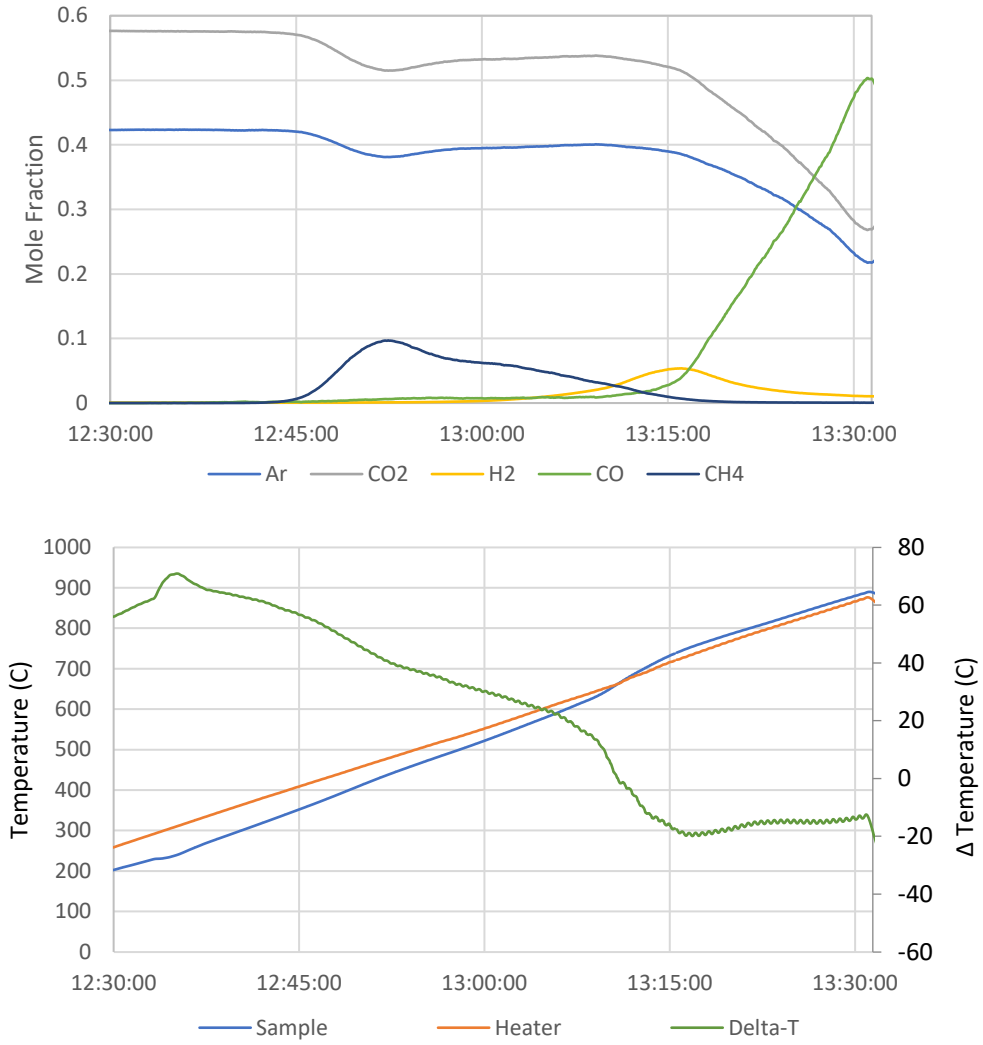

Figure 6-18: Product dry syngas species (top) and temperature profiles (bottom) for CO_2 gasification of lignin at 900°C. (Test C4)

As the reaction progresses both CO_2 consumption and CO production dramatically increase as the temperature rises beyond 700°C, reaching calculated consumption and production rates of 9.28×10^{-6} mol/s and 1.28×10^{-4} mol/s, respectively, as the temperature reaches 900°C. A similar qualitative result for CO generation was previously observed during lignin CO_2 gasification [133], however that mass spectrometry analysis did not quantify the production rate nor was CO_2 (m/z = 44) reported to confirm consumption of that species. Additionally, it reports only the m/z = 28 data and therefore does not distinguish CO from other potential syngas products like C_2H_4. Interestingly, that data also showed lignin samples producing increased levels of CH_4, H_2, and C_2H_2 around that same temperature, suggesting a secondary pyrolysis event occurs at these high temperatures.

Over the period of this experiment, a total of 1.5802 g of dry syngas was produced, representing 89.96%m of the supplied 1.5003g of feedstock and the 0.2065g of CO_2

consumed. The distribution of gaseous species is reported in Table 6-8 and includes a notable increase in the total production of CO. Results indicate the high temperature gasification experiment generated 43.36 mmol more CO than the average of the low temperature CO_2 cases and 44.43 mmol more CO on average than the original pyrolysis cases.

Table 6-8: Aggregate CO_2 consumption and dry syngas production for CO_2 gasification at 900°C (Test C4)

CO_2 consumed		**Dry syngas products**			
Total (mmol)	CO_2/C (effective)	CO_2 (mmol)	CO (mmol)	CH_4 (mmol)	H_2 (mmol)
6.453	0.0765	0.64	45.97	15.50	7.90

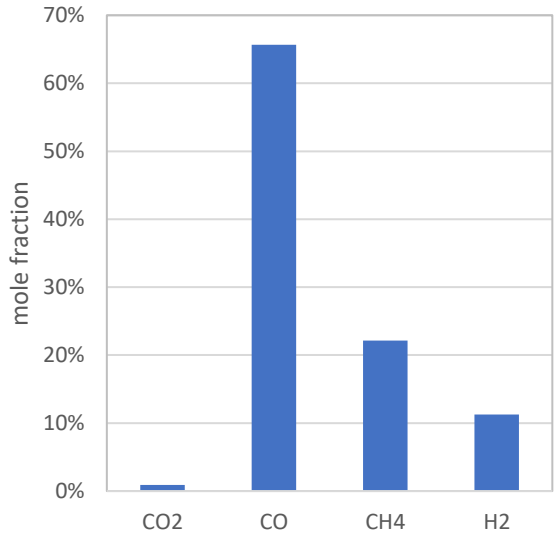

Figure 6-19: Distribution of total dry syngas products generated during CO_2 gasification at 900°C

While initial similarities of this case to the previous cases are expected due to the common temperature profiles, the latter gasification performance is attributable to the increased temperatures reached during char reduction. Further evidence that this high temperature conversion effect primarily influences char reduction is that pyrolysis appears to have ended before the rapid increase in CO_2 consumption. CH_4 production is decreasing at that time and although H_2 production overlaps with the start of the rapidly increasing CO_2 consumption regime, peak H_2 production rates and overall H_2 generated in this case were both greater than in the low temperature experiments. This might indicate that H_2 is not a significant reactant with CO_2 in this test, given the overall increase in total production, but the difference in reaction temperature could offer a complementary mechanism to enhance the rWGS reaction. Pyrolysis at higher temperature does tend to release more hydrogen

from the biomass sample as H_2 [143] and this effect likely contributes to the higher H_2 production rates while also providing additional H_2 that could be consumed in a rWGS reaction. Lignin samples have previously shown increased production rates of hydrogen containing gases at temperatures over 700°C [133]. Since the current data does not show this expected release of hydrogen, it could indicate those species are consumed in reforming or shift reactions with the CO_2, further enhancing the CO production at high temperatures.

Nevertheless, the greatest rate of change in the CO_2 consumption rate occurred as the lignin sample was heated beyond ~700°C. This result further indicates that char reduction likely contributes to CO_2 consumption at this point since the magnitude of the equilibrium constant for the reverse Boudouard reaction becomes greater than 1 under these temperatures (ref. Figure 3-1). While the experimental system is unlikely experiencing equilibrium conditions, such a change to the equilibrium constant indicates the products of the reaction (i.e. CO) become thermodynamically favourable compared to the reactants (i.e. CO_2) and helps to explain the rapid change in CO_2 consumption/CO production rates.

It is possible that several of these discussed processes are reacting in parallel to generate the observed results. For instance, if the reverse Boudouard reaction was the only mechanism active within the system, the ratio between the rate of CO production and CO_2 consumption should be approximately 2:1 based on the stoichiometry of that reaction while the ratio would be 1:1 if rWGS, ODH, or primary water-gas reactions were dominant. As it stands, this ratio is slightly below 2 during the early stages of the experiment, but quickly increases beyond 10 as the reaction temperature approaches the maximum. Although this ratio exceeds the anticipated range, the gasifying agent may not be the only source of CO_2 in the system. Higher temperature pyrolysis is likely to liberate additional gases [138], including CO_2 and CO, that could influence the consumption and production rates, respectively. Unfortunately, char residues could not be recovered from this test case so the mass and elemental analysis that could support this hypothesis could not be completed, nor could a high temperature pyrolysis test be performed to confirm whether additional pyrolysis gases would be released under these conditions.

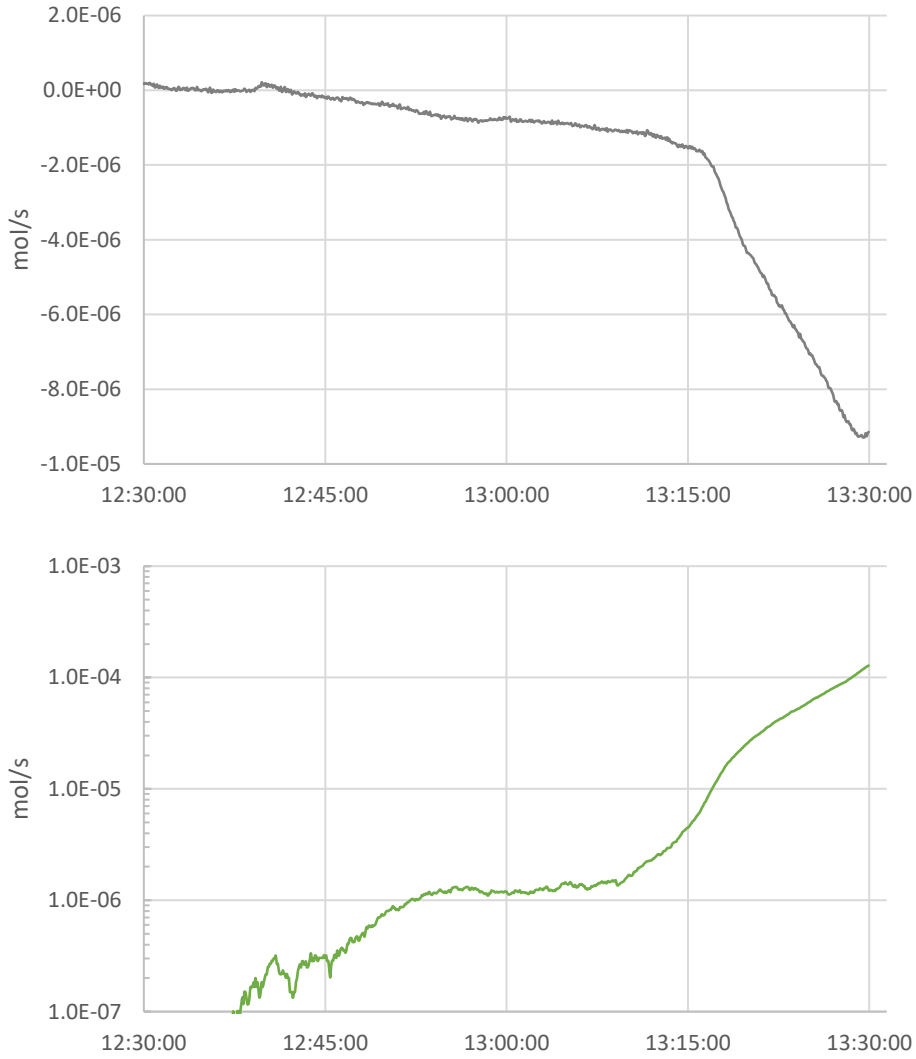

Figure 6-20: Net-CO_2 (top) and CO (bottom, logarithmic scale) production during CO_2 gasification of lignin at 900°C (Test C4)

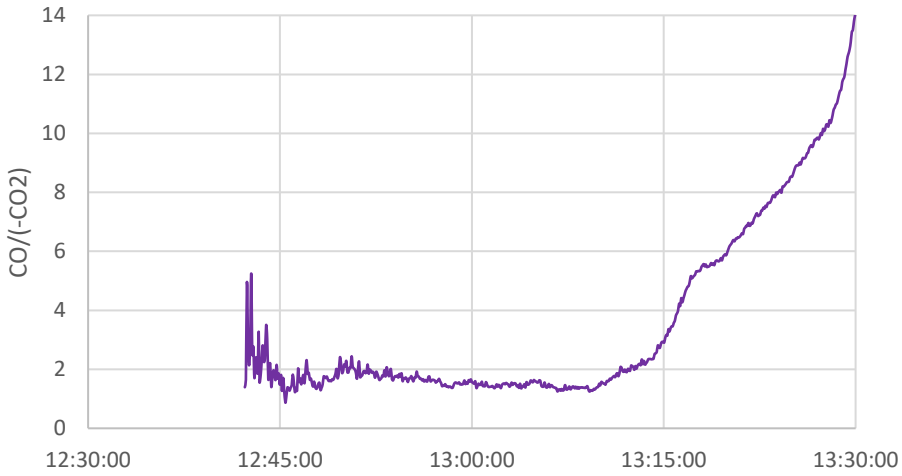

Figure 6-21: Ratio of CO production to CO_2 consumption for CO_2 gasification of lignin at 900°C (Test C4)

6.3.5 CO_2/O_2 co-gasification

Lignin samples are gasified under a mixture of 42 mL/min O_2 and 42 mL/min CO_2 using 90 mL/min of Ar as a tracer gas. The sample is heated at a rate of 8.5°C/min up to the maximum gasification temperature of 600°C. During these tests, *m/z* = 40 and *m/z/* = 44 mass spectra data were corrupted and could not be used. The *m/z* = 20 mass spectrum is substituted to determine the Ar partial pressure and the NDIR data was substituted directly to determine the molar fraction of CO_2 in the syngas.

O_2 consumption in the co-gasification experiments was slightly higher than for the air gasification cases, producing equivalence ratios of λ = 0.564-0.613. This is likely due to the higher partial pressure of O_2 in the gasifying mixture. The oxygen content of the gasifying agent was ~25%v for these co-gasification conditions compared to ~12-15 %v for the air cases. Pyrolysis remains the main process for production of H_2 and CH_4 during these tests, although the distinct pyrolytic events previously seen under inert atmosphere experiments are less evident here. Average amounts of these hydrogen containing products are marginally lower than in the previous cases, possibly suggesting the higher O_2 concentration may have oxidised these species. Profiles of CO_2 production rates indicate that the overall production of CO_2 outpaced any consumption rates as the net-CO_2 remained positive throughout the experiments.

The total CO_2 produced during these cases was lower by 9.5% (3.94 mmoles) on average than under the air gasification conditions, although significant variance in CO_2 production for the co-gasification tests creates some uncertainty around this observation. Nevertheless, this could indicate some CO_2 is reacting with the feedstock in this case. Again, this is not a net-consumption of CO_2 during the experiment, however the counterfactual difference in CO_2 production compared to a traditional air gasification condition implies this difference could be considered evidence of limited CO_2 conversion. CO production, however, does not show a general corresponding enhancement compared to the air gasification case.

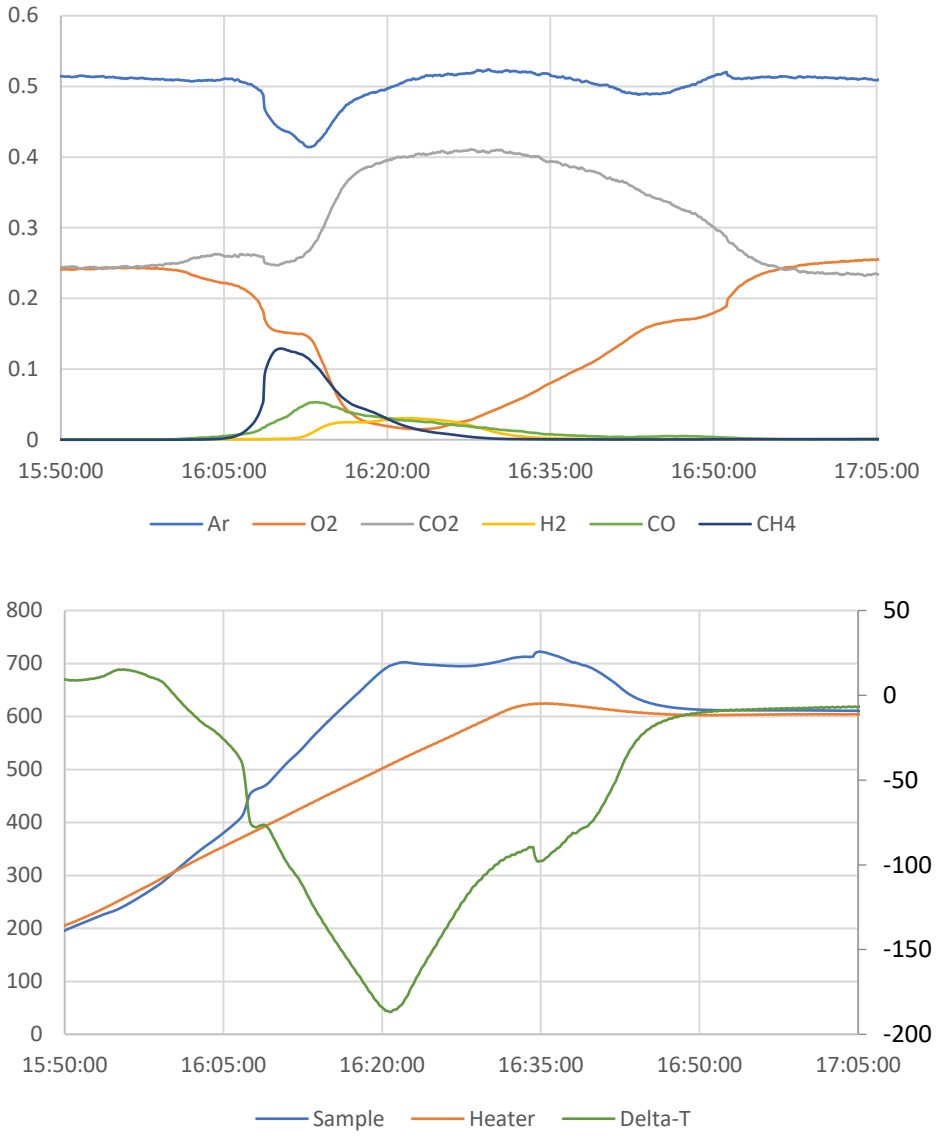

Figure 6-22: Product dry syngas species (top) and temperature profiles (bottom) for O2/CO2 gasification of lignin at ~600℃. (Test M1)

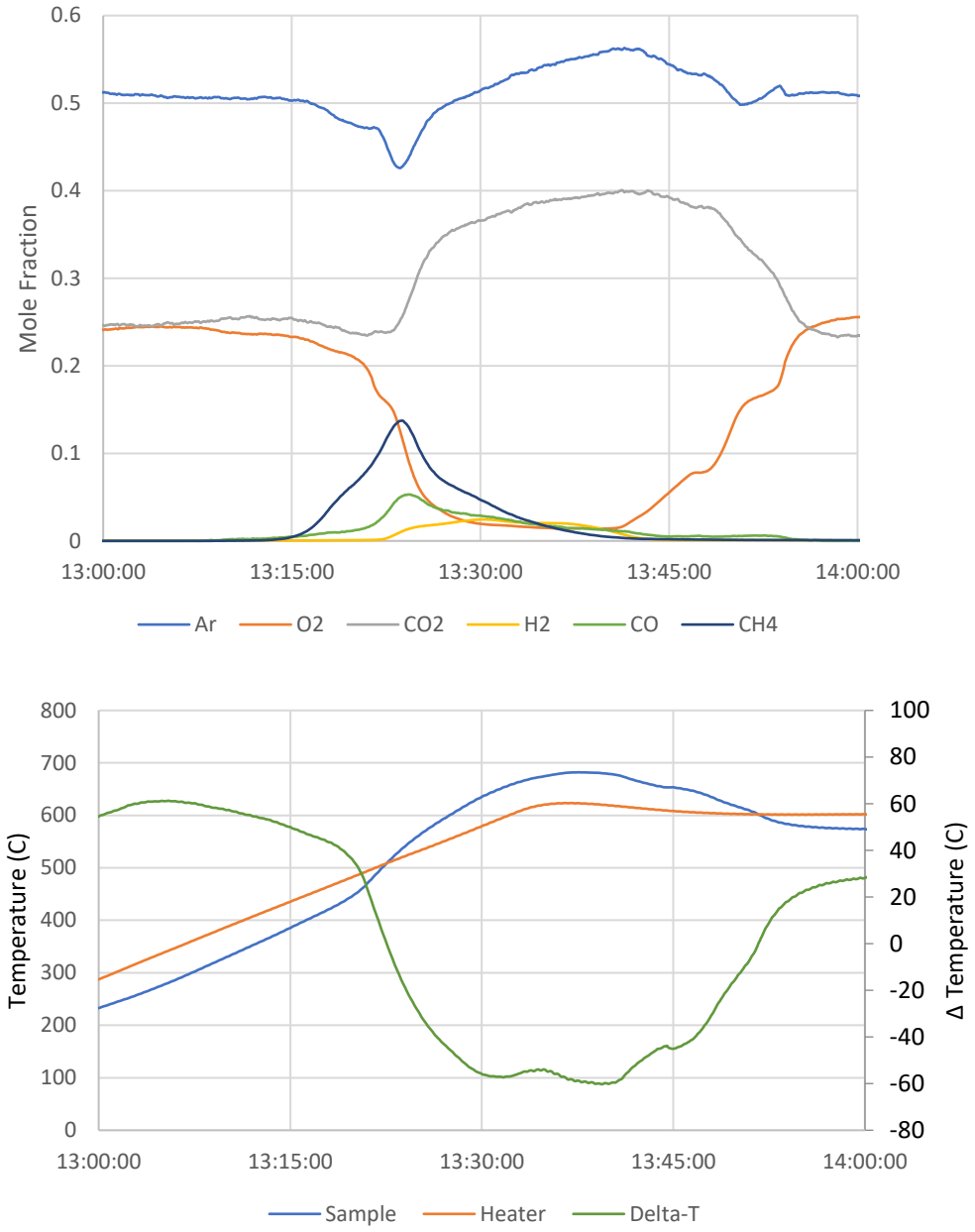

Figure 6-23: Product dry syngas species (top) and temperature profiles (bottom) for O2/CO2 gasification of lignin at ~600℃. (Test M2)

Temperature profiles for these cases highlight some of the experimental variability in the observed processes, particularly in the exothermic behaviour of the oxidation processes. Furthermore, differences in pyrolysis behaviour between the two oxyfuel-CO_2 cases are observed however the overall impact on species production is unclear. Internal variability for this experimental condition is high and creates uncertainty in the repeatability of the observations. Ultimately, clearer data are needed to determine the degree of CO_2 conversion and overall impact of CO_2/oxyfuel gasification processes but this data could form the basis of future work on this topic.

From the data available, there are some common trends for these co-gasification cases that allude to processes previously discussed. While the temperature feature is less pronounced, there is still a clear pyrolytic even that initiates the process and is responsible for the production of CH_4 and H_2 species. Despite the variability, oxidative reactions create high temperatures that generate local regions of enhanced CO production, further suggesting some degree of CO_2 conversion, however the aggregate effect is minimal compared to the air gasification CO production. Nevertheless, the data remain too variable to provide certainty of these effects.

Table 6-9: Aggregate O_2 consumption and dry syngas production for O_2/CO_2 gasification at 600°C

	O_2 consumed		**Dry syngas products**			
	Total (mmol)	λ (effective)	Net-CO_2 (mmol)	CO (mmol)	CH_4 (mmol)	H_2 (mmol)
Test M1	45.77	0.5637	29.52	5.52	10.69	3.15
Test M2	49.81	0.6137	45.30	7.14	10.00	3.85
Mean	47.79	0.5887	37.41	6.33	10.35	3.50

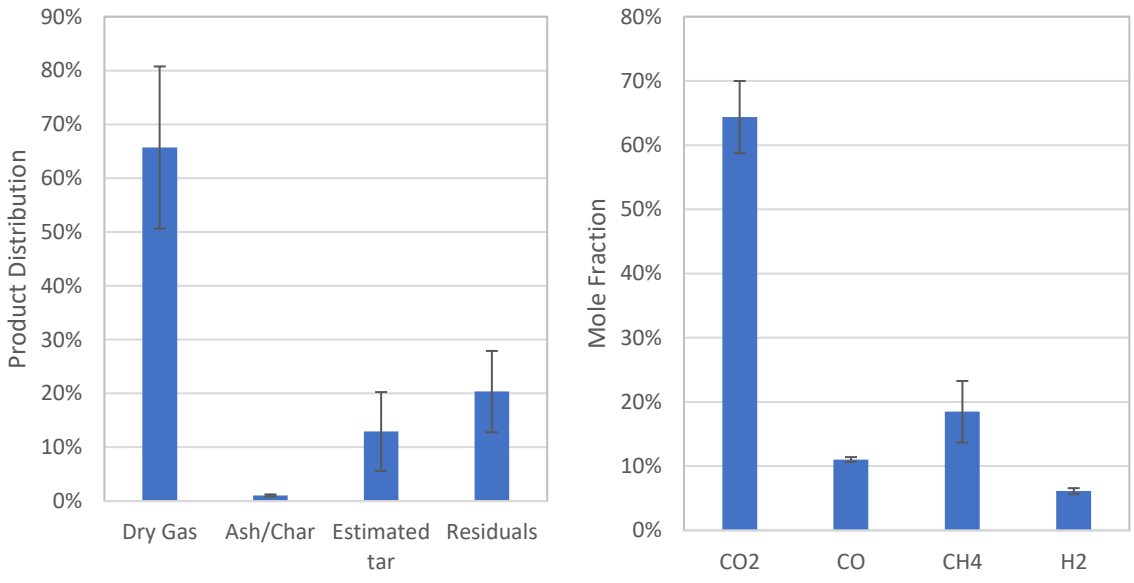

Figure 6-24: Product mass distribution and dry syngas mole fractions for O_2/CO_2 gasification at 600°C

6.4 Conclusions

Experimental pyrolysis and gasification of lignin samples has provided the basis for examining the effect of CO_2 gasification agents at mild reaction temperatures. The following conclusions are drawn for the presented results:

- Pyrolytic decomposition of the feedstock produces significant amounts of CH_4 and is the main source of H_2 for the experiments recorded.
- When supplied at relatively high concentrations in a gasifying agent mixture, CO_2 appears to be consumed in the resulting reaction. This indicates a concentration-based push to drive CO_2 conversion reactions is possible but has limited effectivity.
- Even at low gasification temperatures, small rates of net-CO_2 consumption are observed, although some uncertainty on the efficacy of this process remains.
- Use of CO_2 as a gasifying agent at mild temperatures appears to marginally increase the production of CO compared to pyrolysis under an inert atmosphere.
- CO_2 conversion into CO becomes much more effective at temperatures above 700°C compared to milder temperatures. This is thought to be achieved through the reverse Boudouard reaction acting during char reduction.
- Effects of CO_2 gasification on the production of H_2, CH_4, and char compared to pyrolysis are uncertain at mild gasification temperatures, although the timing of CO production continuing after pyrolysis events have ceased suggests that char may be reactive with the CO_2.
- Use of an O_2/CO_2 gasifying mixture may also have some limited potential to consume CO_2 when compared to traditional air cases, however significant variance in mixed gasification results add some uncertainty.

Since the only observed process that generates CH_4 is the initial pyrolysis of the sample, it must be concluded that this is the source of the relatively high CH_4 content observed in these experiments. Additionally, this means that the CH_4 from pyrolysis is not active with the CO_2 gasifying agent when it is generated, signifying that reforming reactions were not significantly involved in the processes studied here. Combined with the observed performance of the Boudouard reaction, there seems to be some variation in these real gasification tests compared to the expectations from the equilibrium modelling results. It is, of course, important to note that these experiments were conducted on a small sample of biomass and not in a model gasifier with a continuous bed of material thus the CH_4 was produced at lower temperatures and largely removed from the reactor before the main char

reduction process occurred at high temperatures. These are indeed the types of processes that must be better understood in order to design gasifiers capable of achieving the beneficial conditions reported in the simulations of chapters 4 and 5.

When considered in context of the previous modelling scenarios, these conclusions highlight practical challenges to achieving the maximised efficiencies reported in those studies. Efficiency gains in thermodynamic CO_2 gasification simulations occur at lower gasification temperatures and equivalence ratios, however these conditions are difficult to confirm experimentally. Nevertheless, evidence from these experiments shows some amount of mild temperature CO_2 conversion occurs at temperatures comparable to the system modelling cases. Furthermore, pyrolysis effects create more CH_4 and, consequently, less H_2 than predicted under the thermodynamic modelling cases. Although not examined in detail, experimental tar production is a further effect not addressed in the thermodynamic models.

Despite these discussed difficulties, the results generally support the principle of exhaust gas recirculation as a CDU method to enhance gasification. Additionally, examining the NDIR-MS data provides insights into underlying processes contributing to the feedstock conversion. This improved understanding of gasification performance under CO_2 atmospheres will be useful in developing future gasifier designs optimised for CDU applications.

Chapter 7 Conclusions and Future Work

The central goal of this work is to assess the use of recycled CO_2 in integrated gasification cycles as a CDU method for improving the performance of biomass energy and BECCS cycles. In particular, the following relevant topics have been investigated:

- Evaluated system-level impacts of using a direct method for local CO_2 utilisation within biomass energy cycles.
- Evaluated the potential for direct CO_2 utilisation cycles to improve the efficiency of BECCS systems.
- Determined how CO_2 utilisation within these cycles affects the conversion of biomass feedstocks.
- Assessed both the conversion and non-conversion CO_2 utilisation processes and their effects on the overall cycle performance.
- Determined how underlying gasification processes, particularly under a CO_2 gasifying agent, affect the composition of syngas produced from a sample of biomass.

7.1 Principal Findings

Analysis of representative numerical models has examined the capacity for direct CDU in biomass gasification power cycles using EGR enhanced gasification. Both oxyfuel BECCS and air-blown biomass power cycle configurations have shown some benefit of CO_2 gasification as a direct CDU application, with oxyfuel BECCS cycles improving efficiency by up to 10.29%. Further experimental work has studied the conversion of CO_2 in a gasification process to highlight practical challenges of CO_2 gasification under these conditions.

This technical assessment has highlighted the thermodynamic benefits and limitations of EGR enhanced gasification as a direct CDU strategy for a biomass IGC, leading to a detailed understanding of the system thermodynamic conditions under different operating points. It provides a system-level understanding of how EGR influences an IGC and serves as a baseline for future detailed analysis including specific gasifier designs. All cases of exhaust recycling, whether in oxyfuel BECCS configurations or in air/CO_2 IGC configurations, resulted in a system with a high degree of thermal coupling between the gasifier and engine.

Air gasification IGC power cycles studied in Chapter 4 showed minor improvements in indicated output power, system efficiency, and specific emissions under modest exhaust CO_2 recycling conditions. Over certain ranges, EGR supply to the gasifier lowered the air ratio required in the gasifier to maintain full carbon conversion, thus increasing CGE. Recycling 0.136 mol-CO_2/mol-C to a gasifier with an air-ratio of $\lambda = 0.250$ increased overall system efficiency by 1.1% and reduced the specific CO_2 emissions by 46.2 g-CO_2/kWh compared to the reference system configuration.

Significant limitations to those air/CO_2 gasification cycles were caused by exhaust recycling diluting the syngas with excess N_2 and CO_2. Lower LHV, lower EGT, and thus lower equilibrium temperatures were immediate consequences of this inert diluent build-up in the system. High amounts of EGR limits the gasifier thermodynamic performance since lower equilibrium temperatures cause lower CO_2 conversion and thus lower syngas quality. Gasification equilibrium temperatures dropped by 318°C from the reference case when the gasifier had 0.136 mol-CO_2/mol-C of exhaust recycled and the air-ratio reduced to $\lambda = 0.250$. The net-CO_2 utilisation decreased and the H_2:CO ratio tended to increase with exhaust recycling due to lower equilibrium temperatures.

Modelling techniques in Chapter 4 revealed the impact of N_2 dilution is most prevalent in the engine exhaust temperatures. In total, syngas N_2 dilution lowered the overall system efficiency by 2.5 percentage points and increased specific emissions by 72.4 g-kWh, or 6.16%, compared to a N_2-free syngas. This suggests CDU aspects of the system could be further enhanced if additional syngas upgrading or diluent removal is implemented.

Due to unfavourable thermodynamic conditions in the gasifier, most air/CO_2 cases studied showed poor CO_2 conversion to syngas. This indicates the primary use of recycled CO_2 under these conditions is as a heat transfer medium rather than chemically active reagent. Evidence of enhanced CO_2 chemical conversion to CO is limited to the point of full char conversion in 650°C gasifiers, with N_2 dilution of the syngas also diminishing this effect.

Oxyfuel gasification simulations in Chapter 5 showed recycled exhaust gases are an effective gasifying agent for converting biomass feedstocks into syngas fuel, however the integration of recycling in a gasification power system is complex due to thermodynamic coupling of the gasification and power generation processes. Exhaust recycling improved the thermodynamic conditions of gasification through concentration and temperature-based equilibrium shifts, increasing the CGE and consequently improving the indicated energy

efficiency of the cycle. Exhaust recycling also enhanced the reverse Boudouard reaction thermodynamics such that lower equivalence ratios can be used while still fully converting the feedstock carbon content. However, use of idealised power cycle models overpredicts the work output and exhaust temperatures compared to detailed models that account for combustion dynamics and heat losses. This can cause indicated efficiencies in the ideal models to exceed the efficiency of a detailed model by nearly 20%.

These oxyfuel cycles recycling 2.562 molCO_2/molC at an equivalence ratio $\lambda = 0.150$ improved the indicated cycle efficiency by 10.29% compared to a reference IOGC cycle without exhaust recycling at an equivalence ratio $\lambda = 0.300$. Exhaust gases were best used in excess as a gasifying agent rather than in an isolated EGR loop within the engine to control combustion temperatures. The resulting syngas contained sufficient CO_2 concentrations to limit the peak cylinder temperature while simultaneously improving the thermodynamics of the conversion reactions to enhance syngas production in the gasifier.

Gasification in this recycling IOGC is thermodynamically limited to equilibrium temperatures above 576°C and equivalence ratios above $\lambda = 0.130$. Conditions below these limits will not be capable of fully converting the carbon content in the feedstock. This condition also corresponds to the maximum indicated cycle efficiency of 26.92% for the configurations studied. Exhaust recycling leverages both conversion and non-conversion CDU features within the cycle. While conversion of exhaust CO_2 into useful syngas is apparent in all exhaust recycling studies, the role of CO_2 as a heat transfer medium to return waste heat to the gasifier has a predominant effect on gasification thermodynamics and overall cycle efficiency.

Although the specific values of cycle efficiency calculated in Chapter 5 are likely associated with the particular design and operating conditions for the cycle used in this analysis, the comparison of these modelling cases reveals that exhaust recycling techniques are an effective method to enhance the thermodynamic conditions of gasification on a system level. Additional work to expand detailed BECCS cycle models, determine specific economic metrics, or to develop pilot scale plants using these techniques will be useful in further assessing the scale and quantifying the benefits of this cycle design.

Despite the highly promising thermodynamic effects of CO_2 recycling in the integrated models presented in Chapters 4 and 5, experimental studies in Chapter 6 have shown the CO_2 conversion at mild temperatures remains poor for samples of biomass lignin gasified

under CO_2 atmospheres. Real gasification processes have underlying chemical events that can cause the produced syngas to vary from the thermodynamic ideal.

Firstly, pyrolytic decomposition of the feedstock produces significant amounts of CH_4 and is the main source of H_2 for the experiments recorded. Furthermore, CO_2 appears to be consumed in the resulting gasification reaction when supplied at relatively high concentrations in a gasifying agent mixture. This indicates a concentration-based push to drive CO_2 conversion reactions is possible but has limited effectivity. Even at mild gasification temperatures, small rates of net-CO_2 consumption are observed, although some uncertainty on the efficacy of this process remains. Use of CO_2 as a gasifying agent appears to marginally increase the production of CO compared to pyrolysis under an inert atmosphere.

CO_2 conversion into CO becomes much more effective at temperatures above 700°C compared to milder temperatures. This is thought to be achieved through the reverse Boudouard reaction acting during char reduction. Effects of CO_2 gasification on the production of H_2, CH_4, and char compared to pyrolysis are uncertain at mild gasification temperatures, although the timing of CO production continuing after pyrolysis events have ceased suggests that char may be reactive with the CO_2 Use of an O_2/CO_2 gasifying mixture may also have some limited potential to consume CO_2 when compared to traditional air cases, however significant variance in mixed gasification results add some uncertainty.

7.2 Areas for Future Research

Having demonstrated both the thermodynamic benefit and significant practical challenges in experimentally achieving these benefits, a substantial area for future work is in modifying existing biomass gasifier designs to improve mild-temperature conversion performance. Use of kinetic or CFD simulations and exergy analyses will be particularly useful to understand what elements of gasifier design are preventing the full thermodynamic conditions from being realised.

Given the modest improvements to traditional, non-BECCS biomass energy system performance, following work should also adopt an economic scope to determine the feasibility and potential impact of this CDU strategy when applied in practise. Additional work to expand detailed BECCS cycle models, determine specific economic metrics, or to

develop pilot scale plants using these techniques will be useful in further assessing the scale and quantifying the benefits of this cycle design. Furthermore, studies that adopt an economic scope should investigate the potential impacts of CO_2 recycling on the costs of future BECCS deployment. The observed 10% increase in efficiency for the cycles considered appears attractive, but a detailed comparison with existing BECCS cycles on both costs of CO_2 removal and on overall lifecycle emissions will also be needed to ultimately assess the capacity for this novel cycle to contribute to meeting climate targets.

Appendix A - Fundamental thermodynamic identities

Evaluation of any thermodynamic system will consider the fundamental state variables of pressure, temperature, volume, and quantity, either in mass or molar terms. Combined with the first law of thermodynamics (equation (0.1)), the following thermodynamic identities (equations(0.3)-(0.7)) are established for a system that obeys the ideal gas law (equation (0.2)) as its equation of state.

$$\Delta U = \Delta Q + \Delta W \tag{0.1}$$

$$P \cdot V = n \cdot R \cdot T \tag{0.2}$$

$$H = U + P \cdot V \tag{0.3}$$

$$C_V = \left(\frac{\delta U}{\delta T}\right)_V \tag{0.4}$$

$$C_P = \left(\frac{\delta H}{\delta T}\right)_P \tag{0.5}$$

$$\gamma = \frac{C_P}{C_V} \tag{0.6}$$

$$R = C_P - C_V = \gamma - 1 \tag{0.7}$$

Appendix B - Deriving Gibbs free energy changes based on a chemical reaction

For the following reaction at pressure, P_r:

$$\nu_A A + \nu_B B \rightarrow \nu_C C + \nu_D D$$

Use the individual species Gibbs functions in the equation for the reaction change in Gibbs free energy:

$$\Delta G_r = \sum_{products} \nu_i \Delta G_i - \sum_{reactants} \nu_j \Delta G_j$$

$$\Delta G_r = \Delta \mathrm{G}_\mathrm{r}^0 + RT\left(\nu_C \ln\left(\frac{P_C}{P^0}\right) + \nu_D \ln\left(\frac{P_D}{P^0}\right)\right) - RT\left(\nu_A \ln\left(\frac{P_A}{P^0}\right) + \nu_B \ln\left(\frac{P_B}{P^0}\right)\right)$$

Apply rules for logarithm/exponents:

$$\Delta G_r = \Delta \mathrm{G_r}^0 + RT \ln\left(\frac{\left(\frac{P_C}{P^0}\right)^{\nu_C} \cdot \left(\frac{P_D}{P^0}\right)^{\nu_D}}{\left(\frac{P_A}{P^0}\right)^{\nu_A} \cdot \left(\frac{P_B}{P^0}\right)^{\nu_B}}\right)$$

$$\Delta G_r = \Delta \mathrm{G}_\mathrm{r}^0 + RT \ln\left(\frac{\frac{P_C^{\nu_C} P_D^{\nu_D}}{P^{0(\nu_C+\nu_D)}}}{\frac{P_A^{\nu_A} P_B^{\nu_B}}{P^{0(\nu_A+\nu_B)}}}\right) = \Delta \mathrm{G}_\mathrm{r}^0 + RT \ln\left(\frac{(P_r x_C)^{\nu_C}\,(P_r x_D)^{\nu_D}}{(P_r x_A)^{\nu_A}(P_r x_B)^{\nu_B}} \cdot \frac{P^{0(\nu_A+\nu_B)}}{P^{0(\nu_C+\nu_D)}}\right)$$

$$= \Delta \mathrm{G}_\mathrm{r}^0 + RT \ln\left(\frac{x_C^{\nu_C} x_D^{\nu_D}}{x_A^{\nu_A} x_B^{\nu_B}} \frac{P^{0(\nu_A+\nu_B)}}{P^{0(\nu_C+\nu_D)}} \frac{P_r^{(\nu_C+\nu_D)}}{P_r^{(\nu_A+\nu_B)}}\right)$$

$$= \Delta \mathrm{G}_\mathrm{r}^0 + RT \ln\left(\frac{x_C^{\nu_C} x_D^{\nu_D}}{x_A^{\nu_A} x_B^{\nu_B}}\right) + RT \ln\left(\frac{P_r^{(\nu_C+\nu_D-\nu_A-\nu_B)}}{P^{0(\nu_C+\nu_D-\nu_A-\nu_B)}}\right)$$

$$= \Delta \mathrm{G}_r^0 + RT \ln\left(\frac{x_C^{\nu_C} x_D^{\nu_D}}{x_A^{\nu_A} x_B^{\nu_B}}\right) + (\Delta n_r) RT \ln\left(\frac{P_r}{P^0}\right)$$

Appendix C - Reference Infrared and Mass Spectra of Select Gas Species [120]

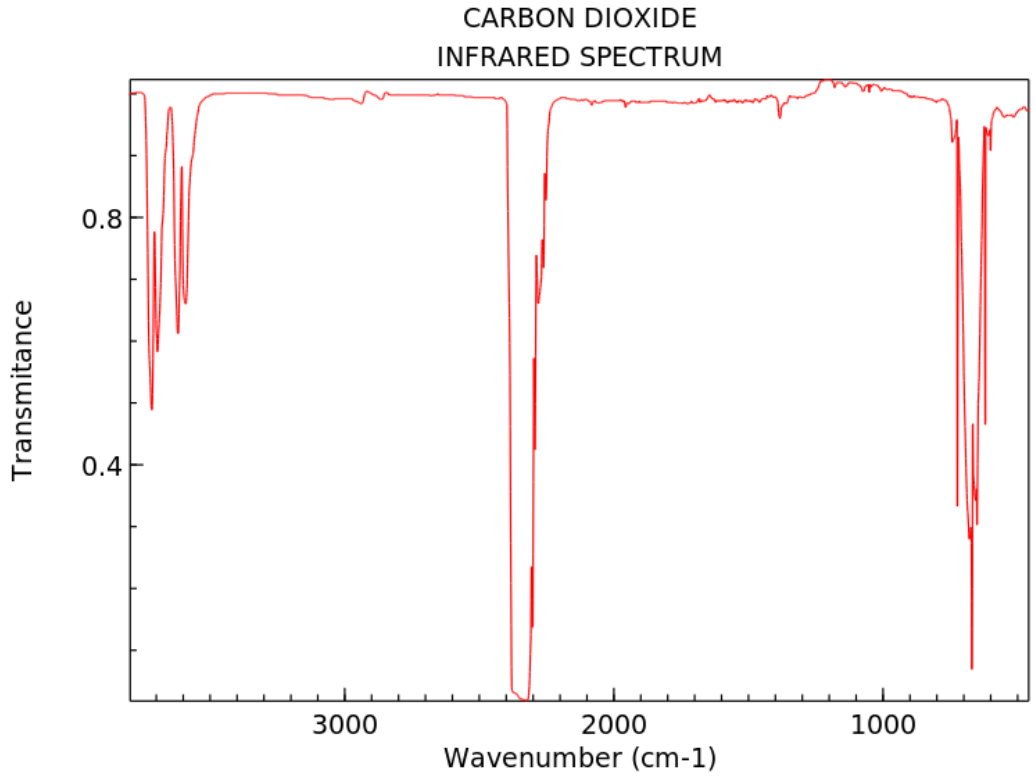

NIST Chemistry WebBook (https://webbook.nist.gov/chemistry)

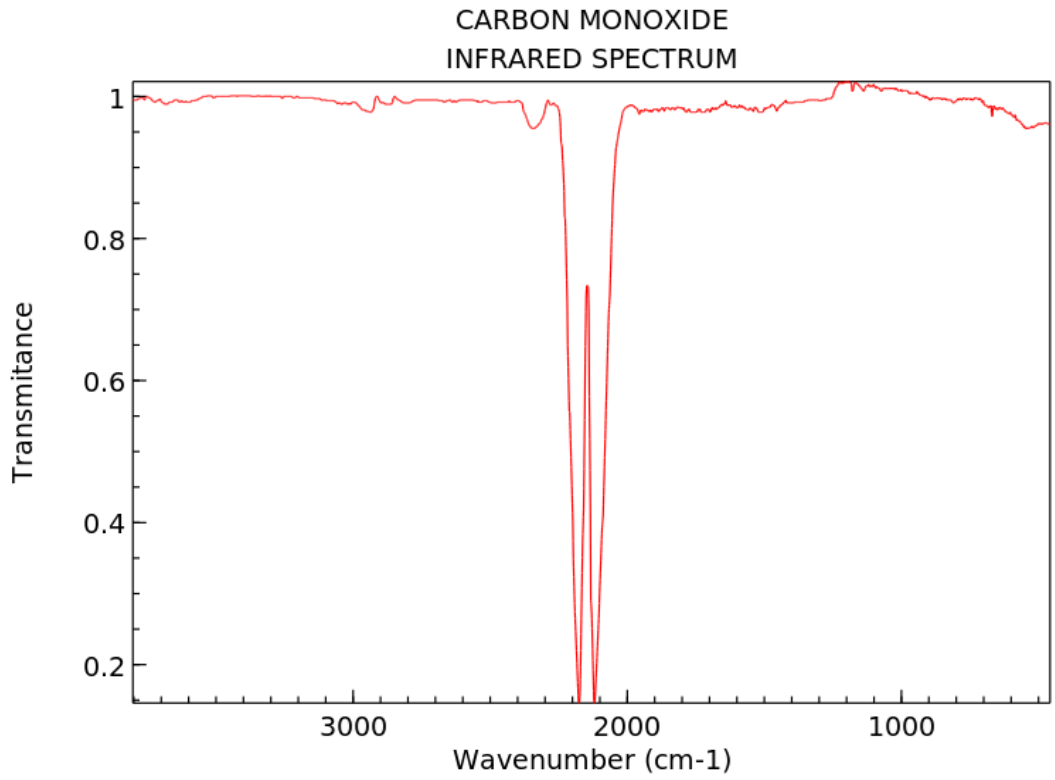

NIST Chemistry WebBook (https://webbook.nist.gov/chemistry)

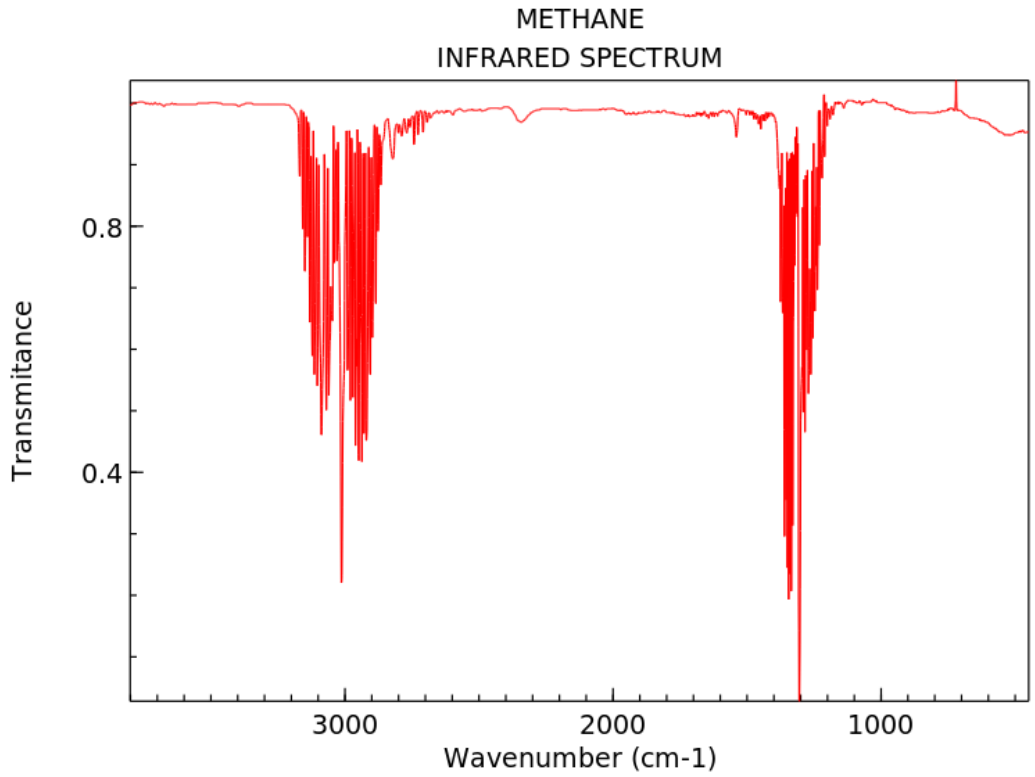

NIST Chemistry WebBook (https://webbook.nist.gov/chemistry)

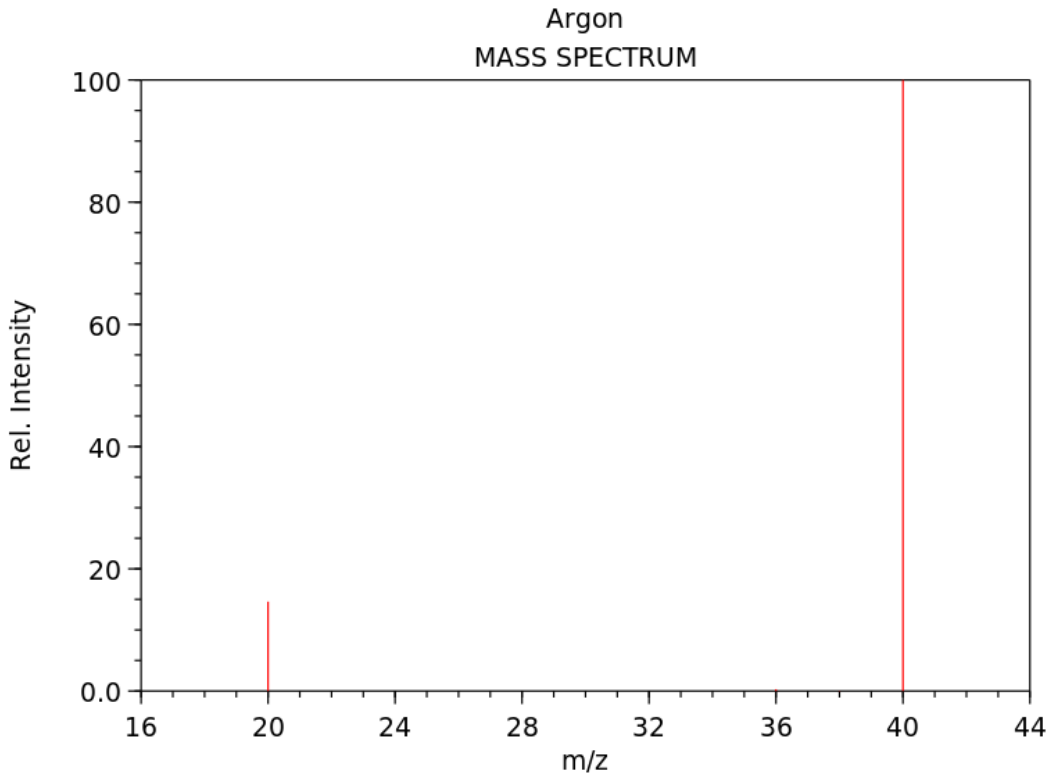

NIST Chemistry WebBook (https://webbook.nist.gov/chemistry)

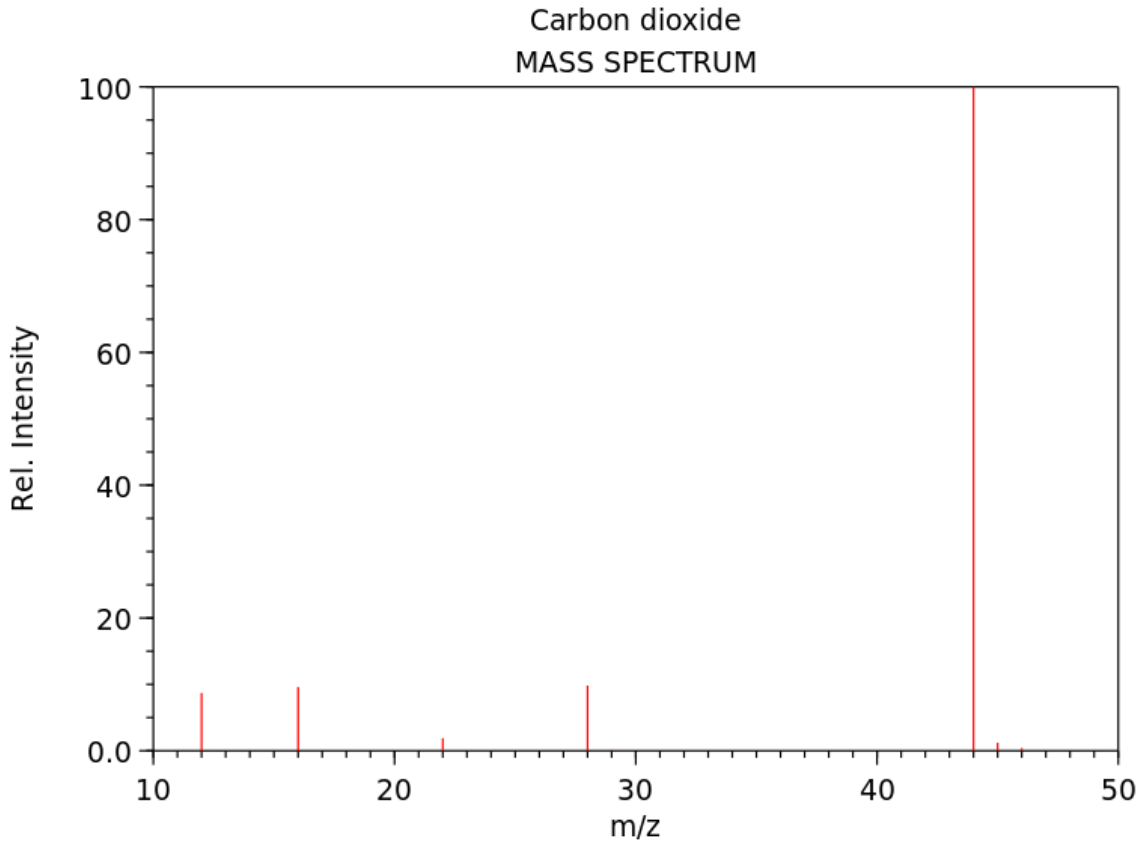

NIST Chemistry WebBook (https://webbook.nist.gov/chemistry)

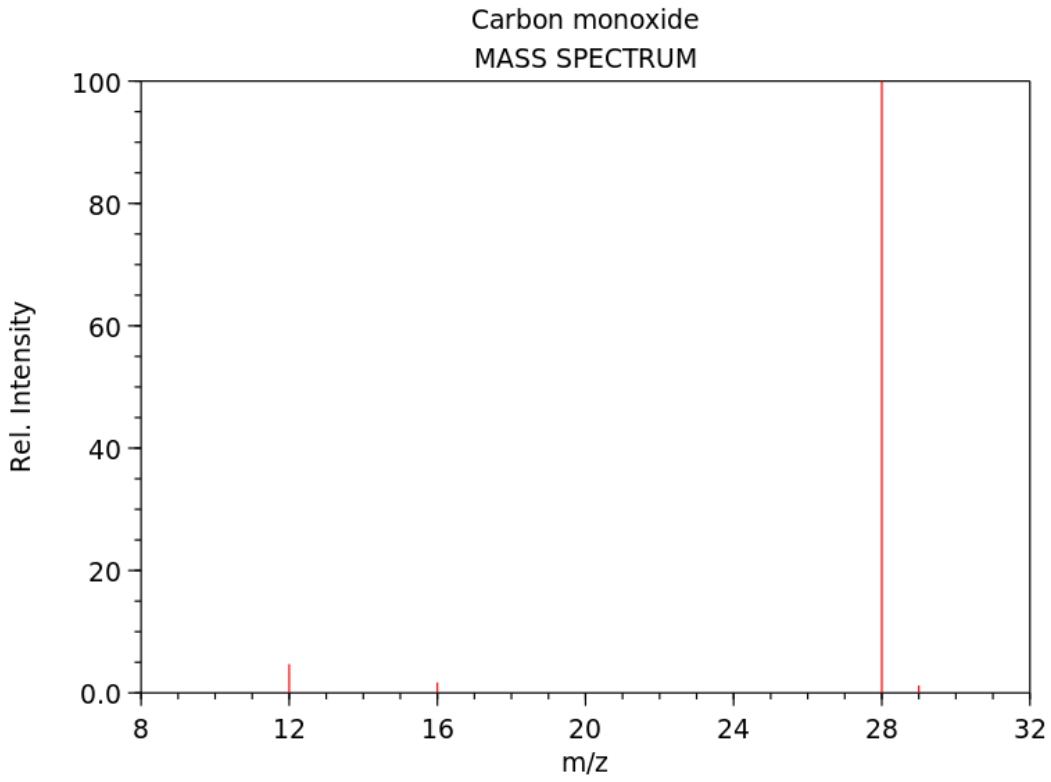

NIST Chemistry WebBook (https://webbook.nist.gov/chemistry)

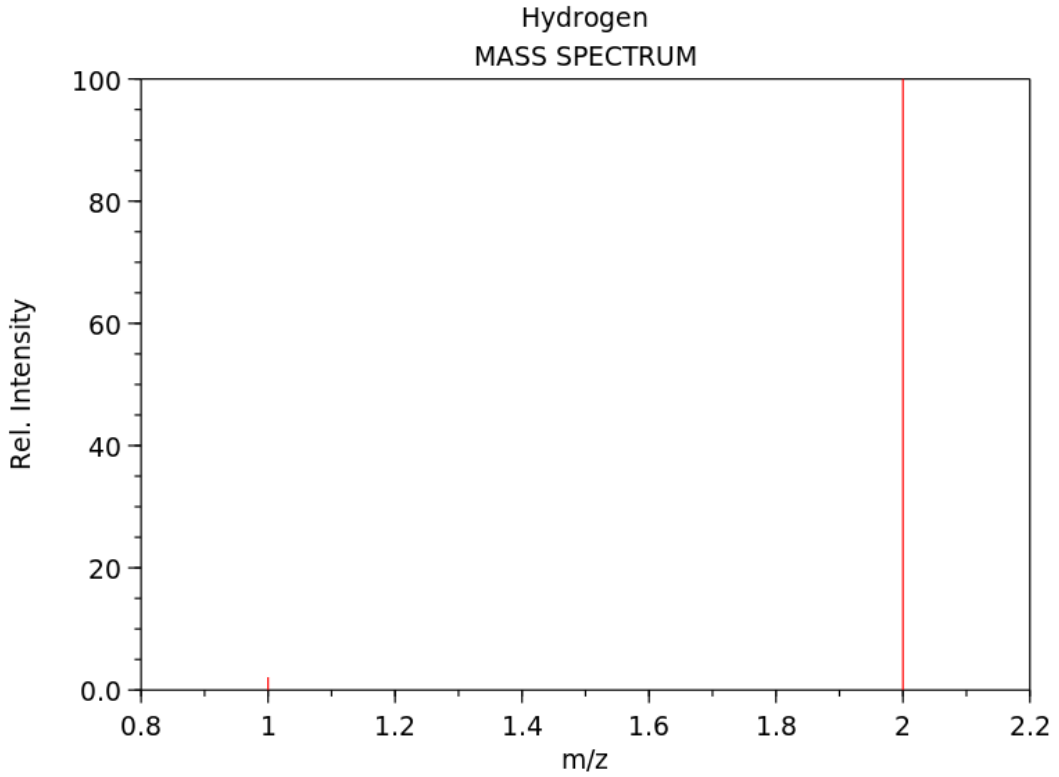

NIST Chemistry WebBook (https://webbook.nist.gov/chemistry)

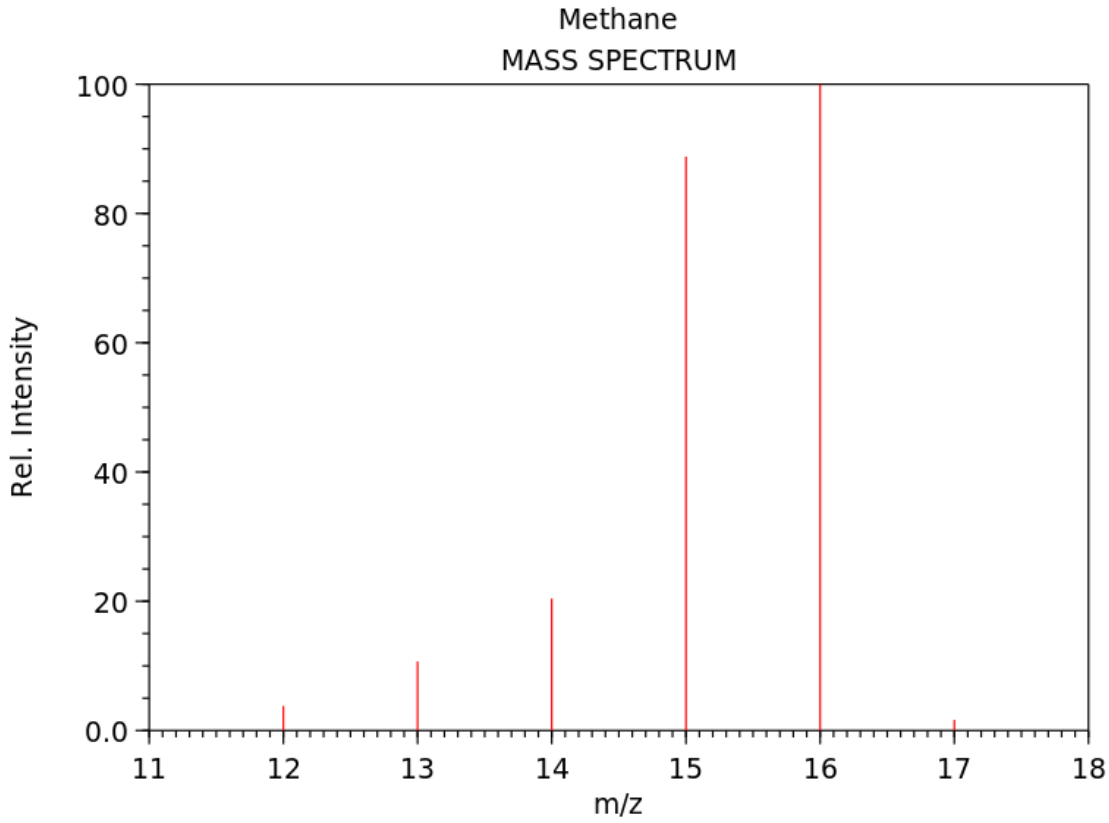

NIST Chemistry WebBook (https://webbook.nist.gov/chemistry)

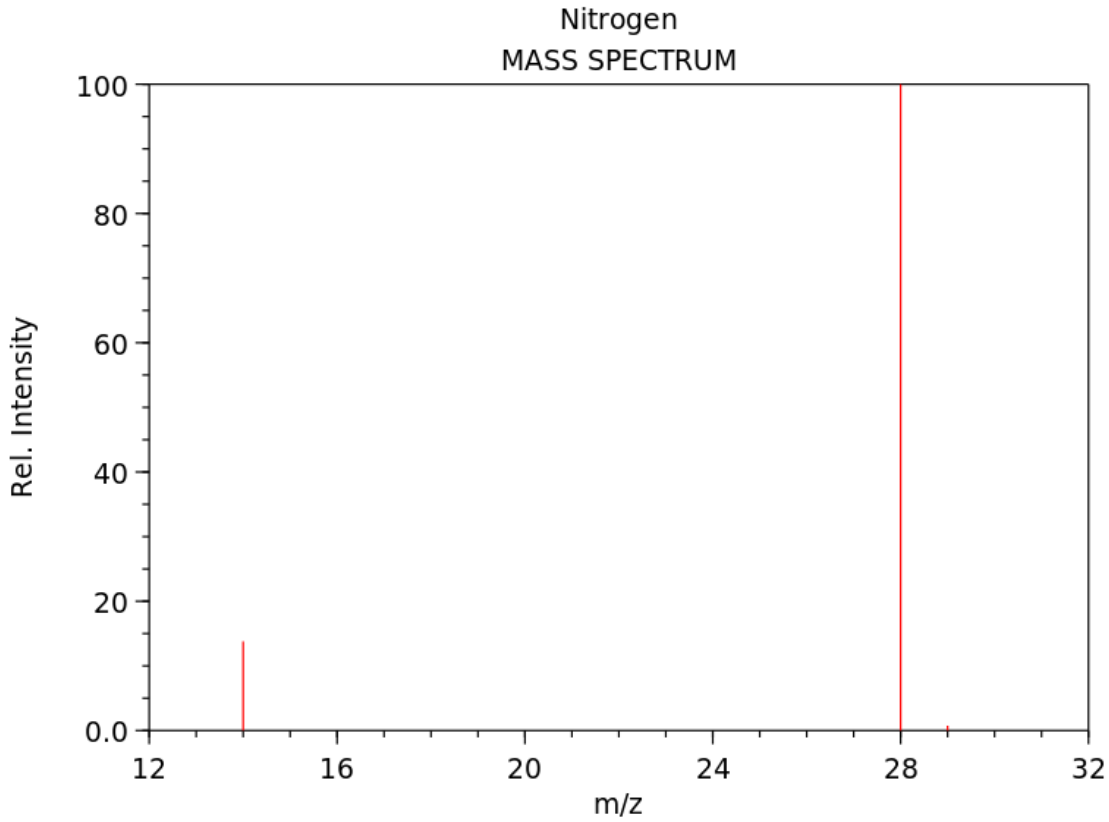

NIST Chemistry WebBook (https://webbook.nist.gov/chemistry)

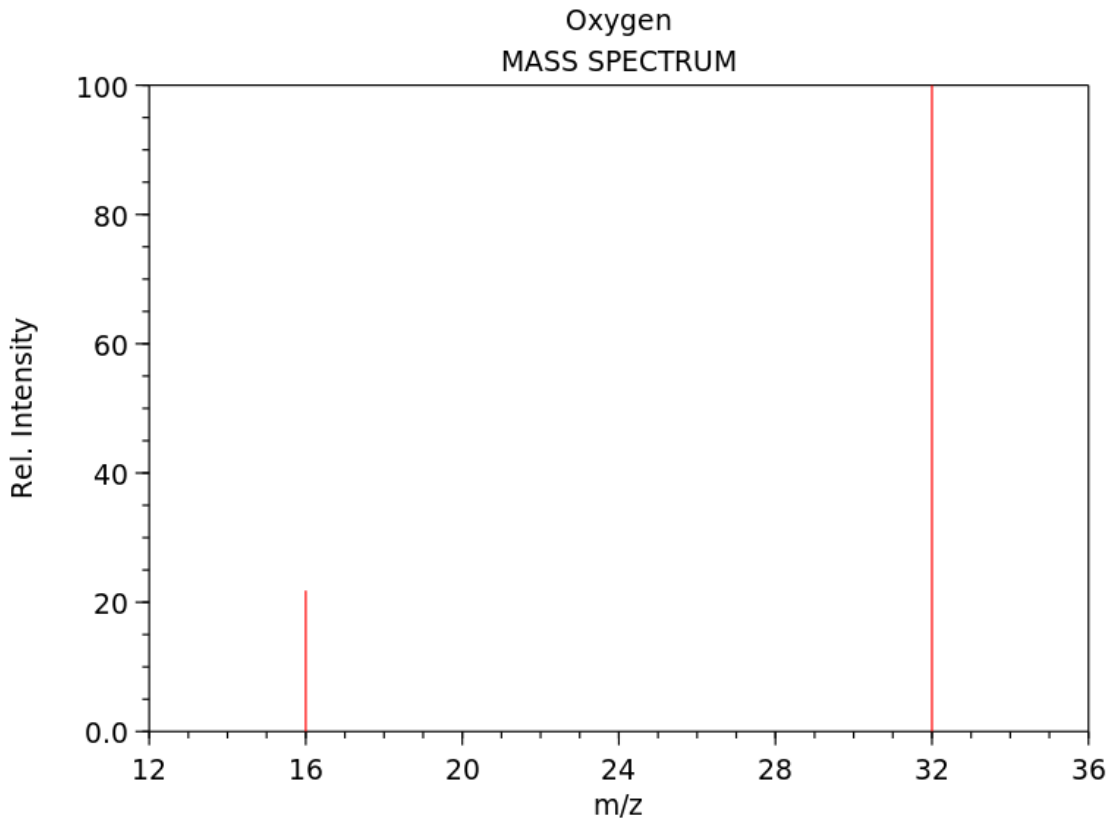

NIST Chemistry WebBook (https://webbook.nist.gov/chemistry)

Appendix D - Experimental Data

99 mL/min Ar: Test P1

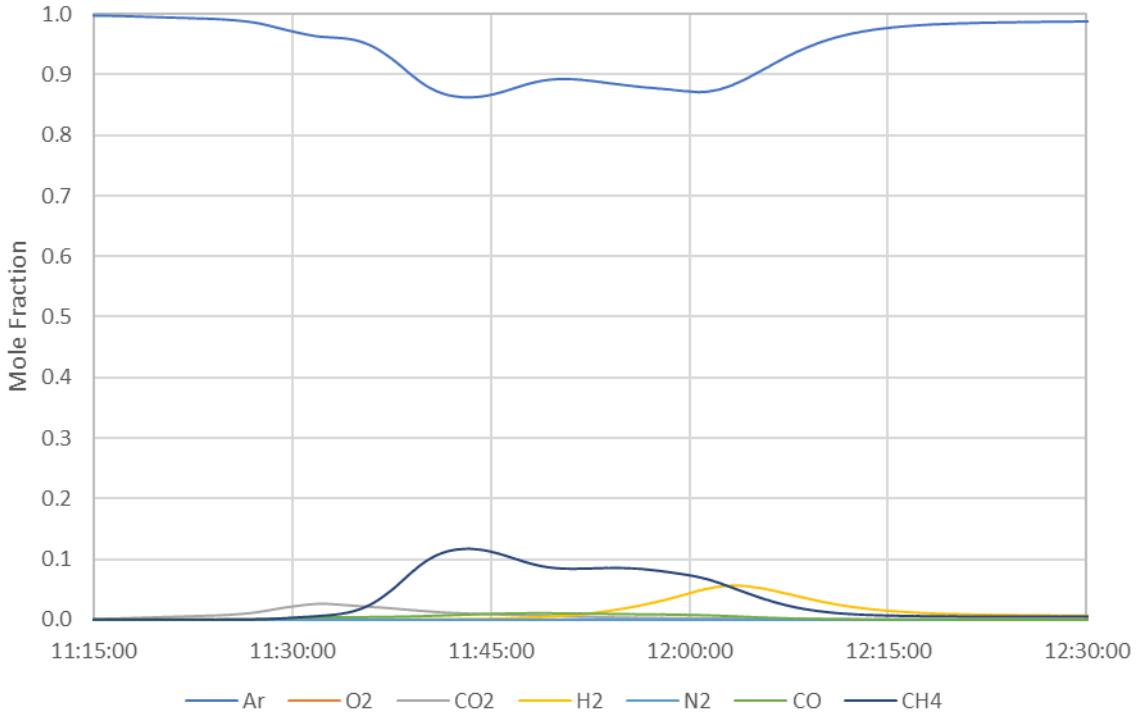

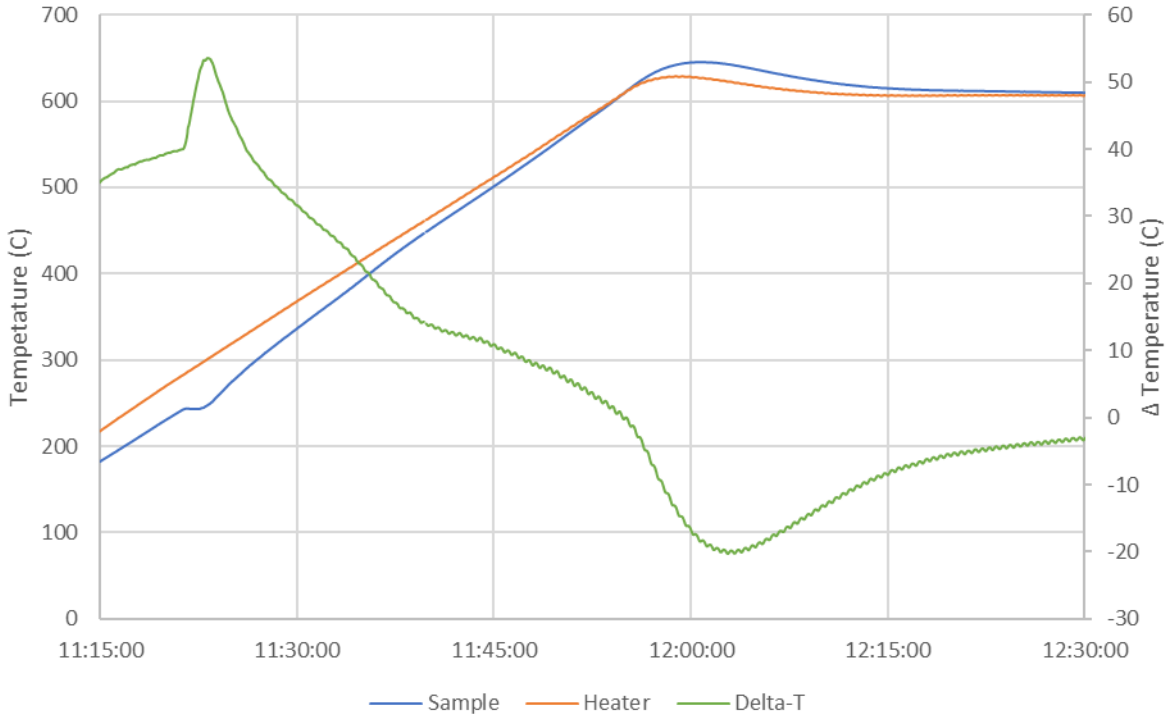

99 mL/min Ar: Test P2

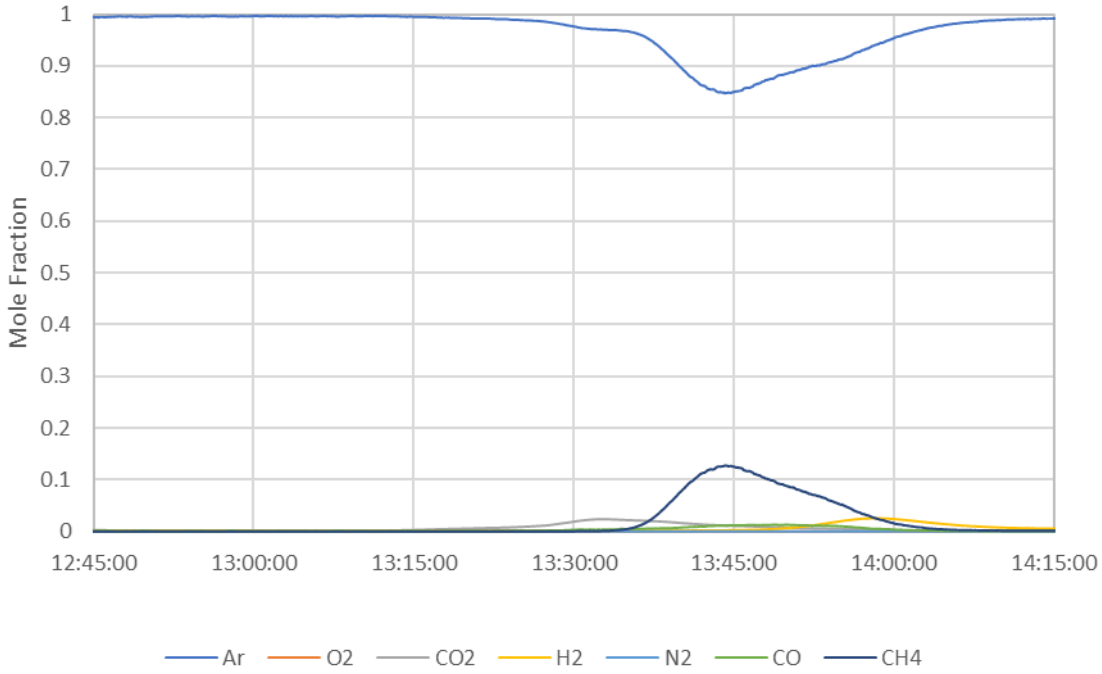

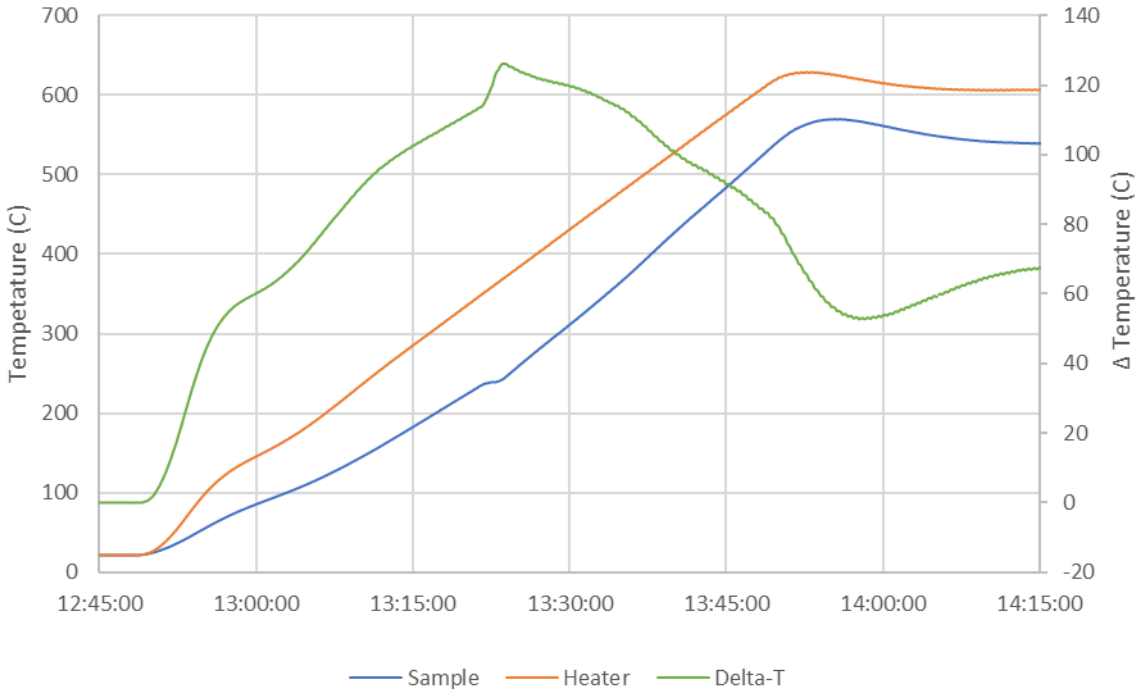

99 mL/min Ar: Test P3

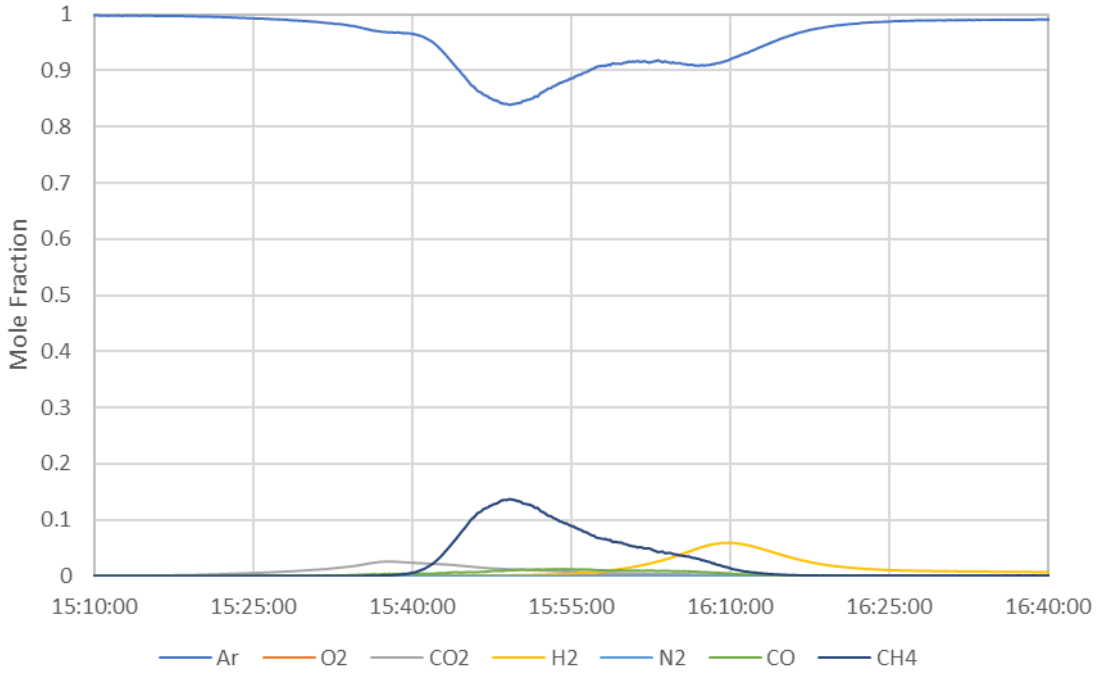

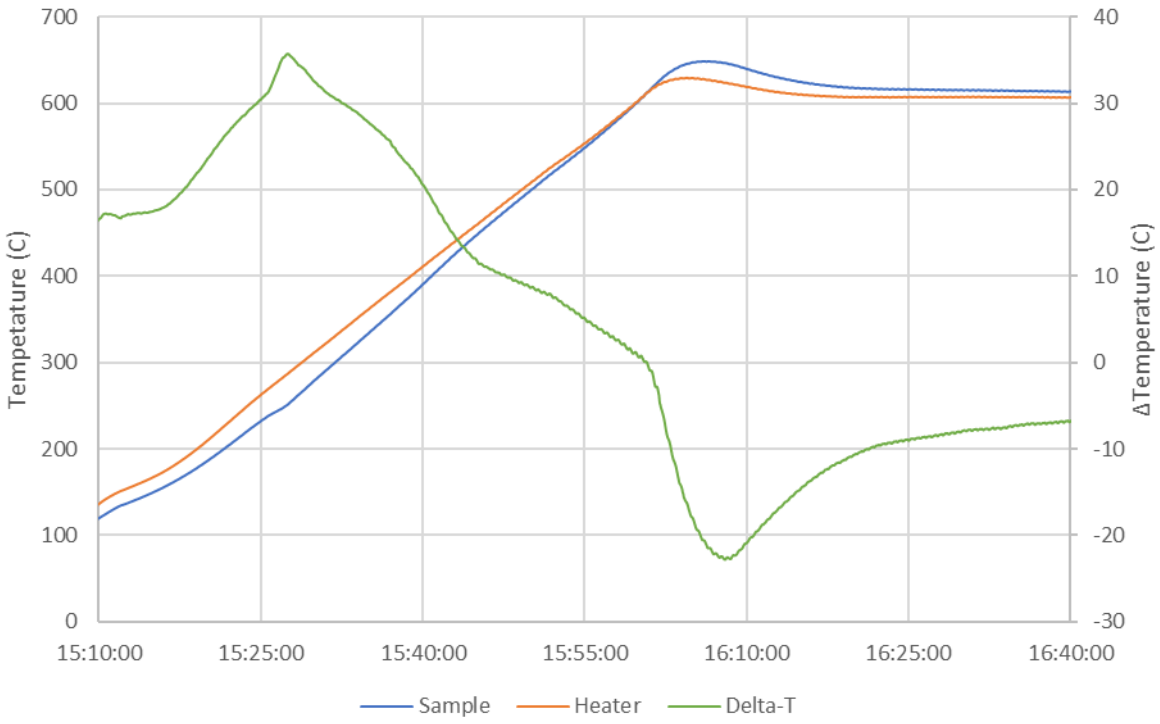

200 mL/min Air, 71 mL/min Ar: Test A1

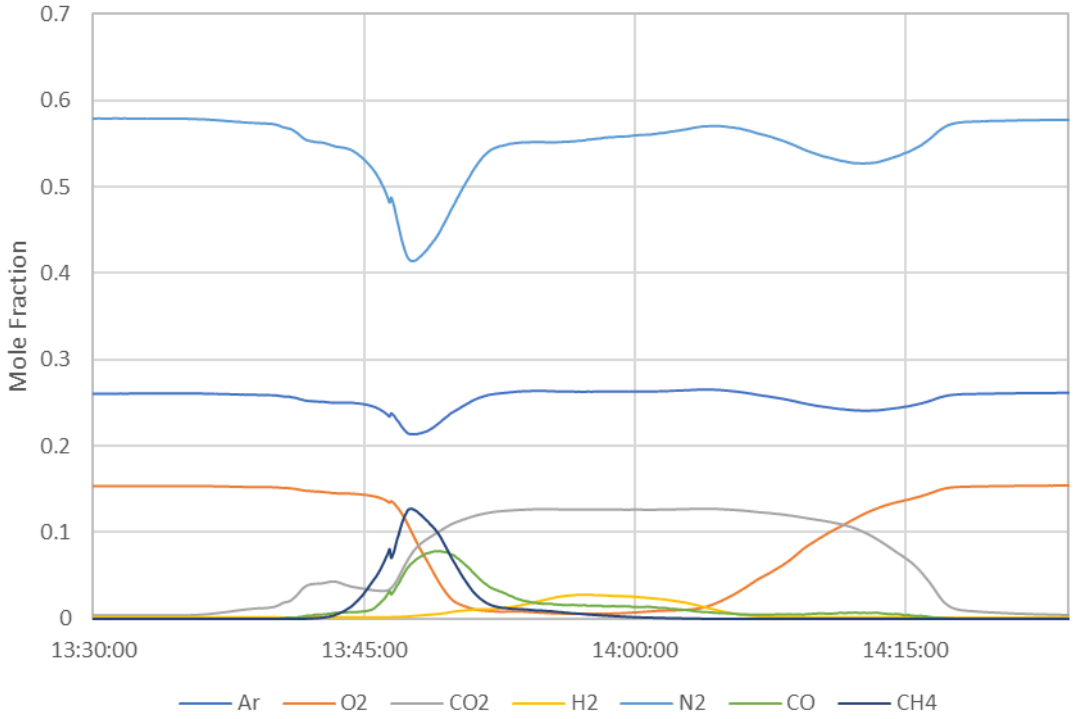

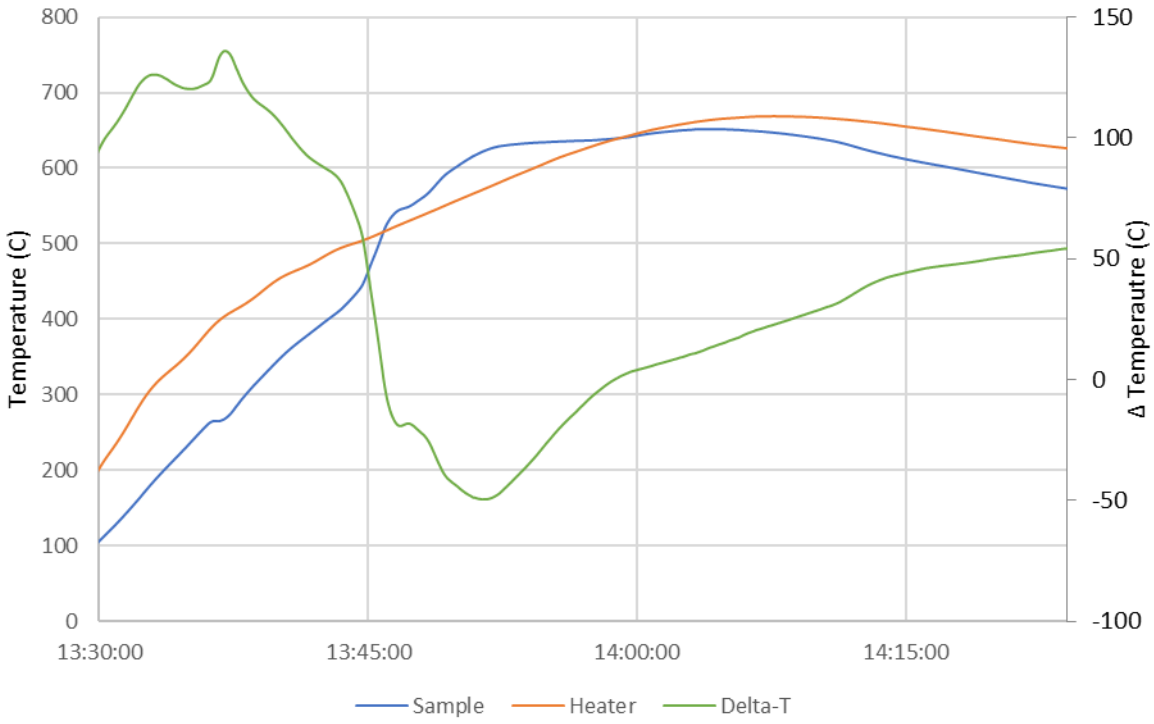

200 mL/min Air, 71 mL/min Ar: Test A2

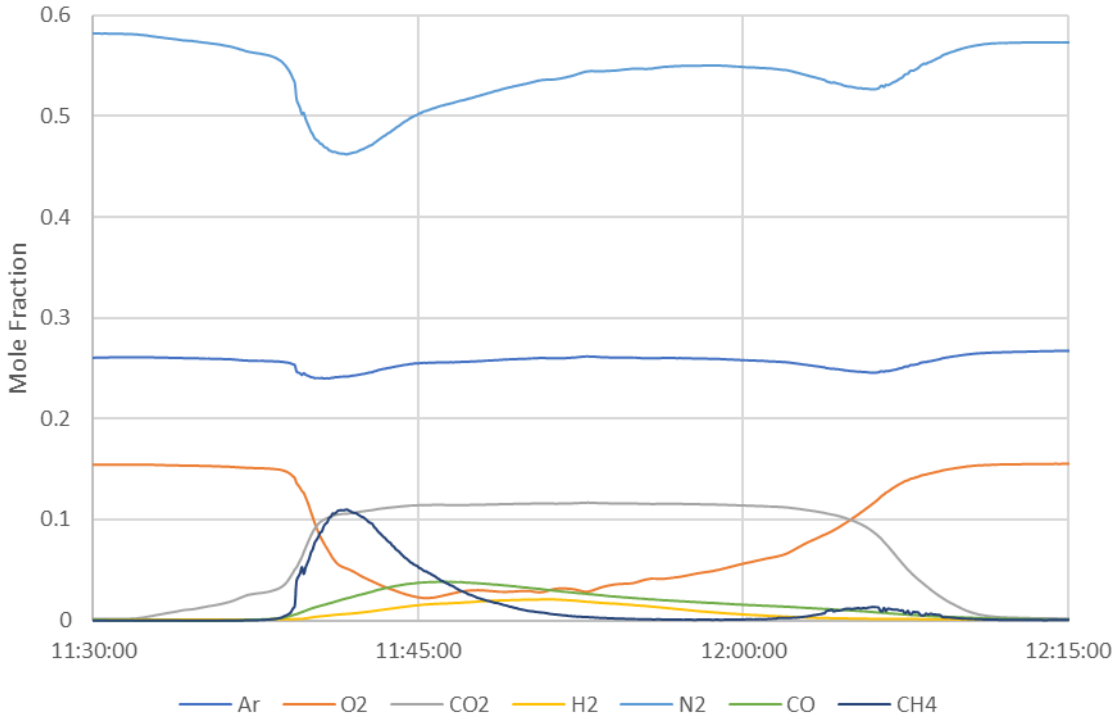

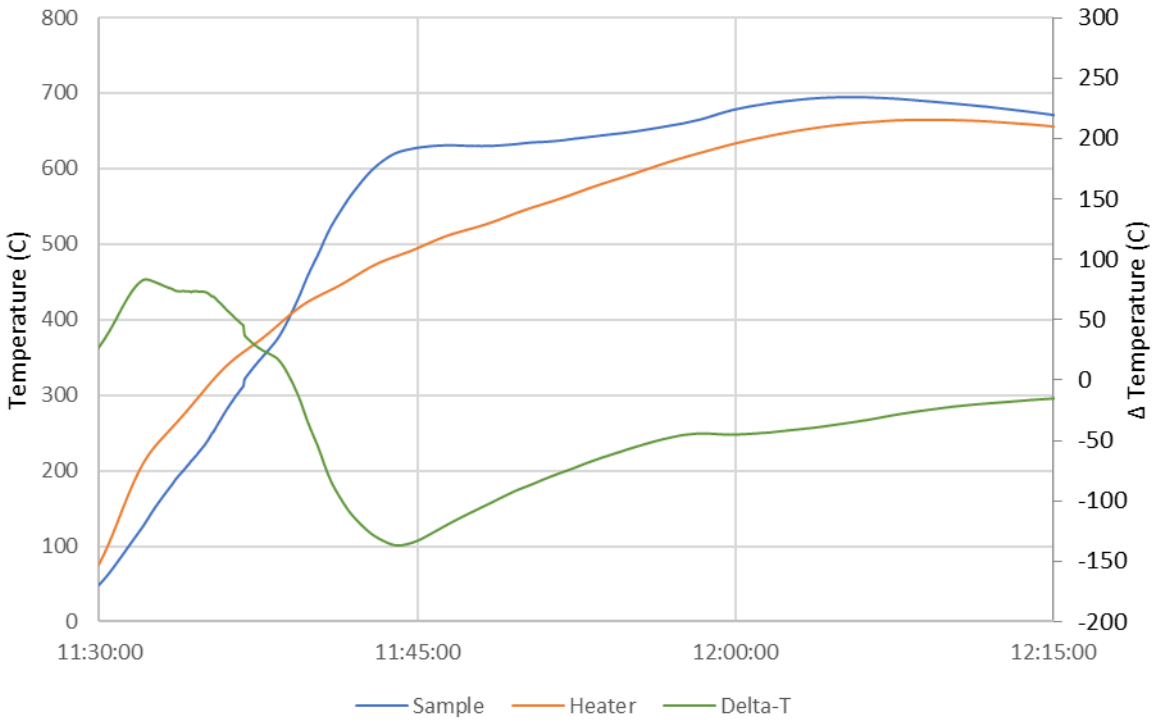

200 mL/min Air, 71 mL/min Ar: Test A3

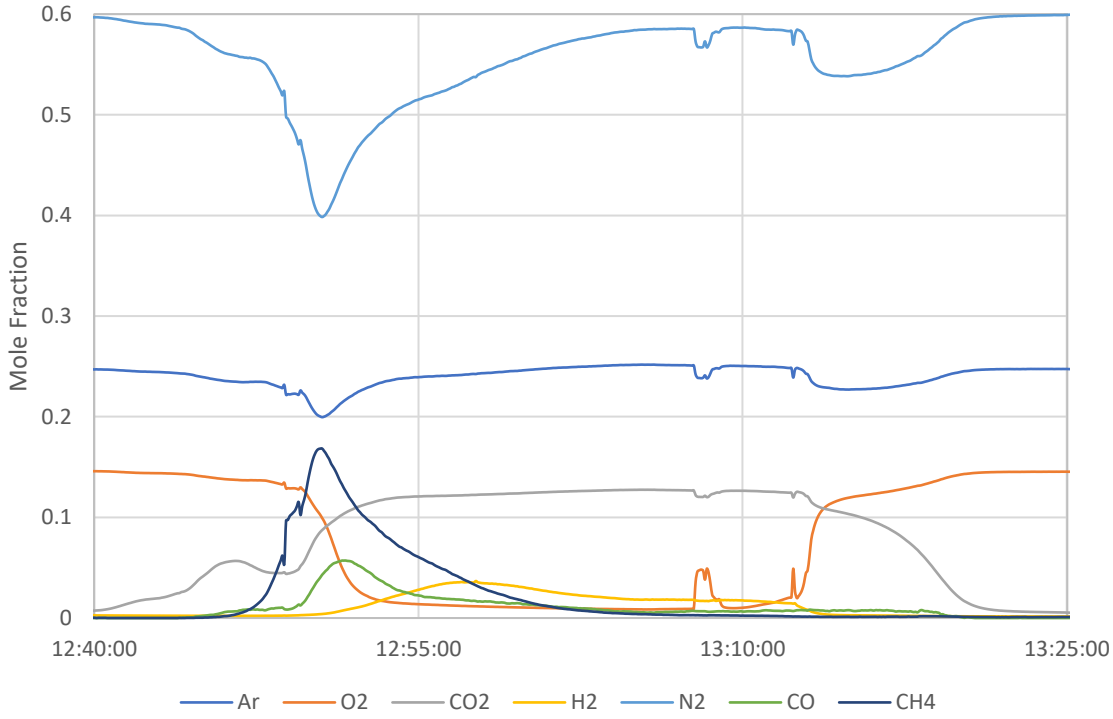

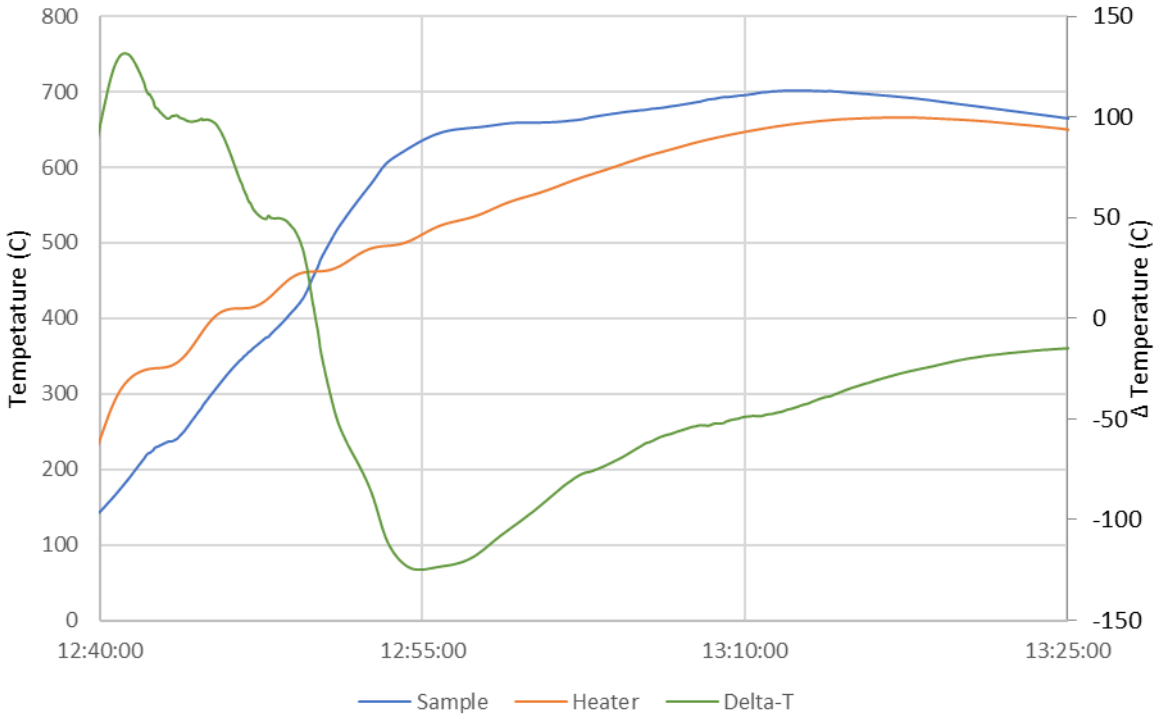

100 mL/min Air, 71 mL/min Ar: Test A4

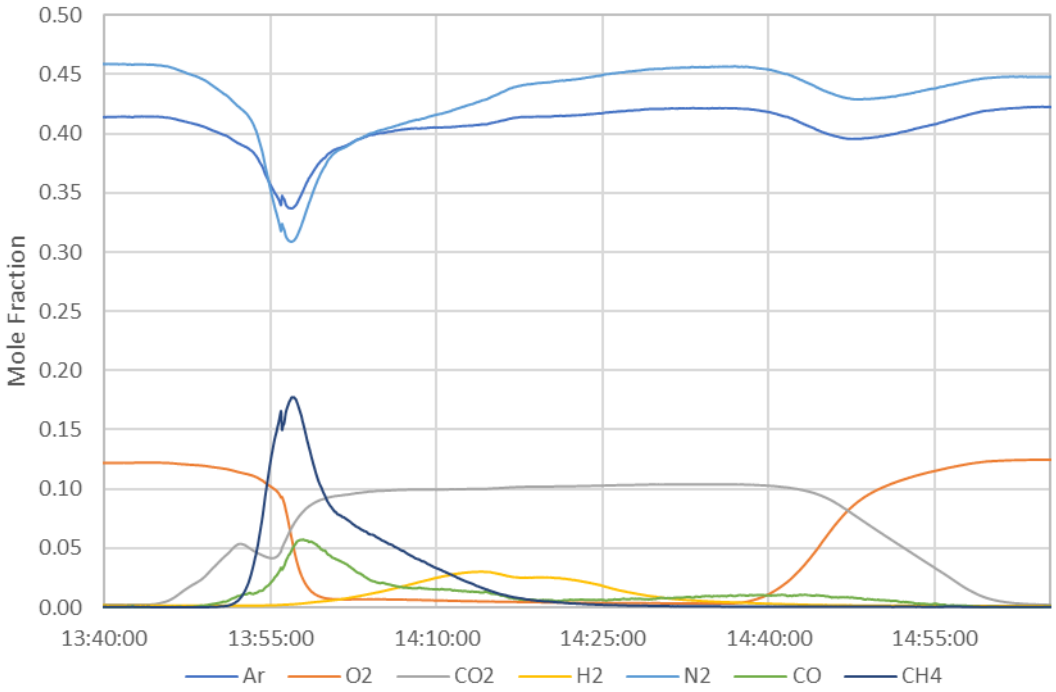

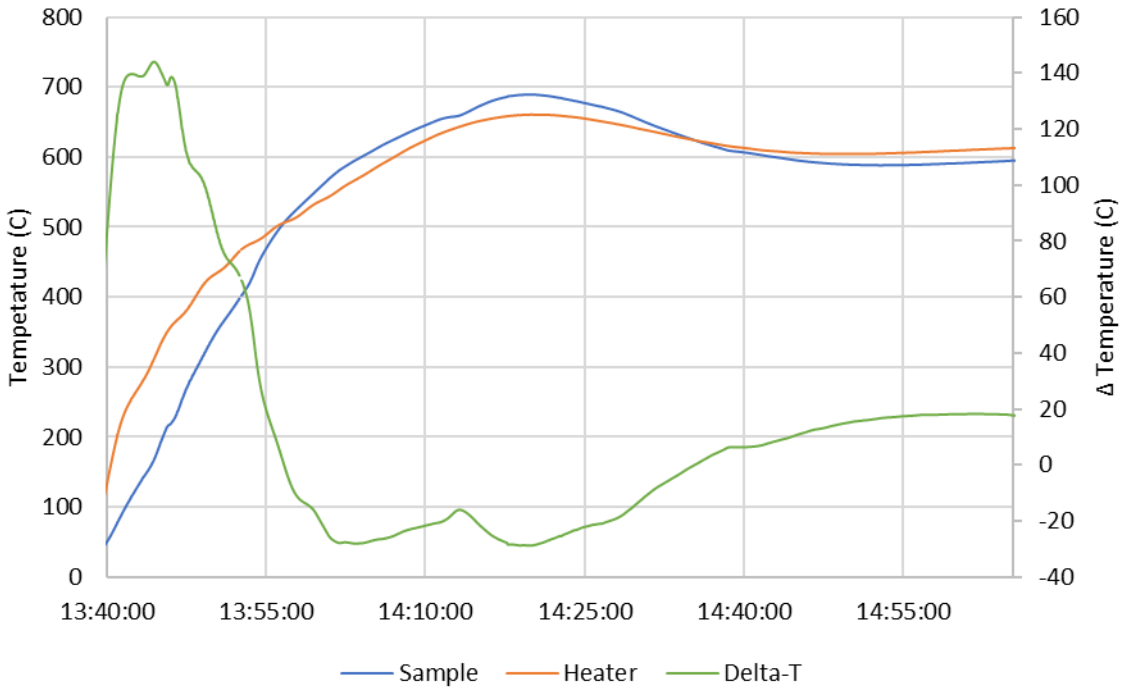

100 mL/min Air, 71 mL/min Ar: Test A5

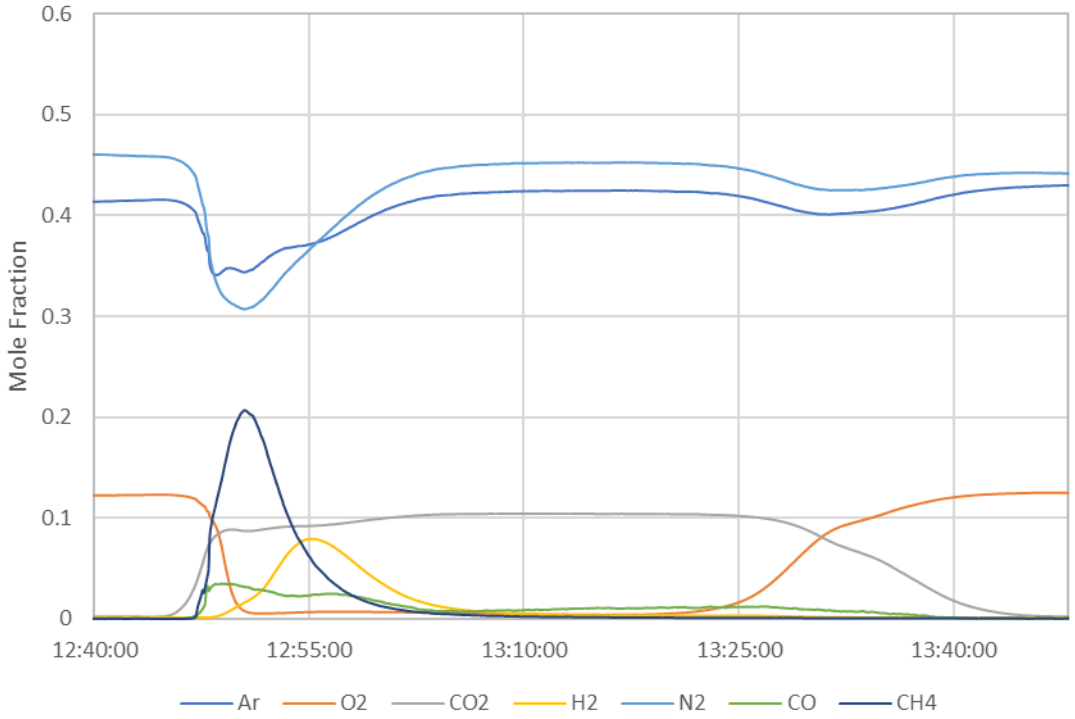

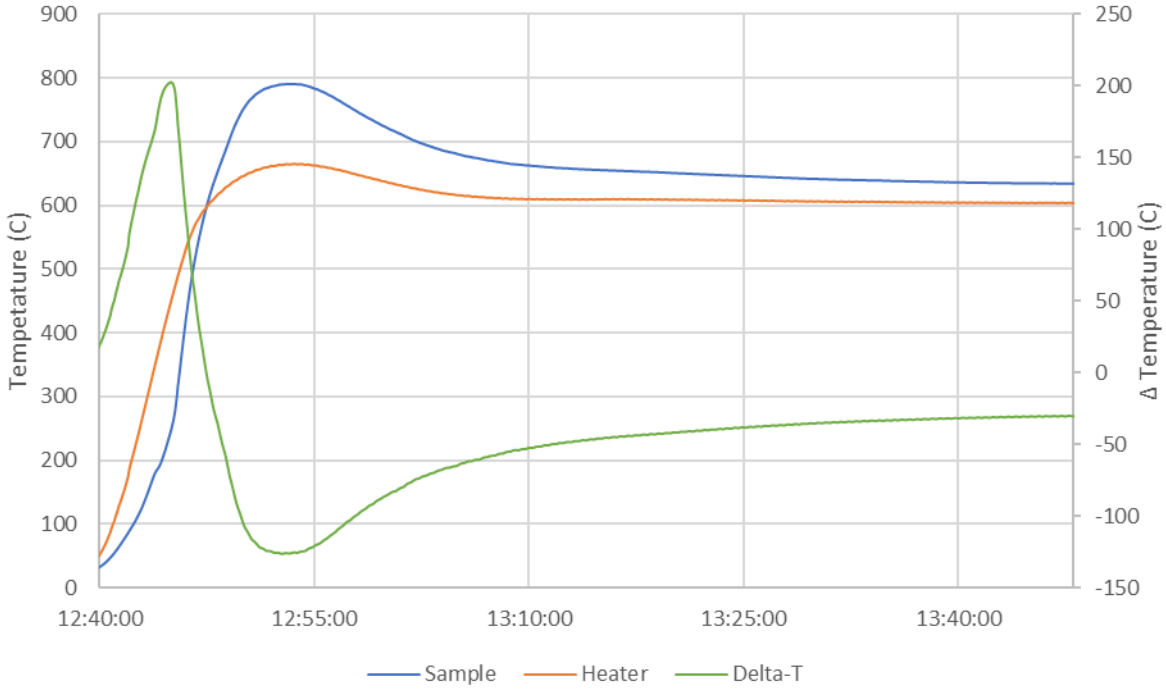

100 mL/min Air, 71 mL/min Ar: Test A6

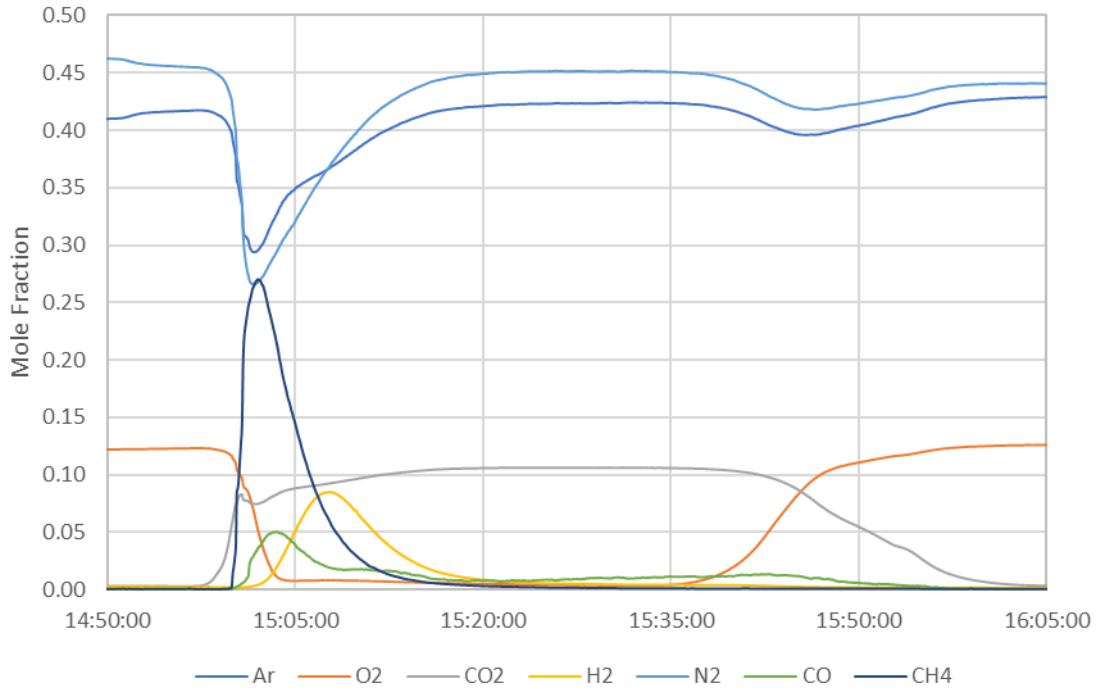

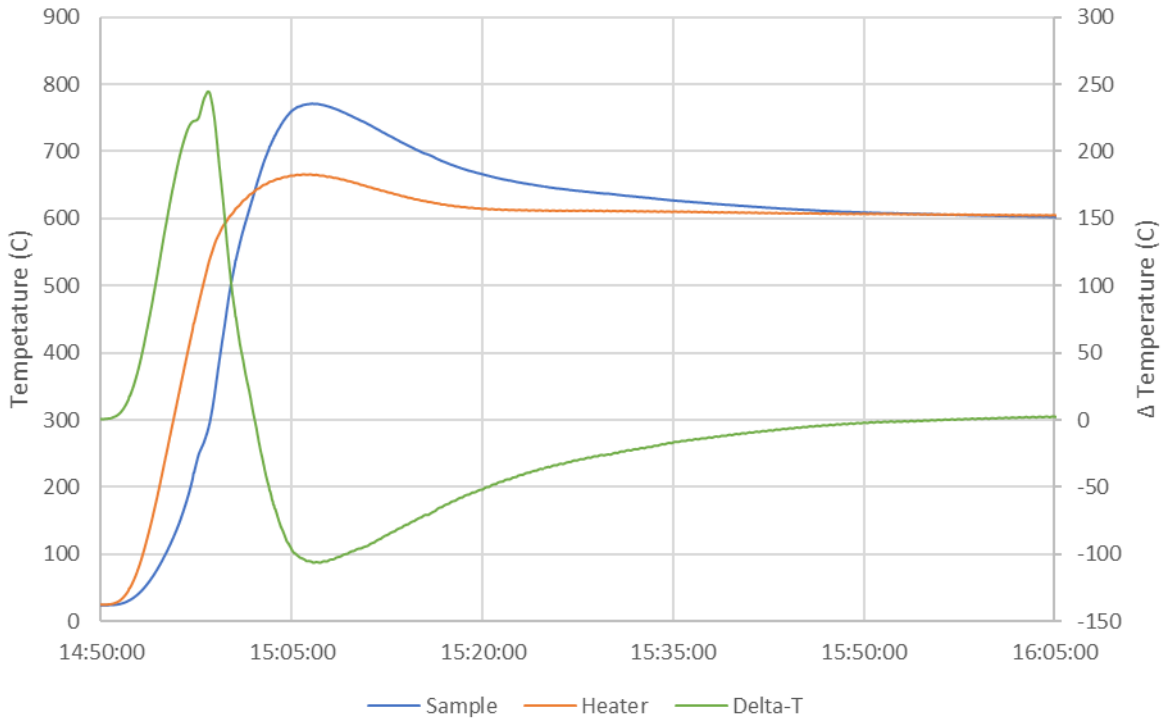

100 mL/min Air, 71 mL/min Ar: Test A7

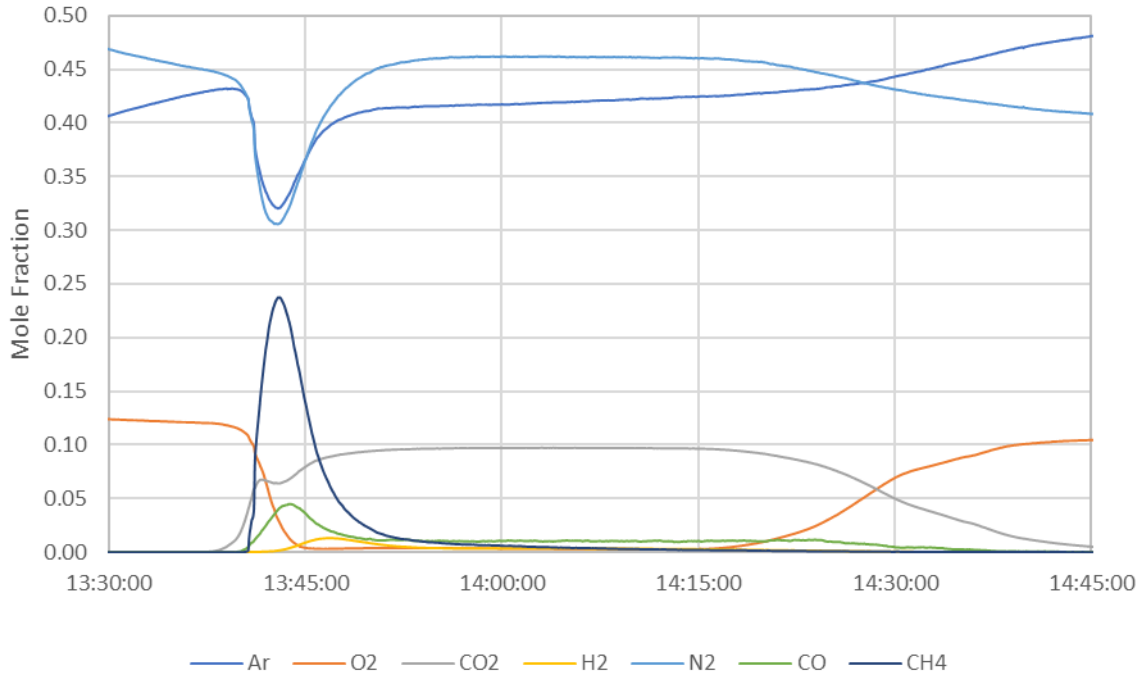

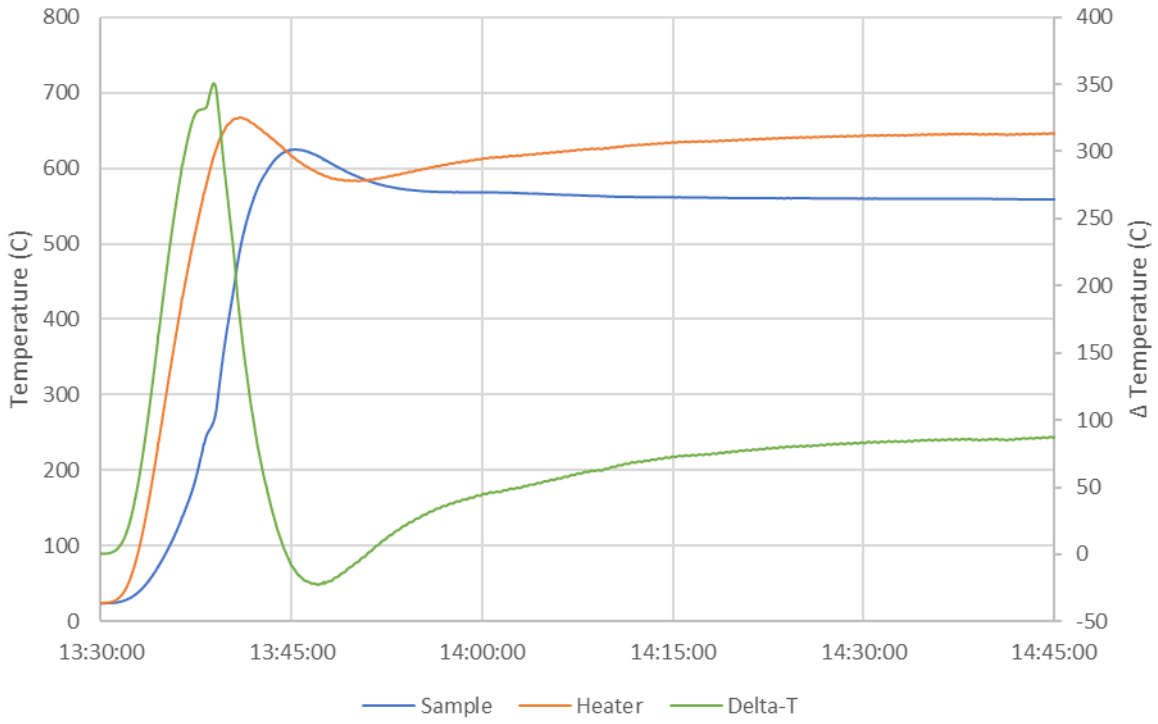

100 mL/min Air, 71 mL/min Ar: Test A8

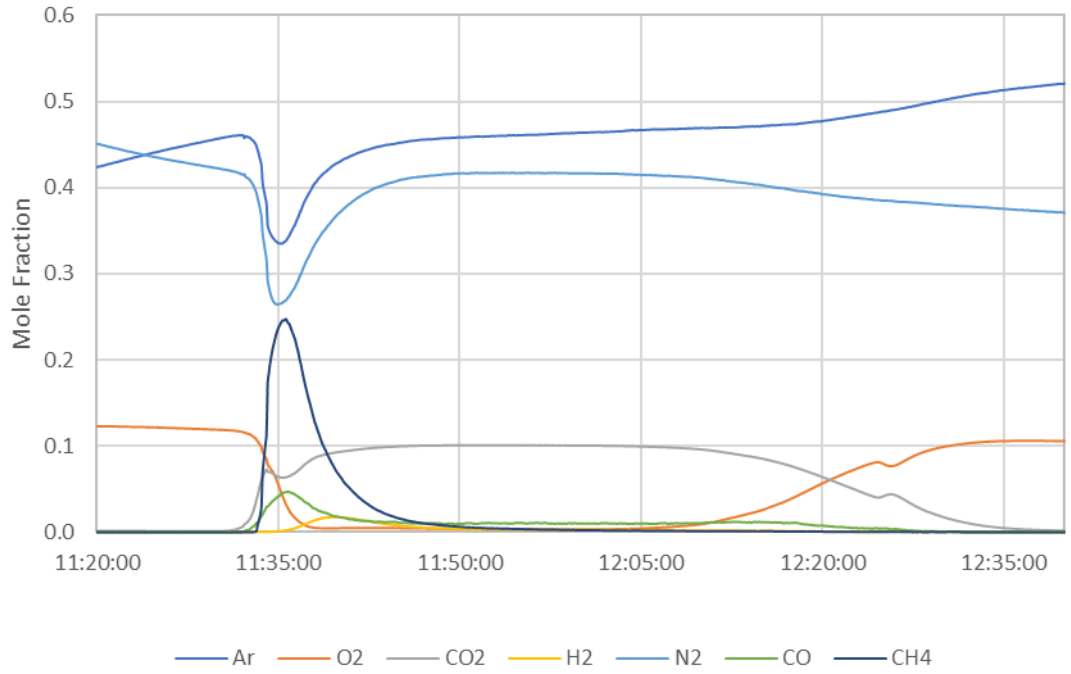

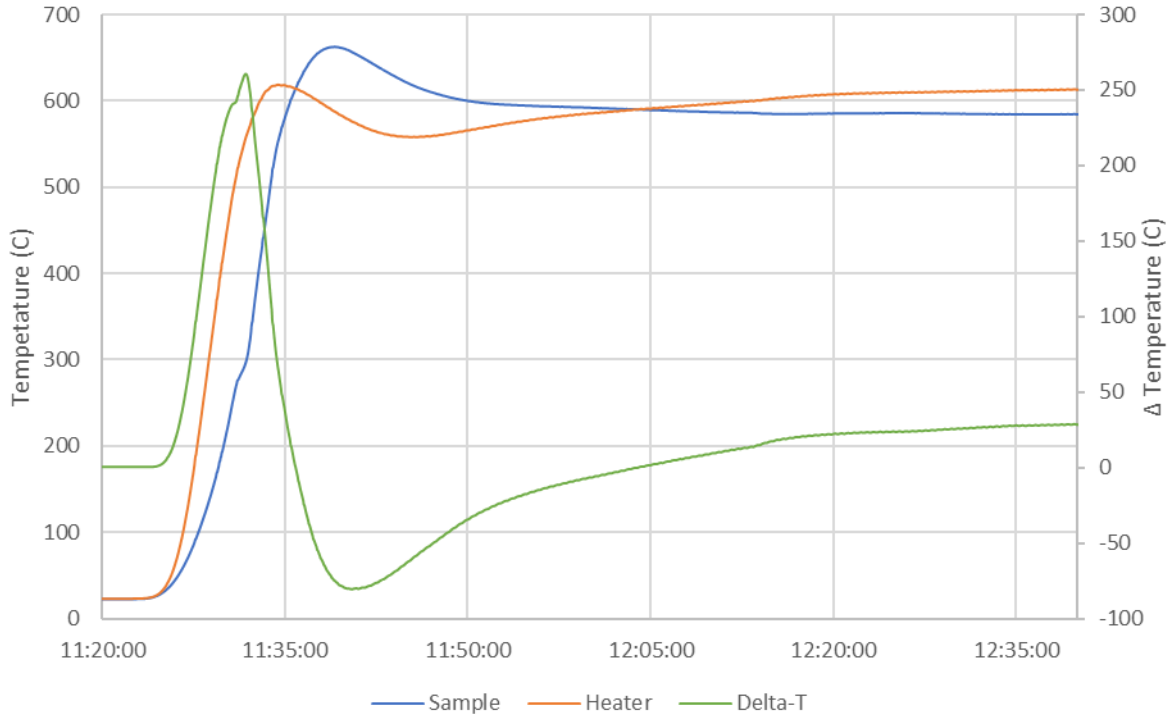

100 mL/min Air, 71 mL/min Ar: Test A9

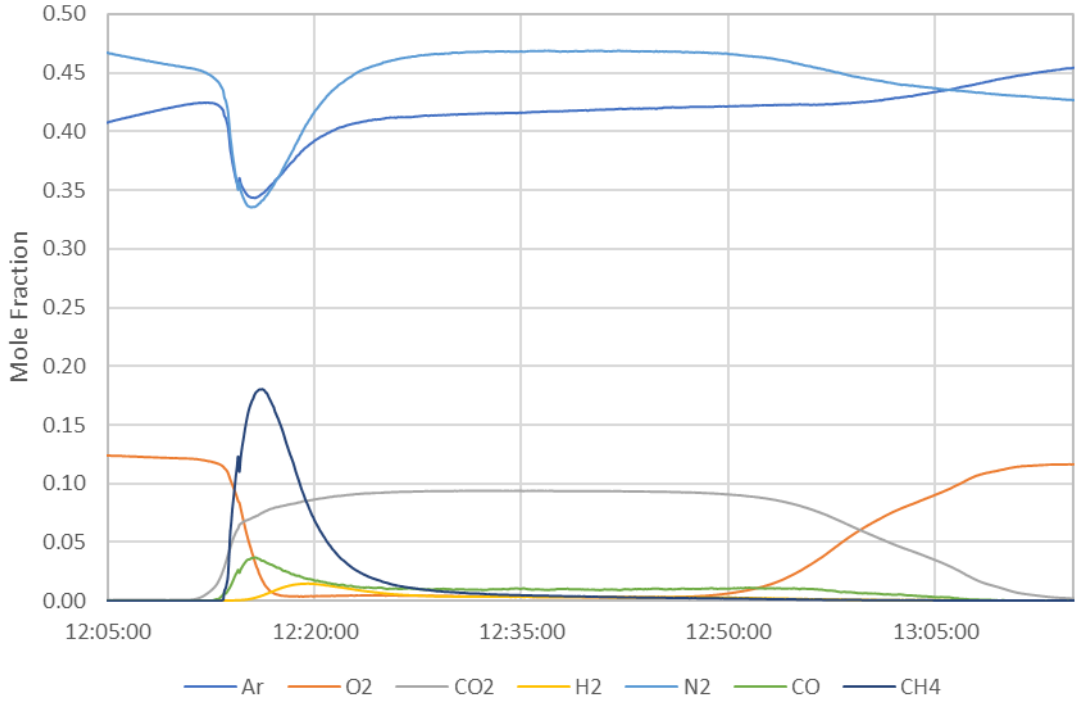

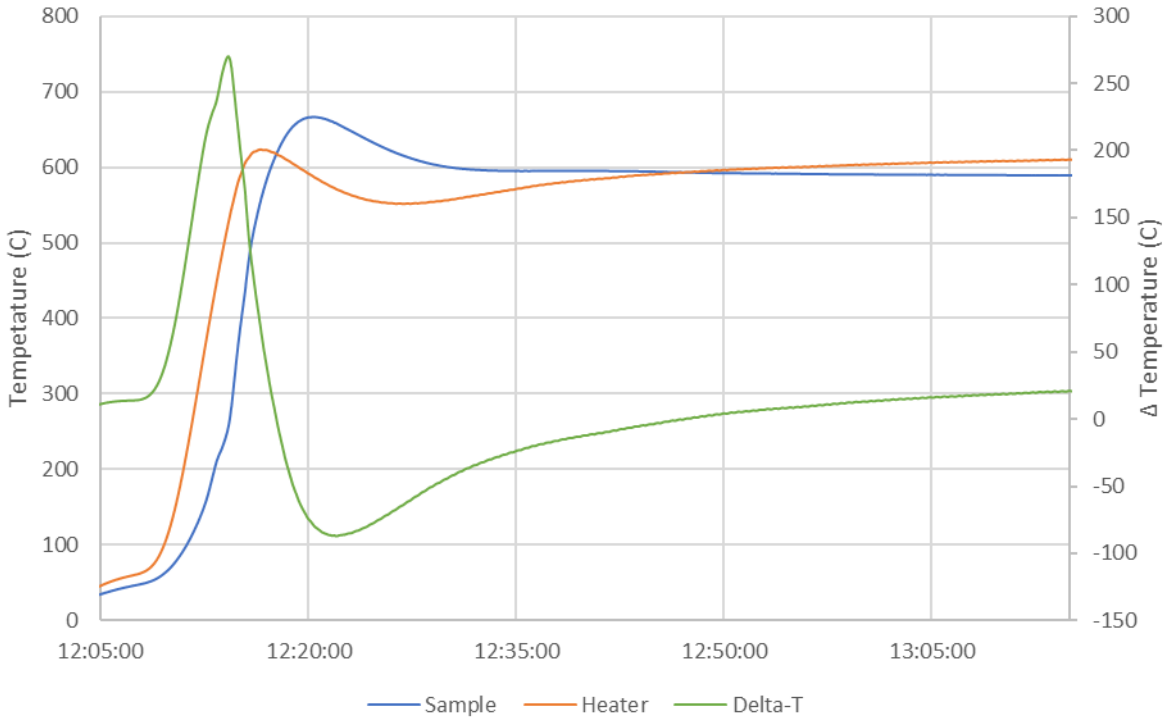

100 mL/min Air, 71 mL/min Ar: Test A10

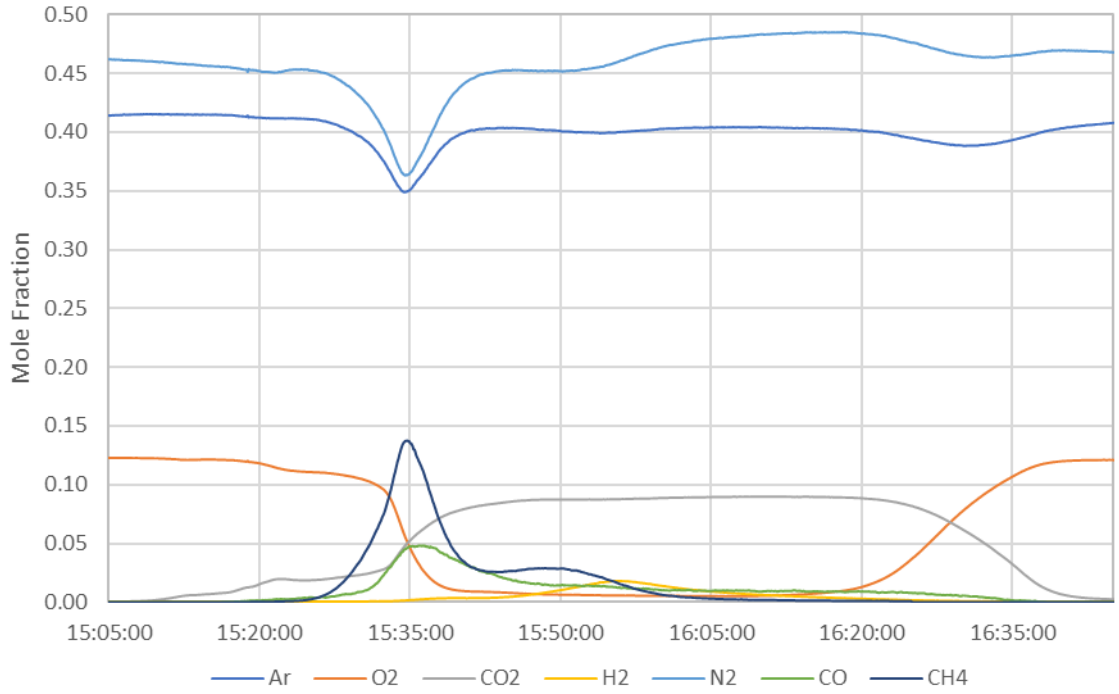

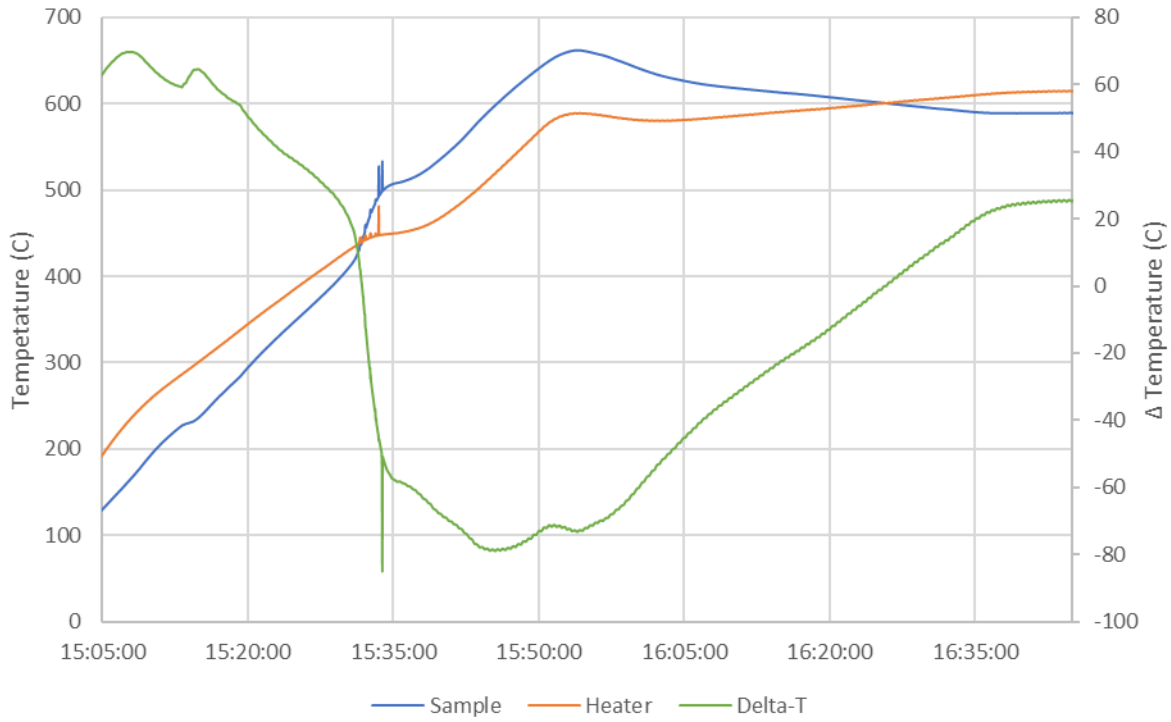

120 mL/min CO_2, 85 mL/min Ar: Test C1

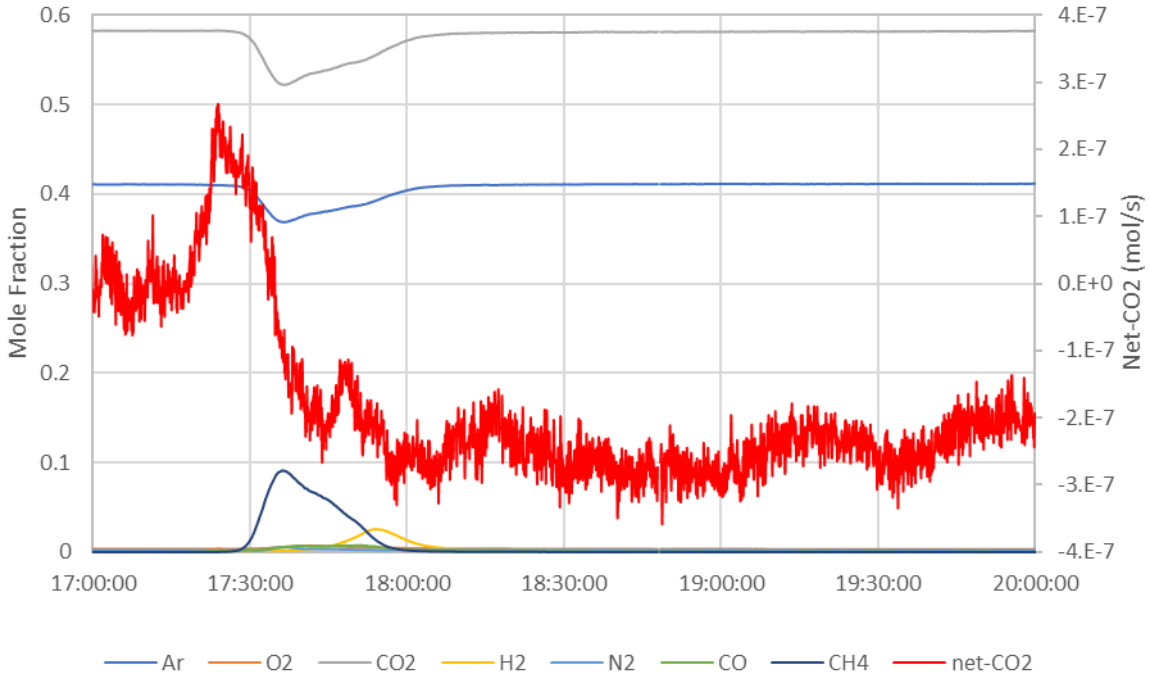

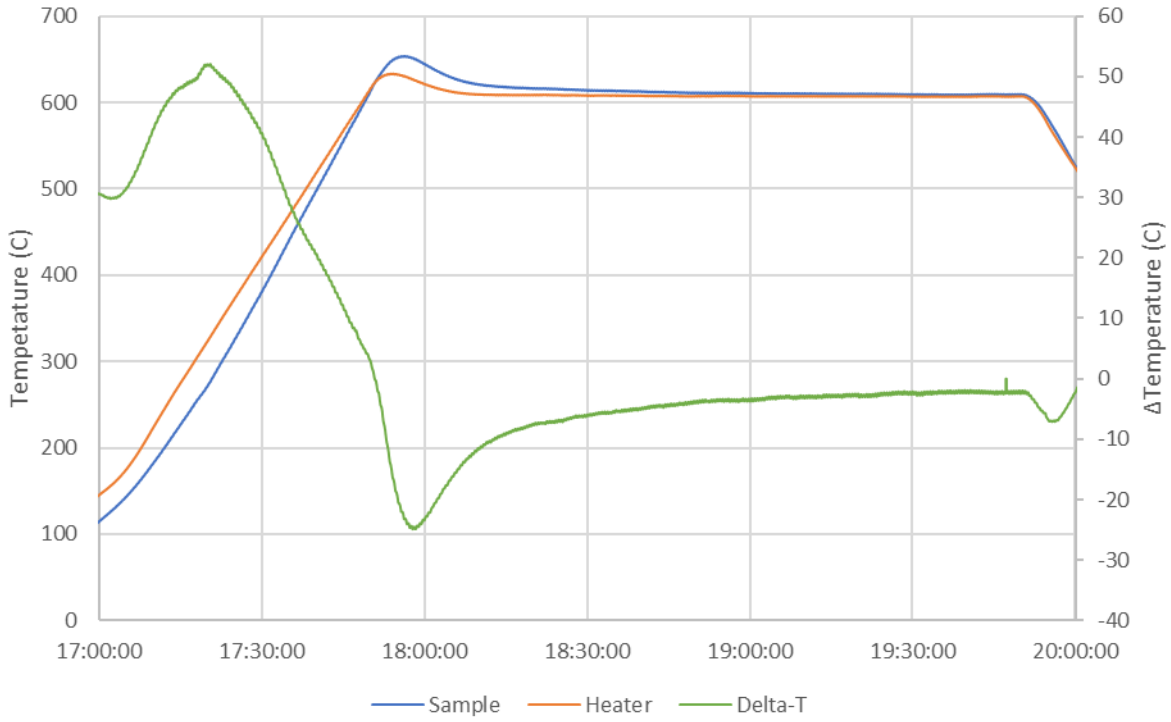

120 mL/min CO_2, 85 mL/min Ar: Test C2

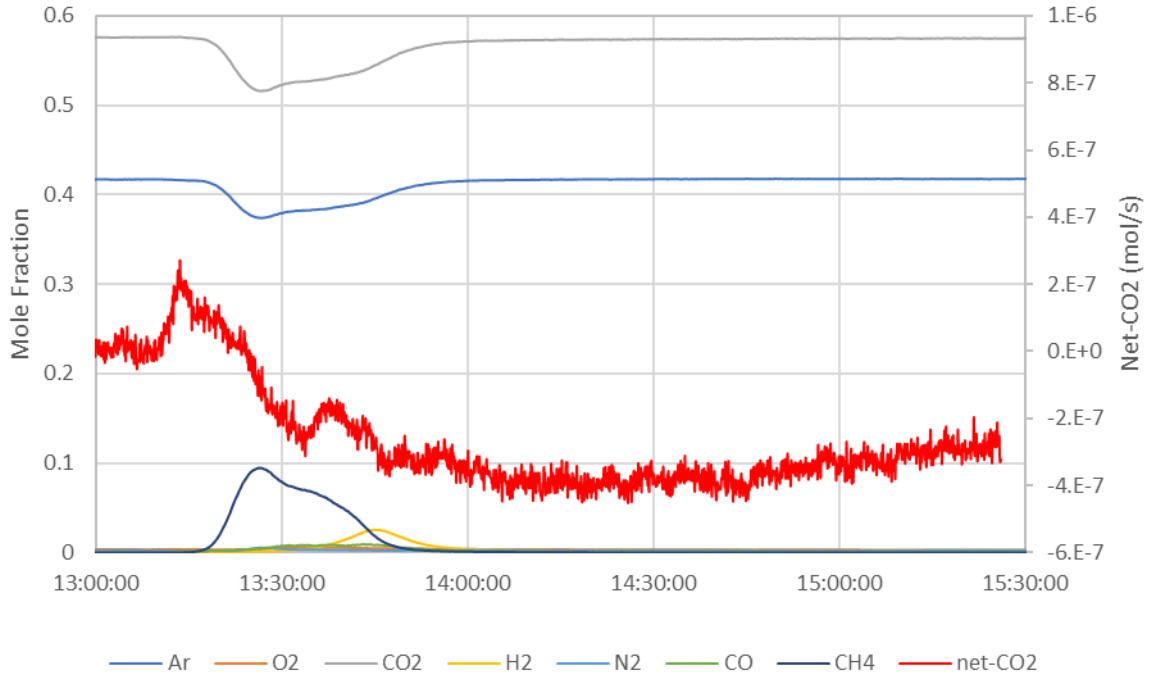

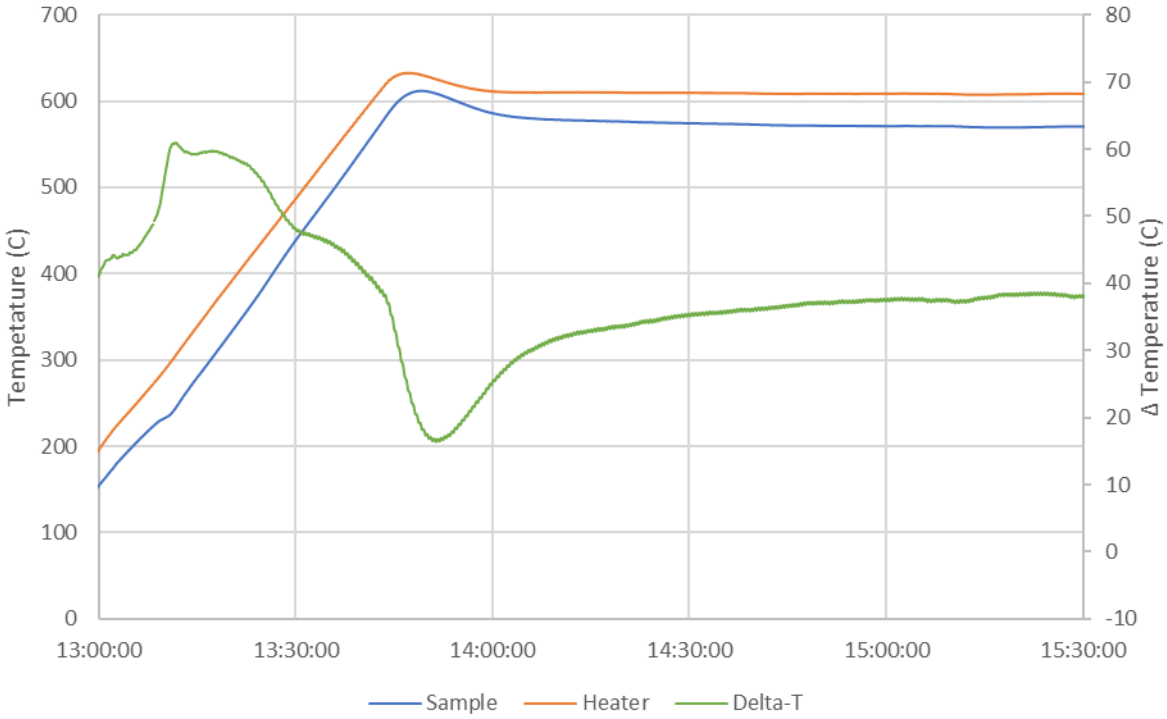

120 mL/min CO_2, 85 mL/min Ar: Test C3

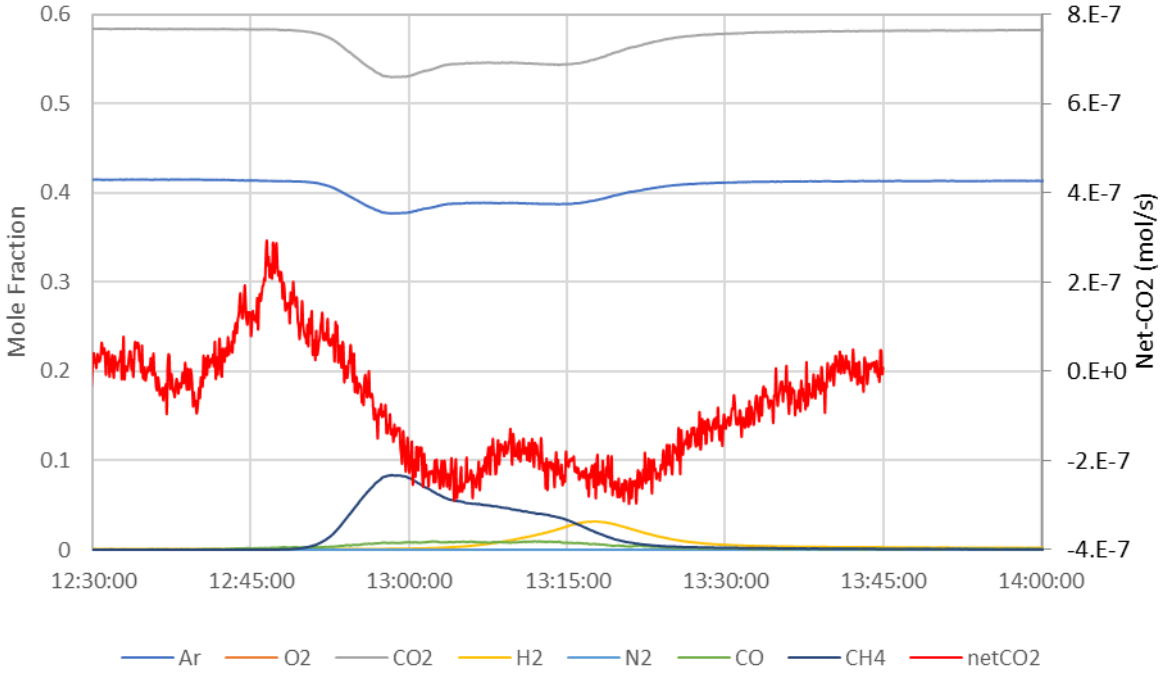

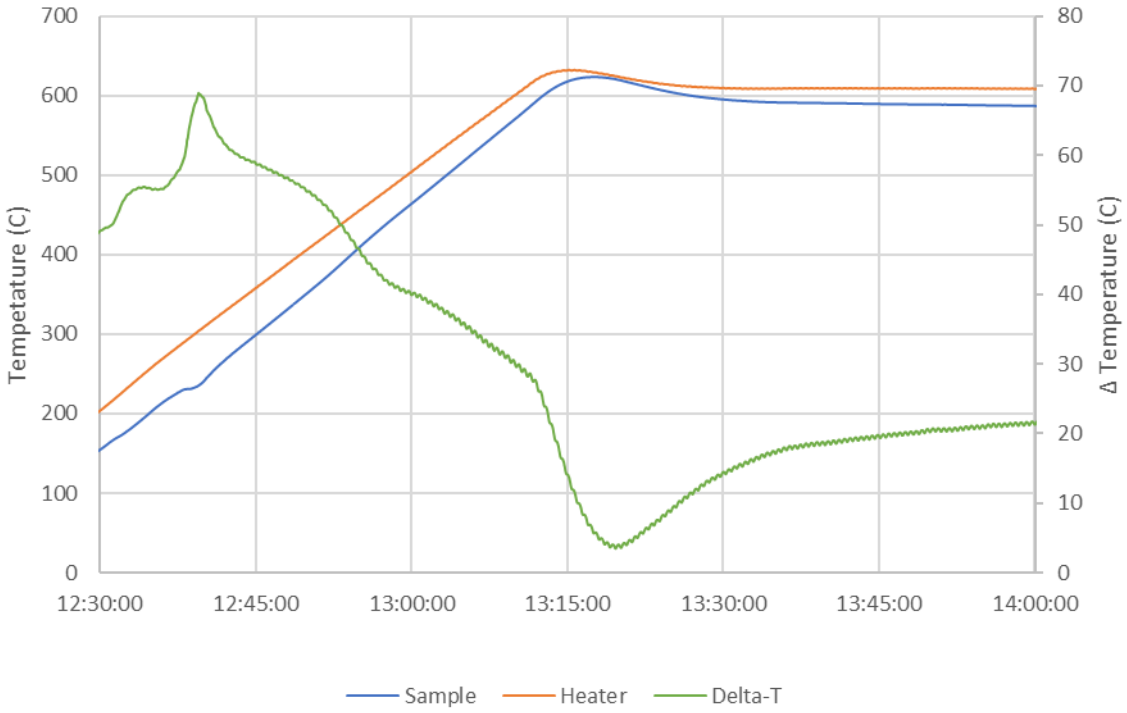

120 mL/min CO_2, 85 mL/min Ar: Test C4

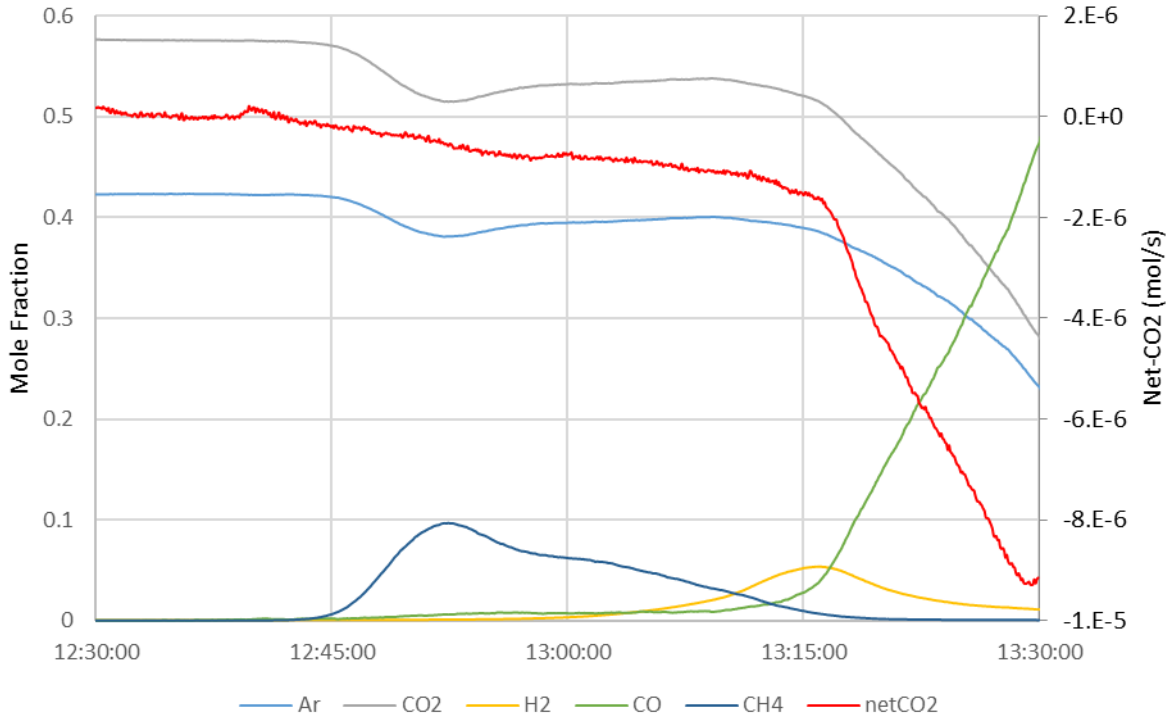

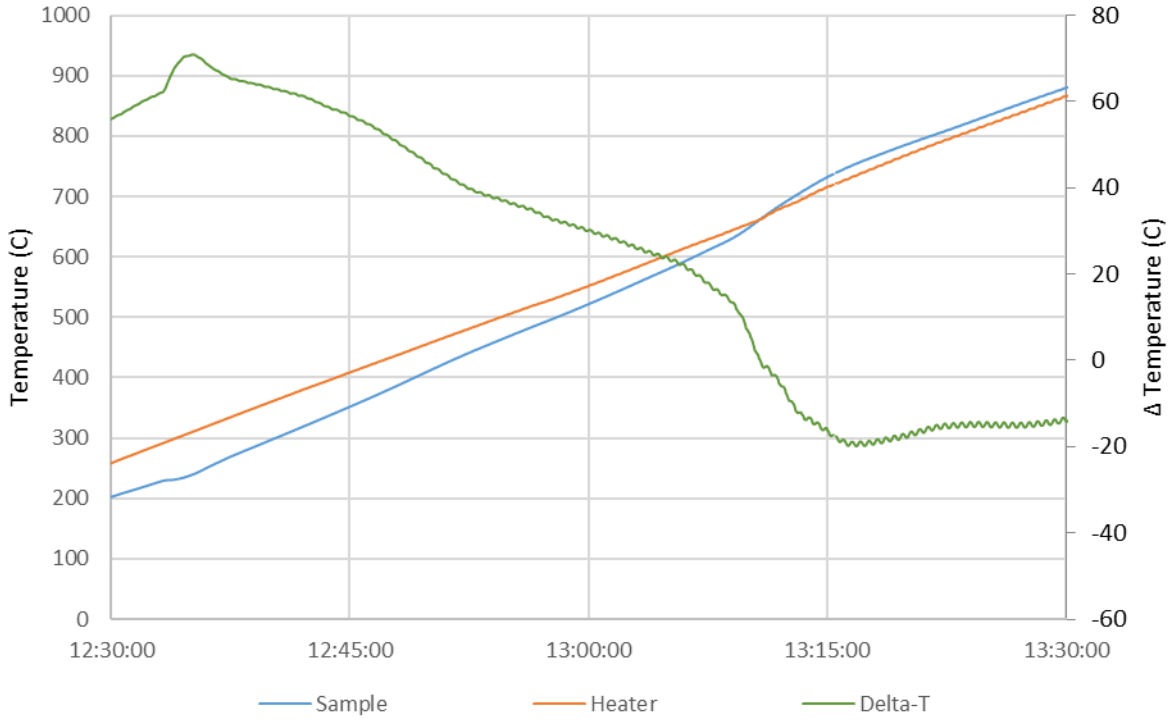

85 mL/min 50%O_2/CO_2, 90 mL/min Ar: Test M1

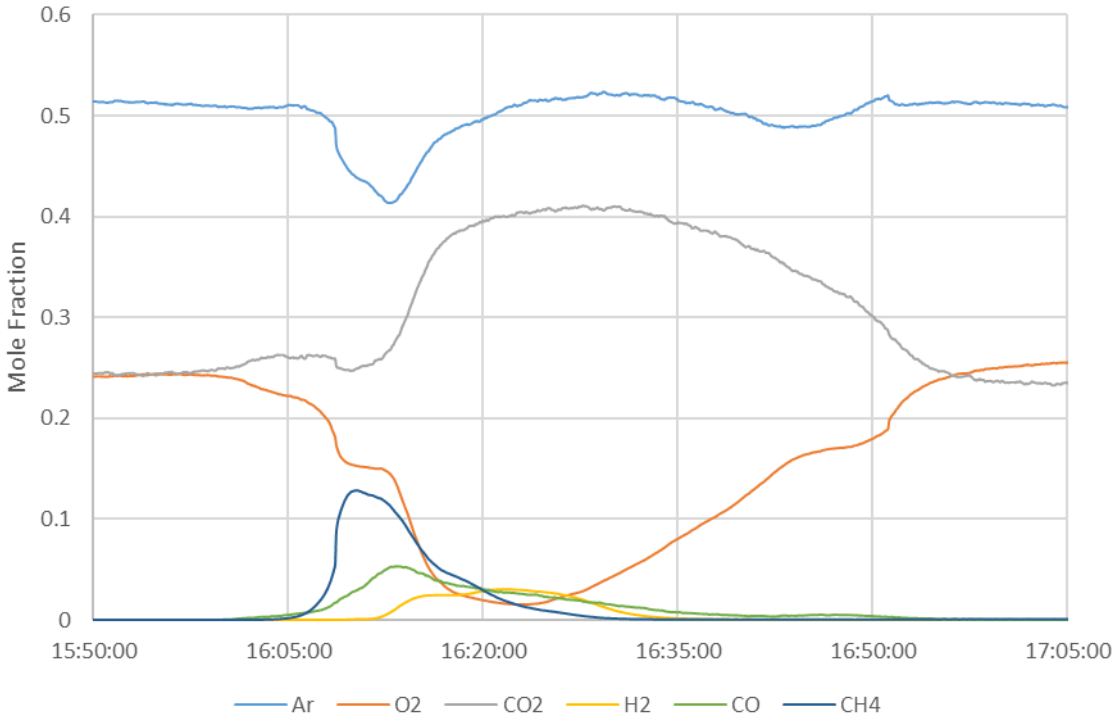

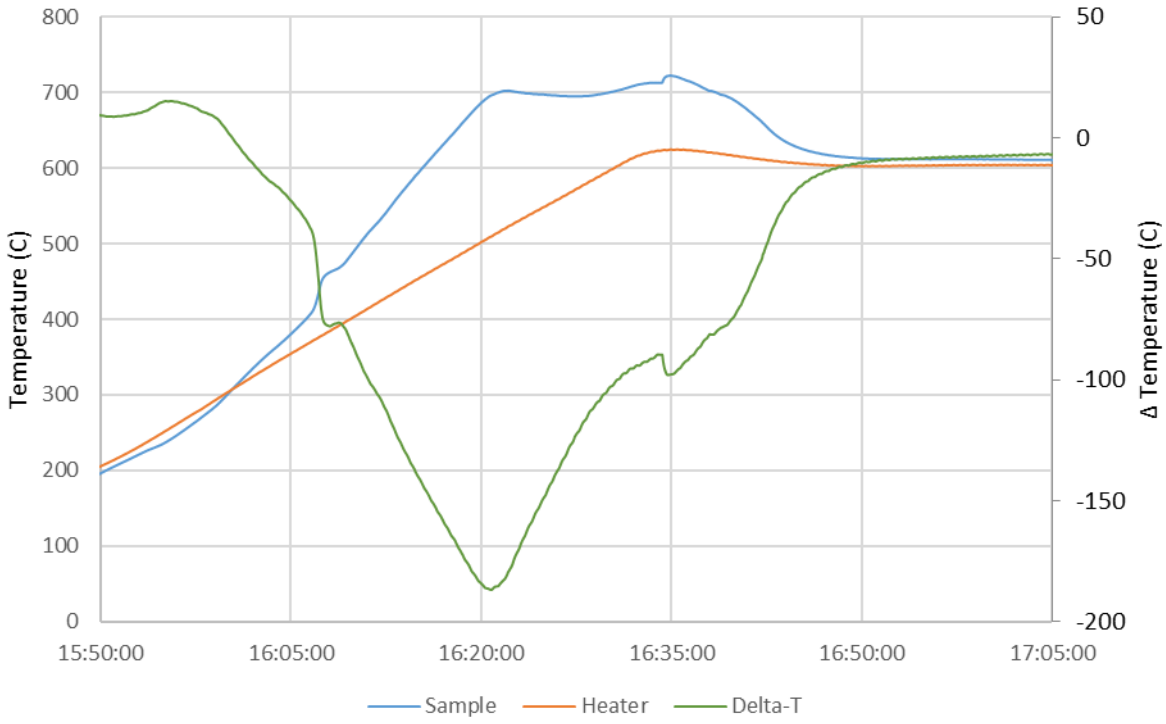

85 mL/min 50%O_2/CO_2, 90 mL/min Ar: Test M2

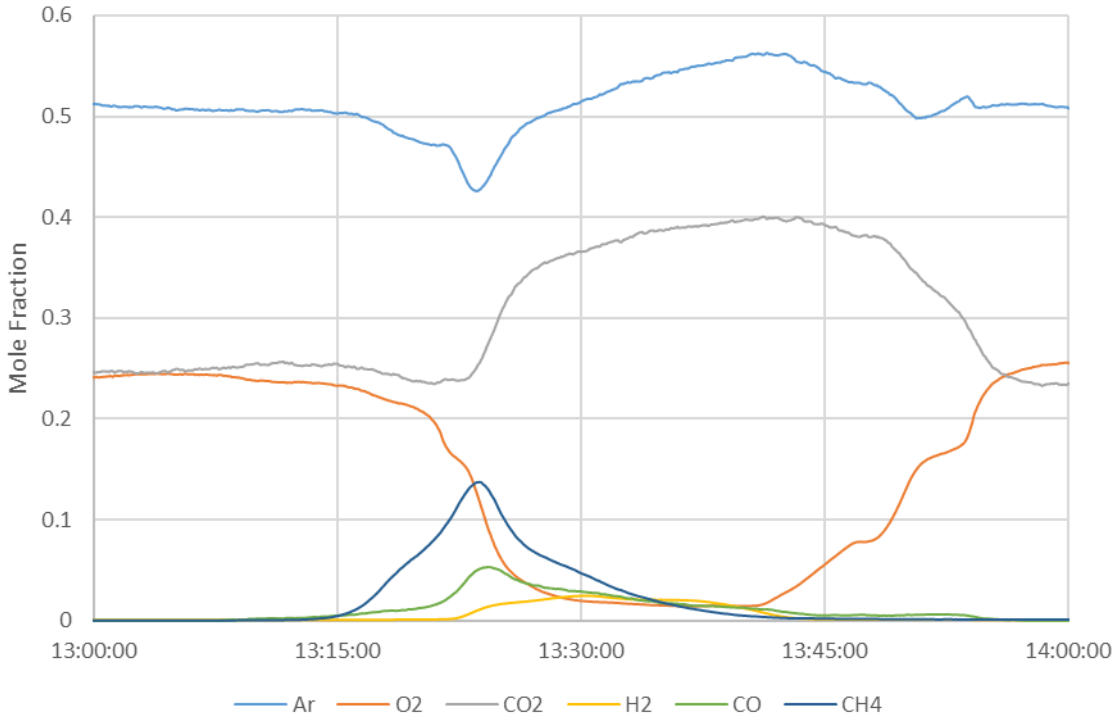

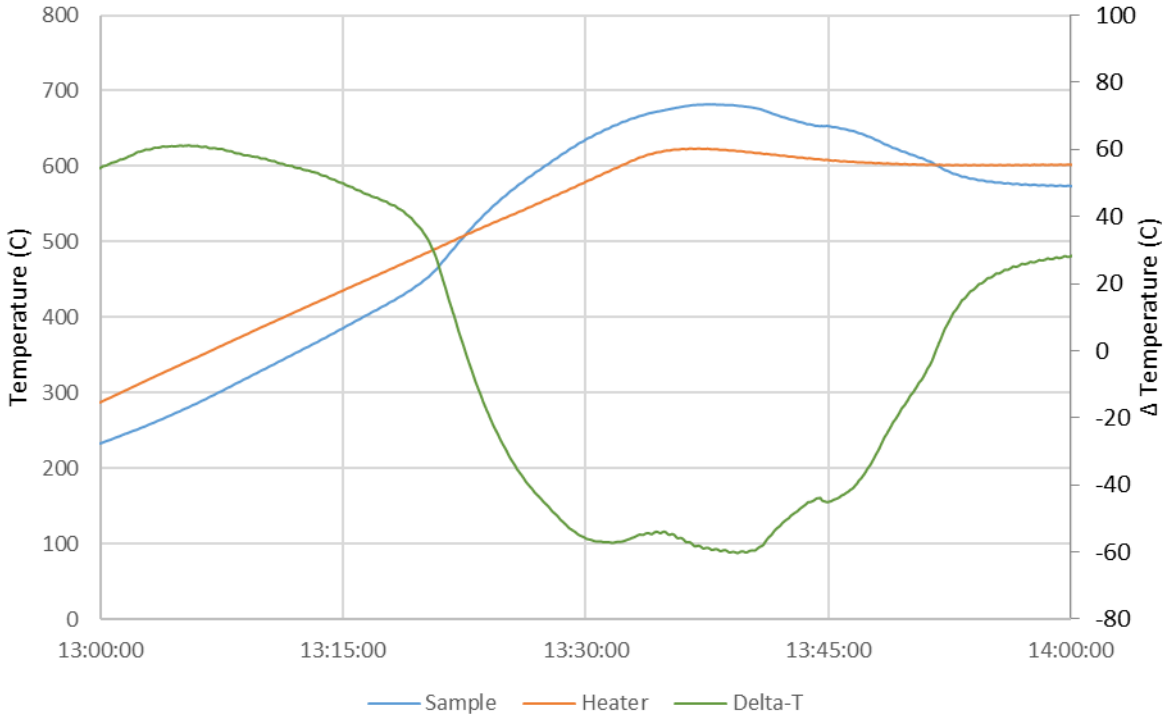

List of References

[1] S. Gulev, P. Thorne, J. Ahn, J. Dentener, M. Domingues, S. Gerland, D. Gong, D. Kaufman, H. Nnamchi, J. Quaas, J. Rivera, S. Sathyendranath, S. Smith, B. Trewin, K. von Shuckman and R. Vose, "Changing State of the Climate System," in *Climate Change 2021: The Physical Science Basis. Contribution of Working Group I to the Sixth Assessment Report of the Intergovernmental Panel on Climate Change*, V. Masson-Delmotte, P. Zhai, A. Pirani, S. Connors, C. Pean, S. Berger, N. Caud, Y. Chen, L. Goldfarb, M. Gomis, M. Huang, K. Leitzell, E. Lonnoy, J. Matthews, T. Maycock, T. Waterfield, O. Yelekci, R. Yu and B. Zhou, Eds., Cambridge University Press, 2021, pp. 290-382.

[2] H. Douville, K. Raghavan, J. Renwick, R. Allan, P. Arias, M. Barlow, R. Cezero-Mota, A. Cherchi, T. Gan, J. Gergis, D. Jiang, A. Khan, W. Pokam Mba, D. Rosenfeld, J. Tierney and O. Zolina, "Water Cycle Changes," in *Climate Change 2021: The Physical Science Basis. Contribution of Working Group I to the Sixth Assessment Report of the Intergovernmental Panel on Climate Change*, V. Masson-Delmotte, P. Zhai, A. Pirani, S. Connors, C. Pean, S. Berger, N. Caud, Y. Chen, L. Goldfarb, M. Gomis, M. Huang, K. Leitzell, E. Lonnoy, J. Matthews, T. Maycock, T. Waterfield, O. Yelekci, R. Yu and B. Zhou, Eds., Cambridge, UK, Cambridge Univesity Press, 2021, pp. 1055-1210.

[3] S. Seneviratne, X. Zhang, M. Adnan, W. Badi, C. Dereczynski, A. DiLuca, S. Ghosh, I. Iskandar, J. Kossin, S. Lewis, F. Otto, I. Pinto, M. Satoh, S. Vincente-Serrano, M. Wehner and Zhou, "Weather and Climate Extreme Events in a Changing Climate," in *Climate Change 2021: The Physical Science Basis. Contribution of Working Group I to the Sixth Assessment Report of the Intergovernmental Panel on Climate Change*, V. Masson-Delmotte, P. Zhai, A. Pirani, S. Connors, C. Pean, S. Berger, N. Caud, Y. Chen, L. Goldfarb, M. Gomis, M. Huang, K. Leitzell, E. Lonnoy, J. Matthews, T. Maycock, T. Waterfield, O. Yelekci, R. Yu and B. Zhou, Eds., Cambridge, UK, Cambridge University Press, 2021, pp. 1513-1766.

[4] B. Fox-Kepmer, H. Hewitt, C. Xiao, G. Adalgeirsdottir, S. Drijfthout, T. Edwards, N. Golledge, M. Hemer, R. Kopp, G. Krinner, A. Mix, D. Notz, S. Nowicki, I. Nurhati, L. Ruiz, J. Sallee, A. Slangen and Y. Yu, "Ocean, Cryosphere and Sea Level Change," in *Climate Change 2021: The Physical Science Basis. Contribution of Working Group I to the Sixth Assessment Report of the Intergovernmental Panel on Climate Change*, V. Masson-Delmotte, P. Zhai, A. Pirani, S. Connors, C. Pean, S. Berger, N. Caud, Y. Chen, L. Goldfarb, M. Gomis, M. Huang, K. Leitzell, E. Lonnoy, J. Matthews, T. Maycock, T. Waterfield, O. Yelekci, R. Yu and B. Zhou, Eds., Cambridge, UK, Cambridge University Press, 2021, pp. 1211-1362.

[5] IPCC, Climate Change 2022: Impacts, Adaptation and Vulnerability. Contribution of Working Group II to the Sixth Assessment Report of the Intergovernmental Panel on Climate Change, H. Portner, D. Roberts, M. Tignor, E. Poloczanska, K. Minterbeck, A. Alegria, M. Craig, S. Langsdorf, S. Loschke, V. Moller, A. Okem and B. Rama, Eds., Cambridge, UK, 2022.

[6] S. E. Schwartz, "Resource Letter GECC-1: The Greenhouse Effect and Climate Change: Earth's Natural Greenhouse Effect," *American Journal of Physics*, vol. 86, no. 8, pp. 565-576, August 2018a.

[7] F. T. MacKenzie and A. Lerman, "Heat Balance of the Atmosphere and Carbon Dioxide," in *Carbon in the Geobiosphere — Earth's Outer Shell —*, vol. 25, Dordrecht, Springer, 2006, pp. 61-88.

[8] S. E. Schwartz, "Resource Letter GECC-2: The Greenhouse Effect and Climate Change: The Intensified Greenhouse Effect," *American Journal of Physics*, vol. 86, no. 9, pp. 645-656, September 2018b.

[9] P. Forster, T. Storelvmo, K. Armour, W. Collins, J. Dufresne, D. Frame, D. Lunt, T. Mauritsen, M. Palmer, M. Watanabe, M. Wild and H. Zhang, "The Earth's Energy Budget, Climate Feedbacks, and Climate Sensitivity," in *Climate Change 2021: The Physical Science Basis. Contribution of Working Group I to the Sixth Assessment Report of the Intergovernmental Panel on Climate Change*, V. Masson-Delmotte, P. Zhai, A. Pirani, S. Connors, C. Pean, S. Berger, N. Caud, Y. Chen, L. Goldfarb, M. Gomis, M. Huang, K. Leitzell, E. Lonnoy, J. Matthews, T. Maycock, T. Waterfield, O. Yelekci, R. Yu and B. Zhou, Eds., Cambridge, UK, Cambridge University Press, 2021, pp. 923-1054.

[10] G. Myhre, D. Shindell, F.-M. Breon, W. Collins, J. Fuglestvedt, J. Huang, D. Koch, J.-F. Lamarque, D. Lee, B. Mendoza, T. Nakajima, A. Robock, G. Stephens, T. Takemura and H. Zhang, "Anthropogenic and Natural Radiative Forcing," in *Climate Change 2013: The Physical Science Basis. Contribution of Working Group I to the Fifth Assessment Report of the Intergovernmental Panel on Climate Change*, Cambridge, United Kingdom and New York, NY, USA, Cambridge Universirty Press, 2013, pp. 659-740.

[11] V. Eyring, N. Gillett, K. Achuta Rao, R. Barimalala, M. Barreriro Parrillo, N. Bellouin, C. Cassou, P. Durack, Y. Kosaka, S. McGregor, S. Min, O. Monrgenstern and Y. Sun, "Human Influence on the Climate System," in *Climate Change 2021: The Physical Science Basis. Contribution of Working Group I to the Sixth Assessment Report of the Intergovernmental Panel on Climate Change*, V. Masson-Delmotte, P. Zhai, A. Pirani, S. Connors, C. Pean, S. Berger, N. Caud, Y. Chen, L. Goldfarb, M. Gomis, M. Huang, K. Leitzell, E. Lonnoy, J. Matthews, T. Maycock, T. Waterfield, O. Yelekci, R. Yu and B. Zhou, Eds., Cambridge, UK, Cambridge University Press, 2021, pp. 423-552.

[12] J. Canadell, P. Monteiro, M. Costa, L. Cotrim da Cunha, P. Cox, A. Eliseev, S. Henson, M. Ishii, S. Jaccard, C. Koven, A. Lohila, P. Patra, S. Piao, J. Rogelj, S. Syampungani, S. Zaehle and K. Zickfeld, "Global Carbon and other Biogeochemical Cycles and Feedbacks," in *Climate Change 2021: The Physical Science Basis. Contribution of Working Group I to the Sixth Assessment Report of the Intergovernmental Panel on Climate Change*, V. Masson-Delmotte, P. Zhai, A. Pirani, S. Connors, C. Pean, S. Berger, N. Caud, Y. Chen, L. Goldfarb, M. Gomis, M. Huang, K. Leitzell, E. Lonnoy, J. Matthews, T. Maycock, T. Waterfield, O. Yelekci, R. Yu and B. Zhou, Eds., Cambridge, UK, Cambridge University Press, 2021, pp. 673-816.

[13] J. Lee, J. Marotzke, G. Bala, L. Cao, S. Corti, J. Dunne, F. Engelbrecht, E. Fischer, J. Fyfe, C. Jones, A. Maycock, J. Mutemis, O. Ndiaye and S. Panickal, "Future Global Climate: Scenario-Based Projections and Near-Term Information," in *Climate Change 2021: The Physical Science Basis. Contribution of Working Group I to the Sixth Assessment Report of the Intergovernmental Panel on Climate Change*, V. Masson-Delmotte, P. Zhai, A. Pirani, S. Connors, C. Pean, S. Berger, N. Caud, Y. Chen, L. Goldfarb, M. Gomis, M. Huang, K. Leitzell, E. Lonnoy, J. Matthews, T. Maycock, T. Waterfield, O. Yelekci, R. Yu and B. Zhou, Eds., Cambridge, UK, Cambridge University Press, 2021.

[14] IPCC, "Summary for Policy Makers," in *Climate Change 2021: The Physical Science Basis. Contribution of Working Group I to the Sixth Assessment Report of the Intergovernmental Panel on Climate Change*, V. Masson-Delmotte, P. Zhai, A. Pirani, S. Connors, C. Pean, S. Berger, N. Caud, Y. Chen, L. Goldfarb, M. Gomis, M. Huang, K. Leitzell, E. Lonnoy, J. Matthews, T. Maycock, T. Waterfield, O. Yelekci, R. Yu and B. Zhou, Eds., Cambridge, UK and New York, NY,USA, Cambridge University Press, 2021, pp. 3-32.

[15] IPCC, in *Climate Change 2022: Mitigation of Climate Change. Contribution of Working Group III to the Sixth Assessment Report of the Intergovernmental Panel on Climate Change*, P. Shukla, J. Skea, R. Slade, A. AlKhourdajie, R. van Diemen, D. McCollum, M. Pathak, S. Some, S. Vyas, R. Fradera, M. Belkacemi, A. Hasija, G. Lisboa, S. Luz and J. Malley, Eds., Cambridge, UK, Cambridge University Press, 2022.

[16] N. S. Bentsen, "Carbon debt and payback time – Lost in the forest?," *Renewable and Sustainable Energy Reviews,* vol. 73, pp. 1211-1217, 2017.

[17] W. Liu, C. Peng, Z. Chen, Y. Liu, J. Yan, J. Li and T. Sang, "Sustainable bioenergy production with little carbon debt in the Loess Plateau of China," *Biotechnology for Biofuels,* vol. 9, no. 161, 2016.

[18] IEA, "Bioenergy Power Generation," International Energy Agency, Paris, 2021.

[19] IEA, “Bioenergy with Carbon Capture and Storage,” International Energy Agency, Paris, 2022.

[20] IPCC, “IPCC special report on the impacts of global warming of 1.5 °C above pre-industrial levels and related global greenhouse gas emission pathways,” V. Masson-Delmotte, P. Zhai, H. O. Portner, D. Roberts, J. Skea, P. R. Shukla, A. Pirani, W. Moufouma-Okia, C. Pean, R. Pidcock, S. Connors, J. B. R. Matthews, Y. Chen, X. Zhou, M. I. Gomis, E. Lonnoy, Maycock, M. Tignor and T. Waterfield, Eds., Geneva, Switzerland, World Meteorological Organization, 2018.

[21] IEA, “About CCUS,” International Energy Agency, Paris, 2021.

[22] *Paris Agreement to the United Nations Framework Convention on Climate Change,* Paris, 2015.

[23] *Climate Change Act 2008,* vol. c. 27.

[24] UK National Statistics, “2016 UK greenhouse gas emissions: final figures - data tables,” London, 2018.

[25] *Carbon Budgets Order 2009,* vol. SI 2009/1259.

[26] *Carbon Budget Order 2011,* vol. SI 2011/1603.

[27] *Carbon Budget Order 2016,* vol. SI 2016/785.

[28] *Carbon Budget Order 2021.*

[29] Department for Business, Energy & Industrial Strategy, “Net Zero Strategy: Build Back Greener,” HM Government, 2021.

[30] Department for Business, Energy & Industrial Strategy, “Energy White Paper: Powering our net zero future,” HM Government, 2020.

[31] Department for Business, Energy, & Industrial Strategy, “Biomass Policy Statement,” HM Government, 2021.

[32] J. Kalina, “Techno-economic assessment of small-scale integrated biomass gasification dual fuel combined cycle power plant,” *Energy,* vol. 141, pp. 2499-2507, 2017.

[33] A. Gomez-Barea, S. Nilsson, F. Barrero and M. Campoy, “Devolatilization of wood and wastes in fluidized bed,” *Fuel Processing Technology,* vol. 91, pp. 1624-1633, 2010.

[34] H. Thunman, F. Niklasson, F. Johnsson and B. Leckner, “Composition of Volatile Gases and Thermochemical Properties of Wood for Modeling of Fixed or Fluidized Beds,” *Energy & Fuels,* vol. 15, pp. 1488-1497, 2001.

[35] D. Neves, H. Thunman, A. Matos, L. Tarelho and A. Gómez-Barea, "Characterization and prediction of biomass pyrolysis products," *Progress in Energy and Combustion Science,* vol. 37, pp. 611-630, 2011.

[36] S. Ascher, W. Sloan, I. Watson and S. You, "A comprehensive artificial neural network model for gasification process prediction," *Applied Energy,* vol. 320, 2022.

[37] P. J. Phillips, C. A. Hahn, P. C. Fontana, A. N. Yates, K. Greene, D. A. Broniatowski and M. A. Przybocki, "Four Principles of Explainable Artificial Intelligence," National Institute of Standars and Technology, 2021.

[38] D. L. Giltrap, R. McKibbin and G. R. G. Barnes, "A steady state model of gas-char reactions in a downdraft biomass gasifier," *Solar Energy,* vol. 74, pp. 85-91, 2003.

[39] J. Yu and J. Smith, "Validation and application of a kinetic model for biomass gasification simulation and optimization in updraft gasifiers," *Chemical Engineering & Processing: Process Intensification,* vol. 125, pp. 214-226, 2018.

[40] C. DiBlasi and C. Branca, "Modeling a stratified downdraft wood gasifier with primary and secondary air entry," *Fuel,* vol. 104, pp. 847-860, 2013.

[41] A. Sharma, "Modeling and simulation of a downdraft biomass gasifier 1. Model development and validation," *Energy Conversion and Management,* vol. 52, pp. 1386-1396, 2011.

[42] P. Basu, Biomass gasification and pyrolysis: Practical design and theory, 2nd ed., Boston: Academic Press, 2013.

[43] E. Ranzi, P. E. Debiagi and A. Frassoldati, "Mathematical Modeling of Fast Biomass Pyrolysis and Bio-Oil Formation," *ACS Sustainable Chemistry & Engineering,* vol. 5, pp. 2867-2881, 2017.

[44] C. A. Koufopanos, N. Papayannakos, G. Maschio and A. Lucchesi, "Modelling of the pyrolysis of biomass particles. Studies on kinetics, thermal and heat transfer effects," *The Canadian journal of chemical engineering,* vol. 64, no. 9, pp. 907-915, 1991.

[45] V. K. Srivasta, Sushil and R. K. Jalan, "Prediction of Concentration in the Pyrolysis of Biomass Material - II," *Energy Conversion and Management,* vol. 37, no. 4, pp. 473-483, April 1996.

[46] B. V. Babu and A. S. Chaurasia, "Modeling, simulation and estimation of optimum parameters in pyrolysis of biomass," *Energy Conversion and Management,* vol. 44, no. 13, pp. 2135-2158, 2003.

[47] A. Chaurasia, "Modeling, simulation and optimization of downdraft gasifier: Studies on chemical kinetics and operating conditions on the performance of the biomass gasification process," *Energy,* vol. 116, pp. 1065-1076, 2016.

[48] N. Bianco, M. C. Paul, G. Brownbridge, D. Nurkowski, A. Salem, U. Kumar, A. Bhave and M. Kraft, "Automated Advanced Calibration and Optimization of Thermochemical Models Applied to Biomass Gasification and Pyrolysis," *Energy & Fuels,* 2018.

[49] U. Kumar and M. C. Paul, "CFD modelling of biomass gasification with a volatile break-up approach," *Chemical Engineering Science,* vol. 195, pp. 413-422, 2019.

[50] A. M. Salem and M. C. Paul, "An Integrated Kinetic Model for Downdraft Gasifier Based on a Novel Approach that Optimises the Reduction Zone of Gasifier," *Biomass and Bioenergy,* vol. 109, pp. 172-181, 2018.

[51] U. Kumar and M. Paul, "Sensitivity analysis of homogeneous reactions for thermochemical conversion of biomass in a downdraft gasifier," *Renewable Energy,* vol. 151, pp. 332-341, 2020.

[52] P. P. Dutta, V. Pandey, A. R. Das, S. Sen and D. C. Baruah, "Down Draft Gasification Modelling and Experimentation of Some Indigenous Biomass for Thermal Applications," in *Energy Procedia,* 2014.

[53] I. Silva, R. Lima, G. Silva, D. Ruzene and D. Silva, "Thermodynamic equilibrium model based on stoichiometric method for biomass gasification: A review of model modifications," *Renewable and Sustainable Energy Reviews,* vol. 114, p. 109305, 2019.

[54] A. Melgar, J. F. Perez, H. Laget and A. Horillo, "Thermochemical equilibrium modelling of a gasifying process," *Energy conversion and management,* vol. 48, pp. 59-67, 2007.

[55] S. Shabbar and I. Janajreh, "Thermodynamic equilibrium analysis of coal gasification using Gibbs energy minimization method," *Energy Conversion and Management,* vol. 65, pp. 755-763, 2013.

[56] M. Puig-Arnavat, J. C. Bruno and A. Coronas, "Modified Thermodynamic Equilibrium Model for Biomass Gasification: A Study of the Influence of Operating Conditions," *Energy & Fuels,* vol. 26, no. 2, pp. 1385-1394, 2012.

[57] E. Biagini, F. Barontini and L. Togniotti, "Development of a bi-equilibrium model for biomass gasification in a downdraft bed reactor," *Bioresource Technology,* vol. 201, pp. 156-165, 2016.

[58] P. Basu, Biomass gasification and pyrolysis: Practical design and theory, 2nd ed., Boston: Academic Press, 2013.

[59] Y. Ji-chao and B. Sobhani, "Integration of biomass gasification with a supercritical CO2 and Kalina cycles in a combined heating and power system: A thermodynamic and exergoeconomic analysis," *Energy,* vol. 222, p. 119980, 2021.

[60] F. Hamrang, A. Shokri, S. M. S. Mahmoudi, B. Ehghaghi and M. Rosen, "Performance Analysis of a New Electricity and Freshwater Production System Based on an Integrated Gasification Combined Cycle and Multi-Effect Desalination," *Sustainability*, vol. 12, no. 19, p. 7996, 2020.

[61] P. Chaiwatanodom, S. Vivanpatarakij and S. Assabumrungrat, "Thermodynamic analysis of biomass gasification with CO2 recycle for synthesis gas production," *Applied Energy*, vol. 114, pp. 10-17, 2014.

[62] B. Prabowo, M. Aziz, K. Umeki, H. Susanto, M. Yan and K. Yoshikawa, "CO2-recycling biomass gasification system for highly efficient and carbon-negative power generation," *Applied Energy*, vol. 158, pp. 97-106, 2015.

[63] K. Austin, J. Baker, B. Sohngen, C. Wade, A. Daigneault, S. Ohrel, S. Ragnauth and A. Bean, "The economic costs of planting, preserving, and managing the world's forests to mitigate climate change," *Nature Communications*, vol. 11, p. 5946, 2020.

[64] C. Gough and P. Upham, "Biomass energy with carbon capture and storage (BECCS or Bio-CCS)," *Greenhouse Gas Sci Technol*, vol. 1, pp. 324-334, 2011.

[65] J. Gibbins and H. Chalmers, "Carbon capture and storage," *Energy Policy*, vol. 36, pp. 4317-4322, 2008.

[66] O. Olsson, C. Bang, M. Borchers, A. Hahn, H. Karjunen, D. Thran and T. Tynjala, "Deployment of BECCS/U value chains: Technological pathways, policy options and business models," IEA, 2020.

[67] M. Bui, C. Adjiman, A. Bardow, E. Anthony, A. Boston, S. Brown, P. Fennell, S. Fuss, A. Galindo, L. Hackett, J. Hallett, H. Herzog, G. Jackson, J. Kemper, S. Krevor, G. Maitland, M. Matuszewski, I. Metcalfe, C. Petit, G. Puxty, J. Reimer, D. Reiner, E. Rubin, S. Scott, N. Shah, B. Smit, J. Trusler, P. Webley, J. Wilcox and N. MacDowell, "Carbon capture and storage (CCS): the way forward," *Energy & Environmental Science*, vol. 11, pp. 1062-1176, 2018.

[68] F. Cheng, A. Small and L. Colosi, "The levelized cost of negative CO2 emissions from thermochemical conversion of biomass coupled with carbon capture and storage," *Energy Conversion and Management*, vol. 237, p. 114115, 2021.

[69] M. Fajardy, J. Morris, A. Gurgel, H. Herzog, N. MacDowell and S. Paltsev, "The economics of bioenergy with carbon capture and storage (BECCS) deployment in a 1.5C or 2C world," *Global Environmental Change*, vol. 68, p. 102262, 2021.

[70] M. Michaga, S. Michailos, M. Akram, E. Cardozo, K. Hughes, D. Ingham and M. Pourkashanian, "Bioenergy with carbon capture and storage (BECCS) potential in jet fuel production from forestry residues: A combined Techno-Economic and Life

Cycle Assessment approach," *Energy Conversion and Management,* vol. 225, p. 115346, 2022.

[71] O. Emenike, S. Michailos, K. Hughes, D. Ingham and M. Pourkashanian, "Techno-economic and environmental assessment of BECCS in fuel generation for FT-fuel, bioSNG and OMEx," *Sustainable Energy and Fuels,* vol. 5, pp. 3382-3402, 2021.

[72] M. Muratori, H. Kheshgi, B. Mignone, H. McJeon and L. Clarke, "The future role of CCS in electricity and liquid fuel supply," in *Energy Procedia,* Lausanne, Switzerland, 2017.

[73] C. Heuberger, I. Staffell, N. Shah and N. MacDowell, "Quantifying the value of CCS for the future electricity system," *Energy & Environmental Science,* vol. 9, pp. 2497-2510, 2016.

[74] C. Hepburn, E. Adlen, J. Beddington, E. A. Carter, S. Fuss, N. MacDowell, J. C. Minx, P. Smith and C. K. Williams, "The technological and economic prospects for CO2 utilization and removal," *Nature,* vol. 575, pp. 87-97, 2019.

[75] J. M. Ahlström , V. Walter, L. Göransson and S. Papadokonstantakis, "The role of biomass gasification in the future flexible power system – BECCS or CCU?," *Renewable Energy,* vol. 190, pp. 596-605, 2022.

[76] J. M. Ahlström, S. Harvey and S. Papadokonstantakis, "Forest residues gasification integrated with electrolysis for production of SNG – modelling and assessment," *Computer aided chemical engineering,* vol. 44, pp. 109-114, 2018.

[77] M. J. Greencorn, S. D. Jackson, J. S. J. Hargreaves, S. Datta and M. C. Paul, "A novel BECCS power cycle using CO2 exhaust gas recycling to enhance biomass gasification," in *International Conference on Applied Energy 2019*, Västerås, Sweden, 2019.

[78] M. J. Greencorn, S. D. Jackson, J. S. J. Hargreaves, S. Datta and M. C. Paul, "Thermodynamic Limitations to Direct CO2 Utilisation within a Small-scale Integrated Biomass Power Cycle," *Energy Conversion and Management,* vol. 269, 2022.

[79] E. Schwab, A. Milanov, S. A. Schunk, A. Behrens and N. Schodel, "Dry Reforming and Reverse Water Gas Shift: Alternatives for Syngas Production?," *Chemie Ingenieur Technik,* vol. 87, no. 4, pp. 347-353, 2015.

[80] P. Lahijani, Z. A. Zainal, M. Mohammadi and A. R. Mohamed, "Conversion of the greenhouse gas CO2 to the fuel gas CO via the Boudouard reaction: A review," *Renewable and Sustainable Energy Reviews,* pp. 615-632, 2015.

[81] D. G. Roberts and D. J. Harris, "A Kinetic Analysis of Coal Char Gasification Reactions at High Pressures," *Energy & Fuels,* vol. 20, pp. 2314-2320, 2006.

[82] G. Wang, J. Zhang, X. Hou, J. Shao and W. Geng, “Study on CO2 gasification properties and kinetics of biomass chars and anthracite char,” *Bioresource Technology,* vol. 177, pp. 66-73, 2015.

[83] C. Guizani, O. Louisnard, F. J. Escudero Sanz and S. Salvador, “Gasification of woody biomass under high heating rate conditions in pure CO2: Experiments and modelling,” *Biomass and Bioenergy,* vol. 83, pp. 169-182, 2015.

[84] H.-H. Bui, L. Wang, K.-Q. Tran and O. Skreiberg, “CO2 gasification of charcoals produced at various pressures,” *Fuel Processing Technology,* vol. 152, pp. 207-214, 2016.

[85] A. Gomez, M. Vargas and N. Mahinpey, “A theoretical model to estimate steamand CO2 gasification rates based on feedstock characterization properties,” *Fuel Processing Technology,* vol. 149, pp. 187-194, 2016.

[86] I. Ahmed and A. K. Gupta, “Characteristics of cardboard and paper gasification with CO2,” *Applied Energy,* vol. 86, pp. 2626-2634, 2009.

[87] I. I. Ahmed and A. K. Gupta, “Kinetics of woodchips char gasification with steam and carbon dioxide,” *Applied Energy,* vol. 88, pp. 1613-1619, 2011.

[88] H. C. Butterman and M. J. Castaldi, “CO2 as a Carbon Neutral Fuel Source via Enhanced Biomass Gasification,” *Environmental science & technology,* vol. 43, no. 23, pp. 9030-9037, December 2009.

[89] Y. Shen, D. Ma and X. Ge, “CO2-looping in biomass pyrolysis or gasification,” *Sustainable Energy & Fuels,* vol. 1, pp. 1700-1729, 2017.

[90] P. Chaiwatanodom, S. Vivanpatarakij and S. Assabumrungrat, “Thermodynamic analysis of biomass gasification with CO2 recycle for synthesis gas production,” *Applied Energy,* vol. 114, pp. 10-17, 2014.

[91] T. Renganathan, M. V. Yadav, S. Pushpavanam, R. K. Voolapalli and Y. S. Cho, “CO2 utilization for gasification of carbonaceous feedstocks: A thermodynamic analysis,” *Chemical Engineering Science,* vol. 83, pp. 159-170, 2012.

[92] A. Ravikiran, T. Renganathan, S. Pushpavanam, R. K. Voolapalli and Y. S. Cho, “Generalized Analysis of Gasifier Performance using Equilibrium Modeling,” *Industrial and Engineering Chemistry Research,* vol. 51, pp. 1601-1611, 2012.

[93] L. Wang, A. N. Izaharuddin, N. Karimi and M. C. Paul, “A numerical investigation of CO2gasification of biomass particles-analysis of energy, exergy and entropy generation,” *Energy,* vol. 228, p. 120615, 2021.

[94] B. Prabowo, H. Susanto, K. Umeki, M. Yan and K. Yoshikawa, “Pilot scale autothermal gasification of coconut shell with CO2-O2 mixture,” *Frontiers in Energy,* vol. 9, no. 3, pp. 362-370, 2015.

[95] V. M. Janganathan and S. Varunkumar, “Net carbon-dioxide conversion and other novel features of packed bed biomass gasification with O2/CO2 mixtures,” *Fuel,* vol. 244, pp. 545-558, 2019.

[96] B. Prabowo, K. Umeki, M. Yan, M. R. Nakamura, M. J. Castaldi and K. Yoshikawa, “CO2–steam mixture for direct and indirect gasification of rice straw in a downdraft gasifier: Laboratory-scale experiments and performance prediction,” *Applied Energy,* vol. 113, pp. 670-679, 2014.

[97] M. E. Walker, J. Abbasian, D. J. Chmielewski and M. J. Castaldi, “Dry Gasification Oxy-combustion Power Cycle,” *Energy & Fuels,* vol. 25, pp. 2258-2266, 2011.

[98] H. Ishii, T. Hayashi, H. Tada, K. Yokohama, R. Takashima and J.-i. Hayashi, “Critical assessment of oxy-fuel integrated coal gasification combined cycles,” *Applied Energy,* pp. 156-169, 2019.

[99] S. Saqline, Z. Chua and W. Liu, “Coupling chemical looping combustion of solid fuels with advanced steam cycles for CO2 capture: A process modelling study,” *Energy Conversion and Management,* vol. 244, p. 114455, 2021.

[100] A. Hofmann, Physical Chemistry Essentials, Cham, Switzerland: Springer, 2018.

[101] R. Holyst and A. Poniewierski, Thermodynamics for Chemists, Physicists, and Engineering, Dordrecht: Springer, 2012.

[102] M. Schmal, Chemical Reaction Engineering, Leiden, NL: CRC Press, 2014.

[103] B. J. McBride, S. Gordon and M. A. Reno, “Coefficients for Calculating Thermodynamic and Transport Properties of Individual Species,” United States, Washington, DC, 1993.

[104] Y. Tan, W. Nookuea, H. Li, E. Thorin and J. Yan, “Evaluation of viscosity and thermal conductivity models for CO2 mixtures applied in CO2 cryogenic process in carbon capture and storage (CCS),” *Applied Thermal Engineering,* vol. 123, pp. 721-733, 2017.

[105] C. R. Wilke, “A Viscosity Equation for Gas Mixtures,” *Journal of Chemical Physics,* vol. 18, no. 4, p. 517, 1950.

[106] H. Cheung, L. A. Bromley and C. R. Wilke, “Thermal Conductivity of Gas Mixtures,” *American Institue of Chemical Engineers Journal,* vol. 8, pp. 221-228, 1962.

[107] M. Friedman and A. Kandel, Calculus Light, Berlin: Springer, 2011.

[108] M. Simone, F. Barontini, C. Nicolella and L. Tognotti, “Gasification of pelletized biomass in a pilot scale downdraft gasifier,” *Bioresource Technology,* vol. 116, pp. 403-412, 2012.

[109] A. M. Salem, I. N. Zaini, M. C. Paul and W. Yang, “The evolution and formation of tar species in a downdraft gasifier:Numerical modelling and experimental validation,” *Biomass and Bioenergy,* vol. 130, p. 105377, 2019.

[110] P. A. Breeze, Combined Heat and Power, London: Elsevier, 2018.

[111] F. Y. Hagos, A. R. Aziz and S. A. Sulaiman, “Trends of Syngas as a Fuel in Internal Combustion Engines,” *Advances in Mechanical Engineering,* pp. 1-10, 2014.

[112] T. A. Milne, R. J. Evans and N. Abatzoglou, “Biomass Gasifier Tars: Their Nature, Formation, and Conversion,” National Renewable Energy Laboratory, Golden, Colorado, 1998.

[113] J. B. Heywood, Internal Combustion Engine Fundamentals, New York: McGraw-Hill, 1988.

[114] C. R. Ferguson and A. T. Kirkpatrick, Internal Combustion Engines Applied Thermosciences, 3rd ed., Chichester: John Wiley & Sons, 2016.

[115] J. I. Ghojel, “Review of the development and applications of the Wiebe function: A tribute to the contribution of Ivan Wiebe to engine research,” *International Journal of Engine Research,* vol. 11, no. 4, pp. 297-312, 1 8 2010.

[116] A. M. Shivapuji and S. Dasappa, “Experiments and Zero D Modeling Studies Using Specific Weibe Coefficients for Producer Gas as Fuel in Spark-ignited Engines,” *Proceedings of the Institution of Mechanical Engineers, Part C: Journal of Mechanical Engineering Science,* vol. 227, no. 3, pp. 504-519, 2012.

[117] A. M. Shivapuji and S. Dasappa, “Analysis of thermodynamic scope engine simulation model empirical coefficients: Suitability assessment and tuning of conventional hydrocarbon fuel coefficients for bio syngas,” *International Journal of Hydrogen Energy,* vol. 42, no. 26, pp. 16834-16854, 29 6 2017.

[118] A. Shivapuji and S. Dasappa, “In-cylinder investigations and analysis of a SI gas engine fuelled with H2 and CO rich syngas fuel: Sensitivity analysis of combustion descriptors for engine diagnostics and control,” *International Journal of Hydrogen Energy,* vol. 39, pp. 15786-15802, 2014.

[119] F. Y. Hagos, A. R. A. Aziz and S. A. Sulaiman, “Effect of Air-fuel Ratio on the Combustion Characteristics of Syngas (H2:CO) in Direct-injection Spark-ignition Engine,” *Energy Procedia,* vol. 61, pp. 2567-2571, 1 1 2014.

[120] W. J. Annand, “Heat Transfer in the Cylinders or Reciprocating Internal Combustion Engines,” *Proceedings of the Institution of Mechanical Engineers,* vol. 177, no. 36, pp. 973-990, 1963.

[121] T. K. Hayes, R. A. White and J. E. Peters, “Combustion Chamber Temperature and Instantaneous Local Heat Flux Measurements in a Spark Ignition Engine,” *SAE Technical Paper 930217,* 1993.

[122] S. Dasappa, G. Sridhar and P. Paul, “Adaptation of small capacity natural gas engine for producer gas operation,” *Proceedings of the Institute of Mechanical Engineers Part C: Journal of Mechanical Engineering Science,* vol. 226, pp. 1568-1578, 2011.

[123] A. Shivapuji, “In-cylinder experimental and modeling studies on producer gas fuelled operation of spark ignited gas engines,” Doctoral thesis, Indian Institute of Science Bangalore, 2015.

[124] F. Y. Hagos, A. R. Aziz and S. A. Sulaiman, “Syngas (H2/CO) in a spark-ignition direct-injection engine. Part 1: Combustion, performance and emissions comparison with CNG,” *International Journal of Hydrogen Energy,* vol. 39, pp. 17884-17895, 2014.

[125] M. J. Greencorn, S. D. Jackson, J. S. J. Hargreaves, S. Datta and M. C. Paul, “Modelling the performance of a syngas fueled engine: Effect of excess air and CO2 as combustion diluents,” in *Low-Carbon Combustion Joint Meeting of the French and British Sections of the Combustion Institute,* Lille, France, 2020.

[126] D. L. Pavia, G. M. Lampman, G. S. Kriz and J. R. Vyvyan, Introduction to Spectrometry, 4 ed., Belmont, CA: Brooks/Cole, 2009.

[127] National Institute of Standards and Technology, “NIST Chemistry WebBook,” 2022. [Online]. Available: https://webbook.nist.gov/chemistry/. [Accessed 20 09 2022].

[128] C. D. Mowry, R. L. Jarek, J. Roman-Kustas, A. C. Telles and A. S. Pimentel, “Gas Analysis by Mass Spectrometry,” in *ASM Handbook,* Sandia National Larboratories, 2019, pp. 143-152.

[129] J. S. Becker, Inorganic Mass Spectrometry Principles and Applications, John Wiley & Sons, Ltd., 2007.

[130] C. D. Le, S. T. Kolaczkowski and D. W. McClymont, “Using quadrupole mass spectrometry for on-line gas analysis – Gasification of biomass and refuse derived fuel,” *Fuel,* vol. 139, pp. 337-345, 2015.

[131] K. Dussan, S. Dooley and R. F. Monaghan, “A model of the chemical composition and pyrolysis kinetics of lignin,” *Proceedings of the Combustion Institute,* pp. 2697-2704, 2019.

[132] G. Bergerhoff and I. D. Brown, Crystallographic Databases, F. H. Allen, G. Bergerhoff and R. Sievers, Eds., Chester: Interational Union of Crystallography, 1987.

[133] M. Sieradzka, A. Mlonka-Mędrala and A. Magdziarz, "Comprehensive investigation of the CO2 gasification process of biomass wastes using TG-MS and lab-scale experimental research," *Fuel,* vol. 330, 2022.

[134] H. Li and A. G. McDonald, "Fractionation and characterization of industrial lignins," *Industrial Crops and Products,* vol. 62, pp. 67-76, 2014.

[135] Y. Lee, J. Park, C. Ryu, K. S. Gang, W. Yang, Y. Park, J. Jung and S. Hyun, "Comparison of biochar properties from biomass residues produced by slow pyrolysis at 500 C," *Bioresource Technology,* vol. 148, pp. 196-201, 2013.

[136] M. B. Figueiredo, I. Hita, P. J. Deuss, R. H. Venderbosch and H. J. Heeres, "Pyrolytic lignin: a promising biorefinery feedstock for the production of fuels and valuable chemicals," *Green Chemistry,* vol. 24, pp. 4680-4702, 2022.

[137] C. Wu, Z. Wang, J. Huang and P. T. Williams, "Pyrolysis/gasification of cellulose, hemicellulose and lignin for hydrogen production in the presence of various nickel-based catalysts," *Fuel,* vol. 106, pp. 697-706, 2013.

[138] P. D. Muley, C. Henkel, K. K. Abdollahi, C. Marculescu and D. Boldor, "A critical comparison of pyrolysis of cellulose, lignin, and pine sawdust using an induction heating reactor," *Energy conversion and Management,* vol. 117, pp. 273-280, 2016.

[139] C. Li, J. Hayashi, Y. Sun, L. Zhang, S. Zhang and S. Wang, "Impact of heating rates on the evolution of function groups of the biochar from lignin pyrolysis," *Journal of Analytical and Applied Pyrolysis,* vol. 155, 2021.

[140] D. Ferdous, A. K. Dalai, S. K. Bej and R. W. Thring, "Pyrolysis of Lignins: Experimental and Kinetics Studies," *Energy & Fuels,* vol. 16, pp. 1405-1412, 2002.

[141] G. Li, C. Liu, X. Cui, Y. Yang and F. Shi, "Oxidative dehydrogenation of light alkanes with carbon dioxide," *Green Chemistry,* vol. 23, pp. 689-707, 2021.

[142] D. Mukherjee, S. Park and B. Reddy, "CO2 as a soft oxidant for oxidative dehydrogenation reaction: An eco benign process for industry," *Journal of CO2 Utilization,* vol. 16, pp. 301-312, 2016.

[143] D. Neves, H. Thunman, A. Matos, L. Tarelho and A. Gomez-Barea, "Characterization and prediction of biomass pyrolysis products," *Progress in Energy and Combustion Science,* vol. 37, pp. 611-630, 2011.

[144] N. P. Perez, E. B. Machin, D. T. Pedroso, J. J. Roberts, J. S. Antunes and J. L. Silveira, "Biomass gasification for combined heat and power generation in the

Cuban context: Energetic and economic analysis," *Applied Thermal Engineering,* vol. 90, pp. 1-12, 2015.

[145] B. Pandey, P. N. Sheth and Y. K. Prajapati, "Air-CO2 and oxygen-enriched air-CO2 biomass gasification in an autothermal downdraft gasifier: Experimental studies," *Energy Conversion and Management,* vol. 270, 2022.

[146] D. Antolini, S. Ail, F. Patuzzi, M. Grigiante and M. Baratieri, "Experimental investigations of air-CO2 biomass gasification in reversed downdraft gasifier," *Fuel,* vol. 253, pp. 1473-1481, 2019.